

**FROM CELL TO ORGANISM: A PREDICTIVE MULTISCALE MODEL
OF DRUG TRANSPORT**

by

Xinyuan Zhang

A dissertation submitted in partial fulfillment
of the requirements for the degree of
Doctor of Philosophy
(Pharmaceutical Sciences)
in The University of Michigan
2010

Doctoral Committee:

Associate Professor Gustavo Rosania, Chair
Professor Gordon L. Amidon
Professor Steven P. Schwendeman
Professor Shuichi Takayama

© Xinyuan Zhang
2010

To my parents and my husband

With all my love and thanks

ACKNOWLEDGEMENTS

I would like to thank my advisor, Dr. Gus R. Rosania, for all of his insightful and valuable guidance during my Ph.D. study. I learned not only scientific knowledge from him, but also the way and attitude of doing science, being honest, creative, and open. His office door is always open and whenever I had questions, I always felt free to go and ask. I am grateful for his continuous support to many decisions I made, such as pursuing Master's degree in Statistics, doing an internship in my last year of study, and attending many conferences to present my work.

I would also like to thank my dissertation committee members, Dr. Gordon L. Amidon, Dr. Steven P. Schwendeman, and Dr. Shuichi Takayama, for their valuable time, suggestions, and input. All the unexpected questions, challenges, discussions, and suggestions made me think further and more deeply about my project. I would like to thank Dr. Stefan Trapp from the Technical University of Denmark and Dr. Richard W. Horobin from the University of Glasgow, for their help with the original model. I thank Dr. Kerby Shedden from the Department of Statistics of the University of Michigan, for all the discussions about my project. From him I learned how the statistics can help in scientific discovery. I appreciated the opportunity of studying population pharmacokinetics from Dr. Rose Feng. Discussions with her and suggestions from her helped me a lot when I was extending cell-based pharmacokinetic models to whole body physiologically-based pharmacokinetic models.

I also received many help from friends, peer students, and alumni of the College of Pharmacy. I would especially like to thank Nan Zheng, Jingyu Jerry Yu, Peng Zou, Jason Baik, Kyoung-Ah Min, Dr. Vivien Chen Nielsen, Maria Posada, Samuel Reinhold, Dr. Jenny Jie Sheng, Dr. Li Zhang, Tien-Yi Lee, Haili Ping, Ke Ma, Hee-Sun Chung, Dr. Theresa Nguyen, and Dr. Yasuhiro Tsume for their friendship and support.

I am indebted to the staff of the College of Pharmacy for all their help, with special thanks to Lynn Alexander, Terri Azar, Pat Greeley, L.D. Hieber, Dr. Cherie Dotson, Jeanne Getty, and Maria Herbel. I feel very sorry that Lynn left us forever. I acknowledge all the financial support for my research from the College of Pharmacy, Fred Lyons Jr. Fellowship, and Schering-Plough Graduate Fellowship.

Lastly, I want to thank my parents for their love, support and patience; my husband, Zhijiang He, for encouraging me, supporting me, and always being my Matlab consultant.

TABLE OF CONTENTS

DEDICATION	ii
ACKNOWLEDGEMENTS	iii
LIST OF TABLES	vii
LIST OF FIGURES	viii
LIST OF APPENDICES	xi
CHAPTER I	1
INTRODUCTION.....	1
Abstract	1
Introduction.....	3
Subcellular compartment --- How do you define it?	4
pH-partition theory and ion-trapping mechanism.....	5
The Goldman-Hodgkin-Katz equation	7
Empirical and semi-empirical models	8
Mechanistic physiologically-based models	14
Comparison of empirical models with mechanistic models	19
Cellular pharmacokinetics modeling in relation to macroscopic ADMET	22
Conclusions.....	23
Specific aims.....	24
References.....	29
CHAPTER II.....	39
A CELL-BASED MOLECULAR TRANSPORT SIMULATOR FOR PHARMACOKINETIC PREDICTION AND CHEMINFORMATIC EXPLORATION.....	39
Abstract.....	39
Introduction.....	41
Methods.....	43
Results.....	51
Discussion.....	59
References.....	75
CHAPTER III	80

SIMULATION-BASED CHEMINFORMATIC ANALYSIS OF ORGANELLE-TARGETED MOLECULES: LYSOSOMOTROPIC MONOBASIC AMINES.....	80
Abstract.....	80
Introduction.....	82
Methods.....	84
Results.....	91
Discussion.....	98
References.....	118
CHAPTER IV.....	123
CELLS ON PORES: A SIMULATION-DRIVEN ANALYSIS OF TRANSCELLULAR SMALL MOLECULE TRANSPORT	123
Abstract.....	123
Introduction.....	125
Materials and Methods.....	126
Results.....	136
Discussion.....	143
References.....	159
CHAPTER V.....	161
SINGLE-CELL PHYSIOLOGICALLY-BASED PHARMACOKINETIC (1CELLPBPK) MODELING OF DRUG DISTRIBUTION IN THE LUNG.....	161
Abstract.....	161
Introduction.....	163
Methods.....	165
Results.....	172
Conclusion and Discussion.....	174
References.....	185
CHAPTER VI.....	189
FINAL DISCUSSION.....	189
Integration of molecular size	190
Integration of molecular interactions	190
Mechanistic models for hypothesis testing and experimental design	191
Extension of 1CellPK towards multiorgan PBPK modeling	192
Disseminating 1CellPK.....	193
References.....	195
APPENDICES.....	197

LIST OF TABLES

Table 1.1: Summary of empirical models for subcellular localization prediction.....	27
Table 1.2: Summary of mechanistic cellular PK models.....	28
Table 2.1. Structures, physicochemical properties, average Caco2 permeabilities, and predictive permeabilities of seven β -adrenergic blockers.....	64
Table 2.2. Comparison of predicted permeability with average Caco2 permeability and PAMA permeability of drugs within the predictive circle in Figure 2.3.....	65
Table 2.3. Correlation of predicted permeability VS. human intestinal permeability.....	67
Table 3.1. The test set of ninety-nine lysosomotropic monobasic amines.	106
Table 4.1. Calculated distribution and logP values for each microspecies of CQ at pH 6.5 and pH 7.4, used as input for 1CellPK.....	147
Table 4.2. Parameter ranges for Monte Carlo simulations.	148
Table 4.3. Simulation and quantitative experimental data of CQ transport across MDCK cells on polyester membranes of varying porosity, at donor compartment pH 6.5 and 7.4.....	150
Table 5.1. Physiological parameters for tissue volumes and blood flow rates in a 250 g rat.	176
Table 5.2. Summary of in vivo, in vitro and physicochemical properties for atenolol, metoprolol, and propranolol.....	177
Table 5.3. Comparison of tissue : unbound plasma partition coefficient ($K_{p,u}$) values in the lung of S-metoprolol	178

LIST OF FIGURES

Figure 2.1. Model of an intestinal epithelial cell.	68
Figure 2.2. Correlation of Caco2 permeability and predicted permeability of seven β -adrenergic blockers.	69
Figure 2.3. Correlation of Caco2 permeability and predicted permeability of thirty-six drugs.....	70
Figure 2.4. Correlation of human intestinal permeability and predicted permeability.....	71
Figure 2.5. Effects of physicochemical properties on intracellular concentration at steady state, of a molecule with metoprolol-like properties (arrows).....	72
Figure 2.6. The chemical space occupied by molecules with ideal pharmacokinetic properties:	73
Figure 2.7. The chemical space defined by metoprolol-like reference molecule.	74
Figure 3.1. Diagrams showing the cellular pharmacokinetic phenomena captured by the two mathematical models used in this study:	111
Figure 3.2. Visualizing the simulated physicochemical property space occupied by lysosomotropic monobasic amines.	112
Figure 3.3. Visualizing the simulated physicochemical property space occupied by selectively lysosomotropic monobasic amines.	113
Figure 3.4. Visualizing the relationship between transcellular permeability and lysosomotropic character.....	114

Figure 3.5. Visualizing the simulated physicochemical property space occupied by molecules with low intracellular accumulation and high permeability.	115
Figure 3.6. Visualizing the simulated physicochemical property space of various classes of non-selective, lysosomotropic molecules.	116
Figure 3.7. Visualizing the effect of extracellular pH on physicochemical property space occupied by selectively-lysosomotropic molecules.	117
Figure 4.1. Microscopic images of polyester membranes and MDCK cells grown on a 0.4 μ m-membrane.	151
Figure 4.2. The relationship between mass transport rate and the initial concentration of CQ in the donor compartment.	152
Figure 4.3. The relationship between intracellular CQ mass and the initial concentration of CQ in the donor compartment.	153
Figure 4.4. Cell images stained with DAPI after transport experiments.	154
Figure 4.5. Histogram plots of Monte Carlo simulations	155
Figure 4.6. CQ binding experiments.	156
Figure 4.7. Effects of lysosomal swelling on CQ intracellular mass accumulation.	157
Figure 4.8. Histograms of log ₁₀ (intracellular mass, pmol/cell).	158
Figure 5.1. Integration of 1CellPK to 1CellPBPK model.	179
Figure 5.2. Comparison of predicted pharmacokinetics of atenolol in the lung and plasma with observed pharmacokinetics.	180
Figure 5.3. Comparison of predicted pharmacokinetics of atenolol in the various tissues with observed pharmacokinetics.	181

Figure 5.4. Comparison of predicted pharmacokinetics of propranolol in the lung and plasma with observed pharmacokinetics.	182
Figure 5.5. Comparison of predicted pharmacokinetics of propranolol in the various tissues with observed pharmacokinetics.	183
Figure 5.6. Effects of the thickness of surface lining liquid in alveoli on drug accumulation in the lung.	184

LIST OF APPENDICES

APPENDIX A	198
1CellPK Matlab Code	198
APPENDIX B	202
Examples of Matlab Code of Monte Carlo Simulations	202
APPENDIX C	210
Scripts	210
APPENDIX D	212
Tables and Figures Regenerated at 410K for Chapter II	212
APPENDIX E	221
Parameters for the Tracheobronchial Airways and Alveolar Region in the Rat	221

CHAPTER I

INTRODUCTION

Abstract

Application of modeling and simulation has been growing significantly in different stages of drug development, from early discovery to late clinical trials, in the past decade. Mechanistic physiologically-based models to predict transport and accumulation of small molecules in organisms provide such a way to integrate information from different resources, including physiological / biological parameters and drug specific properties, for hypothesis testing, mechanisms exploration, guiding experimental design, pharmacokinetic prediction, and extrapolation of pharmacokinetic profiles across species. With the continuously increasing interests and extensive research conducted in areas of systems biology, transporters, metabolic enzymes, and pharmacogenomics, the next step would be quantitatively integrating such information to guide drug development. Cellular pharmacokinetic modeling aims to predict pharmacokinetic behaviors of compounds at cellular / subcellular level by integrating physiological parameters of cells, as well as drug specific information, such as physicochemical properties (pK_a , $\log P$), unbound fraction, active transport, and metabolic information, etc. This review will be focused on recent development of cellular pharmacokinetic models including empirical and mechanistic models. Advantages and disadvantages of each type of models will be discussed. Relationship of cellular

pharmacokinetics (PK) with systemic PK and pharmacodynamics (PD), and potential applications of cellular pharmacokinetic modeling in physiologically-based pharmacokinetic (PBPK) modeling will be included.

Keywords: Modeling and simulation; Cellular pharmacokinetics; Subcellular localization; Physiologically-based pharmacokinetic (PBPK) modeling; Cell permeability; Passive diffusion; Transporters; Metabolic enzymes; Site of action; Absorption, distribution, metabolism, excretion, and toxicity (ADMET)

Introduction

With the development of combinatorial chemistry synthesizing a large number of potential drug candidates is no longer a bottleneck in the drug discovery process. High throughput pharmacological screening methods have also been developed to quickly assay drug biological activity. Besides biological activities the high throughput methods for absorption, distribution, metabolism, excretion, and toxicity (ADMET) prediction are desired and become a major challenge in early drug discovery and development stages. Predictive physiologically-based pharmacokinetic (PBPK) models are mechanism-based mathematical models integrating prior knowledge in a quantitative way to predict pharmacokinetic properties of drugs in organisms (1-3). PBPK modeling covers a wide range of models and address ADMET properties at different levels, from subcellular level, cellular level, tissue, organ, to the whole body (4-12).

Cellular pharmacokinetics describes distribution and accumulation of compounds at cellular / subcellular level. Subcellular distribution may play an important role in determining drug efficacy and toxicity. If the site of the action is located in specific subcellular organelles, while the drug accumulates extracellularly or in other organelles, that might decrease the efficacy and induce non-specific toxicity. Similarly, if a drug targets receptors on extracellular membrane surface, but it accumulates intracellularly due to non-optimized physicochemical properties, it might lead to toxicity as well. Pulmonary toxicity of amiodarone, an antiarrhythmic agent, is observed after chronic administration. One of the explanations of the side effects is intralysosomal accumulation and its main metabolites desethylamiodarone and the drug-induced intracellular storage of phospholipids (13, 14). Recently research shows that in drug-resistant cancer cells, the

intracellular drug concentration often remains high (15, 16). One of the explanations for lack of efficacy is pH dependent ion trapping of weak basic agents to acidic intracellular compartment, extracting drugs away from their intracellular site of action (17-19).

Having observed the impact of subcellular distribution on efficacy and toxicity, interests of quantitatively describing cellular pharmacokinetics have been increasing, and computational models have been developed as tools for understanding drug transport at cellular level, rationale drug design for specific subcellular targeting, and predicting absorption, tissue distribution, and clearance (4, 6, 7, 20-24). A variety of strategies have been adapted to develop cellular pharmacokinetic models to predict subcellular accumulation or drug transport kinetics intracellularly. In general, there are two major classes of mathematical techniques used for predicting cellular pharmacokinetics: empirical models, such as applying statistical analyses to determine the relationship between structures and subcellular localization of small molecules, quantitative structure-activity relationships approaches, or fitting experimental data to get kinetic rate constant in compartmental models (21-31); and mechanism based physiological models (4, 6, 7). This review will be focused on mathematical models have been developed to analyze or predict cellular / subcellular pharmacokinetics rather than summarizing subcellular localization properties of small molecules. Features of each type of models and their potential contribution to systemic PK/PD modeling will be discussed.

Subcellular compartment --- How do you define it?

The definition of subcellular compartment may vary from models to models. Some cellular PK models treat the whole cell as one homogeneous compartment. Subcellular organelles have their unique functions and properties, such as intraluminal

pH, electrochemical potential, lipid bilayer composition, and proteins (17). Thus it is natural to treat each subcellular organelle as independent compartment, such as mitochondria, lysosomes, nuclei, endoplasmic reticulum, and Golgi apparatus. For example, F. Rashid and R. W. Horobin developed a simplistic Chinese box (SCB) model, which defined the cellular / subcellular compartment as boxes (30, 32, 33). They defined ‘a box is a region of an organism considered discrete by a biologist’ (33). Some boxes may contain another box, such as nuclei may contain nucleoli (33). Besides using organelles as subcellular compartment, another strategy to define subcellular compartment is to divide cellular compartment into N compartments, composed of a catenary chain of alternating aqueous and lipid phase as described by S. Balaz et al. (24, 34-36). The model developed by V. Y. Chen et al. defines the subcellular compartment other than cytosol as vesicles (23).

pH-partition theory and ion-trapping mechanism

Physiology of some subcellular organelles has been well studied to date. Mitochondria and lysosomes are relatively independent and membrane-enclosed organelles. Mitochondria are involved in the intrinsic pathway of apoptosis, and thus become a target of anticancer agents (37-39). The respiratory chains located in the mitochondrial inner membrane generate a proton gradient across the membrane, which yields a transmembrane potential and a pH gradient (40, 41). Depending on the cell types and differentiation stages, the ratio of membrane potential and pH gradient might differ (40). Many lipophilic cations have been observed accumulating in mitochondria as a function of the transmembrane electrical potential, which can be predicted by the Nernst equation (21, 40, 42-44), such as rhodamine 123 (40, 42, 45, 46), F16 (37, 38), and the

styryl family (47-50). Lysosomes function as the digestive system of the cell. Many degradative enzymes are located in lysosomes. Lysosomal storage diseases are caused by the mutations in the genes that encode those enzymes (51). Many clinically used drugs target lysosomes, such as antimalarial drug chloroquine (52-54), and antidepressant drugs (55). Lysosomes are acidic intracellular organelles with intraluminal pH of 4.6-5.0 (56), while the cytosolic pH is near neutrality (~ 7.2) (17). The low pH is caused by the activity of a proton ATPase rather than by a Donnan potential for protons, as originally proposed (56). As a result, acidification is accompanied by the generation of an interior positive membrane potential (56).

One of the well-studied mechanisms of lysosomal accumulation of weakly basic molecules is the ion-trapping mechanism, which was described by De Duve et al. as early as in the Seventies (57). For molecules with at least one ionizable group, the proportion of neutral species and ionized species may differ significantly in different pH environment, depending on the acid dissociation constant (pK_a) and pH, which can be described by the Henderson-Hasselbalch equation. For weakly basic molecules with pK_a close to physiological pH, they exist predominantly as neutral species in cytosol (pH ~ 7.2). After neutral molecules enter the acidic subcellular organelles, they become protonated due to the acidic environment. Generally the lipophilicity may differ three orders of magnitude between neutral species and ionized species (7). Thus after entering the acidic compartment, transmembrane permeability of the molecules is reduced due to the protonation, and accumulation is induced.

The Goldman-Hodgkin-Katz equation

The flux of ionic molecules across a biomembrane is a function of the transmembrane electrical potential and the concentration gradient of the molecules across the biomembrane. It can be described by Nernst-Planck equation (equation 1.1).

$$J = -D \left[\frac{dC(x)}{dx} + C(x) \frac{zF}{RT} \frac{dV(x)}{dx} \right], \quad (1.1)$$

The first term is corresponding to the Fick's law of diffusion, which gives the diffusion down the concentration gradient. The second term reflects the flux due to the transmembrane electrical potential. D is the diffusion coefficient (area per time unit). F , R , T , and z are the Faraday constant, molar gas constant, temperature (in Kelvin), and electric charge, respectively. Assume the transport direction (denoted by x) being perpendicular to the membrane, then $dC(x)/dx$ reflects the concentration change along the membrane, and $dV(x)/dx$ reflects the voltage change along the membrane. $C(x)$ indicates the concentration at point x . If transmembrane electrical potential is assumed to be constant along the membrane, and the membrane thickness is d , equation 1.1 is rewritten as equation (1.2) and rearranged to obtain equation 1.3.

$$J = -D \left[\frac{dC(x)}{dx} + C(x) \frac{zF}{RT} \frac{V}{d} \right], \quad (1.2)$$

$$1 = \frac{dC(x)/dx}{-\frac{J}{D} - C(x) \frac{zF}{RT} \frac{V}{d}}, \quad (1.3)$$

Let $N = zFV/RT$, and integration from $x = 0$ to d yields equation 1.4:

$$\int_0^d dx = \int_0^d -\frac{dC(x)/dx}{J/D + NC(x)/d} dx$$

$$\Rightarrow d = -Nd \int_0^d \frac{N/d}{J/D + NC(x)/d} dC(x) \quad , \quad (1.4)$$

$$= -Nd \left[\ln \left| \frac{N}{d} C(d) + \frac{J}{D} \right| - \ln \left| \frac{N}{d} C(0) + \frac{J}{D} \right| \right]$$

Reorganize equation 1.4, one can obtain equation 1.5, which is the explicit expression of flux of ionic molecules across a biomembrane with transmembrane electrical potential and concentration gradient.

$$J = \frac{D}{d} \frac{N}{e^N - 1} (C(0) - e^N C(d)) \quad , \quad (1.5)$$

where D/d can be written as permeability (length per time unit), $C(0)$ is the concentration at outer membrane surface, and $C(d)$ is the concentration at inner membrane surface.

Empirical and semi-empirical models

Statistic based formulas are widely used in predicting different ADME properties, from basic physical properties of drug substances such as in vitro solubility (58-62) to more complex biological properties of drug-organism interaction, such as in vivo bioavailability (63-65). Statistically based empirical formulas are usually built from databases of molecules that have been screened by a specific assay. The assay data is related to the chemical structure of the molecules using probabilistic regression techniques. This probabilistic regression can be summarized as an equation that specifies the relationship between the resulting physicochemical or biological property of interest (the dependent variable of the equation) to different parameters related to the chemical structure of the molecule (the dependent variables of the equation). Using a training set of molecules, quantitative structure-activity relationship (QSAR) equations can be used

to predict the behavior of a previously untested test set of molecules. While QSAR models have been developed to study the physicochemical properties or pharmacological activities of small molecules extensively (66-75), models about structure – subcellular localization relationships (QSLR) are relatively underdeveloped (27-30, 32, 33, 76-78).

Pseudo-equilibrium models

In early nineties, F. Rashid and R. W. Horobin were aware of the importance of physicochemical properties, such as hydrophilicity / lipophilicity ($\log P$), pK_a (and thus electrical charges z), molecular size, and the properties of biological systems, in determining the localization of fluorescent molecules, and developed decision tree – like model, which comprised sets of nested if/then rules (79) to predict subcellular accumulation in various organelles. At the beginning, a simple and generalized model, named the simplistic Chinese box (SCB) model, was developed to describe the interaction of molecular probes within living cell system (30, 32, 33). The SCB model was applied to 41 cationic probes to study their mitochondrial localization as a function of $\log P_{\text{oct}}$ (logarithm of octanol / water partition coefficient) (32). $\log P$ values fell between -3.6 and 21.0. They observed that cationic molecules with $\log P$ between 0 and 5 were expected to accumulate in the mitochondrial inner membrane. Cationic molecules with $\log P < 0$ would be excluded outside cells, and with $\log P > +5$ would bind to external membrane irreversibly (32). The model then was tested with 10 fluorescent mitochondrial probes and 7 vital dyes of mitochondria and the same trend was observed. Later on a library with 50 fluorescent probes with various physicochemical characteristics was studied for their lysosomal accumulation by the same group (30). The conjugated bound number (CBN) was introduced to model non-specific protein binding.

Several scenarios were included: entry of cells, entry of lysosomes, retention in lysosomes, and selectively accumulate in lysosomes. Probes that could enter the cells had $0 < \log P < 5$ and $CNB < 40$. Probes with $\log P > 15$, and / or $CNB > 40$ (regardless of hydrophilicity) could also enter the cell by adsorptive pinocytosis. Markers of fluid phase pinocytosis could also enter the cells and were found having $\log P < 0$, $z < 0$, and $CNB < 40$. After the probes entered the cells, they accumulated in lysosomes and could be categorized into two groups: (1) Probes accumulating in lysosomes by ion trapping mechanisms had $z \leq 0$, $\log P_{\text{cation}} < 0$, but $\log P_{\text{free base}} > 0$, $pK_a \sim 7$, and $CNB < 40$; (2) Probes comprised of hydrolysable lipophilic esters, usually weak acids, had $z \leq 0$, $\log P_{\text{free base}} > 0$, $pK_a \sim 7$, and $CNB < 40$. Those probes were converted into immobile free acids by lysosomal esterases and trapped in lysosomes by precipitation of insoluble weak acids in low pH environments (30). To extend the same strategy to other organelles, such as endoplasmic reticulum, nuclear chromatin, and plasma membrane, amphipathic character (AI), the largest conjugated fragment value (LCF), and LCF/CBN ratio were introduced to the empirical model (29, 79, 80).

Unlike the decision tree – like model, additive models were developed for a combinatorial library of cationic styryl dyes for their chemical properties (e.g. peak emission or excitation wavelength) and subcellular localization properties (mitochondria or non-mitochondria) (21, 81). Model parameters for peak excitation and emission were obtained using least squares to minimize the additive function over all compounds having experimental data (21, 81). The binary localization data were analyzed using factorial logistic regression. Cross-validation was carried out for both the spectral and localization analyses to obtain unbiased estimates of the prediction performance (21, 81).

Back to the Sixties, Hansch et al. published a series of papers describing the relationship between concentration and hydrophobicity (82-85). A representative equation can be expressed by equation 1.7.

$$\pi_x = \log P_x - \log P_H, \quad (1.6)$$

$$\log \frac{1}{C} = a\pi - b\pi^2 + \rho\sigma + c, \quad (1.7)$$

where, P_x and P_H are the partition coefficients of a derivative and the parent molecule, respectively; C is the molar concentration; a , b , ρ and c are constants determined by minimizing least squares. Later on, the Hansch-Fujita equations were extended and applied to a multi aqueous / lipid biosystem to study drug disposition and activity (35, 86, 87). Rather than using organelles as subcellular compartments, the QSAR models divide cellular compartment into continuous aqueous / lipid phases. An empirical disposition equation was used to reduce the number of adjustable parameters, which expressed the concentration after a predetermined time of exposure as a function of octanol/water partition coefficient (35). Adjustable parameters in the final equation were optimized by a combination of linear and non-linear regression analyses (35). Simulated bioactivity - lipophilicity curves agreed well with observer data for 10 compounds. The model could potentially be used to construct concentration - time profiles in smaller biosystems, such as bacterial or mammalian cells (35); or serve as a base for the development of mechanistic models (25, 88-91).

Kinetic models

While the empirical models described above were focused on steady state distribution, kinetic models are always desired to describe the transport as a function of time.

The time of exposure was integrated in the QSAR model discussed above by employing kinetics of the drug-receptor interaction based on mass action law (31). The kinetic model was named QSTAR model. Adjustable parameters in the model were obtained by non-linear regression for 36 compounds (31). The simulated inhibitory potency versus lipophilicity curve agreed well with the observed data (31). This time course of drug concentration in the receptor surroundings serves as the base for constructing the differential equations for the receptor modification proceeding by any proposed mechanisms.

The QSTAR subcellular pharmacokinetic model was further extended by integrating Michaelis-Menten kinetics of enzymatic reactions with respect to its two boundary cases, membrane accumulation, non-covalent protein binding, and excretion (88). Differential equations were solved analytically, so the explicit parameters, such as elimination rate constant, maximal rate, and the Michaelis-Menten constant, were lumped together to form adjustable parameters in the final equation (88). The adjustable parameters were obtained by non-linear regression (88). In the discussion, the authors mentioned that the model “can not be applied to a broader series of compounds having diverse structures since it describes merely the structurally non-specific steps a compound has to undergo in microbial culture and does not incorporate the structural specificity of the enzyme-substrate interaction.”(88)

A two-compartment model, cytosol and vesicles, was developed for a library consisting of 80 fluorescent-tagged triazine compounds (23). First-order kinetics was assumed between each compartment. Coefficients of variation (CV) of pixel intensities were linked to intracellular concentration by a statistical model. Rate constants in the model were obtained by optimization and the solutions within 5% of the best fit were chosen. With the help of subcellular pharmacokinetic modeling, the partition coefficients from the extracellular medium to the cytosol, and from the cytosol to the intracellular vesicles, could be quantitatively defined, which indicated the subcellular sequestration phenomenon. Furthermore it provided bases for analyses of correlation of subcellular transport with chemical structures and physicochemical properties (23).

Fluorescent microscopic imaging technique is one of the most often used methods to detect subcellular localization of small molecules (N. Zheng, manuscript in preparation). However, those methods are mainly applied to fluorescent molecules, which limit the method application to certain class of chemicals. Drug-induced morphology changes of subcellular organelles can be detected using light microscopy or electron microscopy and can be used as surrogate evidence for subcellular localization. Other techniques to determine subcellular localization include cell fractionation, radiography, uptake competition, and metabolic study, which could be labor intensive experiments. Limited information of subcellular localization and less diverse structures of small molecules might limit the development and predictive accuracy of empirical models. Thus mechanism based cellular pharmacokinetic models are developed.

Mechanistic physiologically-based models

Basic principles or mechanisms used in developing mechanistic physiologically-based cellular pharmacokinetic models include: mass balance, Fick's law of diffusion, pH-partitioning theory, ion-trapping mechanism, Henderson-Hasselbalch equation, Nernst-Planck equation, Michaelis-Menten equation, and other specific mechanisms involved. In mechanistic physiologically-based cellular PK models, for the part that is difficult to be modeled with mechanistic strategy, empirical methods are often employed. If some parameters in the mechanistic models are difficult to be measured experimentally, regression methods will also be used to get the estimation.

Generic models --- The History of 1CellPK

Generic models usually only include general mechanisms, such as passive diffusion, and thus can be applied to a large number of molecules.

Mechanistic models were developed for non-polarized suspension cells including cytosol, mitochondria and lysosomes as subcellular compartments (4-7). Many of the equations originally were developed to predict plant uptake (92). The uptake of electrolytes into a single plant cell was modeled. The plant cell was separated into the compartments, cytoplasm and vacuole, and was surrounded by the apoplast (92). Later on the model was applied to tumor cells (7). Passive diffusion was modeled by Fick's law of diffusion for neutral molecules, and by combination of Fick's law of diffusion and Nernst-Planck equation for ionized molecules. Those models considered both the physiological properties of the cells and physicochemical properties of the small molecules, and gave quantitative predictions of concentration-time profiles in functional subcellular organelles.

Specific models

Other than generic models which have been developed for certain classes of molecules, specific cellular pharmacokinetic models also have been developed to study single compounds to understand their transport or effects at cellular level. In specified models, more mechanisms are included other than passive diffusion, such as multiple transporters, specific binding, metabolic enzymes, and pharmacodynamic models.

A series of papers were published to model cellular PK of paclitaxel capturing the effect of P-gp mediated efflux and intracellular binding to tubulins/microtubules (20, 93, 94). Quantification of paclitaxel intracellular pharmacokinetics is important because it is closely related to its pharmacodynamics. At a starting point, the model first assumed passive diffusion of paclitaxel across the cell membrane (93). The model took account into saturable binding to extracellular proteins, saturable and nonsaturable binding to intracellular components, cell density variation, and enhancement of tubulin concentration. The model was validated in human breast MCF7 tumor cells, which had negligible P-gp expression. Later on the effect of P-gp mediated efflux was added into the model and validated in human breast carcinoma BC19 cells that were derived from MCF7 cells transfected with *mdr1* (94). Their study indicated that the P-gp mediated drug efflux accounted for more than 70% of total drug efflux when extracellular concentration was less than 200nM, but less than 30% of total efflux when extracellular concentration was 1000nM. Translating to clinical impact, their findings suggested that if the patient had similar P-gp expression level in tumor as BC19 cells in this study, then the role of P-gp in the efflux was limited since the clinically relevant concentration range was larger than 200nM. They also found the dissociation constant (K_m) of paclitaxel from P-gp measured in this study was three orders of magnitude different from previous

measurement in Caco-2 cell monolayer. That could be due to different cell lines. More importantly, it indicated that the intracellular concentration played a role in determining the real K_m . After being experimentally validated, a parametric study was performed to study the effects of extracellular drug concentration, intracellular drug binding capacity and affinity, and P-gp expression level on the intracellular drug accumulation independently and simultaneously (20). The study showed that the four biological factors determine paclitaxel intracellular concentration interpedently. Among the four factors, extracellular concentration was the most sensitive factor, followed by intracellular binding capacity and affinity. The effect of P-gp expression was relatively minor, suggesting that to improve clinical efficacy, effective delivery of paclitaxel to tumor cells was more important than other factors, such as inhibition of P-gp efflux.

Besides P-gp, other transporters also have been included in cell-based PK modeling. Poirier *et al.* reported a mechanism-based model including active uptake, nonspecific binding, and passive diffusion (95) to help better determine the Michaelis-Menten parameters: V_{max} and K_m . The model was applied to estimate kinetic parameters of *in vitro* transport data from organic anion-transporting peptide (OATP) substrates and substrates of multiple uptake transporters. Compared with conventional two-step approach, the mechanism-based model showed significant improvement of accuracy and precision in V_{max} and K_m estimation. Ranitidine absorptive transport in Caco-2 cells involved carrier-mediated uptake, P-gp mediated efflux, paracellular transport and transcellular transport (96). To capture the complex transport mechanisms, a PK model was developed by Bourdet *et al.* (96). Meanwhile transport experiment of ranitidine was performed in Caco-2 cells in the absence or presence of uptake and efflux inhibitors as a

function of concentration. Parameters in the model were estimated by fitting the experimental data simultaneously using nonlinear least-squares regression. Their simulations suggested that paracellular transport contributed to 60% of total transport. When the P-gp mediated efflux was inhibited, paracellular transport contribution was decreased to 40% of total transport. When the cation-selective apical uptake transporters were inhibited, paracellular transport contributed to 70% of total transport. Modeling and measuring ranitidine transport at different concentrations suggested that paracellular transport was concentration dependent and saturable.

Metabolism is another interested component to be added in cell-based PK models. Theoretically, if the metabolic enzymes are located in cytosol, the substrate concentration points to the intracellular concentration and thus developing cell-based PK model is especially important. A catenary model was developed by Sun *et al.* (97) including passive diffusion, cellular binding, carrier-mediated and efflux transporters-mediated transport, and metabolic enzymes. The model was applied to study the transport and metabolism of baicalein in Caco-2 cells (98).

Some of the advanced cell-based PK models have been linked to PD models (99). A cell-level mathematical model describing the cytokine granulocyte colony-stimulating factor (GCSF) / GCSF receptor (GCSFR) dynamics was developed by Sarkar *et al.* (99). The model started with the trafficking of GCSF/GCSFR system at molecular level. Extracellular GCSF molecules bound to GCSFR at cell surface becoming internalized and undergoing endocytic pathway. At cellular level, the model variables were extracellular ligand concentration, free surface receptors per cell, surface complexes per cell, intracellular ligand concentration per cell, free intracellular receptors per cell,

intracellular complexes per cell, degraded ligand per cell, and cell density, which was ligand dependent cell growth. Those variables changed over time and could be written in ordinary differential equations mechanistically. The cellular PK model was validated experimentally using wild-type GCSF and two single Asp->His mutants. The two mutants had similar affinity to cell-surface receptor as wild-type GCSF, but lower affinity to endosomal receptor, resulting in enhanced ligand recycling and ligand half-life. The PD model was an indirect model and the direct response from GCSF therapy was neutrophil production. In the original PK/PD model, two doses of GCSF were administered subcutaneously. The PK part was fit by a bisegmental absorption model connected with a conventional two-compartment model. The cell-level PK model was integrated in the central compartment in replace of the saturable clearance. By integrating the cell-level model into PK/PD model, the effects of cellular / molecular parameters on pharmacodynamics could be studied mechanistically, such as the effects of endosomal binding affinity and extracellular binding affinity in the absence and presence of nonspecific clearance. Such a model could be valuable in determining important parameters in PK/PD models. And the model was a first attempt to link cell-level PK model to systemic level PD model (99).

Specific cellular pharmacokinetic models require more knowledge about the compounds interested. While generic mechanistic cellular pharmacokinetic models are more useful in early drug discovery for high throughput screening and drug candidate identification, specific cellular pharmacokinetic models will be more useful for compounds in late drug development stage.

Comparison of empirical models with mechanistic models

Both empirical models and mechanistic models have advantages and disadvantages. Empirical models could be developed without knowing the details of how the compounds transport in biosystem, the mechanisms of action, but just based on observations. Many principles or physical laws used in mechanistic models were developed as empirical models, such as Newton's three Laws. Started from simple linear regressions, empirical models become more and more complex with the rapid development of computational tools, new statistical methodology, more and more interactions among scientists with diverse background. However, it requires a large amount of datasets and is difficult to be extrapolated to different scenarios, such as to different classes of molecules. Mechanistic cellular pharmacokinetic models take into account physiological parameters and physicochemical properties of small molecules. Mechanism-based modeling does not require a large dataset of small molecules, but requires knowledge of all input parameters and usually the amount of input parameters is large. Because of the large amount of input parameters, when the predicted values are not close to the observations, it is possible that there are too many adjustable parameters that could be adjusted to make the prediction close to observation. However, the adjusted parameters need to be chosen carefully and based on scientific judgment. Otherwise the model will lead to misinterpretation. It is not encouraged to adjust the parameters just for fitting the observed data. Neither the empirical model nor the mechanistic model is universally applicable in predicting cellular pharmacokinetics.

A comparison of QSAR models with a mechanistic model was conducted by Horobin R.W *et al.* for more than 100 mitochondriotropic agents (79). Both methods could predict lipophilic permanent cations and lipophilic weak acids and had

considerable agreement (79). For electrically neutral species, including two zwitterions, QSAR model did a better prediction than the mechanistic model, because the mechanistic model considered biomembrane as a bulk lipid phase, so did not expect any abrupt increase in uptake about $\log P = 5$ and no accumulation was predicted (79). For lipophilic cations of partially ionized bases, the mechanistic model failed to predict mitochondriotropic behavior in eight of nine cases, while QSAR model successfully predicted all nine cases (79). One of the explanations of the failure of mechanistic model might be that it did not include the complex formation between lipophilic cationic xenobiotics and the cardiolipin presented in the inner mitochondrial membrane (79, 100). Both methods failed to predict mitochondrial accumulation for four partially ionized hydrophilic compounds, among which two compounds were metabolized (79). For five strong acids, which were reported accumulating in isolated mitochondria, both models also failed to predict mitochondrial accumulation (79). And that could be because neither model was intended to handle the isolated organelles (79). Comparison of both types of models in terms of prediction accuracy showed that both approaches were useful but neither one was superior. Nevertheless, to improve the prediction accuracy, mechanistic models could be extended according to the behavior of specific classes of molecules.

Balaz B. et al. also performed a study to compare the predictive ability of a mechanistic model with empirical QSAR models using a dataset of toxicities against *Tetrahymena pyriformis* of 129 phenolic compounds (101). The response was concentration dependent toxicity and descriptors were $\log P$ and pK_a . Predictive sum of squares of deviations between the calculated and experimental values of the omitted

points (PRESS) were calculated as a measurement of predictive ability. For the mechanistic model, concentration was modeled with a disposition function which had physicochemical properties (i.e. logP and pK_a) and the exposure time t as variables (87, 101). The model was further extended to include accumulation in the membranes and protein binding, hydrophobicity-dependent elimination, and hydrophobicity-independent elimination (89, 91). Toxicity T was expressed as the reciprocal concentration (101). For the QSAR modeling, polynomials with cross-terms of logP and pK_a, and their inverse values were used. A total of 113 empirical models were generated that had better statistics (i.e. the correlation coefficient, the fit standard error, and the value of the Fisher test) than the mechanistic model. The best two models were chosen to be compared with the mechanistic model in terms of predictive ability. The mechanistic model had slightly higher PRESS values than the empirical models (leave-one-out cross-validation and two types of leave-several-out cross-validation) (101). To further test the extrapolation ability of different models, the leave-extremes-out (LEO cross-validation) technique was applied to omit compounds with extreme logP and pK_a values and 97 compounds were included with logP between 1.0 and 5.3 and pK_a between 5.0 and 11.0. A total of 105 empirical models were generated that had better statistics than the mechanistic model for the reduced dataset. However the mechanistic based model predicted much better than the empirical models for the compounds falling outside of the parameters space (101). To summarize their findings, all empirical models had similar surface curves in the parameters space generated by the data but very different shapes in the areas outside the parameters space; predictive ability of the mechanism-based model was much better than

empirical models for compounds outside the parameters space. Their study also suggested that mechanistic models could be extended to molecules outside of the dataset.

Although it is difficult to judge which types of model is superior, the comparison of empirical models with mechanistic models performed by different groups using different dataset suggests that mechanistic models could be extended by adding new mechanism, could be extrapolated to compounds not included in the studying dataset, and could be well explained if discrepancies are observed. For empirical models a large dataset including various classes of molecules is critical. Recently, a database containing 945 molecules with various subcellular distribution properties was constructed in our group, which would serve as a starting point for further computational modeling of subcellular distribution (N. Zheng, manuscript in preparation).

Cellular pharmacokinetics modeling in relation to macroscopic ADMET

Scientists have done many *in vitro* and *in vivo* studies to show the contribution of subcellular sequestration on systemic distribution (102-106). Propranolol was found to accumulate in mitochondrial and microsomal fractions in liver, lung, and kidney in rats after i.v. injection (102). The antimalarial drug, mefloquine, showed significant accumulation in lysosomes in rat liver in an *in vivo* study (106). High volume of distribution of mefloquine can be explained by lysosomal trapping (106). Subcellular distribution of basic drugs chlorpromazine, imipramine, and biperiden in rat liver was studied 10 minutes after i.v. administration (103). The relative specific contents (the drug concentration per protein of each fraction divided by that of the total homogenate in lysosomes were found to be the highest compared with in other organelles (103). And their contribution to subcellular distribution depends on the intralysosomal pH (103, 104,

107). Extensive distribution in the lung has been observed for many lipophilic bases (108-113). Lysosomal trapping was proposed as a mechanism contributing to high accumulation in the lung (105, 111-114).

However, quantitative relationship between subcellular distribution and tissue distribution is still under development. Quantitative prediction of subcellular pharmacokinetics itself can be challenging because of the multiple factors, such as the membrane potential, volume, surface area, intraluminal pH values, and intraluminal lipid contents of subcellular compartment, as well as the physicochemical properties of small molecules, and potential interaction / competition among different transport pathways. However, a predictive physiologically-based cellular pharmacokinetic model can be useful in optimization design of small molecules, hypothesis testing, guiding experimental design, and predicting outcomes that are difficult to be measured experimentally. And most importantly cellular pharmacokinetic models could be extrapolated to organ /tissue and systemic levels to be related to macroscopic ADMET properties. Cell-based PK models have been integrated into permeability limited whole body PBPK models to predict concentration-time profiles for a variety of compounds, such as methotexate (115, 116), cyclosporine A and its derivative SDZ IMM 125 (117-119), terbinafine (120), FTY720 (121), everolimus (RAD001) (122), domperidone, a p-glycoprotein (P-gp) substrate (123), and many macromolecules, such as phosphorothioate oligonucleotide ISIS1082 (124), monoclonal antibodies (mAbs) (125-131).

Conclusions

Biodistribution of small molecules at cellular / subcellular level has showed important effects on systemic distribution (102-106). Extensive research that has been

conducted in areas of systems biology, transporters, metabolic enzymes, and pharmacogenomics brings up a question that how that information can be used in drug development efficiently. Modeling and simulation can help to bridge the gap between cellular / subcellular pharmacokinetics and systemic ADMET properties in a quantitative manner. While physiologically-based models have the advantages of being flexible, interpretable, extendable, and extrapolatable; they also have the disadvantage that involves too many parameters, which may induce misinterpretation. Uncertainties and sensitivities associated with model parameters will be two issues in physiologically-based PK modeling.

Specific aims

The intestinal epithelial cells are the absorptive cells responsible for the majority of drug absorption (132). Drugs transport through intestinal epithelium by several routes: passive transcellular transport, carrier-mediated transcellular transport, receptor-mediated endocytosis, paracellular passive transport and transporter-mediated efflux pathways such as P-glycoprotein (P-gp) (132, 133). Among these transport routes passive transcellular process is the predominant pathway for most orally absorbed drugs based on a literature survey (134). Studies show that paracellular pathway is molecular size and charge selective (134-136). Paracellular passive permeability might play a major role in small molecules' transport with molecular weight less than 200 Da (137). Usually passive intestinal permeability is mainly determined by drug physicochemical properties and intestinal physiological properties. To have favorable intestinal permeability drugs should be designed with proper physicochemical properties.

Computational tools to predict drug intestinal permeability are fast and cost effective and thus are promising and desired in early drug development. Computational methods developed for intestinal permeability or oral absorption prediction can be classified into empirical models and mechanism-based models. In early stage of modeling, a single physicochemical property such as octanol-water partition coefficient was used to predict intestinal permeability / oral absorption (138, 139). It is generally admitted that the molecules with higher lipophilicity have higher intestinal permeability (140), however, this is not always valid (141), which indicates that models using a single parameter might be limited in several groups of compounds. Lipinski and coworkers (142) established a simple empirical model, known as the 'rules of 5', to predict good oral absorption molecules based on the physicochemical properties of more than 2000 drug candidates that had entered clinical phase II trials. In this model, molecular weight, lipophilicity, numbers of hydrogen bond donors and acceptors were used as descriptors. Recently quantitative structure-property / activity relationships (QSPR / QSAR) have been introduced to oral absorption, intestinal permeability, and Caco-2 permeability prediction. Descriptors can be classified as one dimensional (molecular weight, atom counts), two dimensional (fragment counts, topological indices, connectivity, flexibility), and three dimensional (molecular surface areas, molecular volume, interaction energies) descriptors (143). However, as discussed above QSAR models require a training set with large diversity to be readily extrapolated to unrelated compounds.

Considering the importance of both permeability and biodistribution at cellular / subcellular levels of small molecules, the aim of this project is to develop a mechanism based cellular pharmacokinetic model to predict transcellular permeability and

subcellular distribution. Furthermore, the cell based PK model will be integrated into whole body physiologically-based PK model to illustrate the effects of subcellular pharmacokinetics on systemic PK.

Passive transport will be considered as a starting point. The following specific aims will be addressed in this study.

- (1). To develop a physiologically-based cellular pharmacokinetic model to characterize transcellular permeability and subcellular accumulation of small molecules as a function of concentration gradient. Model will include physiological parameters of cells as well as physicochemical properties of small molecules; to perform parametric study to illustrate the sensitivity of model parameters; and to validate the model using published PAMPA, Caco-2, and human permeability data.
- (2). To apply the model to analyze and understand relationships between the chemical diversity and intracellular distributions of lysosomotropic monobasic amines.
- (3). To illustrate how a mechanistic model can be used for guiding experimental design and hypothesis testing, using chloroquine as a model drug.
- (4). To integrate the cell-based PK model to whole body physiologically-based PK model to study the effect of subcellular distribution on the lung distribution of weak basic molecules.

Table 1.1: Summary of empirical models for subcellular localization prediction

method	Interested localization	Descriptors	Number of compounds	Reference
QSAR	mito	logP, Z	41	(32)
QSAR	lyso	logP, pK _a , CBN, Z	50	(30)
QSAR	nuclei	logP, pK _a , Z, CBN, AI, LCF, LCF/CBN ratio	44	(27)
QSAR	ER	logP, pK _a , Z, CBN, AI, LCF	37	(29)
QSAR	mito / non-mito	logP, pK _a , Z, CBN, AI, LCF	109	(79)
Descriptor analysis	mito / lyso / nucleus / cyto / ER / Golgi body / plasma membrane / multiple localization	483 2D and 3D MOE descriptors	954	N. Zheng manuscript in preparation

logP: logarithm of the octanol/water partition coefficient

pK_a: negative logarithm of the acidic associate constant

Z: electrical charge

CBN: conjugated bond number

AI: amphiphilicity index

LCF: the largest conjugated fragment

Table 1.2: Summary of mechanistic cellular PK models

Drugs / molecules	Model Components	Cell Type	Relationship with Systemic PK/PD	References
Monovalent small molecules	Passive transcellular transport and subcellular organelles	Epithelial and round shaped non-polarized cells	Absorption, tissue distribution	(4-7)
Paclitaxel	P-gp efflux, extracellular / intracellular binding	Human breast cancer cell lines MCF7 and BC19	Uptake to cancer cells	(20, 93, 94)
Substrates of multiple transporters	Active uptake, passive diffusion, nonspecific binding	Chinese hamster ovary (CHO) cells overexpressing Oatp1a1 or OATP1B1 and rat hepatocytes	Liver clearance	(95)
Ranitidine	Uptake and efflux transporters, paracellular and transcellular transport	Caco-2	Absorption	(96)
Baicalein	Passive diffusion, cellular binding, transporters and enzymes	Caco-2 or other similar <i>in vitro</i> system	Absorption, metabolism	(97, 98)
GCSF	endosomal trafficking, PK/PD	GCSF-dependent human suspension cell line: OCI/AML1	Cell-mediated clearance, link with PD modeling	(99)

References

1. F.P. Theil, T.W. Guentert, S. Haddad, and P. Poulin. Utility of physiologically based pharmacokinetic models to drug development and rational drug discovery candidate selection. *Toxicol Lett.* 138:29-49 (2003).
2. T. Lave, N. Parrott, H.P. Grimm, A. Fleury, and M. Reddy. Challenges and opportunities with modelling and simulation in drug discovery and drug development. *Xenobiotica.* 37:1295-1310 (2007).
3. H.M. Jones, I.B. Gardner, and K.J. Watson. Modelling and PBPK Simulation in Drug Discovery. *Aaps Journal.* 11:155-166 (2009).
4. X. Zhang, K. Shedden, and G.R. Rosania. A cell-based molecular transport simulator for pharmacokinetic prediction and cheminformatic exploration. *Mol Pharm.* 3:704-716 (2006).
5. X. Zhang, N. Zheng, and G.R. Rosania. Simulation-based cheminformatic analysis of organelle-targeted molecules: lysosomotropic monobasic amines. *J Comput Aided Mol Des.* 22:629-645 (2008).
6. S. Trapp, G.R. Rosania, R.W. Horobin, and J. Kornhuber. Quantitative modeling of selective lysosomal targeting for drug design. *Eur Biophys J.* 37:1317-1328 (2008).
7. S. Trapp and R.W. Horobin. A predictive model for the selective accumulation of chemicals in tumor cells. *Eur Biophys J Biophys Lett.* 34:959-966 (2005).
8. T. Watanabe, H. Kusuhara, K. Maeda, Y. Shitara, and Y. Sugiyama. Physiologically based pharmacokinetic modeling to predict transporter-mediated clearance and distribution of pravastatin in humans. *J Pharmacol Exp Ther.* 328:652-662 (2009).
9. M. Kato, Y. Shitara, H. Sato, K. Yoshisue, M. Hirano, T. Ikeda, and Y. Sugiyama. The quantitative prediction of CYP-mediated drug interaction by physiologically based pharmacokinetic modeling. *Pharm Res.* 25:1891-1901 (2008).
10. L. Liu and K.S. Pang. An integrated approach to model hepatic drug clearance. *Eur J Pharm Sci.* 29:215-230 (2006).
11. T. Rodgers and M. Rowland. Physiologically based pharmacokinetic modelling 2: predicting the tissue distribution of acids, very weak bases, neutrals and zwitterions. *J Pharm Sci.* 95:1238-1257 (2006).
12. T. Rodgers, D. Leahy, and M. Rowland. Physiologically based pharmacokinetic modeling 1: predicting the tissue distribution of moderate-to-strong bases. *J Pharm Sci.* 94:1259-1276 (2005).
13. U.E. Honegger, R.D. Zuehlke, I. Scuntaro, M.H. Schaefer, H. Toplak, and U.N. Wiesmann. Cellular accumulation of amiodarone and desethylamiodarone in cultured human cells. Consequences of drug accumulation on cellular lipid metabolism and plasma membrane properties of chronically exposed cells. *Biochem Pharmacol.* 45:349-356 (1993).
14. M.J. Reasor, C.M. McCloud, T.L. Beard, D.C. Ebert, S. Kacew, M.F. Gardner, K.A. Aldern, and K.Y. Hostetler. Comparative evaluation of amiodarone-induced phospholipidosis and drug accumulation in Fischer-344 and Sprague-Dawley rats. *Toxicology.* 106:139-147 (1996).

15. V.Y. Chen and G.R. Rosania. The great multidrug-resistance paradox. *ACS Chem Biol.* 1:271-273 (2006).
16. M. Duvvuri, S. Konkar, K.H. Hong, B.S. Blagg, and J.P. Krise. A new approach for enhancing differential selectivity of drugs to cancer cells. *ACS Chem Biol.* 1:309-315 (2006).
17. M. Duvvuri and J.P. Krise. Intracellular drug sequestration events associated with the emergence of multidrug resistance: a mechanistic review. *Front Biosci.* 10:1499-1509 (2005).
18. V.Y. Chen, M.M. Posada, L.L. Blazer, T. Zhao, and G.R. Rosania. The Role of the VPS4A-Exosome Pathway in the Intrinsic Egress Route of a DNA-Binding Anticancer Drug. *Pharm Res* (2006).
19. V.Y. Chen, M.M. Posada, L. Zhao, and G.R. Rosania. Rapid Doxorubicin Efflux from the Nucleus of Drug-Resistant Cancer Cells Following Extracellular Drug Clearance. *Pharm Res* (2007).
20. S.H. Jang, M.G. Wientjes, and J.L. Au. Interdependent effect of P-glycoprotein-mediated drug efflux and intracellular drug binding on intracellular paclitaxel pharmacokinetics: application of computational modeling. *J Pharmacol Exp Ther.* 304:773-780 (2003).
21. K. Shedden, J. Brumer, Y.T. Chang, and G.R. Rosania. Chemoinformatic analysis of a supertargeted combinatorial library of styryl molecules. *Journal Of Chemical Information And Computer Sciences.* 43:2068-2080 (2003).
22. G.R. Rosania. Supertargeted chemistry: identifying relationships between molecular structures and their sub-cellular distribution. *Curr Top Med Chem.* 3:659-685 (2003).
23. V.Y. Chen, S.M. Khersonsky, K. Shedden, Y.T. Chang, and G.R. Rosania. System dynamics of subcellular transport. *Mol Pharm.* 1:414-425 (2004).
24. S. Balaz. Modeling Kinetics of Subcellular Disposition of Chemicals. *Chem Rev.* 109:1793-1899 (2009).
25. S. Balaz, M. Wiese, P. Dubovsky, P. Baricic, and J.K. Seydel. Quantitative and explicit structure-time-activity relations. *Prog Clin Biol Res.* 291:37-40 (1989).
26. K. Shedden, Q. Li, F. Liu, Y.T. Chang, and G.R. Rosania. Machine vision-assisted analysis of structure-localization relationships in a combinatorial library of prospective bioimaging probes. *Cytometry A* (2009).
27. R.W. Horobin, J.C. Stockert, and F. Rashid-Doubell. Fluorescent cationic probes for nuclei of living cells: why are they selective? A quantitative structure-activity relations analysis. *Histochem Cell Biol.* 126:165-175 (2006).
28. R.W. Horobin and V. Weissig. A QSAR-modeling perspective on cationic transfection lipids. 1. Predicting efficiency and understanding mechanisms. *J Gene Med.* 7:1023-1034 (2005).
29. J. Colston, R.W. Horobin, F. Rashid-Doubell, J. Pediani, and K.K. Johal. Why fluorescent probes for endoplasmic reticulum are selective: an experimental and QSAR-modelling study. *Biotech Histochem.* 78:323-332 (2003).
30. F. Rashid, R.W. Horobin, and M.A. Williams. Predicting the behaviour and selectivity of fluorescent probes for lysosomes and related structures by means of structure-activity models. *Histochem J.* 23:450-459 (1991).

31. S. Balaz, E. Sturdik, M. Rosenberg, J. Augustin, and B. Skara. Kinetics of drug activities as influenced by their physico-chemical properties: antibacterial effects of alkylating 2-furylethylenes. *J Theor Biol.* 131:115-134 (1988).
32. F. Rashid and R.W. Horobin. Interaction of molecular probes with living cells and tissues. Part 2. A structure-activity analysis of mitochondrial staining by cationic probes, and a discussion of the synergistic nature of image-based and biochemical approaches. *Histochemistry.* 94:303-308 (1990).
33. R.W. Horobin and F. Rashid. Interactions of molecular probes with living cells and tissues. Part 1. Some general mechanistic proposals, making use of a simplistic Chinese box model. *Histochemistry.* 94:205-209 (1990).
34. S. Balaz and E. Sturdik. Kinetics of passive transport in water/membrane/water system. A mathematical description. *Gen Physiol Biophys.* 4:105-108 (1985).
35. S. Balaz, E. Sturdik, and J. Augustin. Subcellular distribution of compounds in biosystems. *Bull Math Biol.* 50:367-378 (1988).
36. S. Balaz, E. Sturdik, and J. Augustin. Kinetics of unidirectional transport in multimembrane systems as influenced by binding to macromolecules. *Biophys Chem.* 24:135-142 (1986).
37. V.R. Fantin, M.J. Berardi, L. Scorrano, S.J. Korsmeyer, and P. Leder. A novel mitochondriotoxic small molecule that selectively inhibits tumor cell growth. *Cancer Cell.* 2:29-42 (2002).
38. V.R. Fantin and P. Leder. F16, a mitochondriotoxic compound, triggers apoptosis or necrosis depending on the genetic background of the target carcinoma cell. *Cancer Research.* 64:329-336 (2004).
39. G. Kroemer, L. Galluzzi, and C. Brenner. Mitochondrial membrane permeabilization in cell death. *Physiol Rev.* 87:99-163 (2007).
40. L.B. Chen. Mitochondrial membrane potential in living cells. *Annu Rev Cell Biol.* 4:155-181 (1988).
41. P. Mitchell. Keilin's respiratory chain concept and its chemiosmotic consequences. *Science.* 206:1148-1159 (1979).
42. L.V. Johnson, M.L. Walsh, B.J. Bockus, and L.B. Chen. Monitoring of relative mitochondrial membrane potential in living cells by fluorescence microscopy. *J Cell Biol.* 88:526-535 (1981).
43. S.T. Smiley, M. Reers, C. Mottola-Hartshorn, M. Lin, A. Chen, T.W. Smith, G.D. Steele, Jr., and L.B. Chen. Intracellular heterogeneity in mitochondrial membrane potentials revealed by a J-aggregate-forming lipophilic cation JC-1. *Proc Natl Acad Sci U S A.* 88:3671-3675 (1991).
44. J.S. Modica-Napolitano and J.R. Aprille. Delocalized lipophilic cations selectively target the mitochondria of carcinoma cells. *Advanced Drug Delivery Reviews.* 49:63-70 (2001).
45. T.J. Lampidis, C. Salet, G. Moreno, and L.B. Chen. Effects of the mitochondrial probe rhodamine 123 and related analogs on the function and viability of pulsating myocardial cells in culture. *Agents Actions.* 14:751-757 (1984).
46. L.V. Johnson, M.L. Walsh, and L.B. Chen. Localization of mitochondria in living cells with rhodamine 123. *Proc Natl Acad Sci U S A.* 77:990-994 (1980).

47. H.W. Mewes and J. Rafael. The 2-(dimethylaminostyryl)-1-methylpyridinium cation as indicator of the mitochondrial membrane potential. *FEBS Lett.* 131:7-10 (1981).
48. J. Bereiter-Hahn. Dimethylaminostyrylmethylpyridiniumiodine (daspmi) as a fluorescent probe for mitochondria in situ. *Biochim Biophys Acta.* 423:1-14 (1976).
49. J. Bereiter-Hahn, K.H. Seipel, M. Voth, and J.S. Ploem. Fluorimetry of mitochondria in cells vitally stained with DASPMI or rhodamine 6 GO. *Cell Biochem Funct.* 1:147-155 (1983).
50. D.S. Snyder and P.L. Small. Staining of cellular mitochondria with LDS-751. *J Immunol Methods.* 257:35-40 (2001).
51. G.M. Cooper and R.E. Hausman. *The Cell: A Molecular Approach*, 2000.
52. A.F. Slater. Chloroquine: mechanism of drug action and resistance in *Plasmodium falciparum*. *Pharmacol Ther.* 57:203-235 (1993).
53. J. Zhang, M. Krugliak, and H. Ginsburg. The fate of ferriprotophyrin IX in malaria infected erythrocytes in conjunction with the mode of action of antimalarial drugs. *Mol Biochem Parasitol.* 99:129-141 (1999).
54. H. Ginsburg, S.A. Ward, and P.G. Bray. An integrated model of chloroquine action. *Parasitol Today.* 15:357-360 (1999).
55. J. Kornhuber, P. Tripal, M. Reichel, L. Terfloth, S. Bleich, J. Wiffang, and E. Gulbins. Identification of new functional inhibitors of acid sphingomyelinase using a structure-property-activity relation model. *Journal of Medicinal Chemistry.* 51:219-237 (2008).
56. I. Mellman, R. Fuchs, and A. Helenius. Acidification of the endocytic and exocytic pathways. *Annu Rev Biochem.* 55:663-700 (1986).
57. C. de Duve, T. de Barsey, B. Poole, A. Trouet, P. Tulkens, and F. Van Hoof. Commentary. Lysosomotropic agents. *Biochem Pharmacol.* 23:2495-2531 (1974).
58. A.H. Goller, M. Hennemann, J. Keldenich, and T. Clark. In silico prediction of buffer solubility based on quantum-mechanical and HQSAR- and topology-based descriptors. *J Chem Inf Model.* 46:648-658 (2006).
59. J. Huuskonen, M. Salo, and J. Taskinen. Aqueous solubility prediction of drugs based on molecular topology and neural network modeling. *J Chem Inf Comput Sci.* 38:450-456 (1998).
60. J.S. Delaney. Predicting aqueous solubility from structure. *Drug Discov Today.* 10:289-295 (2005).
61. X.Q. Chen, S.J. Cho, Y. Li, and S. Venkatesh. Prediction of aqueous solubility of organic compounds using a quantitative structure-property relationship. *J Pharm Sci.* 91:1838-1852 (2002).
62. V. Tantishaiyakul. Prediction of the aqueous solubility of benzylamine salts using QSPR model. *J Pharm Biomed Anal.* 37:411-415 (2005).
63. K. Brendel, E. Comets, C. Laffont, C. Laveille, and F. Mentre. Metrics for external model evaluation with an application to the population pharmacokinetics of gliclazide. *Pharm Res.* 23:2036-2049 (2006).
64. S. Ekins and J. Rose. In silico ADME/Tox: the state of the art. *J Mol Graph Model.* 20:305-309 (2002).

65. J.P. Bai, A. Utis, G. Crippen, H.D. He, V. Fischer, R. Tullman, H.Q. Yin, C.P. Hsu, L. Jiang, and K.K. Hwang. Use of classification regression tree in predicting oral absorption in humans. *J Chem Inf Comput Sci.* 44:2061-2069 (2004).
66. J.W. McFarland, C.M. Berger, S.A. Froshauer, S.F. Hayashi, S.J. Hecker, B.H. Jaynes, M.R. Jefson, B.J. Kamicker, C.A. Lipinski, K.M. Lundy, C.P. Reese, and C.B. Vu. Quantitative structure-activity relationships among macrolide antibacterial agents: in vitro and in vivo potency against *Pasteurella multocida*. *J Med Chem.* 40:1340-1346 (1997).
67. J.F. Blake. Chemoinformatics - predicting the physicochemical properties of 'drug-like' molecules. *Curr Opin Biotechnol.* 11:104-107 (2000).
68. A.K. Ghose and G.M. Crippen. Quantitative structure-activity relationship by distance geometry: quinazolines as dihydrofolate reductase inhibitors. *J Med Chem.* 25:892-899 (1982).
69. A.K. Ghose and G.M. Crippen. Use of physicochemical parameters in distance geometry and related three-dimensional quantitative structure-activity relationships: a demonstration using *Escherichia coli* dihydrofolate reductase inhibitors. *J Med Chem.* 28:333-346 (1985).
70. A.K. Ghose and G.M. Crippen. Modeling the benzodiazepine receptor binding site by the general three-dimensional structure-directed quantitative structure-activity relationship method REMOTEDISC. *Mol Pharmacol.* 37:725-734 (1990).
71. Y. Marrero Ponce, M.A. Cabrera Perez, V. Romero Zaldivar, H. Gonzalez Diaz, and F. Torrens. A new topological descriptors based model for predicting intestinal epithelial transport of drugs in Caco-2 cell culture. *J Pharm Pharm Sci.* 7:186-199 (2004).
72. V. Svetnik, A. Liaw, C. Tong, J.C. Culberson, R.P. Sheridan, and B.P. Feuston. Random forest: a classification and regression tool for compound classification and QSAR modeling. *J Chem Inf Comput Sci.* 43:1947-1958 (2003).
73. S.A. Wildman and G.M. Crippen. Three-dimensional molecular descriptors and a novel QSAR method. *J Mol Graph Model.* 21:161-170 (2002).
74. C. Hansch. The QSAR paradigm in the design of less toxic molecules. *Drug Metab Rev.* 15:1279-1294 (1984).
75. A. Leo, C. Hansch, and C. Church. Comparison of parameters currently used in the study of structure-activity relationships. *J Med Chem.* 12:766-771 (1969).
76. R.W. Horobin. Structure-staining relationships in histochemistry and biological staining. I. Theoretical background and a general account of correlation of histochemical staining with the chemical structure of the reagents used. *J Microsc.* 119:345-355 (1980).
77. R.W. Horobin. Structure-staining relationships in histochemistry and biological staining. Part 3. Some comments on the intentional and artifactual staining of lipids. *Acta Histochem Suppl.* 24:237-246 (1981).
78. F. Rashid and R.W. Horobin. Accumulation of fluorescent non-cationic probes in mitochondria of cultured cells: observations, a proposed mechanism, and some implications. *J Microsc.* 163:233-241 (1991).
79. R.W. Horobin, S. Trapp, and V. Weissig. Mitochondriotropics: a review of their mode of action, and their applications for drug and DNA delivery to mammalian mitochondria. *J Control Release.* 121:125-136 (2007).

80. R.W. Horobin. Biological staining: mechanisms and theory. *Biotech Histochem.* 77:3-13 (2002).
81. G.R. Rosania, J.W. Lee, L. Ding, H.S. Yoon, and Y.T. Chang. Combinatorial approach to organelle-targeted fluorescent library based on the styryl scaffold. *J Am Chem Soc.* 125:1130-1131 (2003).
82. C. Hansch, P.P. Maloney, T. Fujita, and R.M. Muir. Correlation of Biological Activity of Phenoxyacetic Acids with Hammett Substituent Constants and Partition Coefficients. *Nature.* 194:178 - 180 (1962).
83. C. Hansch and T. Fujita. ρ - σ - π Analysis. A Method for the Correlation of Biological Activity and Chemical Structure. *J Am Chem Soc.* 86:1616-1626 (1964).
84. T. Fujita, J. Iwasa, and C. Hansch. A New Substituent Constant, π , Derived from Partition Coefficients. *J Am Chem Soc.* 86:5175-5180 (1964).
85. C. Hansch and A. Leo. in S. R. Heller, Ed., *Exploring QSAR. Fundamentals and Applications in Chemistry and Biology*, American Chemical Society, Washington, DC, 1995.
86. J.W. McFarland. On the parabolic relationship between drug potency and hydrophobicity. *J Med Chem.* 13:1192-1196 (1970).
87. S. Balaz, E. Sturdik, and M. Tichy. Hansch approach and kinetics of biological activities. *Quant Struct Act Relat* 4:77-81 (1985).
88. S. Balaz, M. Wiese, and J.K. Seydel. A kinetic description of the fate of chemicals in biosystems. *Sci Total Environ.* 109-110:357-375 (1991).
89. S. Balaz, M. Wiese, and J.K. Seydel. A time hierarchy-based model for kinetics of drug disposition and its use in quantitative structure-activity relationships. *J Pharm Sci.* 81:849-857 (1992).
90. S. Balaz. Model-based description of distribution of chemicals in biosystems for the continuous dose. *SAR QSAR Environ Res.* 4:177-187 (1995).
91. S. Balaz, K. Pirsellova, T.W. Schultz, and J. Hermens. Kinetics of subcellular distribution of multiply ionizable compounds: A mathematical description and its use in QSAR. *Journal Of Theoretical Biology.* 178:7-16 (1996).
92. S. Trapp. Plant uptake and transport models for neutral and ionic chemicals. *Environ Sci Pollut Res.* 11:33-39 (2004).
93. H.J. Kuh, S.H. Jang, M.G. Wientjes, and J.L. Au. Computational model of intracellular pharmacokinetics of paclitaxel. *J Pharmacol Exp Ther.* 293:761-770 (2000).
94. S.H. Jang, M.G. Wientjes, and J.L. Au. Kinetics of P-glycoprotein-mediated efflux of paclitaxel. *J Pharmacol Exp Ther.* 298:1236-1242 (2001).
95. A. Poirier, T. Lave, R. Portmann, M.E. Brun, F. Senner, M. Kansy, H.P. Grimm, and C. Funk. Design, data analysis, and simulation of in vitro drug transport kinetic experiments using a mechanistic in vitro model. *Drug Metab Dispos.* 36:2434-2444 (2008).
96. D.L. Bourdet, G.M. Pollack, and D.R. Thakker. Intestinal Absorptive Transport of the Hydrophilic Cation Ranitidine: A Kinetic Modeling Approach to Elucidate the Role of Uptake and Efflux Transporters and Paracellular vs. Transcellular Transport in Caco-2 Cells. *Pharm Res.* 23:1178-1187 (2006).

97. H. Sun and K.S. Pang. Permeability, transport, and metabolism of solutes in Caco-2 cell monolayers: a theoretical study. *Drug Metab Dispos.* 36:102-123 (2008).
98. H. Sun, L. Zhang, E.C. Chow, G. Lin, Z. Zuo, and K.S. Pang. A catenary model to study transport and conjugation of baicalein, a bioactive flavonoid, in the Caco-2 cell monolayer: demonstration of substrate inhibition. *J Pharmacol Exp Ther.* 326:117-126 (2008).
99. C.A. Sarkar and D.A. Lauffenburger. Cell-level pharmacokinetic model of granulocyte colony-stimulating factor: implications for ligand lifetime and potency in vivo. *Mol Pharmacol.* 63:147-158 (2003).
100. E. Goormaghtigh, P. Huart, M. Praet, R. Brasseur, and J.M. Ruyschaert. Structure of the adriamycin-cardiolipin complex. Role in mitochondrial toxicity. *Biophys Chem.* 35:247-257 (1990).
101. S. Balaz and V. Lukacova. Subcellular pharmacokinetics and its potential for library focusing. *J Mol Graph Model.* 20:479-490 (2002).
102. D.W. Schneck, J.F. Pritchard, and A.H. Hayes, Jr. Studies on the uptake and binding of propranolol by rat tissues. *J Pharmacol Exp Ther.* 203:621-629 (1977).
103. J. Ishizaki, K. Yokogawa, M. Hirano, E. Nakashima, Y. Sai, S. Ohkuma, T. Ohshima, and F. Ichimura. Contribution of lysosomes to the subcellular distribution of basic drugs in the rat liver. *Pharm Res.* 13:902-906 (1996).
104. J. Ishizaki, K. Yokogawa, F. Ichimura, and S. Ohkuma. Uptake of imipramine in rat liver lysosomes in vitro and its inhibition by basic drugs. *J Pharmacol Exp Ther.* 294:1088-1098 (2000).
105. K. Yokogawa, J. Ishizaki, S. Ohkuma, and K. Miyamoto. Influence of lipophilicity and lysosomal accumulation on tissue distribution kinetics of basic drugs: a physiologically based pharmacokinetic model. *Methods Find Exp Clin Pharmacol.* 24:81-93 (2002).
106. H. Glaumann, A.M. Motakefi, and H. Jansson. Intracellular distribution and effect of the antimalarial drug mefloquine on lysosomes of rat liver. *Liver.* 12:183-190 (1992).
107. J. Ishizaki, K. Yokogawa, E. Nakashima, S. Ohkuma, and F. Ichimura. Characteristic subcellular distribution, in brain, heart and lung, of biperiden, trihexyphenidyl, and (-)-quinuclidinyl benzylate in rats. *Biol Pharm Bull.* 21:67-71 (1998).
108. N. Yata, T. Toyoda, T. Murakami, A. Nishiura, and Y. Higashi. Phosphatidylserine as a determinant for the tissue distribution of weakly basic drugs in rats. *Pharm Res.* 7:1019-1025 (1990).
109. A. Hayes and R.G. Cooper. Studies on the absorption, distribution and excretion of propranolol in rat, dog and monkey. *J Pharmacol Exp Ther.* 176:302-311 (1971).
110. J.A. Street, B.A. Hemsworth, A.G. Roach, and M.D. Day. Tissue levels of several radiolabelled beta-adrenoceptor antagonists after intravenous administration in rats. *Arch Int Pharmacodyn Ther.* 237:180-190 (1979).
111. J. Ishizaki, K. Yokogawa, E. Nakashima, S. Ohkuma, and F. Ichimura. Uptake of basic drugs into rat lung granule fraction in vitro. *Biol Pharm Bull.* 21:858-861 (1998).

112. A.G. Wilson, R.D. Pickett, T.E. Eling, and M.W. Anderson. Studies on the persistence of basic amines in the rabbit lung. *Drug Metab Dispos.* 7:420-424 (1979).
113. J.K. Seydel and O. Wassermann. NMR-studies on the molecular basis of drug-induced phospholipidosis. Interaction between chlorphentermine and phosphatidylcholine. *Naunyn Schmiedebergs Arch Pharmacol.* 279:207-210 (1973).
114. A.C. MacIntyre and D.J. Cutler. The potential role of lysosomes in tissue distribution of weak bases. *Biopharm Drug Dispos.* 9:513-526 (1988).
115. R.L. Dedrick, D.S. Zaharko, and R.J. Lutz. Transport and binding of methotrexate in vivo. *J Pharm Sci.* 62:882-890 (1973).
116. R.J. Lutz, R.L. Dedrick, J.A. Straw, M.M. Hart, P. Klubes, and D.S. Zaharko. The kinetics of methotrexate distribution in spontaneous canine lymphosarcoma. *J Pharmacokinet Biopharm.* 3:77-97 (1975).
117. R. Kawai, M. Lemaire, J.L. Steimer, A. Bruelisauer, W. Niederberger, and M. Rowland. Physiologically based pharmacokinetic study on a cyclosporin derivative, SDZ IMM 125. *J Pharmacokinet Biopharm.* 22:327-365 (1994).
118. R. Kawai, D. Mathew, C. Tanaka, and M. Rowland. Physiologically based pharmacokinetics of cyclosporine A: extension to tissue distribution kinetics in rats and scale-up to human. *J Pharmacol Exp Ther.* 287:457-468 (1998).
119. C. Tanaka, R. Kawai, and M. Rowland. Physiologically based pharmacokinetics of cyclosporine A: reevaluation of dose-nonlinear kinetics in rats. *J Pharmacokinet Biopharm.* 27:597-623 (1999).
120. M. Hosseini-Yeganeh and A.J. McLachlan. Physiologically based pharmacokinetic model for terbinafine in rats and humans. *Antimicrob Agents Chemother.* 46:2219-2228 (2002).
121. G.M. Meno-Tetang, H. Li, S. Mis, N. Pyszczynski, P. Heining, P. Lowe, and W.J. Jusko. Physiologically based pharmacokinetic modeling of FTY720 (2-amino-2[2-(-4-octylphenyl)ethyl]propane-1,3-diol hydrochloride) in rats after oral and intravenous doses. *Drug Metab Dispos.* 34:1480-1487 (2006).
122. R. Laplanche, G.M. Meno-Tetang, and R. Kawai. Physiologically based pharmacokinetic (PBPK) modeling of everolimus (RAD001) in rats involving non-linear tissue uptake. *J Pharmacokinet Pharmacodyn.* 34:373-400 (2007).
123. F. Fenneteau, J. Turgeon, L. Couture, V. Michaud, J. Li, and F. Nekka. Assessing drug distribution in tissues expressing P-glycoprotein through physiologically based pharmacokinetic modeling: model structure and parameters determination. *Theor Biol Med Model.* 6:2 (2009).
124. B. Peng, J. Andrews, I. Nestorov, B. Brennan, P. Nicklin, and M. Rowland. Tissue distribution and physiologically based pharmacokinetics of antisense phosphorothioate oligonucleotide ISIS 1082 in rat. *Antisense Nucleic Acid Drug Dev.* 11:15-27 (2001).
125. L.T. Baxter, H. Zhu, D.G. Mackensen, and R.K. Jain. Physiologically based pharmacokinetic model for specific and nonspecific monoclonal antibodies and fragments in normal tissues and human tumor xenografts in nude mice. *Cancer Res.* 54:1517-1528 (1994).

126. L.T. Baxter, H. Zhu, D.G. Mackensen, W.F. Butler, and R.K. Jain. Biodistribution of monoclonal antibodies: scale-up from mouse to human using a physiologically based pharmacokinetic model. *Cancer Res.* 55:4611-4622 (1995).
127. S.W. Friedrich, S.C. Lin, B.R. Stoll, L.T. Baxter, L.L. Munn, and R.K. Jain. Antibody-directed effector cell therapy of tumors: analysis and optimization using a physiologically based pharmacokinetic model. *Neoplasia.* 4:449-463 (2002).
128. G.Z. Ferl, V. Kenanova, A.M. Wu, and J.J. DiStefano. A two-tiered physiologically based model for dually labeled single-chain Fv-Fc antibody fragments. *Mol Cancer Ther.* 5:1550-1558 (2006).
129. L.Y. Fang and D.X. Sun. Predictive physiologically based pharmacokinetic model for antibody-directed enzyme prodrug therapy. *Drug Metab Dispos.* 36:1153-1165 (2008).
130. J.P. Davda, M. Jain, S.K. Batra, P.R. Gwilt, and D.H. Robinson. A physiologically based pharmacokinetic (PBPK) model to characterize and predict the disposition of monoclonal antibody CC49 and its single chain Fv constructs. *Int Immunopharmacol.* 8:401-413 (2008).
131. H. Sato, Y. Sugiyama, Y. Sawada, T. Iga, and M. Hanano. Physiologically based pharmacokinetics of radioiodinated human beta-endorphin in rats. An application of the capillary membrane-limited model. *Drug Metab Dispos.* 15:540-550 (1987).
132. P.V. Balimane, S. Chong, and R.A. Morrison. Current methodologies used for evaluation of intestinal permeability and absorption. *J Pharmacol Toxicol Methods.* 44:301-312 (2000).
133. P.V. Balimane and S. Chong. Cell culture-based models for intestinal permeability: a critique. *Drug Discov Today.* 10:335-343 (2005).
134. P. Stenberg, K. Luthman, and P. Artursson. Virtual screening of intestinal drug permeability. *J Control Release.* 65:231-243 (2000).
135. V. Pade and S. Stavchansky. Estimation of the relative contribution of the transcellular and paracellular pathway to the transport of passively absorbed drugs in the Caco-2 cell culture model. *Pharm Res.* 14:1210-1215 (1997).
136. G.M. Pauletti, F.W. Okumu, and R.T. Borchardt. Effect of size and charge on the passive diffusion of peptides across Caco-2 cell monolayers via the paracellular pathway. *Pharm Res.* 14:164-168 (1997).
137. H. Lennernas. Does fluid flow across the intestinal mucosa affect quantitative oral drug absorption? Is it time for a reevaluation? *Pharm Res.* 12:1573-1582 (1995).
138. T. Nook, E. Doelker, and P. Buri. Intestinal-Absorption Kinetics Of Various Model-Drugs In Relation To Partition-Coefficients. *International Journal Of Pharmaceutics.* 43:119-129 (1988).
139. P. Artursson, K. Palm, and K. Luthman. Caco-2 monolayers in experimental and theoretical predictions of drug transport. *Adv Drug Deliv Rev.* 46:27-43 (2001).
140. M. Yazdanian, S.L. Glynn, J.L. Wright, and A. Hawi. Correlating partitioning and caco-2 cell permeability of structurally diverse small molecular weight compounds. *Pharm Res.* 15:1490-1494 (1998).
141. P. Wils, A. Warnery, V. Phung-Ba, S. Legrain, and D. Scherman. High lipophilicity decreases drug transport across intestinal epithelial cells. *J Pharmacol Exp Ther.* 269:654-658 (1994).

142. C.A. Lipinski, F. Lombardo, B.W. Dominy, and P.J. Feeney. Experimental and computational approaches to estimate solubility and permeability in drug discovery and development settings. *Adv Drug Deliv Rev.* 46:3-26 (2001).
143. C.A. Bergstrom. In silico predictions of drug solubility and permeability: two rate-limiting barriers to oral drug absorption. *Basic Clin Pharmacol Toxicol.* 96:156-161 (2005).

CHAPTER II

A CELL-BASED MOLECULAR TRANSPORT SIMULATOR FOR PHARMACOKINETIC PREDICTION AND CHEMINFORMATIC EXPLORATION

Abstract

In the body, cell monolayers serve as permeability barriers, determining transport of molecules from one organ or tissue compartment to another. After oral drug administration, for example, transport across the epithelial cell monolayer lining the lumen of the intestine determines the fraction of drug in the gut that is absorbed by the body. By modeling passive transcellular transport properties in the presence of an apical to basolateral concentration gradient, we demonstrate how a computational, cell-based molecular transport simulator can be used to define a physicochemical property space occupied by molecules with desirable permeability and intracellular retention characteristics. Considering extracellular domains of cell surface receptors located on the opposite side of a cell monolayer as a drug's desired site of action, simulation of transcellular transport can be used to define the physicochemical properties of molecules with maximal transcellular permeability but minimal intracellular retention. Arguably, these molecules would possess very desirable features: least likely to exhibit nonspecific toxicity, metabolism, and side effects associated with high (undesirable) intracellular accumulation; and most likely to exhibit favorable bioavailability and efficacy associated with maximal rates of transport across cells and minimal intracellular retention, resulting

in (desirable) accumulation at the extracellular site of action. Simulated permeability values showed good correlations with PAMPA, Caco-2, and intestinal permeability measurements, without “training” the model and without resorting to statistical regression techniques to “fit” the data. Therefore, cell-based molecular transport simulators could be useful *in silico* screening tools for chemical genomics and drug discovery.

Keywords: Metoprolol; permeability; chemical space; computer aided drug design; virtual screening; chemical genomics; cellular pharmacokinetics; cheminformatics; drug transport; PAMPA; Biopharmaceutics Classification System

Introduction

Drug uptake and transport across cell monolayers is an important determinant of *in vivo* bioavailability, biodistribution and activity (1). However, enzymes of low selectivity metabolize drugs inside cells (2, 3). High permeability-high solubility drugs administered at high concentrations diffuse across cells fast enough – saturating transporters and enzymes- that only an insignificant fraction is diverted (4, 5). However, high intracellular drug concentrations can also be toxic. For example, unwanted accumulation of small molecules in mitochondria can interfere with mitochondrial function, inducing apoptosis (6, 7). Similarly, unintentional accumulation of molecules in other organelles can induce phenotypic effects unrelated to a drug's primary mechanism of action – manifesting as non-specific toxicity (8). Nevertheless, many drugs are agonists or antagonists of cell surface receptors (9). Since receptor ligand binding domains are extracellular, intracellular drug accumulation is not essential for bioactivity (10). Thus, molecules designed to reach and accumulate at a desired extracellular site of action should combine high transcellular permeability with minimal intracellular accumulation. These desirable biopharmaceutical properties can lead, in turn, to more potent, bioavailable, stable, and nontoxic drug candidates.

Poor pharmacokinetics and toxicity are important causes of failure in later, clinical stages of drug development (4, 11, 12). Therefore, ADMET (absorption, distribution, metabolism, elimination, and toxicity) profiling is desirable as early as possible, before drug candidates are tested in patients. High throughput *in silico* ADMET models are one way to predict favored pharmacokinetics and toxicity profiles, early in the design of new drugs (12). Mapping chemical spaces occupied by molecules possessing a

desirable therapeutic activity and favored ADMET properties can be used to guide the design, synthesis, and selection of series of lead compounds (13-15). Along these lines, we sought to develop a fast, flexible, and scalable computational tool for predicting epithelial transcellular passive permeability and intracellular accumulation, which are important determinants of oral absorption prediction and toxicity prediction, respectively (16-18).

Drug solubility and intestinal permeability are the two key criteria for the FDA's Biopharmaceutics Classification System (BCS) (19). At early stages of drug development mathematical models built on the basis of data derived from *in vitro* experiments such as PAMPA (parallel artificial membrane permeation assay) and Caco-2 assay are widely used to predict human intestinal permeability. Most existing mathematical models to predict intestinal permeability are based on statistical regression methods that correlate PAMPA, Caco-2, or rat or human intestinal permeability measurements to 2D and/or 3D molecular descriptors (20-22). However, the predictive power of these statistical models is inherently dependent on the quality of training data set, as well as the variability and reproducibility of the experimental assay. Furthermore, because of the statistical nature of the regression relationship, large amounts of data are needed to generate good models covering large realms of chemical space. To complement statistical regression methods, we decided to pursue a mechanism-based, mathematical modeling strategy to predict transcellular passive permeability, while also predicting the intracellular concentration of drug and its accumulation in organelles. In addition, on the basis of permeability and intracellular concentration of a reference “lead” compound, we also sought a nonstatistical method that could map cell-

permeant/impermeant and cell-toxic/nontoxic chemical spaces relative to that compound, to help guide drug lead development efforts of pharmaceutical scientists and medicinal chemists.

Here, we present a mechanism-based modeling strategy that can predict intestinal transcellular passive permeability, as well as drug accumulation within cells. Mathematically, the model describes transcellular transport of small molecules based on a physical, compartmental model of a cell, coupling sets of differential equations describing the physics of passive diffusion of small molecules across membranes delimiting the different compartments (23). Without incorporating enzymatic mechanisms or specific binding interactions, the current version of the model can predict the behavior of nonzwitterionic, monocharged small molecules possessing one ionizable functional group in the physiological pH range. Nevertheless, the behavior of more complex molecules and mechanisms such as carrier mediated transport, metabolic processes, or multiple ionizable groups can be incorporated one by one in subsequent versions of the model, to predict the transport of low permeability, natural product like molecules, and to mimic more complex, physiological conditions.

Methods

Starting with a cell-based, molecular mass transport model developed to study the accumulation of lipophilic cations in tumor cells (23), we adapted the Nernst-Planck and Fick equations to simulate transport of molecules across epithelial cell monolayers, in the presence of an apical-to-basolateral, transcellular concentration gradient. For weakly-basic / acid, drug-like small molecule, the cellular pharmacokinetic model considers three physicochemical properties as the most important determinants of intracellular

accumulation and transport: (1) the logarithm of the lipid/water partition coefficient of the neutral form of the molecule, $\log P_n$; (2) the logarithm of the lipid/water partition coefficient of the ionized form of the molecule, $\log P_d$; (3) and the negative logarithm of the dissociation constant of the protonated functional group, pK_a . Drug concentrations in different intracellular compartments are coupled to each other according to the topological organization of the cell (Figure 2.1A, B). Different organelles have different pHs and transmembrane electrical potentials, so a molecule's charge in different organelles can vary according to the molecule's pK_a , and transport properties across the membranes delimiting different compartments can vary depending on the membranes' electrical potential (24-27). With the model developed herein, the concentration of molecules in different subcellular compartments and the transcellular permeability coefficient (P_{eff}) can be calculated for different time intervals after cells are exposed to drug (see appendix A).

For modeling drug accumulation in the cytosolic compartment, the mitochondrial compartment, and the basolateral compartment, the total mass change of the molecule with time can be expressed by equations 2.1-2.3:

$$\frac{dm_c}{dt} = A_a J_{a,c} - A_m J_{c,m} - A_b J_{c,b}, \quad (2.1)$$

$$\frac{dm_m}{dt} = A_m J_{c,m}, \quad (2.2)$$

$$\frac{dm_b}{dt} = A_b J_{c,b}, \quad (2.3)$$

where J is the net flux from the 'positive' side to the 'negative' side, m is the total molecular mass, t is time, A is membrane surface area, subscripts c , a , b , and m indicate cytosolic, apical, basolateral, and mitochondrial respectively. The direction from

apical to basolateral compartment was defined from the ‘positive’ side to the ‘negative’ side.

To solve the above equations, the relationships between fluxes and masses must be specified. The bridge between these quantities is the concentration in each compartment. Each side of equations 2.1, 2.2 and 2.3 is divided by the volumes of each compartment to get equations 2.4, 2.5, and 2.6.

$$\frac{dC_c}{dt} = \frac{A_a}{V_c} J_{a,c} - \frac{A_m}{V_c} J_{c,m} - \frac{A_b}{V_c} J_{c,b}, \quad (2.4)$$

$$\frac{dC_m}{dt} = \frac{A_m}{V_m} J_{c,m}, \quad (2.5)$$

$$\frac{dC_b}{dt} = \frac{A_b}{V_b} J_{c,b}, \quad (2.6)$$

where C_c , C_m , and C_b are cytosolic, mitochondrial, and basolateral concentration and V_c , V_m , and V_b are volumes of cytosolic, mitochondrial, and basolateral compartments respectively. The passive diffusion flux of neutral molecules across membranes is described by Fick’s First Law:

$$J = P(a_o - a_i), \quad (2.7)$$

where J is the molecular flux from the out side to the inside (i) (‘negative’ side) of the membrane, P is the permeability of the molecules across cellular membranes, and a is the activity of the molecules. For electrolytes the driving forces across cellular membrane are not only chemical potential but also electrical potential, which is described by the Nernst-Planck equation. With the assumption of a linear potential gradient across the membrane, a net current flow of zero and with each ion flux is at steady state, an analytical solution for the flux of the ion is

$$J = P \frac{N}{e^N - 1} (a_o - a_i e^N), \quad (2.8)$$

where $N = zEF / RT$, z is the electric charge, F is the Faraday constant, E is the membrane potential, R is the universal gas constant, and T is the absolute temperature (23). If equations 2.7 and 2.8 are combined, the net fluxes across each membrane for both neutral forms and ionic forms can be described by equation 2.9.

$$J = P_n (a_{o,n} - a_{i,n}) + P_d \frac{N}{e^N - 1} (a_{o,d} - a_{i,d} e^N), \quad (2.9)$$

where P_n is the permeability of neutral form across the membrane, P_d is the permeability of ionized form across the membrane, $a_{o,n}$ and $a_{i,n}$ are the activities of neutral form outside and inside respectively, $a_{o,d}$ and $a_{i,d}$ are the activities of ionized form outside and inside respectively. So the net fluxes across each membrane are

$$J_{a,c} = P_n (a_{n,a} - a_{n,c}) + P_d \frac{N_a}{e^{N_a} - 1} (a_{d,a} - a_{d,c} e^{N_a}), \quad (2.10)$$

$$J_{c,m} = P_n (a_{n,c} - a_{n,m}) + P_d \frac{N_m}{e^{N_m} - 1} (a_{d,c} - a_{d,m} e^{N_m}), \quad (2.11)$$

$$J_{c,b} = P_n (a_{n,c} - a_{n,b}) + P_d \frac{N_b}{e^{N_b} - 1} (a_{d,c} - a_{d,b} e^{N_b}), \quad (2.12)$$

where $J_{a,c}$, $J_{c,m}$, and $J_{c,b}$ are net flux across apical membrane, mitochondrial membrane, and basolateral membrane, respectively; $a_{a,n}$, $a_{c,n}$, $a_{m,n}$, and $a_{b,n}$ are the neutral molecular form activities in the apical compartment, cytosolic compartment, mitochondrial compartment and basolateral compartment, respectively; $a_{a,d}$, $a_{c,d}$, $a_{m,d}$ and $a_{b,d}$ are the ionized molecular form activities in the apical compartment, cytosolic compartment, mitochondrial compartment and basolateral compartment, respectively; N_a , N_m , and N_b are the N values for apical membrane, mitochondrial membrane and

basolateral membrane, respectively. The Henderson-Hasselbalch equation (2.13) describes the activity ratio of neutral form molecules and ionized form molecules,

$$\log \frac{a_d}{a_n} = i(pH - pK_a), \quad (2.13)$$

where a_d and a_n are the ionized molecular form and the neutral molecular form, respectively, i is 1 for acids and -1 for bases; pK_a is the negative logarithm of the dissociation constant. Therefore,

$$a_d = a_n \times 10^{i(pH - pK_a)}, \quad (2.14)$$

The relationship of the activities (a_n and a_d) and the total molecular concentration can be expressed by equation 2.15 and 2.16 (28),

$$f_n = a_n / C_t = \frac{1}{W / \gamma_n + K_n / \gamma_n + W \times 10^{i(pH - pK_a)} / \gamma_d + K_d \times 10^{i(pH - pK_a)} / \gamma_d}, \quad (2.15)$$

$$f_d = a_d / C_t = f_n 10^{i(pH - pK_a)}, \quad (2.16)$$

W is the volumetric water fraction, γ the activity coefficient, and K_n and K_d the sorption coefficients of the neutral and the ionized molecules respectively. K_n and K_d are estimated by equation 2.17, where L is the lipid fraction in each compartment and $K_{ow,n/d} = 10^{\log P_{n/d,lip}}$ ($\log P_{n,lip}$ and $\log P_{d,lip}$ calculated with equations 2.28-2.31).

$$K_{n/d} = L \times 1.22 \times K_{ow,n/d}, \quad (2.17)$$

The activity coefficient of all neutral molecules (γ_n) is related to the ionic strength I (moles). Using the Setchenov equation, at $I = 0.3$ mol, γ_n is 1.23. The activity of ions (γ_d) is calculated with the Davies approximation of the modified Debye-Hückel equation (23). For monovalent ions at $I = 0.3$ mol, γ_d is 0.74. For conditions outside the cell, no corrections for the ionic strength are made, and activities are set approximately equal to

concentration ($\gamma = 1$) (23). Plug equation 2.15 and 2.16 into equations 2.10, 2.11 and 2.12 to get equations 2.18, 2.19 and 2.20.

$$J_{a,c} = P_n(f_{n,a}C_a - f_{n,c}C_c) + P_d \frac{N_a}{e^{N_a} - 1} (f_{d,a}C_a - f_{d,c}C_c e^{N_a}), \quad (2.18)$$

$$J_{c,m} = P_n(f_{n,c}C_c - f_{n,m}C_m) + P_d \frac{N_m}{e^{N_m} - 1} (f_{d,c}C_c - f_{d,m}C_m e^{N_m}), \quad (2.19)$$

$$J_{c,b} = P_n(f_{n,c}C_c - f_{n,b}C_b) + P_d \frac{N_b}{e^{N_b} - 1} (f_{d,c}C_c - f_{d,b}C_b e^{N_b}), \quad (2.20)$$

Plug equations 2.18, 2.19 and 2.20 into equations 2.4, 2.5, and 2.6 to get equations 2.21, 2.22, and 2.23.

$$\begin{aligned} \frac{dC_c}{dt} = & \frac{A_a}{V_c} [P_n(f_{n,a}C_a - f_{n,c}C_c) + P_d \frac{N_a}{e^{N_a} - 1} (f_{d,a}C_a - f_{d,c}C_c e^{N_a})] \\ & - \frac{A_c}{V_c} [P_n(f_{n,c}C_c - f_{n,m}C_m) + P_d \frac{N_m}{e^{N_m} - 1} (f_{d,c}C_c - f_{d,m}C_m e^{N_m})] \\ & - \frac{A_b}{V_c} [P_n(f_{n,c}C_c - f_{n,b}C_b) + P_d \frac{N_b}{e^{N_b} - 1} (f_{d,c}C_c - f_{d,b}C_b e^{N_b})] \end{aligned}, \quad (2.21)$$

$$\frac{dC_m}{dt} = \frac{A_m}{V_m} [P_n(f_{n,c}C_c - f_{n,m}C_m) + P_d \frac{N_m}{e^{N_m} - 1} (f_{d,c}C_c - f_{d,m}C_m e^{N_m})], \quad (2.22)$$

$$\frac{dC_b}{dt} = \frac{A_b}{V_b} [P_n(f_{n,c}C_c - f_{n,b}C_b) + P_d \frac{N_b}{e^{N_b} - 1} (f_{d,c}C_c - f_{d,b}C_b e^{N_b})], \quad (2.23)$$

The membrane permeability P (23) can be estimated using:

$$P = DK / \Delta x, \quad (2.24)$$

D is the diffusion coefficient which is about 10^{-14} m² / s for organic molecules in biomembranes. K is the partition coefficient, and approximates K_{ow} . Δx is the membrane thickness and is considered about 50 nm for biomembranes. Plugging these estimated numbers into equation 2.24 and doing a logarithm conversion gives equation 2.25.

$$\log P = \log K_{ow} - 6.7, \quad (2.25)$$

Per definition, the transcellular permeability coefficient (P_{eff}) is calculated using:

$$P_{eff} = \frac{dC_b \times V_b}{dt \times A_{aa} \times C_a}, \quad (2.26)$$

where A_{aa} is the cellular monolayer area, dC_b the total concentration change in basolateral compartment with time dt , and C_a the concentration in apical compartment, which is assumed to be constant in this model.

MATLAB[®] was used to solve the system of coupled differential equations (equations 2.21, 2.22, and 2.23). The concentrations in cytosol (C_c), mitochondria (C_m), basolateral compartment (C_b), and transcellular permeability coefficient (P_{eff}) were solved numerically. Cellular parameters describing the intestinal epithelial cell were obtained from the literature. The MATLAB[®] solver, graphics scripts, and model parameters are included as appendix A.

Using this model, permeability and intracellular concentration of 36 compounds were calculated (Figures 2.2, 2.3). These compounds were selected on the basis of the following criteria: (1) they are monoionized or neutral in the physiological pH environment; (2) their $\log P_n$, pK_a , and Caco-2 permeability were experimentally measured and published. The octanol/water partition coefficients ($\log P_n$) were obtained from SRC PhysProp Database and other references in the scientific literature (29-31), and pK_a values were also experimental data obtained from several published articles (10, 32-40). The partition coefficients of the ionized state of the molecules ($\log P_d$) were estimated from $\log P_n$ according to equation 2.27 (23).

$$\log P_d = \log P_n - 3.7, \quad (2.27)$$

Equations 2.28-2.31 were used to obtain the liposomal partition coefficient for both neutral forms and ionic forms of bases and acids (34). For ampholytes to get the liposomal partitioning, the equation for neutral forms of bases was applied.

$$\text{for neutral forms of bases: } \log P_{n,lip} = 0.33 \log P_n + 2.2, R^2 = 0.69, (2.28)$$

$$\text{for cationic forms of bases: } \log P_{d,lip} = 0.37 \log P_d + 2, R^2 = 0.49, (2.29)$$

$$\text{for neutral forms of acids: } \log P_{n,lip} = 0.37 \log P_n + 2.2, R^2 = 0.89, (2.30)$$

$$\text{for anionic forms of acids: } \log P_{d,lip} = 0.33 \log P_d + 2.6, R^2 = 0.72, (2.31)$$

Additional literature references, $\log P_n$, $\log P_d$, pK_a values, and calculated permeability and intracellular concentration obtained with our model are included in the appendix A.

Linear regression was used to compare predicted permeability values with the Caco-2, PAMPA, and human intestinal permeability adopted from the literature (1, 12, 40-47). As noticed, Caco-2 permeability data obtained from different references differ even for the same drug, thus the mean values of Caco-2 permeability obtained from different literature sources were used to compare with the predicted permeability.

Cell-permeant nontoxic chemical space, cell-permeant toxic chemical space, cell-impermeant chemical space, cell-permeant chemical space, cell-toxic chemical space, and cell-nontoxic chemical space were defined by calculating P_{eff} , C_c , and C_m of weakly basic monocationic molecules spanning pK_a from 1 to 14, $\log P_n$ from -5 to +5, and $\log P_d$ from -5 to +5. Each one of these physicochemical parameters was varied independently in 0.1 unit intervals, and combined with the other parameters. To evaluate the robustness of the results obtained with the model, chemical space plots were visually inspected for

reproducibility and consistency after changing one parameter at a time while keeping the others unchanged. The change of $\log P_n$ and $\log P_d$ were discussed under two conditions: (1). $\log P_n$ and $\log P_d$ changed independently; and (2). $\log P_n$ and $\log P_d$ linked to each other by equations 2.27 to 2.31. Parameter values used in calculation are included in the appendix A. .

Results

A cellular pharmacokinetic model of passive transcellular drug transport

Transcellular permeability is a key property determining biodistribution of soluble drug molecules from one body compartment to another. For an orally administered drug with high solubility, the transcellular permeability of the cells lining the intestine determines the fraction of drug in the intestine that is absorbed by the body. In epithelial cells lining the lumen of the intestine (Figure 2.1A), apical microvilli make the apical surface area (48) much greater than the basolateral surface area (9). The length of an epithelial cell is approximately 10 to 15 μm . A_{aa} is the effective cross-sectional area of each cell, corresponding to the total area of the cell monolayer across which transport occurs, divided by the total number of cells involved in the transcellular transport process. Finally, the total volume of the cell V constrains its overall geometry in relation to A_a , A_b , and A_{aa} . On the basis of these parameters, the apical-to-basolateral permeability of an intestinal epithelial cell can be calculated with equation 2.26.

Setting cellular parameters to mimic an intestinal epithelial cell, the model captures the mass transport followed by a weak base or acid (nonzwitterionic molecule), through said cell (Figure 2.1B). Such molecules exist as equilibrium mixtures of neutral

and ionic states, their proportions determined by the pH of the immediate environment. In the case of high solubility-high permeability molecules, passive diffusion is the dominant transcellular transport mechanism (4, 5, 46, 49), driven by concentration gradients of drugs and ions, and the transmembrane electrical potential. Assuming that mixing of molecules within each subcellular compartment is faster than the rate at which they traverse the delimiting membranes, the mass of drug in each compartment can be modeled using a set of coupled differential equations based on an empirical relationship between lipophilicity and transmembrane permeability of small molecules, and Fick's Law of diffusion (23). To traverse the cell, molecules first cross the apical membrane, distributing homogeneously in the cytosol and partitioning into cytoplasmic lipids. From the cytosol, they also partition into and out of organelles, and exit the cell across the basolateral membrane.

After simulating the transcellular transport process, the calculated permeability values were found to be consistent with the experimental values. Specifically, we first considered the intracellular concentration and permeability coefficient of molecules with physicochemical properties resembling β -adrenergic receptor blockers: metoprolol and related compounds (Figure 2.2; Table 2.1). Metoprolol is orally bioavailable, but less permeable and less toxic than more hydrophobic relatives, such as propranolol (50). Comparing the calculated results (Table 2.1) with the experimental data (Table 2.2), the calculated permeability coefficient of metoprolol is similar to the human permeability coefficient measured in intestinal perfusion experiments (51), and the coefficient of propranolol is 1 order of magnitude smaller than human permeability coefficients (51).

The *in silico* permeabilities are generally within an order of magnitude of experimentally measured Caco-2 and human intestinal permeability.

Comparing the calculated permeabilities with experimental permeability data

Correlation of predicted permeability with Caco-2 permeability and human intestinal permeability were plotted to evaluate the model. Figure 2.2 is the scatter plot of predicted permeability and Caco-2 permeability of seven β -adrenergic receptor blockers - alprenolol, atenolol, metoprolol, oxprenolol, pindolol, practolol, and propranolol - possessing the same core structure (Table 2.1). This homologous set of drugs has similar pK_a values (Table 2.1). A significant relationship was observed.

Next, we examined the correlation of predicted and Caco-2 permeability of 36 structurally unrelated compounds (including the 7 shown in Figure 2.2; Figure 2.3). By visual inspection, the predicted permeability of compounds shown in Figure 2.3 can be readily categorized into two groups: high permeability and low permeability. Using the predicted permeability of metoprolol (No. 18) as a reference (dashed horizontal line), compounds that fall into the dashed oval are predicted to be high permeability by the model and also exhibit high permeability in Caco-2 assays. Most high permeability compounds transport predominantly by the transcellular pathway with some exceptions: for example, P-glycoprotein reportedly affects acebutolol (No. 1 in Figure 2.3) intestinal absorption (52). In the scatter plot, the predicted permeability of acebutolol was higher than the Caco-2 permeability, which is consistent with P-glycoprotein efflux not being captured by the model. In contrast, many (predicted) low permeability drugs and molecules possess a significant paracellular or active transport pathway. For example, mannitol (No. 17 in Figure 2.3) is widely used as a passive paracellular permeability

marker, so its measured permeability reflects paracellular transport - not only the passive transcellular diffusive permeability that is predicted by the model. Conversely, taurocholic acid and valproic acid are substrates of transporters (41), which leads to higher measured permeability, well above the passive permeability predicted by the model.

Next, the calculated permeability of compounds that fell into the dashed oval in Figure 2.3 (those with correctly predicted, high Caco-2 permeability) were compared with PAMPA assay results, as reported in the scientific literature (Table 2.2). For each individual PAMPA assay result, compounds with higher-than-metoprolol permeability were defined “high permeability” and lower-than-metoprolol permeability were defined “low permeability” (53-55). Table 2.2 shows that PAMPA permeability measured in different conditions is different and is affected by buffer conditions (54). According to FDA waiver guidance (56) the reference drugs ketoprofen and naproxen would be misclassified in two PAMPA measurement, using metoprolol as the internal reference in the published data sets (Table 2.2). Nevertheless, both naproxen and ketoprofen are correctly classified by our computational model.

To compare the predicted permeability with human intestinal permeability, a scatter plot was graphed (Figure 2.4). Since human intestinal permeability data are scarce, among the 36 compounds used in this study (those with experimentally measured $\log P$, pK_a , and possessing only one ionizable functional group in the physiological pH range) we only found 10 of them having human intestinal permeability data. A significant linear relationship was obtained.

Probing the effects of drug physicochemical properties on cellular pharmacokinetics

The physicochemical properties of drug molecules influence intracellular concentration and transcellular permeability. For a monovalent cationic weak base, the model explicitly considers how three different parameters (the logarithm of the lipid/water partition coefficient of the neutral form of the molecule, $\log P_n$; the logarithm of the lipid/water partition coefficient of the ionized form of the molecule, $\log P_d$; and the negative logarithm of the dissociation constant of the protonated functional group, pK_a) can affect these properties. *In silico*, one can change each property one at a time, keeping the others unchanged. Two conditions were considered here: (1) $\log P_n$ and $\log P_d$ vary independently (Figure 2.5A); and (2) $\log P_n$ and $\log P_d$ are linked by equations 2.27 to 2.31 (Figure 2.5B). Although the actual relationship between $\log P_n$ and $\log P_d$ of a molecule is neither perfectly linear nor completely independent, simulating these two extremes conditions linking $\log P_n$ and $\log P_d$ is one way to assess how physicochemical properties affect calculated permeability and intracellular concentration. For a metoprolol-like molecule cytosolic concentrations remain low and constant as $\log P_n$ is varied between -5 and +3 (Figure 2.5A left and Figure 2.5B left). However, increasing $\log P_n$ from +3 to +5 increases cytosolic concentration to levels that greatly exceed the extracellular drug concentration. For mitochondrial concentrations, as $\log P_n$ increases from -5 to 5, there is a pronounced decrease in mitochondrial sequestration. For the transcellular permeability, there is an increase in permeability between $\log P_n = 3$ and $\log P_n = 5$, in parallel to the increase in cytosolic concentration. Thus, for a metoprolol-like molecule, the desired $\log P_n$ lies between 2 and 3, at which cytosolic and mitochondrial concentrations are minimal, whereas transcellular permeability is maximal.

Just as for the $\log P_n$ parameter, the $\log P_d$ values of a metoprolol-like molecule were varied to determine the effect on intracellular concentrations and permeability coefficients. For $\log P_d$ values less than 2, the intracellular concentration of drug at the steady state is low and constant (Figure 2.5A middle and Figure 2.5B middle). However if $\log P_d$ increases above 2, cytosolic concentrations increase and greatly exceed extracellular drug concentration. For $\log P_d$ values greater than 3, there is more than a 10-fold increase in mitochondrial concentration above the extracellular concentration. Nevertheless, increasing $\log P_d$ has the greatest influence on the transcellular permeability value, with increasing $\log P_d$ associated with the fastest rates of transcellular transport. Thus, according to these simulations, increasing $\log P_d$ leads to the very desirable effects of increasing transcellular transport rates, although it also leads to the very undesirable effect of increasing cytosolic and mitochondrial drug accumulation.

Finally, the pK_a value of a metoprolol-like molecule was varied, to study the effect on subcellular transport and biodistribution properties. Compared to the other two parameters, increasing pK_a from 9 to 14 has little effect on transmembrane permeability (Figure 2.5A right and Figure 2.5B right). However, decreasing it from 9 to 7 greatly increased the permeability. Lowering the pK_a below 9 increased the cytosolic concentration, while increasing it above 9 increased the mitochondrial concentration. Thus the pK_a of metoprolol is near the point where cytosolic and mitochondrial concentrations are minimized while transcellular permeability is maximized. Again, by varying the physicochemical properties of a metoprolol-like molecule one at a time, the simulations suggests that the cellular pharmacokinetic properties of metoprolol are quite

good and would be difficult to improve by varying the physicochemical properties of the molecule, one at a time.

Chemical space definitions and solutions

Molecules with intracellular concentrations less than - and permeability values greater than - those for a molecule with metoprolol-like physicochemical properties would possess desirable pharmacokinetic properties would be expected to lead to even higher oral bioavailability, improved biodistribution, and decreased metabolism, relative to metoprolol. To identify the physicochemical properties associated with such molecules, we proceeded to calculate the intracellular concentrations and transcellular permeability values of over a million different possible combinations of pK_a , $\log P_n$ and $\log P_d$. Four different regions of chemical space were defined relative to the steady-state permeability and intracellular concentration of a molecule with metoprolol-like properties as follows: (1) Permeant: Molecules with calculated P_{eff} equal to or larger than P_{eff} of the reference. (2) Impermeant: Molecules with calculated P_{eff} less than the reference P_{eff} . (3) Nontoxic: Molecules with both C_{cyto} and C_{mito} equal to or less than C_{cyto} and C_{mito} of the reference molecule. (4) Toxic: Molecules with either C_{cyto} or C_{mito} larger than C_{cyto} or C_{mito} of the reference molecule. Again, two independent set of simulations were carried out, to represent linearly correlated and uncorrelated $\log P_n$ and $\log P_d$ values.

Complete analysis of regions of physicochemical property space surrounding molecules with metoprolol-like properties (Figure 2.6) reveal the extent to which cell permeability and intracellular accumulation may be related to the physicochemical properties of the molecules. First, we consider the simulations in which $\log P_n$ and $\log P_d$ are varied independently from each other. Note that about 42.7% of total chemical space

is occupied by combinations of pK_a , $\log P_n$, and $\log P_d$ that would make molecules more permeant than a molecule with metoprolol-like properties (Figure 2.6A). The remaining 57.3% is occupied by combinations of pK_a , $\log P_n$, and $\log P_d$ that would make molecules less permeant than a molecule with metoprolol-like properties. Combinations of pK_a , $\log P_n$, and $\log P_d$ that lead to intracellular concentrations greater than those obtained with a molecule with metoprolol-like physicochemical properties lie within “toxic” chemical space, by definition. This region of chemical space comprises 60.6% of the total chemical space, with the remaining 39.4% falling in “nontoxic” space (Figure 2.6B). If cellular permeability and toxicity were completely unrelated to each other, one would expect that 16.8% of the molecules would fall under “permeantnontoxic” space (16.8% permeant nontoxic) 39.4% nontoxic 42.7% permeant). However, the actual fraction of molecules falling in cell permeant-nontoxic space (Figure 2.6C) is 1.5%, as permeability and intracellular accumulation are partly related to each other. Thus, while combinations of pK_a , $\log P_n$, and $\log P_d$ promoting permeability and nontoxicity work against each other to some degree, there is a small chunk of physicochemical property space where molecules with greater permeability than metoprolol, but reduced intracellular accumulation, may reside. Indeed, there may be a small but significant number of molecules possessing a desirable combination of physicochemical properties leading to improved bioavailability and biodistribution properties relative to a molecule with metoprolol-like features.

Last, we mapped the chemical space surrounding a molecule with metoprolol-like physicochemical properties, under conditions in which $\log P_n$ and $\log P_d$ are perfectly coupled to each other in a linear relationship (Figure 2.7). Under these conditions, physicochemical property space is reduced to a plane, with a molecule of metoprolol-like

features sitting at the intersection of the boundary delimiting permeant-impermeant and toxic-nontoxic space (Figure 2.7). The impermeant nontoxic and the impermeant toxic were 47.6% and 7.5% of the total space. Most importantly, while permeant toxic occupies 43.7% of the total space respectively, permeant nontoxic occupies 0.11% of this space. Thus, our simulations also indicate that the extent to which $\log P_n$ and $\log P_d$ are coupled can severely restrict the ability to find a metoprolol-like molecule with improved biopharmaceutical features. Furthermore, examining where permeant nontoxic space exists relative to metoprolol, one finds that lowering the pK_a may be the only way to both increase the permeability and decrease the intracellular accumulation (toxicity) of metoprolol. For the β -blockers, the pK_a of the molecule is determined by an isopropyl amine group that is shared by all the congeners (Table 2.1), and therefore this group may be essential for receptor binding. One way around this constraint would be to change the ionization properties of the molecules by making them zwitterionic at physiological pH. However, the current model cannot capture the behavior of zwitterions, so a theoretical analysis of this optimization strategy must await development and validation of more advanced versions of the model.

Discussion

Transport of small molecules into and out of cells and organelles is determined by both passive and active transport mechanisms. The cellular pharmacokinetic model elaborated in this study specifically captures passive transport mechanisms, determined by the physicochemical properties of small molecules, their interactions with phospholipid bilayers, and the concentration gradients of ions and macromolecules across cellular membranes (22, 48, 57, 58). Empirical (12, 22, 59) and theoretical (60-62)

considerations establish three physicochemical properties of small molecules as key determinants of passive transport across membranes: size, charge, and lipophilicity. Most molecules used for drug discovery and chemical genomics investigations are “small”, i.e. between 200 and 800 daltons, and therefore similar in size. Thus, the model is suitable for comparing the behavior of small molecules within this limited size range, where the main physicochemical properties influencing the distribution of molecules in cells are the multiple ionization states, and the lipophilicity of each ion.

For model validation, metoprolol was used as a reference because it is an FDA-approved drug that is 95% absorbed in the gastrointestinal tract (1), and it is recommended as an internal standard - to be included in experiments that assess drug permeability (56) - by the FDA. Metoprolol is generally included in published PAMPA, Caco-2, and intestinal permeability datasets, as a reference point with which to establish the threshold between high and low permeability compounds. Several metoprolol relatives - like atenolol - are orally bioavailable, moderate absorption, low metabolism, low toxicity, renally cleared (36, 63-66) with a well-characterized, passive-transport absorption mechanism (67), *in vitro* and *in vivo* permeability characteristics (51, 68) and measured micro $pK_a/(logP)$ properties (34). Using the physicochemical properties of metoprolol as a reference, cell-based molecular transport simulations were used to calculate the pharmaceutical properties of related β -adrenergic receptor antagonists. Setting cellular parameters and model geometry to mimic an intestinal epithelial cell, the simulations permitted testing the effects of different biological and chemical parameters on intracellular concentrations and transcellular permeability coefficients, through time. The steady-state values for high permeability compounds were comparable to

experimental measurements obtained through intestinal, *in vivo* perfusion experiments, and Caco-2, *in vitro* permeability assays (22, 69, 70). In addition, running over a million different combinations of $\log P_n$, $\log P_d$, and pK_a through the simulation allowed us to define a physicochemical property space leading to the most desirable biopharmaceutical characteristic (higher transcellular permeability with lower intracellular accumulation), relative to the simulated characteristics of a metoprolol-like molecule.

We note that, since intracellular accumulation and permeability are related to each other, optimizing a single biopharmaceutical property (permeability) of a compound at a time may lead to unfavorable biodistribution properties (intracellular accumulation) associated with toxicity or drug clearance by metabolism. Indeed, complex properties like bioavailability may be predictable as nonlinear functions of the fundamental physicochemical properties of molecules, under conditions in which transcellular transport is maximized and intracellular concentrations are minimized. Due to the limited experimental data available for fitting statistical models, and the relatively complex behaviors apparent in the simplified model presented in this study, our results suggest that purely empirical, statistical regression models built from human, Caco-2, or even PAMPA permeability data would be comparatively limited in their ability to predict bioavailability of small molecule drugs. Thus, cellular pharmacokinetic simulations could be used to complement to the more conventional, regression-based statistical approaches. This is especially true in situations when the statistical models lack power, such as when assay measurements are too variable or of low quality, or when a training dataset is unavailable, of dubious quality, or too sparse. With continued validation and refinement,

cell-based mass transport simulators can become increasingly sophisticated in their ability to capture more complex phenomena of pharmaceutical importance.

Admittedly the scope of the current, passive diffusion model is narrow, as its predictions apply only to nonzwitterionic, monocharged molecules within a limited size range, administered at high concentrations so that they saturate specific binding sites on intracellular proteins, enzymes, and transporters. However the therapeutic impact of the model could be substantial, since 80% of currently marketed therapeutic products are small molecules, administered orally and at high concentrations (19). Moreover the majority of these do target cell surface receptors or ion channels (9). The FDA's Biopharmaceutics Classification System (47) recognizes four classes of oral drug products: class I (high solubility-high permeability); class II (low solubility-high permeability); class III (high solubility-low permeability); and class IV (low solubility-low permeability). The model is mostly relevant to class I and II small molecule drugs, which turn out to be very common and well-behaved, encompassing about half of the drug products on the market (19). Since extracellular receptor binding allows maximizing a drug's transcellular permeability while minimizing intracellular accumulation, our model provides a mechanistic explanation as to why the major class of well-behaved, orally bioavailable drugs currently on the market does often target extracellular domains of cell surface receptors.

To conclude, cell-based molecular transport simulators can be used to make other predictions in addition to transcellular permeability, which could also be experimentally tested. Because each component that goes into the model can be studied and improved independently, more precise membrane transport equations including additional variables

(such as molecular weight)(60, 62) and additional subcellular compartments could be readily incorporated into the models, albeit at the expense of greater computational complexity. Indeed, by checking predictions with experiments, the model can be gradually improved and evolved, and its scope can be extended to describe the transport of an increasing variety of molecules (such as zwitterions), under increasingly diverse conditions. Using single cells as pharmacokinetic units, it should be possible to model transport functions in multicellular organizations, simulating transport functions in tissues and even organs, and even incorporate intracellular enzymatic, transporter, and specific binding and nonspecific absorption activities through the Michaelis-Menten equation and binding isotherms. By coupling cell-based, molecular transport simulators to other cheminformatic analysis tools (such as computational pK_a and $\log P$ calculators), *in silico* screening experiments may be performed - rapidly, inexpensively, reproducibly, and reliably - on a large number of molecules, to explore the diversity of large collections of molecules in terms of their cellular pharmacokinetic and pharmacodynamic properties.

Table 2.1. Structures, physicochemical properties, average Caco2 permeabilities, and predictive permeabilities of seven β -adrenergic blockers. The $\log P_{n, lip}$ values are the calculated liposomal $\log P_n$ which were used in permeability calculation.

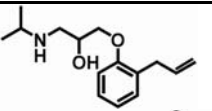
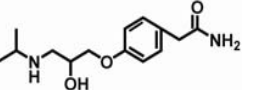
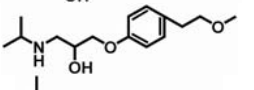
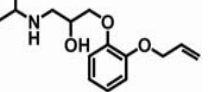
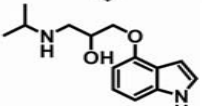
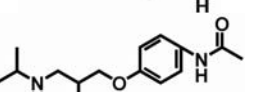
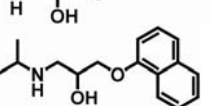
Name	Structures	pK_a	$\log P_n$ (29)	$\log P_{n, lip}$	Caco-2 P_{eff} (10^{-6} cm/s)	Calculated		
						P_{eff} (10^{-6} cm/s)	C_{cyto} (mM)	C_{mito} (mM)
alprenolol		9.60 (40)	3.10	3.22	95.70	103.38	8.52	11.59
atenolol		9.60 (40)	0.16	2.25	1.07	8.42	2.23	8.76
metoprolol		9.70 (40)	1.88	2.82	40.15	36.63	4.13	12.95
oxprenolol		9.50 (40)	2.10	2.89	97.25	44.29	4.58	8.40
pindolol		9.70 (40)	1.75	2.78	54.53	32.56	3.86	12.65
practolol		9.50 (40)	0.79	2.46	2.91	14.35	2.60	7.29
propranolol		9.49 (33)	2.98 (31)	3.18	34.80	92.47	7.76	8.81

Table 2.2. Comparison of predicted permeability with average Caco2 permeability and PAMA permeability of drugs within the predictive circle in Figure 2.3. Permeability values are in unit of 10^{-6} cm/sec. Metoprolol was chosen a reference compound. (H stands for ‘high permeability’, L stands for ‘low permeability’)

Drugs	Predicted Permeability		PAMPA (54)		PAMPA (55) (at pH7.4)		PAMPA (53) (at pH7.4)		Human intestinal permeability (47)		FDA Waiver Guidance (56)	Tentative BCS Classification (47)
alprenolol	103.38	H	11.50	H			15.1	H				
antipyrine	209.00	H	2.87	L	0.82	L	13.2	H	560	H	H	
chlorpromazine	737.26	H					4.0	H				1
clonidine	45.92	H	10.41	H			14.0	H				
desipramine	468.18	H	16.98	H			14.6	H	450	H		
diazepam	201.67	H										
diltiazem	127.52	H	19.21	H	14	H	18.5	H				2
ibuprophen	280.35	H	21.15	H			6.8	H				2
imipramine	442.66	H	19.36	H			8.4	H				
indomethacin	354.22	H					2.4	L				
ketoprofen	145.35	H	2.84	L	0.043	L	16.7	H	870	H	H	
lidocaine	130.27	H										
metoprolol	36.63	ref	7.93	ref	1.2	ref	3.5	ref	134	ref	H	
naproxen	152.87	H	5.01	L	0.23	L	10.6	H	850	H	H	
oxprenolol	44.29	H	14.64	H								
phenytoin	90.53	H	38.53	H			5.1	H				
pindolol	32.65	L	4.91	L			4.9	H				
piroxicam	1542.75	H	10.87	H			8.2	H	665	H		
propranolol	92.47	H	26.33	H	12	H	23.5	H	291	H	H	1
trimethoprim	194.61	H	3.14	L	2.2	H	5.0	H				4
valproic acid	126.91	H										3

verapamil	208.36	H	23.02	H	14	H	7.4	H	680	H	H	1
warfarin	113.88	H					12.3	H				

Table 2.3. Correlation of predicted permeability VS. human intestinal permeability.
 (Permeability values are in unit of 10^{-6} cm/sec.)

Name	Human Permeability (47)	log(Peff, human)	Predicted Permeability	log(Peff, predicted)
antipyrine	560.00	-3.25	209.00	-3.68
atenolol	20.00	-4.70	8.42	-5.07
desipramine	450.00	-3.35	468.18	-3.33
ketoprofen	870.00	-3.06	145.35	-3.84
metoprolol	134.00	-3.87	36.63	-4.44
naproxen	850.00	-3.07	152.87	-3.82
piroxicam	665.00	-3.18	1542.75	-2.81
propranolol	291.00	-3.54	92.47	-4.03
terbutaline	30.00	-4.52	24.15	-4.62
verapamil	680.00	-3.17	208.36	-3.68

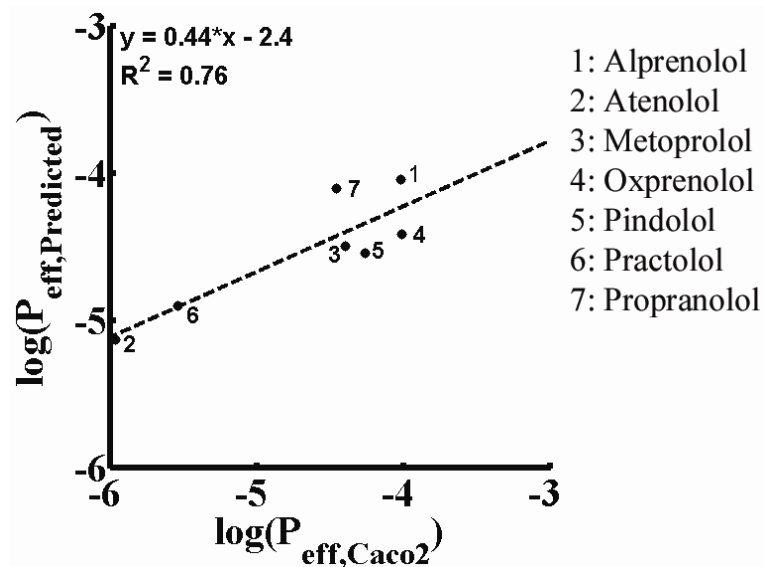


Figure 2.2. Correlation of Caco2 permeability and predicted permeability of seven β -adrenergic blockers. The X-axis indicates the logarithm values of average measured Caco2 permeability (cm/sec) and the Y-axis indicate the logarithm values of predicted permeability (cm/sec). The dotted line is the linear regression line. The linear regression equation is $y = 0.44x - 2.4 (R^2 = 0.76)$, the significance F of regression given by EXCEL is 0.011 (confidence level is 95%). Numbers 1 through 7 indicate alprenolol, atenolol, metoprolol, oxprenolol, pindolol, practolol, and propranolol respectively. The structures, physicochemical properties, average Caco2 permeability and predictive permeability were summarized in Table 2.1.

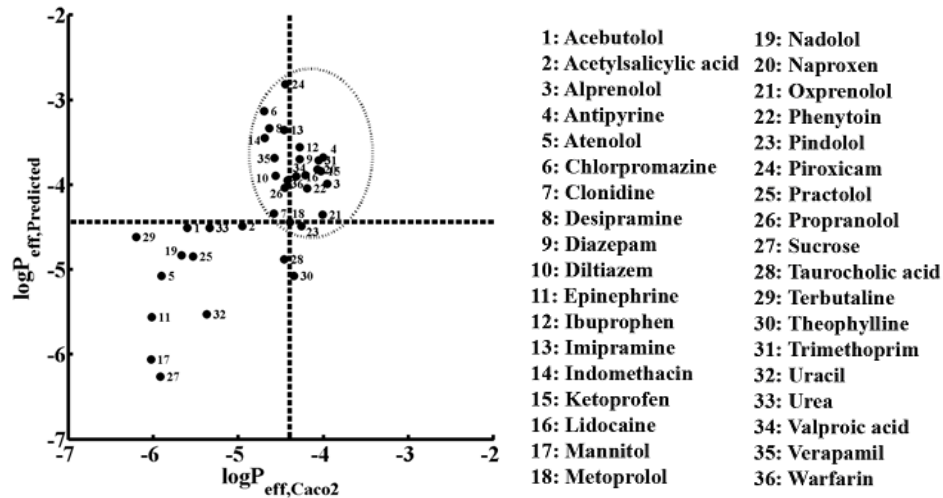


Figure 2.3. Correlation of Caco2 permeability and predicted permeability of thirty-six drugs. The X-axis indicates the logarithm values of average measured Caco2 permeability (cm/sec) and the Y-axis indicate the logarithm values of predicted permeability (cm/sec). Metoprolol (No.18) was used as a reference drug. Details of calculated permeability and average Caco2 permeability were included in the Supplementary Materials.

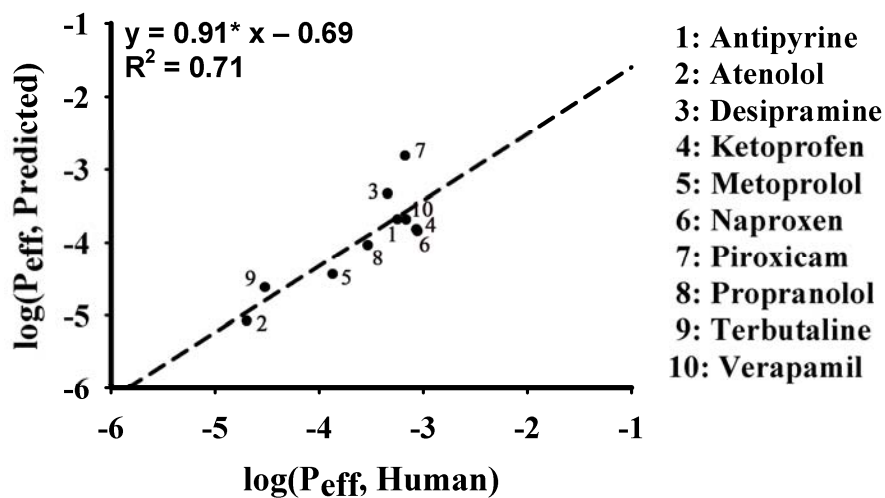


Figure 2.4. Correlation of human intestinal permeability and predicted permeability. The X-axis indicates the logarithm values of measured human intestinal permeability (cm/sec) and the Y-axis indicate the logarithm values of predicted permeability (cm/sec). A simple linear relation was obtained and expressed by the equation: $y = 0.91x - 0.69 (R^2 = 0.71)$, the significance F of regression given by EXCEL is 0.0016 (confidence level is 95%). Calculated permeability and human intestinal permeability numbers were listed in Table 2.3.

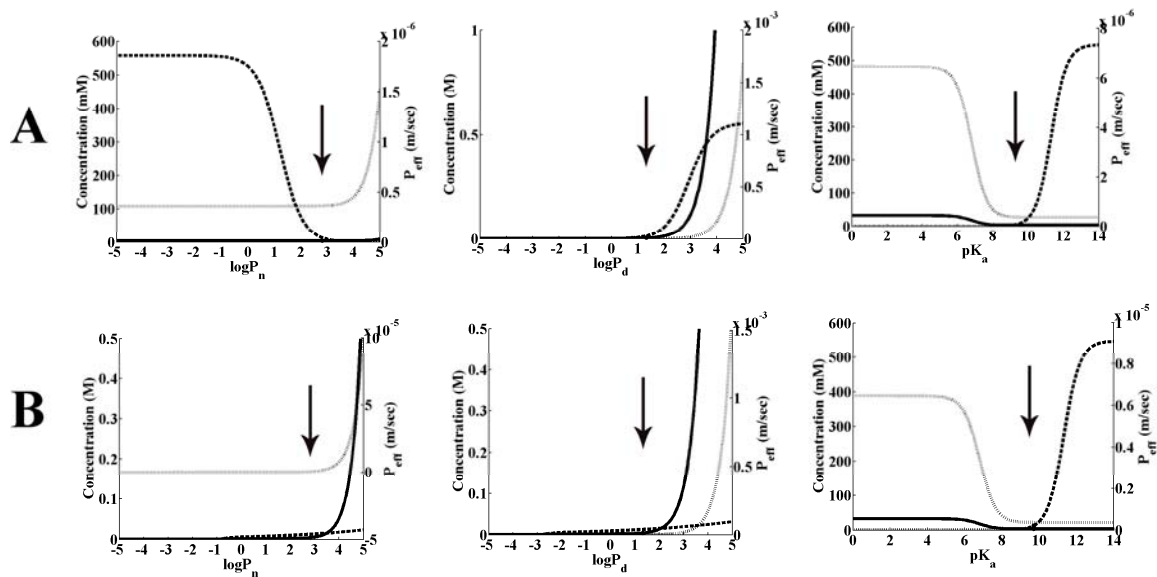


Figure 2.5. Effects of physicochemical properties on intracellular concentration at steady state, of a molecule with metoprolol-like properties (arrows). (A). $\log P_n$ and $\log P_d$ are not associated. (B). $\log P_n$ and $\log P_d$ are associated by a simple linear relationship expressed as equations 2.27-2.29. The arrows indicate the liposomal $\log P_n$, $\log P_d$, $\log P_{n, lip}$ and $\log P_{d, lip}$, which were used in permeability calculation. (solid line = cytosolic; dark dotted line = mitochondrial) and permeability (light stippled line)

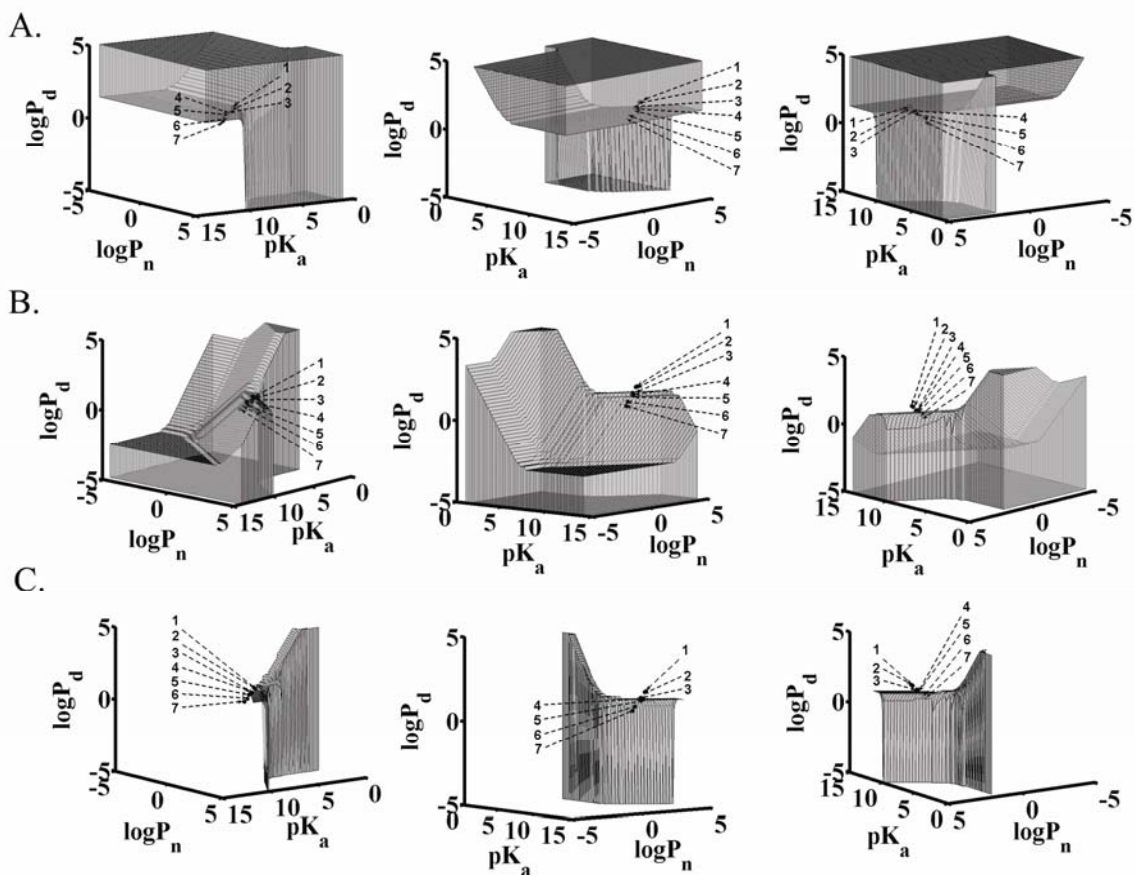


Figure 2.6. The chemical space occupied by molecules with ideal pharmacokinetic properties: A) permeability (defined as molecules with calculated P_{eff} equal or larger than P_{eff} of a molecule with metoprolol-like properties); B) intracellular accumulation (defined as molecules with both calculated C_{cyto} and C_{mito} equal or less than that of the metoprolol-like reference molecule); and, C) permeability and intracellular accumulation (defined as molecules with calculated P_{eff} equal or larger than P_{eff} , and C_{cyto} and C_{mito} equal or less than C_{cyto} and C_{mito} calculated for a molecule with metoprolol-like properties). Each row represents the same spaces with different rotating aspects. $\log P_n$ and $\log P_d$ are not associated (change independently). Numbers 1 through 7 are alprenolol, propranolol, oxprenolol, metoprolol, pindolol, practolol, and atenolol respectively. The $\log P_n$ and $\log P_d$ values of each molecule were liposomal $\log P$ s used in calculation, which were listed in Table 2.1.

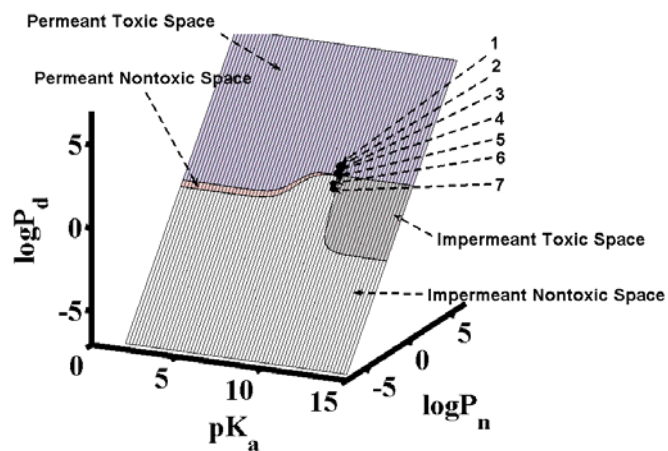


Figure 2.7. The chemical space defined by metoprolol-like reference molecule. $\log P_n$ and $\log P_d$ are associated by a simple linear relationship expressed as equations 2.27-2.29. Numbers 1 through 7 are alprenolol, propranolol, oxprenolol, metoprolol, pindolol, practolol, and atenolol respectively. The $\log P_n$ and $\log P_d$ values of each molecule were liposomal logPs used in calculation, which were listed in Table 2.1.

References

1. P. Artursson and J. Karlsson. Correlation between oral drug absorption in humans and apparent drug permeability coefficients in human intestinal epithelial (Caco-2) cells. *Biochem Biophys Res Commun.* 175:880-885 (1991).
2. V.J. Wacher, L. Salphati, and L.Z. Benet. Active secretion and enterocytic drug metabolism barriers to drug absorption. *Adv Drug Deliv Rev.* 46:89-102 (2001).
3. S. Graham-Lorence and J.A. Peterson. P450s: Structural similarities and functional differences. *Faseb J.* 10:206-214 (1996).
4. X. Cao, L.X. Yu, C. Barbaciru, C.P. Landowski, H.C. Shin, S. Gibbs, H.A. Miller, G.L. Amidon, and D. Sun. Permeability dominates in vivo intestinal absorption of P-gp substrate with high solubility and high permeability. *Mol Pharm.* 2:329-340 (2005).
5. M.V. Varma, K. Sateesh, and R. Panchagnula. Functional role of P-glycoprotein in limiting intestinal absorption of drugs: contribution of passive permeability to P-glycoprotein mediated efflux transport. *Mol Pharm.* 2:12-21 (2005).
6. V.R. Fantin and P. Leder. F16, a mitochondriotoxic compound, triggers apoptosis or necrosis depending on the genetic background of the target carcinoma cell. *Cancer Res.* 64:329-336 (2004).
7. J.S. Modica-Napolitano and J.R. Aprile. Delocalized lipophilic cations selectively target the mitochondria of carcinoma cells. *Adv Drug Deliv Rev.* 49:63-70 (2001).
8. K.B. Wallace. Doxorubicin-induced cardiac mitochondriopathy. *Pharmacol Toxicol.* 93:105-115 (2003).
9. P.L. Freddolino, M.Y.S. Kalani, N. Vaidehi, W.B. Floriano, S.E. Hall, R.J. Trabanino, V.W.T. Kam, and W.A. Goddard. Predicted 3D structure for the human beta 2 adrenergic receptor and its binding site for agonists and antagonists. *Proc Natl Acad Sci U S A.* 101:2736-2741 (2004).
10. T.J. Fitzsimmons, X.L. Zhao, and S.A. Wank. The extracellular domain of receptor activity-modifying protein 1 is sufficient for calcitonin receptor-like receptor function. *J Biol Chem.* 278:14313-14320 (2003).
11. T. Kennedy. Managing the drug discovery/development interface. *Drug Discovery Today.* 2:436-444 (1997).
12. G. Camenisch, J. Alsenz, H. van de Waterbeemd, and G. Folkers. Estimation of permeability by passive diffusion through Caco-2 cell monolayers using the drugs' lipophilicity and molecular weight. *Eur J Pharm Sci.* 6:317-324 (1998).
13. D.G. Lloyd, G. Golfis, A.J. Knox, D. Fayne, M.J. Meegan, and T.I. Oprea. Oncology exploration: charting cancer medicinal chemistry space. *Drug Discov Today.* 11:149-159 (2006).
14. T.I. Oprea, I. Zamora, and A.L. Ungell. Pharmacokinetically based mapping device for chemical space navigation. *J Comb Chem.* 4:258-266 (2002).
15. T.I. Oprea. Chemical space navigation in lead discovery. *Curr Opin Chem Biol.* 6:384-389 (2002).

16. S. Balaz and V. Lukacova. Subcellular pharmacokinetics and its potential for library focusing. *JOURNAL OF MOLECULAR GRAPHICS & MODELLING*. 20:479-490 (2002).
17. S. Balaz, K. Pirsellova, T.W. Schultz, and J. Hermens. Kinetics of subcellular distribution of multiply ionizable compounds: A mathematical description and its use in QSAR. *Journal Of Theoretical Biology*. 178:7-16 (1996).
18. R. Dvorsky, S. Balaz, and R.J. Sawchuk. Kinetics of subcellular distribution of compounds in simple biosystems and its use in QSAR. *J Theor Biol*. 185:213-222 (1997).
19. G.L. Amidon, H. Lennernas, V.P. Shah, and J.R. Crison. A theoretical basis for a biopharmaceutic drug classification: the correlation of in vitro drug product dissolution and in vivo bioavailability. *Pharm Res*. 12:413-420 (1995).
20. P. Stenberg, K. Luthman, and P. Artursson. Prediction of membrane permeability to peptides from calculated dynamic molecular surface properties. *Pharm Res*. 16:205-212 (1999).
21. U. Norinder, T. Osterberg, and P. Artursson. Theoretical calculation and prediction of Caco-2 cell permeability using MolSurf parametrization and PLS statistics. *Pharm Res*. 14:1786-1791 (1997).
22. S. Winiwarter, N.M. Bonham, F. Ax, A. Hallberg, H. Lennernas, and A. Karlen. Correlation of human jejunal permeability (in vivo) of drugs with experimentally and theoretically derived parameters. A multivariate data analysis approach. *J Med Chem*. 41:4939-4949 (1998).
23. S. Trapp and R.W. Horobin. A predictive model for the selective accumulation of chemicals in tumor cells. *Eur Biophys J Biophys Lett*. 34:959-966 (2005).
24. M. Duvvuri, Y.P. Gong, D. Chatterji, and J.P. Krise. Weak base permeability characteristics influence the intracellular sequestration site in the multidrug-resistant human leukemic cell line HL-60. *Journal Of Biological Chemistry*. 279:32367-32372 (2004).
25. S. Davis, M.J. Weiss, J.R. Wong, T.J. Lampidis, and L.B. Chen. Mitochondrial And Plasma-Membrane Potentials Cause Unusual Accumulation And Retention Of Rhodamine-123 By Human-Breast Adenocarcinoma-Derived Mcf-7 Cells. *Journal Of Biological Chemistry*. 260:3844-3850 (1985).
26. K. Shedden, J. Brumer, Y.T. Chang, and G.R. Rosania. Chemoinformatic analysis of a supertargeted combinatorial library of styryl molecules. *Journal Of Chemical Information And Computer Sciences*. 43:2068-2080 (2003).
27. V.Y. Chen, S.M. Khersonsky, K. Shedden, Y.T. Chang, and G.R. Rosania. System dynamics of subcellular transport. *Mol Pharm*. 1:414-425 (2004).
28. S. Trapp. Plant uptake and transport models for neutral and ionic chemicals. *Environ Sci Pollut Res*. 11:33-39 (2004).
29. U.S.A. Interactive PhysProp Database Demo; available from Syracuse Research Corporation (SRC). (<http://www.syrres.com/esc/physdemo.htm>).
30. L. Xing and R.C. Glen. Novel methods for the prediction of logP, pK(a), and logD. *J Chem Inf Comput Sci*. 42:796-805 (2002).
31. D. Vrakas, C. Giaginis, and A. Tsantili-Kakoulidou. Different retention behavior of structurally diverse basic and neutral drugs in immobilized artificial membrane

- and reversed-phase high performance liquid chromatography: comparison with octanol-water partitioning. *J Chromatogr A*. 1116:158-164 (2006).
32. C. Zhou, Y. Jin, J.R. Kenseth, M. Stella, K.R. Wehmeyer, and W.R. Heineman. Rapid pKa estimation using vacuum-assisted multiplexed capillary electrophoresis (VAMCE) with ultraviolet detection. *J Pharm Sci*. 94:576-589 (2005).
 33. Y. Ishihama, M. Nakamura, T. Miwa, T. Kajima, and N. Asakawa. A rapid method for pKa determination of drugs using pressure-assisted capillary electrophoresis with photodiode array detection in drug discovery. *J Pharm Sci*. 91:933-942 (2002).
 34. K. Balon, B.U. Riebesehl, and B.W. Muller. Drug liposome partitioning as a tool for the prediction of human passive intestinal absorption. *Pharmaceutical Research*. 16:882-888 (1999).
 35. F. Wohnsland and B. Faller. High-throughput permeability pH profile and high-throughput alkane/water log P with artificial membranes. *J Med Chem*. 44:923-930 (2001).
 36. D.G. McDevitt. Comparison of pharmacokinetic properties of beta-adrenoceptor blocking drugs. *Eur Heart J*. 8 Suppl M:9-14 (1987).
 37. A. Avdeef, P. Artursson, S. Neuhoff, L. Lazorova, J. Grasjo, and S. Tavelin. Caco-2 permeability of weakly basic drugs predicted with the double-sink PAMPA pKa(flux) method. *Eur J Pharm Sci*. 24:333-349 (2005).
 38. V. Martinez, M.I. Maguregui, R.M. Jimenez, and R.M. Alonso. Determination of the pKa values of beta-blockers by automated potentiometric titrations. *J Pharm Biomed Anal*. 23:459-468 (2000).
 39. N. Castela-Papin, S. Cai, J. Vatier, F. Keller, C.H. Souleau, and R. Farinotti. Drug interactions with diosmectite: a study using the artificial stomach-duodenum model. *Int J Pharm*. 182:111-119 (1999).
 40. K. Palm, K. Luthman, A.L. Ungell, G. Strandlund, and P. Artursson. Correlation of drug absorption with molecular surface properties. *J Pharm Sci*. 85:32-39 (1996).
 41. S. Yee. In vitro permeability across Caco-2 cells (colonic) can predict in vivo (small intestinal) absorption in man--fact or myth. *Pharm Res*. 14:763-766 (1997).
 42. M. Yazdanian, S.L. Glynn, J.L. Wright, and A. Hawi. Correlating partitioning and caco-2 cell permeability of structurally diverse small molecular weight compounds. *Pharm Res*. 15:1490-1494 (1998).
 43. M.C. Gres, B. Julian, M. Bourrie, V. Meunier, C. Roques, M. Berger, X. Boulenc, Y. Berger, and G. Fabre. Correlation between oral drug absorption in humans, and apparent drug permeability in TC-7 cells, a human epithelial intestinal cell line: comparison with the parental Caco-2 cell line. *Pharm Res*. 15:726-733 (1998).
 44. J.D. Irvine, L. Takahashi, K. Lockhart, J. Cheong, J.W. Tolan, H.E. Selick, and J.R. Grove. MDCK (Madin-Darby canine kidney) cells: A tool for membrane permeability screening. *J Pharm Sci*. 88:28-33 (1999).
 45. L. Hovgaard, H. Brondsted, A. Buur, and H. Bundgaard. Drug delivery studies in Caco-2 monolayers. Synthesis, hydrolysis, and transport of O-cyclopropane carboxylic acid ester prodrugs of various beta-blocking agents. *Pharm Res*. 12:387-392 (1995).

46. V. Pade and S. Stavchansky. Estimation of the relative contribution of the transcellular and paracellular pathway to the transport of passively absorbed drugs in the Caco-2 cell culture model. *Pharm Res.* 14:1210-1215 (1997).
47. N.A. Kasim, M. Whitehouse, C. Ramachandran, M. Bermejo, H. Lennernas, A.S. Hussain, H.E. Junginger, S.A. Stavchansky, K.K. Midha, V.P. Shah, and G.L. Amidon. Molecular properties of WHO essential drugs and provisional biopharmaceutical classification. *Mol Pharm.* 1:85-96 (2004).
48. H.H.F. Refsgaard, B.F. Jensen, P.B. Brockhoff, S.B. Padkjaer, M. Guldbrandt, and M.S. Christensen. In silico prediction of membrane permeability from calculated molecular parameters. *Journal Of Medicinal Chemistry.* 48:805-811 (2005).
49. K. Palm, K. Luthman, J. Ros, J. Grasjo, and P. Artursson. Effect of molecular charge on intestinal epithelial drug transport: pH-dependent transport of cationic drugs. *Journal Of Pharmacology And Experimental Therapeutics.* 291:435-443 (1999).
50. G.A. Siebert, D.Y. Hung, P. Chang, and M.S. Roberts. Ion-trapping, microsomal binding, and unbound drug distribution in the hepatic retention of basic drugs. *Journal Of Pharmacology And Experimental Therapeutics.* 308:228-235 (2004).
51. G.L. Amidon and TSRL. Inc The Modern Biopharmaceutics™ Version 6 Computer Based Training Software 2004.
52. T. Terao, E. Hisanaga, Y. Sai, I. Tamai, and A. Tsuji. Active secretion of drugs from the small intestinal epithelium in rats by P-glycoprotein functioning as an absorption barrier. *J Pharm Pharmacol.* 48:1083-1089 (1996).
53. C. Zhu, L. Jiang, T.M. Chen, and K.K. Hwang. A comparative study of artificial membrane permeability assay for high throughput profiling of drug absorption potential. *Eur J Med Chem.* 37:399-407 (2002).
54. M. Fujikawa, R. Ano, K. Nakao, R. Shimizu, and M. Akamatsu. Relationships between structure and high-throughput screening permeability of diverse drugs with artificial membranes: application to prediction of Caco-2 cell permeability. *Bioorg Med Chem.* 13:4721-4732 (2005).
55. E.H. Kerns, L. Di, S. Petusky, M. Farris, R. Ley, and P. Jupp. Combined application of parallel artificial membrane permeability assay and Caco-2 permeability assays in drug discovery. *J Pharm Sci.* 93:1440-1453 (2004).
56. FDA. Guidance for Industry: Waiver of In Vivo Bioavailability and Bioequivalence Studies for Immediate-Release Solid Oral Dosage Forms Based on a Biopharmaceutics Classification System.
57. P. Artursson, K. Palm, and K. Luthman. Caco-2 monolayers in experimental and theoretical predictions of drug transport. *Advanced Drug Delivery Reviews.* 46:27-43 (2001).
58. A. Malkia, L. Murtomaki, A. Urtti, and K. Kontturi. Drug permeation in biomembranes in vitro and in silico prediction and influence of physicochemical properties. *Eur J Pharm Sci.* 23:13-47 (2004).
59. C.A. Lipinski, F. Lombardo, B.W. Dominy, and P.J. Feeney. Experimental and computational approaches to estimate solubility and permeability in drug discovery and development settings. *Adv Drug Deliv Rev.* 46:3-26 (2001).

60. R.F. Flewelling and W.L. Hubbell. The membrane dipole potential in a total membrane potential model. Applications to hydrophobic ion interactions with membranes. *Biophys J.* 49:541-552 (1986).
61. R.F. Flewelling and W.L. Hubbell. Hydrophobic ion interactions with membranes. Thermodynamic analysis of tetraphenylphosphonium binding to vesicles. *Biophys J.* 49:531-540 (1986).
62. J. Schamberger and R.J. Clarke. Hydrophobic ion hydration and the magnitude of the dipole potential. *Biophys J.* 82:3081-3088 (2002).
63. U. Borchard. Pharmacokinetics of beta-adrenoceptor blocking agents: clinical significance of hepatic and/or renal clearance. *Clin Physiol Biochem.* 8 Suppl 2:28-34 (1990).
64. W. Kirch and K.G. Gorg. Clinical pharmacokinetics of atenolol--a review. *Eur J Drug Metab Pharmacokinet.* 7:81-91 (1982).
65. R. Mehvar, M.E. Gross, and R.N. Kreamer. Pharmacokinetics of atenolol enantiomers in humans and rats. *J Pharm Sci.* 79:881-885 (1990).
66. J.G. Riddell, D.W. Harron, and R.G. Shanks. Clinical pharmacokinetics of beta-adrenoceptor antagonists. An update. *Clin Pharmacokinet.* 12:305-320 (1987).
67. S. Neuhoff, A.L. Ungell, I. Zamora, and P. Artursson. pH-dependent bidirectional transport of weakly basic drugs across Caco-2 monolayers: Implications for drug-drug interactions. *Pharmaceutical Research.* 20:1141-1148 (2003).
68. E. Walter, S. Janich, B.J. Roessler, J.M. Hilfinger, and G.L. Amidon. HT29-MTX/Caco-2 cocultures as an in vitro model for the intestinal epithelium: In vitro in vivo correlation with permeability data from rats and humans. *Journal Of Pharmaceutical Sciences.* 85:1070-1076 (1996).
69. W.J. Egan and G. Lauri. Prediction of intestinal permeability. *Advanced Drug Delivery Reviews.* 54:273-289 (2002).
70. A. Kulkarni, Y. Han, and A.J. Hopfinger. Predicting caco-2 cell permeation coefficients of organic molecules using membrane-interaction QSAR analysis. *Journal Of Chemical Information And Computer Sciences.* 42:331-342 (2002).

CHAPTER III

SIMULATION-BASED CHEMINFORMATIC ANALYSIS OF ORGANELLE-TARGETED MOLECULES: LYSOSOMOTROPIC MONOBASIC AMINES

Abstract

Cell-based molecular transport simulations are being developed to facilitate exploratory cheminformatic analysis of virtual libraries of small drug-like molecules. For this purpose, mathematical models of single cells are built from equations capturing the transport of small molecules across membranes. In turn, physicochemical properties of small molecules can be used as input to simulate intracellular drug distribution, through time. Here, with mathematical equations and biological parameters adjusted so as to mimic a leukocyte in the blood, simulations were performed to analyze steady-state, relative accumulation of small molecules in lysosomes, mitochondria, and cytosol of this target cell, in the presence of a homogenous extracellular drug concentration. Similarly, with equations and parameters set to mimic an intestinal epithelial cell, simulations were also performed to analyze steady state, relative distribution and transcellular permeability in this non-target cell, in the presence of an apical-to-basolateral concentration gradient. With a test set of ninety-nine lysosomotropic small molecules gathered from the scientific literature, simulation results helped analyze relationships between the chemical diversity of these molecules and their intracellular distributions.

Keywords: Cheminformatics; Lysosomotropic; Cellular pharmacokinetics; Drug transport; Small molecule permeability; Subcellular localization; Simulation; Rational drug design

Introduction

Weakly basic molecules possessing one or more amine groups accumulate in lysosomes and other membrane-bound acidic organelles because of the well-known ion trapping mechanism (1-3). Amines generally have a pK_a value in the physiological pH range. Accordingly, they exist as a combination of ionized (protonated) and neutral (unprotonated) species. Because the pH of lysosomes is one or more units lower than the pH of the cytosol, the relative concentration of neutral and ionized species inside the lysosomes shifts towards the protonated, ionized state. Conversely, because the pH of the cytosol is higher, the relative concentration of neutral and ionized species in the cytosol shifts towards the neutral, unprotonated state. Since charged molecules are less membrane-permeant, the protonated species become trapped inside the membrane-bounded compartments, relative to the neutral species. Within an acidic lysosome, the concentration of the neutral, membrane-permeant species is lower than its concentration in the more basic cytosol. This leads to a concentration gradient of the neutral form of the molecule across the lysosomal membrane, further driving the uptake of the neutral species of the molecule into the acidic organelle.

In medicinal chemistry, the ability to modify the chemical structure of small molecules so as to tailor lysosomotropic behavior may be important for decreasing unwanted side effects, as much as it may be important for increasing efficacy. For many monobasic amines that target extracellular domains of cell surface receptors and ion channels, lysosomal accumulation can be considered as a secondary effect of the physicochemical properties of the molecule (4-8). Previously, many monobasic amines have been experimentally analyzed in cell-based assays, in terms of their ability to

accumulate in lysosomes (6, 9-12). In response to ion trapping, cells exposed to monobasic amines swell and become replete with large vacuoles (6, 9, 10, 13-15). With a phase contrast microscope, swollen lysosomes can be easily discerned and scored. Furthermore, as monobasic amines accumulate in lysosomes, they can increase the pH of the organelle through a buffering effect, or by shuttling protons out of the lysosome, across the lysosomal membranes (16). Therefore, such molecules “compete” with each other for lysosomal accumulation, providing another way to assay for lysosomotropic behavior (16, 17). A third way to assay lysosomotropic behavior is by labeling lysosomes with fluorescent probes (e.g. LysoTracker® dyes) (17). As lysosomes expand in response to accumulation of lysosomotropic agents, they accumulate increasing amounts of the LysoTracker® dye and the cells become brightly labeled. By virtue of these effects on live cells, many monobasic amines have been positively identified as “lysosomotropic”.

Nevertheless, different studies analyzing lysosomotropic monobasic amines have also identified molecules that deviate from expectations. Furthermore, there is a broad range of concentrations at which vacuolation becomes apparent, spanning several orders of magnitude (10, 18-20). In addition, there are monobasic amines that do not exhibit any vacuolation-inducing behavior (6, 9, 10, 13, 14, 21), and do not compete with the lysosomal uptake of other lysosomotropic probes (6, 16), or that are cytotoxic (21). Most importantly, some lysosomotropic molecules have been reported to accumulate in other organelles, such as mitochondria (22). Alprenolol, chlorpromazine, fluoxetine, propranolol and diltiazem are some of the FDA approved drugs in this category (6, 16, 22, 23) that have been classified as being both lysosomotropic and mitochondriotropic by

different investigators. In addition, certain monobasic amines may accumulate in lysosomes to a much greater extent than ion trapping mechanisms would predict (20).

These apparent discrepancies in terms of the lysosomotropic behavior prompted us to begin exploring the relationship between the phenotypic effects of monobasic amines, and their subcellular distribution in lysosomes vs. other organelles. We decided to use a cell-based molecular transport simulator (24, 25) to begin exploring the different possible behaviors of monobasic amines inside cells based on the ion trapping mechanism, paying special attention to their accumulation in lysosomes, cytosol and mitochondria. The simulations help assess the entire range of expected variation in intracellular transport behaviors, based solely on the biophysical principles underlying the ion trapping mechanism. In turn, the expected range of transport behaviors can be related to experimental observations of a lysosomotropic test set of molecules obtained from published research articles. Because the ability to optimize the subcellular transport of small molecules could have practical applications in drug development, we also deem it important to analyze the distribution of molecules inside non-target cells mediating drug transport in the presence of a transcellular concentration gradient. In fact, although direct experimental measurement of subcellular concentration in the presence of a transcellular concentration gradient would be difficult, this may be the most relevant condition for drug uptake and transport throughout the different tissues of the body.

Methods

Modeling cell pharmacokinetics of target cells in suspension: the T-model

For subcellular compartments delimited by membranes, passive transport of small molecules in and out of these compartments is determined by the interaction of the molecules with the membrane, the concentration gradient of molecules across the membrane, the local microenvironment on either side of the membrane, and the transmembrane electrical potential (24, 25). Drug-membrane interactions are largely dependent on the physicochemical properties of small molecules (such as pK_a and lipophilicity) and the environmental condition (such as local pH values and membrane potentials). Based on the biophysics of membrane transport, mass transfer of drug molecules between different organelles in a cell surrounded by a homogeneous extracellular drug concentration has been modeled mathematically by Trapp and Horobin (25) (Figure 3.1a). Accordingly, three coupled ordinary differential equations (3.1, 3.2, and 3.3) describe the concentration change with time in each subcellular / cellular compartment.

$$\frac{dC_c}{dt} = \frac{A_c}{V_c} \times J_{o,c} - \frac{A_m}{V_c} \times J_{c,m} - \frac{A_l}{V_c} \times J_{c,l}, \quad (3.1)$$

$$\frac{dC_m}{dt} = \frac{A_m}{V_m} \times J_{c,m}, \quad (3.2)$$

$$\frac{dC_l}{dt} = \frac{A_l}{V_l} \times J_{c,l}, \quad (3.3)$$

where C indicates the *concentration*, J indicates the *flux*, A and V indicate the *membrane surface area* and *volume* respectively. The subscripts o,c,l , and m indicate *extracellular compartment*, *cytosol*, *lysosomes*, and *mitochondria* respectively. The directions of fluxes are indicated by the orders of the subscripts, e.g. $J_{c,m}$ represents the flux from cytosol to mitochondria. Calculations for fluxes between each pair of compartments were the same as

described before (25). The ordinary differential equations were numerically solved (supplemental materials) (24).

An important feature of this model is that at steady state, the drug accumulation in the cytosol is only dependent on the drug concentration outside the cell, the plasma membrane permeability properties, and the ionic conditions of the cytosol and the extracellular medium. Similarly, the drug accumulation inside any given organelle is only dependent on the drug concentration in the cytosol, the permeability properties of the membrane delimiting the organelle, the ionic conditions of the cytosol and the inner lumen of the organelle. Consequently, one can use the same equations to analyze steady state distribution drugs in lysosomes or mitochondria (and other organelles) simply by adjusting the pH of the organelle, the transmembrane electrical potential, and the organelle volume, surface area, and lipid fraction. For mitochondria, the inner lumen pH was set at 8 (25) and the membrane potential was set at -150 mV (26). Mitochondria were modeled as spheres with 1 μm radius. For lysosomes, the inner lumen pH was set at 5 (1, 27-29) and the membrane potential was set at +10 mV (30). Leukocytes were modeled as spherical objects of 10 μm in diameter. Plasma membrane potential was set at -60 mV (31). Extracellular pH was set at 7.4 (blood). Cytosolic pH was set at 7.0 (32). Since we are more interested in the drug aqueous concentration in cytosol, the lipid fraction was set at 0 in calculation. Other model parameters were adapted from literature (25). Hereafter, this cellular pharmacokinetic model applicable to free floating cells in suspension (e.g. leukocytes in circulation) will be dubbed Trapp's Model or 'T-Model'.

Modeling cellular pharmacokinetics of non-target, polarized epithelial cells: the R-model

For modeling drug transport across polarized epithelial cells (24), the cell surface area is divided into apical and basolateral membrane domains (Figure 3.1b). Similarly, the extracellular space is divided into apical and basolateral extracellular compartments. Accordingly, drug uptake into the cell is represented by mass transfer of drug molecules from the apical extracellular medium into the cytosol, across the apical membrane. Drug efflux from the cells is represented by mass transfer from the cytosol to the basolateral medium, across the basolateral membrane. Because the apical membrane is normally covered with microvilli, the apical membrane surface area (A_a) can be adjusted independently from the basolateral membrane (A_b). Similarly, the extracellular pH of the apical (pH_a) and basolateral compartments (pH_b), and transmembrane electrical potentials across apical and basolateral membranes (E_a and E_b) can be independently adjusted, so as to mimic the local microenvironment of the epithelial cells.

A cellular pharmacokinetic model for simulating intracellular concentration and passive transcellular permeability in the presence of a transcellular concentration gradient was developed previously by our group (24, 33). Mass transport across the boundary of each compartment can be described by equations 3.4 to 3.7.

$$\frac{dC_c}{dt} = \frac{A_a}{V_c} J_{a,c} - \frac{A_m}{V_c} J_{c,m} - \frac{A_b}{V_c} J_{c,b}, \quad (3.4)$$

$$\frac{dC_m}{dt} = \frac{A_m}{V_m} J_{c,m}, \quad (3.5)$$

$$\frac{dC_l}{dt} = \frac{A_l}{V_l} J_{c,l}, \quad (3.6)$$

$$\frac{dC_b}{dt} = \frac{A_b}{V_b} J_{c,b}, \quad (3.7)$$

The subscripts a and b indicate ‘apical’ and ‘basolateral’ respectively. Other symbols and subscripts mean the same as those in the T-model. As in the T-model, the inner lumen pH of mitochondria was set at 8 (25) and the mitochondrial membrane potential was set at -150 mV (26). For lysosomes, the inner lumen pH was set at 5 (1, 27-29) and the membrane potential was set at +10 mV (30). Epithelial cells were modeled as cubical objects of 10 μm in length. Again since we are more interested in the drug aqueous concentration in cytosol the lipid fraction was set to 0. All other model parameters used in calculation were obtained from the literature (24), and can be found in the supplemental materials. To maintain sink condition in the basolateral compartment, we set the volume of the basolateral compartment (V_b) equal to the human blood volume (4.7 L).

From simulating cytosol to basolateral flux of molecules in an intestinal epithelial cell, the transcellular permeability of the intestinal epithelial cell monolayer corresponds to the following equation (24):

$$P_{eff} = \frac{dm_b}{C_a \cdot A_{aa} \cdot dt}, \quad (3.8)$$

where P_{eff} is the effective permeability, C_a is the initial concentration in the apical compartment and is considered to be constant, dm_b/dt is the change in drug mass in the basolateral compartment per unit time, and A_{aa} is the apparent cross sectional area of the cell, which would approximately correspond to the total area of the surface over which drug transport is occurring divided by the number of cells that are effectively transporting drug. Henceforth, this cellular pharmacokinetic model that applies in non-target epithelial cells will be dubbed Rosania’s Model or ‘R-Model’.

Analyzing organelle-targeting and transcellular permeability with R- and T-models

To analyze the intracellular distribution of monovalent weakly basic molecules possessing amine functionality, all different combinations of a) octanol : water partition coefficients of the neutral form of the molecule ($\log P_n$); b) octanol : water partition coefficients of the ionized form of the molecule ($\log P_d$); and c) pK_a were used as input. $\log P_n$ and $\log P_d$ spanned a range from -5 to +5, while $\log P_d$ was constrained to a value less than or equal to $\log P_n$. pK_a spanned a range from 0 to 14. pK_a , $\log P_n$, and $\log P_d$ were varied in 0.2 unit increments (24). The molecular charge (z) was set equal to 1, which means the simulated whole physicochemical space is specific for monovalent amine-containing molecules. With R- and T-Model, simulations were performed until the system reached steady state (normally, at 10^6 seconds after beginning of the simulation). For R-Model simulations, initial apical drug concentration was set at 1 mM, and basolateral drug concentration was set at 0 mM. For T-model simulations, extracellular drug concentration was set at 1 mM, and kept constant. Accordingly, for each combination of pK_a , $\log P_n$, and $\log P_d$ used as input, there are seven output values: C_{cytoR} , C_{mitoR} , C_{lysoR} (the steady-state cytosolic, mitochondrial and lysosomal concentration estimated with the R-model); P_{eff} (the steady-state effective permeability estimated with the R-Model); and C_{cytoT} , C_{mitoT} , and C_{lysoT} (the steady-state cytosolic, mitochondrial and lysosomal concentrations estimated with the T-Model).

A test set of monobasic amines with associated lysosomotropic behaviors

Focusing on lysosomal targeting, ninety-nine monobasic amines (Table 3.1) were found by searching PubMed abstracts and titles for articles containing the word “lysosome”, “lysosomal”, or “lysosomotropic”; from other articles referenced by these articles; and from current review articles describing the lysosomal accumulation of

weakly basic molecules (1). There are more lysosomotropic amine-containing molecules besides molecules included in our table (for example, zwitterions or dibasic amines). However since R- and T-Models have been validated mostly with molecules possessing one ionizable functional group, lysosomotropic amines with more than one ionizable functionality were not included. To estimate the pK_a (at 37 °C), $\log P_n$ and $\log P_d$ for each molecule, we used ChemAxon (<http://www.chemaxon.com>). A liposomal approximation (24, 34) was applied for $\log P_n$ and $\log P_d$ based on the values obtained from ChemAxon. Intracellular distributions were analyzed for those ninety-nine molecules at steady state with the T-model and R-model. Transcellular permeability was analyzed for the ninety-nine molecules at steady state with the R-model.

Interactive visualization of simulation results

Visualization of simulation results was performed with the Miner3D[®] software package (Dimension 5, Ltd., Slovakia, EU). Simulation results were graphed as 3D scatter plots to shape the chemical spaces with $\log P_n$, $\log P_d$ and pK_a plotted on the three coordinate axes, and the analyzed steady state concentration or permeability determining the color and intensity of the points. For linking simulation results with the test set of lysosomotropic molecules, we used the pK_a , $\log P_n$ and $\log P_d$ values obtained after liposomal approximations (24).

To plot different chemical spaces we set a threshold concentration value to define accumulation in a specific subcellular compartment. For intracellular concentration, the threshold lysosomal accumulation for lysosomotropic molecules was $C_{lyso}T \geq 2 \text{ mM}$ (i.e. two-fold greater than extracellular concentration). The thresholds for selective lysosomal accumulation were $C_{lyso}T \geq 2 \text{ mM}$; $C_{lyso}T / C_{mito}T \geq 2$; and $C_{lyso}T / C_{cyto}T \geq 2$. The

threshold for mitochondrial accumulation was $C_{\text{mito}}T \geq 2$ mM. The thresholds for selective mitochondrial accumulation were $C_{\text{mito}}T \geq 2$ mM; $C_{\text{mito}}T / C_{\text{lyso}}T \geq 2$; and $C_{\text{mito}}T / C_{\text{cyto}}T \geq 2$. The threshold for cytosolic accumulation was $C_{\text{cyto}}T \geq 2$ mM. The thresholds for selective cytosolic accumulation were $C_{\text{cyto}}T \geq 2$ mM; $C_{\text{cyto}}T / C_{\text{mito}}T \geq 2$; and $C_{\text{cyto}}T / C_{\text{mito}}T \geq 2$. The reason for using the two-fold concentration value as a threshold is because it gave the highest percentage of correct classification and lowest incorrect classification rate for the test set of lysosomotropic molecules (as detailed in the Results section).

As recommended by the FDA, the permeability value of metoprolol was used as a threshold to distinguish high vs. low permeability molecules (24). Previously we calculated permeability for metoprolol, using the pK_a and $\log P_n$ obtained from experimental measurements, to be equal to 35×10^{-6} cm/sec (24). In the present study, we used this value as a threshold to distinguish high vs. low permeability molecules. In addition, we arbitrarily set a value of 1×10^{-6} cm/sec as a cut-off number to distinguish low from negligible permeability molecules. Accordingly, three permeability classes were defined as: negligible ($P_{\text{eff}} < 1 \times 10^{-6}$ cm/sec); low ($1 \leq P_{\text{eff}} < 35 \times 10^{-6}$ cm/sec); and high ($P_{\text{eff}} \geq 35 \times 10^{-6}$ cm/sec).

Results

Defining a lysosomal accumulation threshold for lysosomotropic molecules

We began by exploring the simulated property space occupied by monobasic amines, in relation to the test set of molecules obtained from published research articles (Table 3.1). Three different lysosomal concentration thresholds (2, 4 and 8 mM) were

tested in terms of their ability to discriminate lysosomotropic vs. non-lysosomotropic compounds (Figure 3.2). For compounds with ≥ 2 mM accumulation in lysosomes (Figure 3.2a-d), eight (8) of the test compounds were below the accumulation threshold (Figure 3.2a, b), while ninety-one (91) were above the threshold (Figure 3.2c, d). For compounds with ≥ 4 mM accumulation in lysosomes (Figure 3.2e-h), twelve (12) of the test compounds were below the accumulation threshold (Figure 3.2e, f), while eighty-seven (87) were above the threshold (Figure 3.2g, h). For compounds with a ≥ 8 mM accumulation in lysosomes (Figure 3.2i-l), fifty-six (56) lie below the accumulation threshold (Figure 3.2i, j) while forty-three (43) are above (Figure 3.2k, l).

We established that a lysosomal accumulation threshold of 2 mM is best suited to distinguish lysosomotropic from non-lysosomotropic molecules, since it gave the highest correct classification in terms of matching simulation results with the experimentally-observed, lysosomotropic behaviors. Accordingly, for a lysosomal accumulation threshold of 2mM, of the 8 molecules that were below the accumulation threshold, 5 (62.5%) have been positively identified as non-lysosomotropic. Conversely, of the 91 above the threshold, 8 (8.8%) non-lysosomotropic molecules have been incorrectly classified as lysosomotropic. For a lysosomal accumulation threshold of 4 mM, of the 12 below the threshold, 5 (41.7%) have been identified as non-lysosomotropic. Conversely, of the 87 above threshold, 8 (9.2%) non-lysosomotropic molecules have been incorrectly classified as lysosomotropic. For a lysosomal accumulation threshold of 8 mM, of the 56 below the threshold, 9 have been positively identified as non-lysosomotropic (16.1%). Conversely, of the 43 above the threshold, 4 (9.3%) non-lysosomotropic molecules have been incorrectly classified as lysosomotropic.

The test set appears highly clustered in relation to the available lysosomotropic, physicochemical property space

Exploring the relationship between the physicochemical properties of the test set of molecules obtained from the literature with that of the theoretical physicochemical property space occupied by molecules that accumulate in lysosomes at the different threshold values, we observed that most of the test molecules tend to be clustered in very specific region of “lysosomotropic space”. In fact, physicochemical property space occupied by molecules that accumulate in lysosomes at ≥ 2 mM (Figure 3.2b) appears largely similar to the space of molecules that accumulate at ≥ 4 mM (Figure 3.2f) and at ≥ 8 mM (Figure 3.2j). It was surprising that most lysosomotropic molecules in the reference set were calculated to have a lysosomal accumulation between 2- and 8-fold over the extracellular medium, although the largest portion of the calculated physicochemical property space that can be occupied by monobasic amines corresponds to > 8 -fold lysosomal accumulation.

Using simulation results to define the expected transport classes for monovalent weak bases

Using a 2-fold or greater concentration of drug over the extracellular medium to distinguish high vs. low lysosomal, mitochondrial and cytosolic concentration, and by incorporating high vs. low permeability classification obtained with the R-model, a total of 16 classes of molecules can be defined *a priori* (Table 3.1). By mapping the test set of molecules to these 16 different classes, we find that some classes of molecules are well-represented by a number of molecules, while other classes of molecules are not represented at all (Table 3.1). However, according the simulation results, several of these *a priori* classifications are deemed to be “non-existent” by virtue of our being unable to

find a combination of physicochemical properties consistent with the corresponding class of molecules in simulations.

Simulation results point to general trends in lysosomotropic behaviors

For the test set of molecules, we observed that the simulated intracellular accumulation in non-target cells (R-Model) is much lower than the corresponding accumulation in target cells (T-model) (Table 3.1). The simulations yielded lysosomal accumulation occurring for a broad range of transcellular permeability values (Table 3.1). Unexpectedly, for most lysosomotropic molecules, the simulations indicate that mitochondrial accumulation may be much greater than lysosomal or cytosolic accumulation, suggesting that lysosomotropic behavior may not be exclusively related to selective accumulation in lysosomes. Lastly, we observed that none of the lysosomotropic molecules in the test set are able to accumulate in cytosol to a greater extent than they accumulate in mitochondria or in lysosomes (Table 3.1). In fact, plotting the physicochemical property space of such molecules yielded an empty space (data not shown), indicating that the lack of such type of molecules in the reference set is not because the test set is a biased sample, but rather it is expected based on the calculated cellular pharmacokinetic properties of monovalent weak bases.

Calculating the physicochemical space occupied by selectively lysosomotropic molecules

Selectively lysosomotropic molecules were defined as those that accumulate in lysosomes to a 2-fold (or greater) level over the extracellular medium, cytosol, and mitochondria. Out of the 91 reference lysosomotropic molecules (Figure 3.3a, out of

circle), only seventeen (17) (Figure 3.3c, d green circle) appear to be selective in terms of lysosomal accumulation. These 17 molecules (Figure 3.3c) appear clustered at the middle pK_a value of the test set of molecules comparing with non-lysosomotropic molecules (Figure 3.3a, in blue circle) and non-selectively lysosomotropic molecules. Plotting the theoretical physicochemical property space occupied by selectively lysosomotropic molecules related to the reference molecules reveals that the test set of molecules that accumulate in lysosomes are highly clustered (Figure 3.3b) in the middle pK_a and high $\log P_d$ values. This can also be observed in the corresponding plot of non-selectively lysosomotropic and non-lysosomotropic physicochemical property space (Figure 3.3d).

Analyzing the effect of transcellular permeability on selective lysosomal accumulation

Next, we analyzed the relationship between selective lysosomal accumulation in target cells, and transcellular permeability in non-target cells, to determine if the ability to develop selective lysosomotropic agents may be constrained by desirably high transcellular permeability characteristics important for intestinal drug absorption and systemic tissue penetration (Figure 3.4). As a reference, the permeability of metoprolol ($P_{\text{eff}} = 35 \times 10^{-6}$ cm/sec) was used to distinguish high permeability from low permeability drugs. Accordingly, three permeability categories were defined: Negligible Permeability ($P_{\text{eff}} < 1 \times 10^{-6}$ cm/sec; Figure 3.4a, b); Low Permeability ($1 \leq P_{\text{eff}} < 35 \times 10^{-6}$ cm/sec; Figure 3.4c, d); and High Permeability ($P_{\text{eff}} \geq 35 \times 10^{-6}$ cm/sec, Figure 3.4e, f).

With increasing permeability, the simulation results indicate that physicochemical space occupied by selective lysosomotropic molecules shifts towards lower pK_a values and higher $\log P_d$ values. The position of selective lysosomotropic chemical space in

relation to the reference set of non-selective lysosomotropic or non-lysosomotropic molecules can be seen, for molecules with $P_{\text{eff}} < 1 \times 10^{-6}$ cm/sec (Figure 3.4a); $1 \leq P_{\text{eff}} < 35 \times 10^{-6}$ cm/sec (Figure 3.4c); and $P_{\text{eff}} \geq 35 \times 10^{-6}$ cm/sec (Figure 3.4e). Accordingly, there is only one (1) selectively-lysosomotropic reference molecule with $P_{\text{eff}} < 1 \times 10^{-6}$ cm/sec (Figure 3.4b; green arrow); five (5) with $1 \leq P_{\text{eff}} < 35 \times 10^{-6}$ cm/sec (Figure 3.4d; green arrow); and eleven (11) with $P_{\text{eff}} \geq 35 \times 10^{-6}$ cm/sec (Figure 3.4f; green arrow). Thus, high permeability and selective lysosomal accumulation are not mutually exclusive. Nevertheless, we observed that the selective lysosomotropic reference molecules with negligibly low and high permeability are tightly clustered in a small region of chemical space, at mid pK_a and high $\log P_d$ values.

Demarcating the physicochemical property space of extracellular targeted molecules

Extracellular-targeted molecules can be defined as those whose intracellular accumulation at steady state is less than the extracellular concentration (24). For drug development, such a class of molecules is important as many drug targets are extracellular. Accordingly, we analyzed simulation results to determine if there were molecules with low intracellular accumulation and high permeability, which would be desirable for the pharmaceutical design of orally absorbed drugs (Figure 3.5). By maximizing permeability and minimizing intracellular accumulation, (using $P_{\text{eff}} \geq 35 \times 10^{-6}$ cm/sec, $C_{\text{cyto}} < 1\text{mM}$, $C_{\text{mito}} < 1\text{mM}$, and $C_{\text{lyso}} < 1\text{mM}$ as thresholds in both the R and T models), we found five (5) molecules falling into this class (Figure 3.5a, b, c; green circle): pyrimidine, benzocaine, β -naphthylamine, 8-aminoquinoline, and the anti-epileptic drug candidate AF-CX1325XX. These are monobasic amines with $pK_a < 4.5$. Molecules with $pK_a > 4.5$ (the physicochemical property space shown in Figure 3.5c)

exhibit intracellular accumulation in lysosomes, cytosol or mitochondria to levels above those found in the extracellular medium. Figure 3.5b shows the physicochemical space of molecules with high permeability and low intracellular accumulation. Figure 3.5c shows the physicochemical space of molecules with high intracellular accumulation regardless of permeability. Again we can see that molecules with low intracellular accumulation have a $pK_a < 4.5$ and with high intracellular accumulation have a $pK_a > 4.5$.

Many reported lysosomotropic molecules appear to accumulate in mitochondria

For the majority of the reportedly lysosomotropic monobasic amines in the test set, the model suggests that they accumulate in mitochondria more than they accumulate in lysosomes. In total, 56 of the 91 lysosomotropic molecules in the test set accumulate in mitochondria at 2-fold or greater levels than they accumulate in lysosomes, cytosol, or the extracellular medium (Figure 3.6a; Table 3.1, selectively mitochondrotropic compounds underlined). These molecules have a pK_a of 8.2 or greater, a $\log P_n$ of 1.5 or greater, and span a wide range of transcellular permeability values – from impermeant to very highly permeant. In addition, eighteen (18) lysosomotropic molecules also exhibit mitochondrial and high cytosolic accumulation, at concentrations comparable to the concentrations at which they accumulate in lysosomes (Figure 3.6b; Table 3.1). Again, these molecules span a broad range of transcellular permeability values, from impermeant to highly permeant. Plotting the theoretical physicochemical property space occupied by lysosomotropic molecules with predicted, selective mitochondrial accumulation reveals that the molecules in the test set are clustered in this realm of physicochemical property space (Figure 3.6c). Similarly, plotting the physicochemical property space occupied by

lysosomotropic molecules that are predicted to accumulate in cytosol and mitochondria reveals that the molecules are clustered in this realm of chemical space.

Calculated effect of pH in apical compartment on permeability and biodistribution

Based on the simulations, the accumulation of monobasic amines in lysosomes is largely dependent on the difference in pH of between lysosome and extracellular medium (data not shown). While the pH of the medium bathing the target cells is expected to be rather constant, the pH surrounding an intestinal epithelial cell is expected to vary along the intestinal tract (35). To test if this variation would lead to major differences in the observed trends, we decided to test the extent to which the calculated chemical space occupied by selectively lysosomotropic molecules was affected by variation in the apical pH of non-target cells (Figure 3.7). We note that for selectively lysosomotropic molecules with negligible (Figure 3.7a), low (Figure 3.7b), and high (Figure 3.7c) permeability, the theoretical physicochemical property space occupied by selectively lysosomotropic molecules is similar, and the test molecules that fall into that region of chemical space tend to be the same. Similarly, other regions of physicochemical property space occupied with molecules of different permeability tend to be similar, with variations in the apical pH of the intestinal epithelial cell in a pH range of 4.5 to 6.8 (data not shown).

Discussion

Modeling the cellular pharmacokinetics of monobasic amines

Over the past few years, mathematical models of cellular pharmacokinetics have been developed, based on coupled sets of differential equations capturing the

transmembrane diffusion of small molecules. Previously, these models have been used to simulate the intracellular distribution of lipophilic cations in tumor cells (25), and the distribution and passage of small molecules across intestinal epithelial cells (24). For a monovalent weakly acidic or weakly basic small molecule drug, three input physical-chemical properties are used to simulate cellular drug transport and distribution: the logarithms of the lipid/water partition coefficient of the neutral form of the molecule ($\log P_n$) and ionized form ($\log P_d$), and the negative logarithm of the dissociation constant of the ionizable group (pK_a). For monovalent weak bases, the transcellular permeability values calculated with this approach were comparable with measured human intestinal permeability and Caco-2 permeability, yielding good predictions (24). Similarly, the corresponding mathematical models were able to predict mitochondrial accumulation of lipophilic cationic substances in tumor cells (22, 25).

For analyzing the lysosomotropic behavior of monovalent weak bases possessing amine functionality, we adapted these two mathematical models to simulate the cellular pharmacokinetic behavior of target cells exposed to a homogeneous extracellular drug concentration, and non-target cells mediating drug absorption in the presence of an apical-to-basolateral concentration gradient. The results we obtained establish a baseline, expected concentration of small drug-like molecules in mitochondria, lysosomes and cytosol of target cells, as well as permeability in non-target cells. With a test set of small molecules obtained from published research articles, the simulations permit exploring the relationship between physicochemical properties of the molecules, their simulated intracellular distributions and transport behavior, and experimentally reported cellular phenotypes.

Simulation-based analysis and classification of lysosomotropic behavior

By analyzing the intracellular distribution and transcellular transport characteristics of a test set of molecules, together with more general physicochemical space plots covering all possible combinations of pK_a , $\log P_n$ and $\log P_d$, sixteen *a priori* classes of lysosomotropic behavior for monobasic amines were defined (Table 3.1). However, we noted that several of these classes are deemed to be non-existent by the simulations – meaning that there is no combination of pK_a , $\log P_n$ and $\log P_d$ that will yield a molecule in such a class. For other classes, it was not possible to find a molecule in the reference set of lysosomotropic molecules whose calculated properties would lie within the physicochemical property space defining the hypothetical class of molecules. This is certainly the case for positively-identified, non-lysosomotropic molecules. These results argue for expanding the test set of monovalent, weakly basic molecules, so as to represent all possible classes of intracellular transport behaviors.

An equally important observation from the simulation resides in the tight clustering of the reference molecules in constrained regions of physicochemical property space, in relation to the simulated physicochemical property space that is actually available for molecules in the different lysosomotropic and permeability categories. Thus, the diversity of lysosomotropic behaviors represented by the test set of molecules is significantly limited. Indeed, the simulations indicate that expanding the reference set of molecules to unexplored regions of physicochemical property space could be used to find molecules that better represent different types of expected cellular pharmacokinetic behaviors. For example, in the case of low or high permeability molecules that are selectively lysosomotropic, most of the molecules in the reference set are clustered at the high levels of pK_a and high $\log P$, whereas the simulations indicate that it should be

possible to find molecules with lower pK_a and lower $\log P$. The reason for the limited chemical diversity of reported lysosomotropic molecules is certainly related to the choice of molecules that have been tested experimentally and reported in the literature: the emphasis has not been on the probing the chemical diversity of lysosomotropic character, but rather, in analyzing the lysosomotropic character in a related series of compounds (for example, studies looking at mono, bi, and tri-substituted amines, functionalized with various aliphatic groups (9)). In other cases, the emphasis has been on studying the lysosomotropic character of a specific type of compound developed against a specific drug target (6) (for example, beta-adrenergic receptor antagonists such as propranolol, atenolol, practolol, etc), rather than on the full chemical space occupied by lysosomotropic, monovalent weakly basic amines.

Further experimental validation and testing of expected transport behaviors

Using lysosomal swelling, cell vacuolation and intralysosomal pH measurements as phenotypic read outs, it may be possible to test both R- and T-model prediction about the varying extent of lysosomal accumulation of monovalent weak bases as a function of the molecule's chemical structure or physicochemical properties. For example, the models make quantitative predictions about the lysosomal concentration of molecules of varying chemical structure. Previous studies looking at the lysosomotropic behavior of various molecules have reported differences in vacuolation induction for different probes, at extracellular drug concentrations ranging from high millimolar to micromolar range (10, 13, 16). Also, for some molecules vacuolation occurs after less than an hour incubation, while for other probes vacuolation occurs after twenty-four hour incubation, or longer (6, 9, 10, 13, 14, 16). Combinatorial libraries of fluorescent molecules are

available today (36, 37), offering yet another way to test predictions about the intracellular accumulation and distribution of probes. Furthermore, with organelle-selective markers and kinetic microscopic imaging instruments, the rate and extent of swelling of lysosomes and other organelles could be monitored dynamically after exposure of cells to monovalent weakly basic molecules (37). For such studies, cheminformatic analysis tools are being developed to relate the intracellular distribution of small molecules as apparent in image data, with chemical structure and physicochemical features of the molecules, and the predicted subcellular distribution (38, 39). Lastly, more quantitative assessments of model predictions can be made by directly monitoring the total intracellular drug mass (40, 41), as well as drug mass associated with the lysosomal compartment (20, 42, 43). Recently, methods are being developed to rapidly isolate the lysosomes and measure intralysosomal drug concentrations (43).

To test model predictions about the lysosomotropic behavior of small molecules in the presence of an apical-to-basolateral concentration gradient, various *in vitro* cell culture models have been developed to assess drug intestinal permeability and oral absorption (44). These are Caco-2, MDCK, LLC-PK1, 2/4/A1, TC-7, HT-29, and IEC-18 cell models (44). Among those models Caco-2 (human colon adenocarcinoma) cell monolayer is the most well-established cell model and has been widely accepted by pharmaceutical companies and academic research groups interested in studying drug permeability characteristics (44). In addition to Caco-2 cells, MDCK (Madin-Darby canine kidney) is a dog renal epithelia cell line and is another widely used cell line in studying cell permeability characteristics (45).

Towards a computer-aided design of organelle-targeted molecules: implications for drug discovery and development

The ability to rationally tailor the transcellular permeability and subcellular distribution of monobasic amines can have important applications in medicinal chemistry efforts aimed at enhancing the efficacy of small molecules against specific targets, decreasing non-specific unwanted interactions with non-intended targets that lead to side effects and toxicity, as well as enhancing transcellular permeability for maximizing tissue penetration and oral bioavailability. For many FDA approved drugs, lysosomal accumulation of the molecules would appear to be a non-specific effect of the molecule's chemical structure. For example, in the case of the beta-adrenergic receptor antagonists like propranolol, the drug's target is a cell surface receptor located at the plasma membrane. Thus, lysosomal (and any other intracellular) accumulation observed for this molecule is most likely an unintended consequence of its chemical structure (2, 6, 15, 16, 43, 46). In general, due to the abundance of lysosomotropic drugs (6, 9, 10, 16), lysosomal accumulation seems to be tolerated, although it may not be a desirable property.

Nevertheless, there are certain classes of therapeutic agents where lysosomal accumulation may be highly desirable. For example, Toll-like receptor molecules are transmembrane proteins in the lysosomes of leukocytes (dendritic cells and macrophages). These receptors can be activated by endocytosed proteins, DNA and carbohydrates, and they generate inflammatory responses as part of the innate immune system (47, 48). Small molecule agents that either block or activate Toll-like receptors are being sought to inhibit inflammatory reactions (associated with autoimmune diseases) or promote resistance against viral infections, respectively (49, 50). A different class of

molecules where lysosomal accumulation would be highly desirable involves agents that affect lysosomal enzymes involved in tissue remodeling (51). Tissue remodeling is the basis of diseases like osteoporosis, which involves the loss of bone mass due to an imbalance in the rate of bone deposition and bone resorption.

From the simulations, mitochondria also appear as an important site of accumulation of monobasic amines – even for many molecules that have been previously classified as being “lysosomotropic”. Our simulation results indicate that monovalent weak bases can selectively accumulate in mitochondria at very high levels –in fact, at much higher levels than they appear to be able to accumulate in lysosomes. From a drug toxicity standpoint, unintended accumulation of small molecules in mitochondria can interfere with mitochondrial function, leading to cellular apoptosis (52-54). Conversely, intentional targeting of small molecule therapeutic agents to mitochondria can be a desirable feature for certain classes of drugs: mitochondria dysfunction can cause a variety of diseases, so there is great interest in developing mitochondriotropic drugs (22, 55-57).

Nevertheless, perhaps the most important classes of subcellularly-targeted molecules are those that are aimed at extracellular domains of cell surface receptors (24). Many ‘blockbuster’ drugs in the market today target cell surface receptors, ion channels, and other extracellular enzymes, making extracellular space one of the most valuable sites-of-action for drug development (58). Extracellular-acting therapeutic agents include anticoagulants that interfere with clotting factors in the blood, agents that interfere with pro-hormone processing enzymes, ion channel blockers for treating heart conditions, GPCR antagonists for hypertension, inflammation and a variety of other different

conditions, and many CNS-active agents that act on neurotransmitter receptors, transport and processing pathways. In order to target extracellular domains of blood proteins, cell surface receptors and ion channels, it is desirable that a molecule would have high transcellular permeability to facilitate absorption and tissue penetration. In addition, it would be desirable that the molecule would also have low intracellular accumulation so as to maximize extracellular concentration. The simulation results indicate that indeed, finding monovalent weak bases with high permeability and low intracellular accumulation in both target and non-target cells is possible, with several molecules in the reference set residing in this realm of physicochemical property space.

To conclude, cell based molecular transport simulators constitute a promising cheminformatic analysis tool for analyzing the subcellular transport properties of small molecules. The ability to combine results from different models, visualize simulations representing hundreds of thousands of different combinations of physicochemical properties, and relate these simulation results to the chemical structure and phenotypic effects of specific drugs and small drug-like molecules adds a new dimension to the existing mathematical models. As related to the specific class of lysosomotropic monobasic amines analyzed in this study, interactive visualization of simulation results point to a richness in subcellular transport and distribution behavior that is otherwise difficult to appreciate. We anticipate that the complexity of subcellular transport behaviors will ultimately be exploited in future generations of small molecule drug candidates “supertargeted” to their sites of action (59), be it in the extracellular space, the cytosol, mitochondria, lysosomes and potentially other intracellular organelles.

Table 3.1. The test set of ninety-nine lysosomotropic monobasic amines. Based on simulation results, compounds were classified by permeability (P_{eff} calculated with the R-model) and subcellular concentrations (calculated with the T-model) as follows: **Low permeability:** $P_{\text{eff}} < 35 \times 10^{-6}$ cm/sec; **High permeability:** $P_{\text{eff}} \geq 35 \times 10^{-6}$ cm/sec; **Lyso:** $C_{\text{lysoT}} > 2$ mM; **Mito:** $C_{\text{mitoT}} > 2$ mM; **Cyto:** $C_{\text{cytoT}} \geq 2$ mM; **Non-lyso:** $C_{\text{lysoT}} < 2$ mM; **Non-mito:** $C_{\text{mitoT}} < 2$ mM; **Non-cyto:** $C_{\text{cytoT}} < 2$ mM. Compounds appear in **gray background** if they were reported as non-lysosomotropic in published research articles; in *italics* if they appear as selective lysosomotropic in the simulations ($C_{\text{lysoT}} \geq 2$ mM; $C_{\text{lysoT}}/C_{\text{mitoT}} \geq 2$ mM; $C_{\text{lysoT}}/C_{\text{cytoT}} \geq 2$ mM); underlined if they appear as selectively mitochondriotropic in the simulations ($C_{\text{mitoT}} \geq 2$ mM, $C_{\text{mitoT}}/C_{\text{lysoT}} \geq 2$ mM, $C_{\text{mitoT}}/C_{\text{cytoT}} \geq 2$ mM). In the table, a particular class “exists” if one can find a combination of physicochemical properties (within the range of pK_a , $\log P_n$, and $\log P_d$ input values) that yields the expected behaviour in the simulation.

Category 1: Low Permeability, Non-lyso, Mito, Non-cyto							Chemical space exists.				
Category 2: Low Permeability, Non-lyso, Non-mito, Non-cyto							Chemical space exists.				
Category 3: Low Permeability, Non-lyso, Non-mito, Cyto							Chemical space does not exist.				
Category 4: Low Permeability, Non-lyso, Mito, Cyto							Chemical space exists.				
Category 5: Low Permeability, Lyso, Mito, Non-cyto							Chemical space exists.				
Category 6: Low Permeability, Lyso, Non-mito, Non-cyto							Chemical space exists.				
Name	pK_a	$\log P_n$	$\log P_d$	C_{cytoR}	C_{mitoR}	C_{lysoR}	P_{eff}	C_{cytoT}	C_{mitoT}	C_{lysoT}	Reference
<i>lidocaine</i>	7.2	2.71	1.16	0.15	0.06	1.74	26.67	1.87	0.81	22.26	(10)
Category 7: Low Permeability, Lyso, Non-mito, Cyto							Chemical space exists.				
Name	pK_a	$\log P_n$	$\log P_d$	C_{cytoR}	C_{mitoR}	C_{lysoR}	P_{eff}	C_{cytoT}	C_{mitoT}	C_{lysoT}	Reference
<i>17-DMAG</i>	7.31	2.46	0.87	0.15	0.06	1.69	13.01	2.05	0.81	22.73	(60)
<i>beta-dimethylaminoethylchloride</i>	7.63	2.48	0.9	0.23	0.08	1.5	11.76	2.64	0.91	17.52	(21)
<i>diethylaminoethyl chloride</i>	8.16	2.71	1.16	0.53	0.24	1.36	19.93	3.83	1.72	9.87	(21)
<i>triethanolamine</i>	8.14	1.52	-0.18	0.4	0.14	1.39	0.91	3.57	1.25	12.35	(21)
Category 8: Low Permeability, Lyso, Mito, Cyto							Chemical space exists.				
Name	pK_a	$\log P_n$	$\log P_d$	C_{cytoR}	C_{mitoR}	C_{lysoR}	P_{eff}	C_{cytoT}	C_{mitoT}	C_{lysoT}	Reference
<i>17-DMAP</i>	8.3	2.47	0.89	0.62	0.31	1.35	10.79	4.17	2.08	9.07	(60)
<u>2-amino-1-butanol</u>	9.49	2.04	0.55	1.67	9.57	1.29	5.84	10.16	58.1	7.82	(21)

<u>2-amino-2-methyl-1,3-propanediol</u>	<u>9.14</u>	<u>1.56</u>	<u>0</u>	<u>1.44</u>	<u>3.32</u>	<u>1.3</u>	<u>1.58</u>	<u>8.01</u>	<u>18.52</u>	<u>7.22</u>	(21)
<u>2-amino-2-methyl-1-propanol</u>	<u>9.68</u>	<u>1.92</u>	<u>0.41</u>	<u>1.73</u>	<u>14.32</u>	<u>1.29</u>	<u>4.27</u>	<u>10.85</u>	<u>89.76</u>	<u>8.06</u>	(21)
<u>2-aminoethanol(ethanolamine)</u>	<u>9.22</u>	<u>1.75</u>	<u>0.22</u>	<u>1.51</u>	<u>4.42</u>	<u>1.29</u>	<u>2.66</u>	<u>8.62</u>	<u>25.18</u>	<u>7.36</u>	(21)
<u>2-diethylaminoethanol</u>	<u>9.22</u>	<u>2.23</u>	<u>0.62</u>	<u>1.46</u>	<u>3.58</u>	<u>1.29</u>	<u>6.62</u>	<u>8.19</u>	<u>20.09</u>	<u>7.27</u>	(21)
<u>2-dimethylamino-2-methyl-1-propanol</u>	<u>9.25</u>	<u>2.17</u>	<u>0.55</u>	<u>1.47</u>	<u>3.76</u>	<u>1.29</u>	<u>5.65</u>	<u>8.31</u>	<u>21.23</u>	<u>7.3</u>	(21)
<u>2-dimethylaminoethanol</u>	<u>8.71</u>	<u>2.01</u>	<u>0.37</u>	<u>0.96</u>	<u>0.81</u>	<u>1.32</u>	<u>3.42</u>	<u>5.44</u>	<u>4.56</u>	<u>7.46</u>	(21)
<u>2-methylaminoethanol</u>	<u>9.46</u>	<u>1.89</u>	<u>0.32</u>	<u>1.63</u>	<u>7.29</u>	<u>1.29</u>	<u>3.41</u>	<u>9.67</u>	<u>43.34</u>	<u>7.66</u>	(21)
<u>3-amino-1-propanol</u>	<u>9.49</u>	<u>1.77</u>	<u>0.24</u>	<u>1.66</u>	<u>8.67</u>	<u>1.29</u>	<u>2.85</u>	<u>9.99</u>	<u>52.26</u>	<u>7.76</u>	(21)
<u>3-aminopropanal</u>	<u>9.14</u>	<u>1.77</u>	<u>0.24</u>	<u>1.46</u>	<u>3.6</u>	<u>1.29</u>	<u>2.76</u>	<u>8.17</u>	<u>20.17</u>	<u>7.25</u>	(61)
<u>3-dimethylamino-1-propanol</u>	<u>8.83</u>	<u>2.03</u>	<u>0.39</u>	<u>1.08</u>	<u>1.13</u>	<u>1.31</u>	<u>3.66</u>	<u>5.98</u>	<u>6.25</u>	<u>7.23</u>	(21)
<u>4-amino-1-butanol</u>	<u>9.55</u>	<u>1.92</u>	<u>0.41</u>	<u>1.69</u>	<u>10.52</u>	<u>1.29</u>	<u>4.24</u>	<u>10.34</u>	<u>64.43</u>	<u>7.88</u>	(21)
ammonia	<u>8.55</u>	<u>1.81</u>	<u>0.41</u>	<u>1.05</u>	<u>1.08</u>	<u>1.31</u>	<u>3.8</u>	<u>5.67</u>	<u>5.82</u>	<u>7.08</u>	(21)
<u>atenolol</u>	<u>9.32</u>	<u>2.29</u>	<u>0.76</u>	<u>1.57</u>	<u>5.7</u>	<u>1.29</u>	<u>9.32</u>	<u>9.15</u>	<u>33.13</u>	<u>7.5</u>	(6)
<u>atropine</u>	<u>9.02</u>	<u>2.67</u>	<u>1.23</u>	<u>1.44</u>	<u>3.36</u>	<u>1.3</u>	<u>26.87</u>	<u>7.98</u>	<u>18.66</u>	<u>7.18</u>	(10), (16)
<u>benzylamine</u>	<u>9.17</u>	<u>2.58</u>	<u>1.24</u>	<u>1.6</u>	<u>6.38</u>	<u>1.29</u>	<u>28.25</u>	<u>9.32</u>	<u>37.22</u>	<u>7.52</u>	(10)
<u>butylamine</u>	<u>9.84</u>	<u>2.39</u>	<u>0.95</u>	<u>1.78</u>	<u>24.35</u>	<u>1.28</u>	<u>14.95</u>	<u>11.54</u>	<u>157.56</u>	<u>8.31</u>	(21)
<u>diethylamine</u>	<u>10.2</u>	<u>2.36</u>	<u>0.84</u>	<u>1.82</u>	<u>45</u>	<u>1.28</u>	<u>11.68</u>	<u>12.09</u>	<u>298.98</u>	<u>8.53</u>	(10), (21)
<u>dimethylamine</u>	<u>10.15</u>	<u>2.13</u>	<u>0.59</u>	<u>1.81</u>	<u>38.7</u>	<u>1.28</u>	<u>6.56</u>	<u>11.98</u>	<u>255.81</u>	<u>8.48</u>	(21)
<u>ethylamine</u>	<u>9.86</u>	<u>2.11</u>	<u>0.62</u>	<u>1.78</u>	<u>22.73</u>	<u>1.28</u>	<u>6.99</u>	<u>11.46</u>	<u>146.61</u>	<u>8.28</u>	(21)
<u>guanidine</u>	<u>12.09</u>	<u>1.82</u>	<u>0.39</u>	<u>1.86</u>	<u>461.27</u>	<u>1.28</u>	<u>4.17</u>	<u>12.78</u>	<u>3164.97</u>	<u>8.8</u>	(10), (21)
<u>hexylamine</u>	<u>9.84</u>	<u>2.66</u>	<u>1.24</u>	<u>1.79</u>	<u>25.48</u>	<u>1.28</u>	<u>29.17</u>	<u>11.59</u>	<u>165.24</u>	<u>8.33</u>	(21)
<u>isobutylamine</u>	<u>9.87</u>	<u>2.4</u>	<u>0.95</u>	<u>1.79</u>	<u>25.47</u>	<u>1.28</u>	<u>14.96</u>	<u>11.59</u>	<u>165.19</u>	<u>8.33</u>	(21)
<u>isopropanolamine</u>	<u>9.26</u>	<u>1.89</u>	<u>0.38</u>	<u>1.55</u>	<u>5.16</u>	<u>1.29</u>	<u>3.87</u>	<u>8.94</u>	<u>29.72</u>	<u>7.44</u>	(21)
<u>isopropylamine</u>	<u>10.06</u>	<u>2.25</u>	<u>0.78</u>	<u>1.81</u>	<u>37.09</u>	<u>1.28</u>	<u>10.16</u>	<u>11.95</u>	<u>244.64</u>	<u>8.47</u>	(21)
<u>methylamine</u>	<u>9.72</u>	<u>2</u>	<u>0.5</u>	<u>1.74</u>	<u>16.1</u>	<u>1.29</u>	<u>5.27</u>	<u>11.02</u>	<u>101.71</u>	<u>8.12</u>	(21)
metoclopramide	<u>8.73</u>	<u>2.56</u>	<u>0.99</u>	<u>1.05</u>	<u>1.06</u>	<u>1.31</u>	<u>14.48</u>	<u>5.81</u>	<u>5.82</u>	<u>7.22</u>	(14), (13)
<u>morpholine</u>	<u>8.21</u>	<u>2.02</u>	<u>1.25</u>	<u>1.36</u>	<u>2.95</u>	<u>1.3</u>	<u>27.55</u>	<u>6.62</u>	<u>14.36</u>	<u>6.31</u>	(10)
N-acetylprocainamide	<u>8.73</u>	<u>2.51</u>	<u>0.93</u>	<u>1.04</u>	<u>1.02</u>	<u>1.31</u>	<u>12.59</u>	<u>5.76</u>	<u>5.66</u>	<u>7.25</u>	(10),(13)
NAMA	<u>8.72</u>	<u>2.38</u>	<u>0.79</u>	<u>1.02</u>	<u>0.97</u>	<u>1.31</u>	<u>9.09</u>	<u>5.68</u>	<u>5.36</u>	<u>7.29</u>	(14)
N,N-dimethyl-3-chloropropylamine	<u>8.38</u>	<u>2.5</u>	<u>0.92</u>	<u>0.69</u>	<u>0.38</u>	<u>1.34</u>	<u>11.66</u>	<u>4.41</u>	<u>2.45</u>	<u>8.54</u>	(21)

N,N-dimethyl-benzylamine	8.67	2.84	1.3	1.02	0.98	1.31	29.42	5.65	5.4	7.25	(10)
pentylamine	9.84	2.53	1.09	1.78	24.35	1.28	20.64	11.54	157.56	8.31	(21)
practolol	9.32	2.47	0.97	1.59	6.15	1.29	15.16	9.3	35.98	7.54	(6)
propylamine	9.85	2.27	0.8	1.78	23.26	1.28	10.58	11.49	150.19	8.29	(21)
s-butylamine	10.07	2.4	0.95	1.81	39.59	1.28	15.03	12	261.77	8.49	(21)
t-butylamine	10.27	2.27	0.81	1.83	59.14	1.28	10.92	12.26	395.97	8.59	(21)
triethylamine	9.84	2.59	1.02	1.76	18.05	1.29	17.49	11.18	114.96	8.18	(21)
trimethylamine	9.23	2.25	0.64	1.47	3.67	1.29	6.94	8.25	20.66	7.28	(10)
tris(hydroxymethyl)methylamine	8.64	1.2	-0.4	0.93	0.75	1.32	0.58	5.29	4.25	7.51	(10), (21)

Category 9: High Permeability, Non-lyso, Mito, Cyto

Chemical space does not exist.

Category 10: High Permeability, Non-lyso, Non-mito, Cyto

Chemical space does not exist.

Category 11: High Permeability, Non-lyso, Mito, Non-cyto

Chemical space exists.

Category 12: High Permeability, Non-lyso, Non-mito, Non-cyto

Chemical space exists.

Name	pK _a	logP _n	logP _d	C _{cyto} R	C _{mito} R	C _{lyso} R	P _{eff}	C _{cyto} T	C _{mito} T	C _{lyso} T	
3-aminoquinoline	4.63	2.65	2.00	0.73	0.73	1.12	398.87	0.82	0.82	1.25	(1)
8-aminoquinoline	4.07	2.65	2.00	0.78	0.78	0.90	425.43	0.81	0.81	0.94	(1)
AF-CX1325XX	1.95	2.18	0.7	0.8	0.8	0.8	148	0.81	0.81	0.81	(62)
aniline	4.5	2.62	1.2	0.73	0.73	1.1	372.35	0.82	0.81	1.22	(10)
benzocaine	2.7	2.78	1.41	0.8	0.8	0.8	588.46	0.81	0.81	0.82	(13)
beta-naphthylamine	4.12	2.95	1.57	0.77	0.77	0.93	838.56	0.81	0.81	0.98	(10)
pyrimidine	1.55	2.17	1.4	0.8	0.8	0.8	144.65	0.81	0.81	0.81	(10)
pyridine	4.95	2.44	1.88	0.69	0.69	1.3	229.69	0.82	0.82	1.56	(10)

Category 13: High Permeability, Lyso, Non-mito, Non-cyto

Chemical space exists.

Name	pK _a	logP _n	logP _d	C _{cyto} R	C _{mito} R	C _{lyso} R	P _{eff}	C _{cyto} T	C _{mito} T	C _{lyso} T	
17-AEP	6.59	2.56	0.99	0.14	0.09	2.43	37.31	1.17	0.80	20.89	(60)
1-aminoisoquinoline	6.88	2.74	1.94	0.36	0.30	1.45	123.44	1.53	1.28	6.16	(1)
1-dodecylimidazole	6.56	3.65	3.3	0.64	0.81	1.36	2615.12	1.27	1.61	2.7	(21)
eserine	6.46	3.03	1.51	0.15	0.11	2.51	137.8	1.09	0.81	17.74	(10)
harmine	5.95	2.81	2.06	0.38	0.36	1.82	265.16	0.91	0.88	4.40	(1)

<i>imidazole</i>	6.73	2.12	1.59	0.51	0.56	1.39	52.47	1.41	1.53	3.81	(21)
<i>papaverine</i>	6.07	3.1	2.39	0.37	0.35	1.72	489.43	0.94	0.91	4.42	(1)
<i>pilocarpine</i>	6.39	2.38	1.89	0.48	0.51	1.44	109.54	1.1	1.18	3.32	(10)
<i>s-collidine</i>	7.06	2.71	1.71	0.3	0.2	1.47	74.19	1.76	1.18	8.61	(21)

Category 14: High Permeability, Lyso, Non-mito, Cyto**Chemical space exists.**

Name	pK _a	logP _n	logP _d	C _{cyto} R	C _{mito} R	C _{lyso} R	P _{eff}	C _{cyto} T	C _{mito} T	C _{lyso} T	
<i>cyproheptadine</i>	7.77	3.67	2.23	0.35	0.14	1.41	235.81	3.02	1.22	12.12	(63)
<i>diltiazem</i>	7.89	3.08	1.57	0.37	0.14	1.4	51.38	3.23	1.25	12.07	(16)
<i>N-dodecylmorpholine</i>	7.5	3.58	2.14	0.24	0.1	1.49	203.16	2.44	0.98	15.24	(21)

Category 15: High Permeability, Lyso, Mito, Non-cyto**Chemical space exists.****Category 16: High Permeability, Lyso, Mito, Cyto****Chemical space exists.**

Name	pK _a	logP _n	logP _d	C _{cyto} R	C _{mito} R	C _{lyso} R	P _{eff}	C _{cyto} T	C _{mito} T	C _{lyso} T	
<u>4-aminopyridine</u>	<u>8.63</u>	<u>2.18</u>	<u>1.59</u>	<u>1.71</u>	<u>11.8</u>	<u>1.29</u>	<u>64.2</u>	<u>9.96</u>	<u>68.73</u>	<u>7.5</u>	(10)
<u>4-aminoquinaldine</u>	<u>8.5</u>	<u>2.7</u>	<u>1.82</u>	<u>1.49</u>	<u>4.21</u>	<u>1.29</u>	<u>104.97</u>	<u>7.87</u>	<u>22.31</u>	<u>6.85</u>	(10)
4-aminoquinoline	7.98	2.65	2.00	1.29	2.56	1.30	152.07	5.73	11.40	5.79	(1)
<u>4-dimethylaminopyridine</u>	<u>8.47</u>	<u>2.53</u>	<u>1.98</u>	<u>1.67</u>	<u>9.26</u>	<u>1.29</u>	<u>156.25</u>	<u>9.28</u>	<u>51.49</u>	<u>7.16</u>	(10)
<u>9-aminoacridine</u>	<u>8.97</u>	<u>3.11</u>	<u>2.4</u>	<u>1.76</u>	<u>18.6</u>	<u>1.28</u>	<u>419.24</u>	<u>10.96</u>	<u>115.66</u>	<u>7.99</u>	(10)
<u>alprenolol</u>	<u>9.32</u>	<u>3.04</u>	<u>1.71</u>	<u>1.67</u>	<u>9.42</u>	<u>1.29</u>	<u>84.41</u>	<u>10.09</u>	<u>56.88</u>	<u>7.77</u>	(6)
<u>amantadine</u>	<u>10.33</u>	<u>2.57</u>	<u>2.04</u>	<u>1.86</u>	<u>288.64</u>	<u>1.28</u>	<u>186.33</u>	<u>12.73</u>	<u>1973.95</u>	<u>8.77</u>	(16)
amiodarone	8.17	4.58	3.38	0.88	0.74	1.32	3439.62	4.69	3.96	7.07	(4)
<u>amitriptyline</u>	<u>9.41</u>	<u>3.7</u>	<u>2.27</u>	<u>1.67</u>	<u>9.14</u>	<u>1.29</u>	<u>306.28</u>	<u>10.07</u>	<u>55.23</u>	<u>7.78</u>	(64)
biperiden	8.97	3.25	1.76	1.36	2.57	1.3	89.81	7.43	14.07	7.1	(65)
<u>chlorphentermine</u>	<u>10.24</u>	<u>3</u>	<u>1.62</u>	<u>1.84</u>	<u>65.54</u>	<u>1.28</u>	<u>70.54</u>	<u>12.32</u>	<u>439.85</u>	<u>8.61</u>	(66), (46)
chlorpromazine	8.87	3.7	2.27	1.33	2.33	1.3	288.89	7.19	12.66	7.05	(16)
<u>desipramine</u>	<u>9.66</u>	<u>3.4</u>	<u>2.01</u>	<u>1.76</u>	<u>18.13</u>	<u>1.29</u>	<u>170.9</u>	<u>11.17</u>	<u>115.25</u>	<u>8.17</u>	(12)
<u>dibutylamine</u>	<u>10.36</u>	<u>2.93</u>	<u>1.48</u>	<u>1.84</u>	<u>72.43</u>	<u>1.28</u>	<u>51.13</u>	<u>12.37</u>	<u>487.37</u>	<u>8.63</u>	(21)
<u>dihydroalprenolol</u>	<u>9.32</u>	<u>3.11</u>	<u>1.69</u>	<u>1.63</u>	<u>7.53</u>	<u>1.29</u>	<u>80.09</u>	<u>9.69</u>	<u>44.73</u>	<u>7.65</u>	(7)
dizocilpine	8.3	3.29	1.89	0.80	0.55	1.33	110.20	4.61	3.18	7.70	(67)
<u>dodecylamine</u>	<u>9.84</u>	<u>3.44</u>	<u>2.12</u>	<u>1.8</u>	<u>31.89</u>	<u>1.28</u>	<u>221.84</u>	<u>11.8</u>	<u>208.84</u>	<u>8.41</u>	(21)
<u>ephedrine</u>	<u>9.19</u>	<u>2.63</u>	<u>1.94</u>	<u>1.8</u>	<u>31.41</u>	<u>1.28</u>	<u>146.48</u>	<u>11.65</u>	<u>202.78</u>	<u>8.29</u>	(10)

<u>fluoxetine</u>	<u>9.45</u>	<u>3.58</u>	<u>3.01</u>	<u>1.84</u>	<u>69.46</u>	<u>1.28</u>	<u>1731.76</u>	<u>12.27</u>	<u>463.16</u>	<u>8.55</u>	(4), (23)
imipramine	8.87	3.52	2.07	1.31	2.21	1.3	181.73	7.09	11.95	7.04	(4)
<u>iprindole</u>	<u>9.36</u>	<u>3.54</u>	<u>2.09</u>	<u>1.64</u>	<u>7.71</u>	<u>1.29</u>	<u>201.32</u>	<u>9.74</u>	<u>45.89</u>	<u>7.67</u>	(66)
<u>mecamylamine</u>	<u>10.49</u>	<u>2.93</u>	<u>2.27</u>	<u>1.86</u>	<u>297.05</u>	<u>1.28</u>	<u>316.44</u>	<u>12.73</u>	<u>2032.53</u>	<u>8.77</u>	(10)
<u>memantine</u>	<u>10.31</u>	<u>2.85</u>	<u>1.46</u>	<u>1.84</u>	<u>73.92</u>	<u>1.28</u>	<u>48.83</u>	<u>12.38</u>	<u>497.49</u>	<u>8.63</u>	(11)
<u>octylamine</u>	<u>9.84</u>	<u>2.92</u>	<u>1.53</u>	<u>1.79</u>	<u>27.27</u>	<u>1.28</u>	<u>56.92</u>	<u>11.66</u>	<u>177.38</u>	<u>8.35</u>	(21)
<u>perhexiline</u>	<u>10.2</u>	<u>3.83</u>	<u>3.28</u>	<u>1.86</u>	<u>244.79</u>	<u>1.28</u>	<u>3237.19</u>	<u>12.7</u>	<u>1671.65</u>	<u>8.76</u>	(4), (68)
<u>phentermine</u>	<u>10.25</u>	<u>2.83</u>	<u>1.43</u>	<u>1.83</u>	<u>64.21</u>	<u>1.28</u>	<u>45.54</u>	<u>12.31</u>	<u>430.76</u>	<u>8.61</u>	(66)
<u>piperidine</u>	<u>10.03</u>	<u>2.37</u>	<u>1.64</u>	<u>1.85</u>	<u>148.62</u>	<u>1.28</u>	<u>74.09</u>	<u>12.6</u>	<u>1009.79</u>	<u>8.71</u>	(10)
promazine	8.87	3.53	2.08	1.31	2.21	1.30	185.96	7.09	11.95	7.04	(64)
<u>propranolol</u>	<u>9.32</u>	<u>3.03</u>	<u>1.59</u>	<u>1.62</u>	<u>7.16</u>	<u>1.29</u>	<u>63.51</u>	<u>9.59</u>	<u>42.38</u>	<u>7.62</u>	(10)
<u>sertraline</u>	<u>9.5</u>	<u>3.85</u>	<u>2.51</u>	<u>1.73</u>	<u>14.07</u>	<u>1.29</u>	<u>537.84</u>	<u>10.79</u>	<u>87.84</u>	<u>8.02</u>	(64)
thioridazine	8.61	4.01	2.61	1.11	1.27	1.31	608.81	5.96	6.80	7.02	(64)
<u>tributylamine</u>	<u>10.44</u>	<u>3.45</u>	<u>2.1</u>	<u>1.85</u>	<u>102.49</u>	<u>1.28</u>	<u>213.44</u>	<u>12.51</u>	<u>694.01</u>	<u>8.68</u>	(10)
<u>verapamil</u>	<u>9.33</u>	<u>3.7</u>	<u>2.27</u>	<u>1.63</u>	<u>7.53</u>	<u>1.29</u>	<u>304.48</u>	<u>9.69</u>	<u>44.71</u>	<u>7.65</u>	(16)

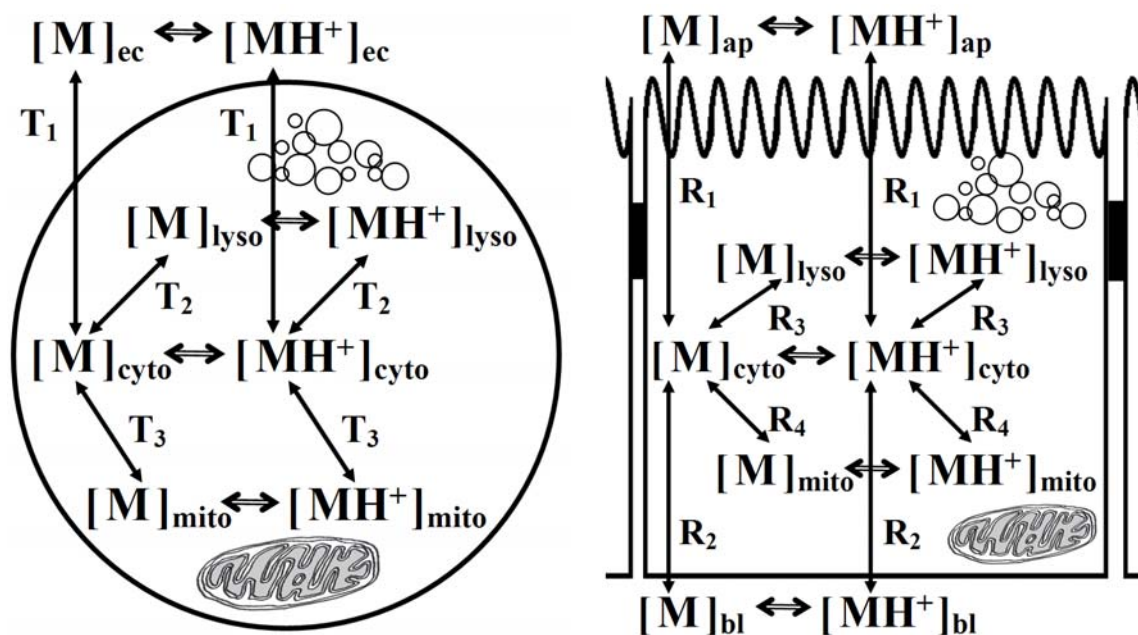


Figure 3.1. Diagrams showing the cellular pharmacokinetic phenomena captured by the two mathematical models used in this study: (left) the T-Model for a leukocyte-like cell in suspension and (right) the R-Model for an epithelial-like cell.

Key:

ap: apical compartment; bl: basolateral compartment; cyto: cytosol; mito: mitochondria; lyso: lysosome; T1: flux of the ionized/unionized form between the cytosol and the extracellular compartment; T2: flux of the ionized/unionized form between the cytosol and lysosome; T3: flux of the ionized/unionized form between the cytosol and the extracellular compartment; R1: flux of the ionized/unionized form between the cytosol and the apical compartment; R2: flux of the ionized/unionized form between the cytosol and the basolateral compartment; R3: flux of the ionized/unionized form between the cytosol and the lysosome; R4: flux of the ionized/unionized form between the cytosol and the mitochondria.

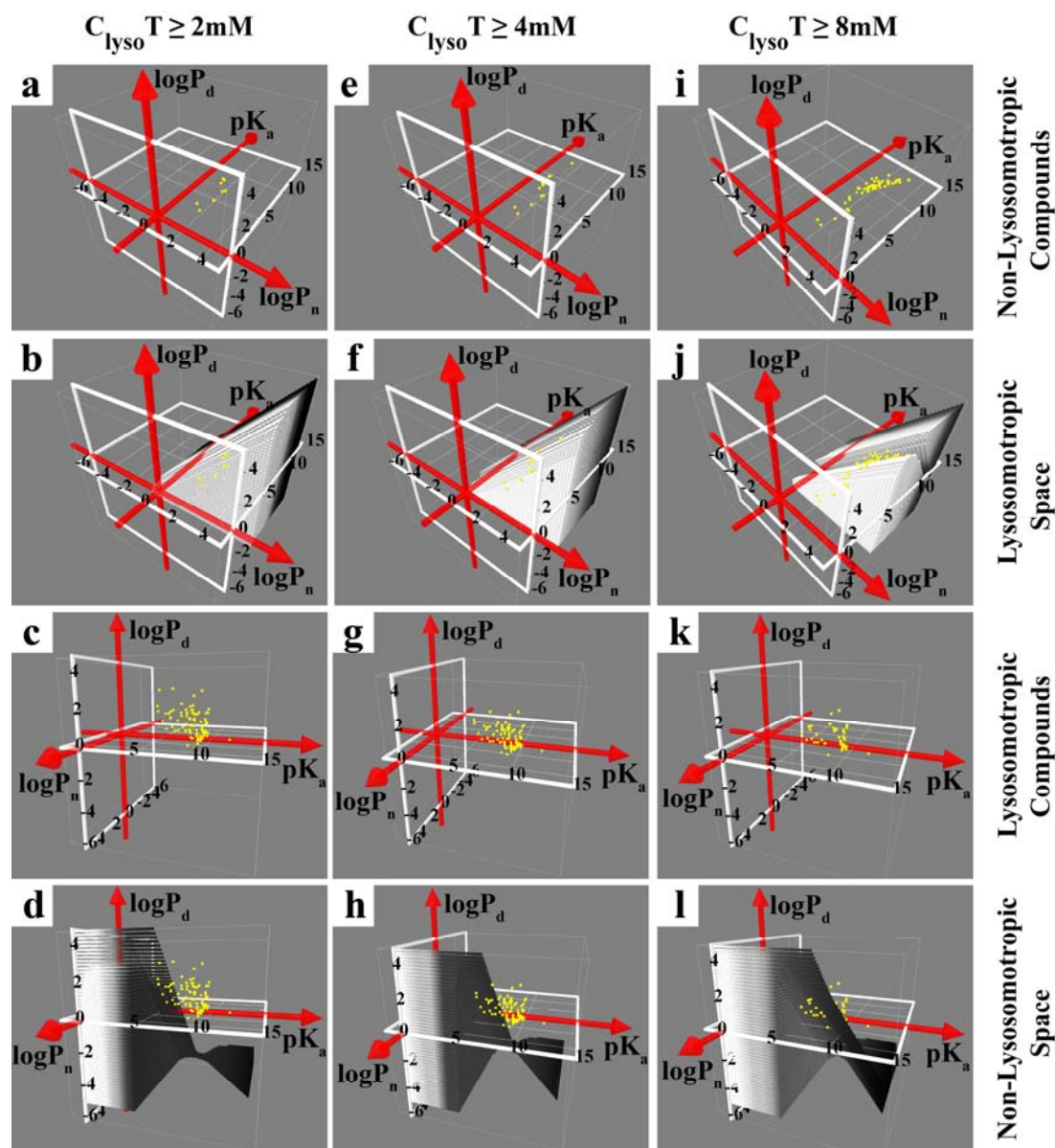


Figure 3.2. Visualizing the simulated physicochemical property space occupied by lysosomotropic monobasic amines. Individual molecules in the test set are indicated by yellow dots. To discriminate between lysosomotropic vs. non-lysosomotropic molecules, three lysosomal concentrations were explored as thresholds: 2 mM (a-d); 4 mM (e-h); and 8 mM (i-l). Columns show non-lysosomotropic molecules (a, e, i); non-lysosomotropic molecules plus lysosomotropic space (b, f, j); lysosomotropic molecules (c, g, k); and lysosomotropic molecules plus non-lysosomotropic space (d, h, l).

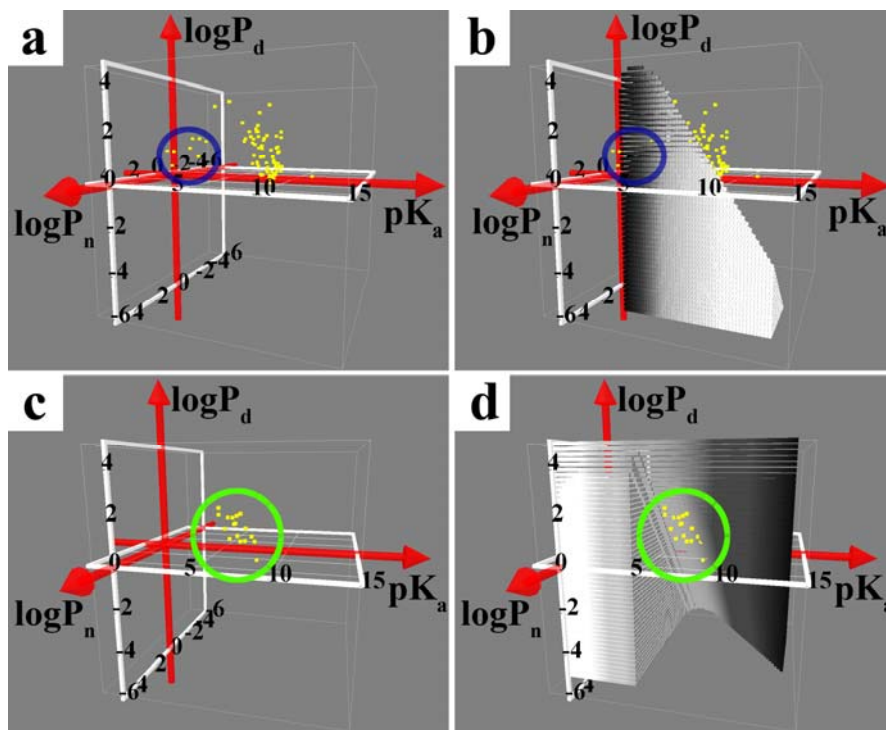


Figure 3.3. Visualizing the simulated physicochemical property space occupied by selectively lysosomotropic monobasic amines. Individual molecules in the test set are indicated by yellow dots. The four graphs show: (a) non-lysosomotropic molecules (inside blue circle) and non-selective lysosomotropic molecules (outside blue circle); (b) physicochemical property space occupied by selectively lysosomotropic molecules, in relation to non-lysosomotropic molecules (inside blue circle) and non-selective lysosomotropic molecules (outside blue circle); (c) selectively lysosomotropic molecules (inside green circle); (d) selectively lysosomotropic molecules (yellow dots in green circle) in relation to the union of non-selective lysosomotropic and non-lysosomotropic physicochemical property space.

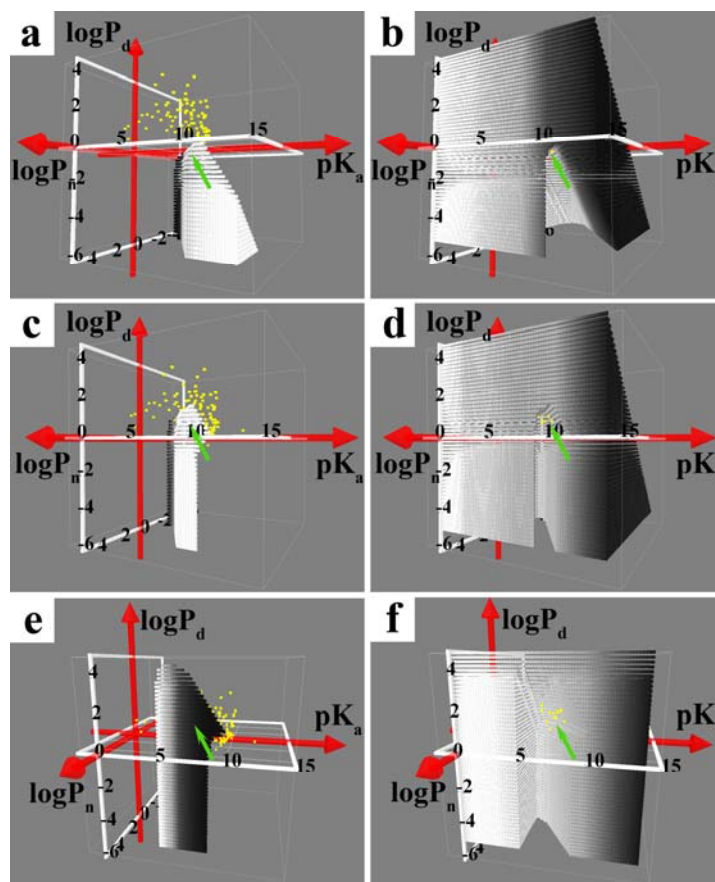


Figure 3.4. Visualizing the relationship between transcellular permeability and lysosomotropic character. Individual molecules in the test set are indicated by yellow dots. The six graphs show: (a) physicochemical property space occupied by molecules with $P_{\text{eff}} < 1 \times 10^{-6}$ cm/s, in relation to non-selectively, lysosomotropic molecules; (b) selectively lysosomotropic molecules with $P_{\text{eff}} < 1 \times 10^{-6}$ cm/s (yellow dots) in relation to the union of physicochemical property spaces occupied by non-selectively lysosomotropic, non-lysosomotropic, and selectively lysosomotropic molecules with $P_{\text{eff}} > 1 \times 10^{-6}$ cm/s; (c) physicochemical property space occupied by molecules with 1×10^{-6} cm/s $< P_{\text{eff}} < 35 \times 10^{-6}$ cm/s, in relation to non-selectively lysosomotropic molecules; (d) selectively lysosomotropic molecules with 1×10^{-6} cm/s $< P_{\text{eff}} < 35 \times 10^{-6}$ cm/s in relation to the union of physicochemical property spaces occupied by non-selectively lysosomotropic, non-lysosomotropic, and selectively lysosomotropic molecules excluding those with 1×10^{-6} cm/s $< P_{\text{eff}} < 35 \times 10^{-6}$ cm/s; (e) physicochemical property space occupied by molecules with $P_{\text{eff}} > 35 \times 10^{-6}$ cm/s, in relation to non-selectively, lysosomotropic molecules; (f) selectively lysosomotropic molecules with $P_{\text{eff}} > 35 \times 10^{-6}$ cm/s in relation to the union of physicochemical property spaces occupied by non-selectively lysosomotropic, non-lysosomotropic, and selectively lysosomotropic molecules with $P_{\text{eff}} < 35 \times 10^{-6}$ cm/s. Green arrow point to the general region of physicochemical property space where the reference molecules are visibly clustered.

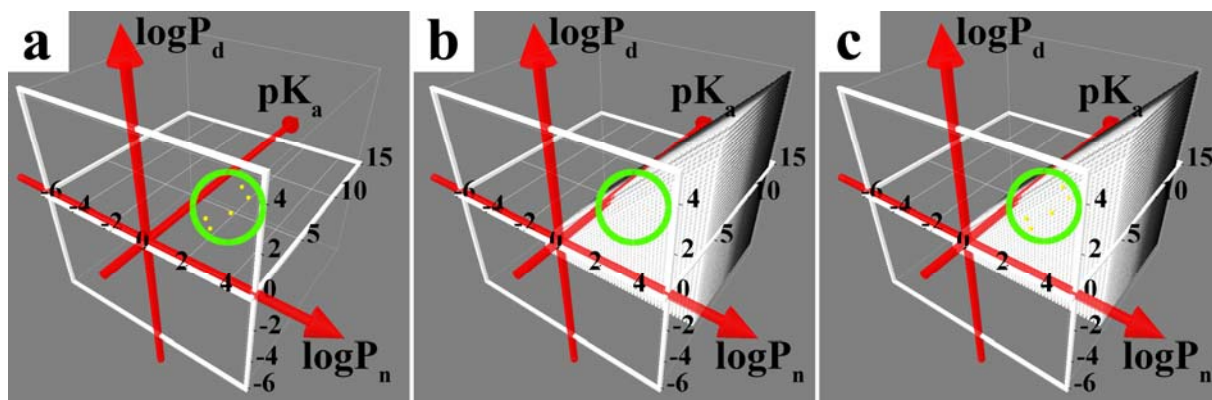


Figure 3.5. Visualizing the simulated physicochemical property space occupied by molecules with low intracellular accumulation and high permeability. Individual molecules in the test set are indicated by yellow dots. The three graphs show: (a) molecules with low intracellular accumulation and high permeability (inside green circle); (b) physicochemical property space occupied by molecules with calculated low intracellular accumulation and high permeability (green circle same as in Figure 3.5a); (c) the simulated physicochemical property space occupied by molecules with high intracellular accumulation, regardless of permeability (green circle same as in Figure 3.5a).

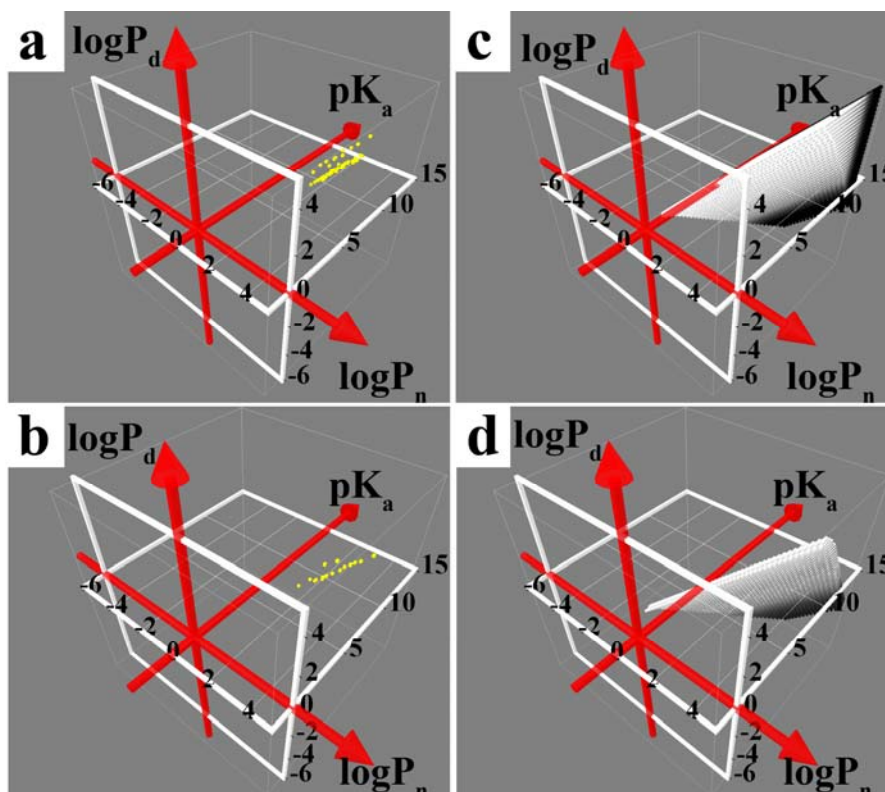


Figure 3.6. Visualizing the simulated physicochemical property space of various classes of non-selective, lysosomotropic molecules. Individual molecules in the test set are indicated by yellow dots. The four graphs show: (a) fifty-six selectively mitochondriotropic molecules; (b) 18 lysosomotropic, molecules which are not selective in terms of lysosomal, mitochondrial or cytosolic accumulation; (c) the simulated physicochemical property space occupied by lysosomotropic molecules that are also selectively mitochondriotropic; (d) the simulated physicochemical property space of non-selective lysosomotropic, non-selective mitochondriotropic molecules.

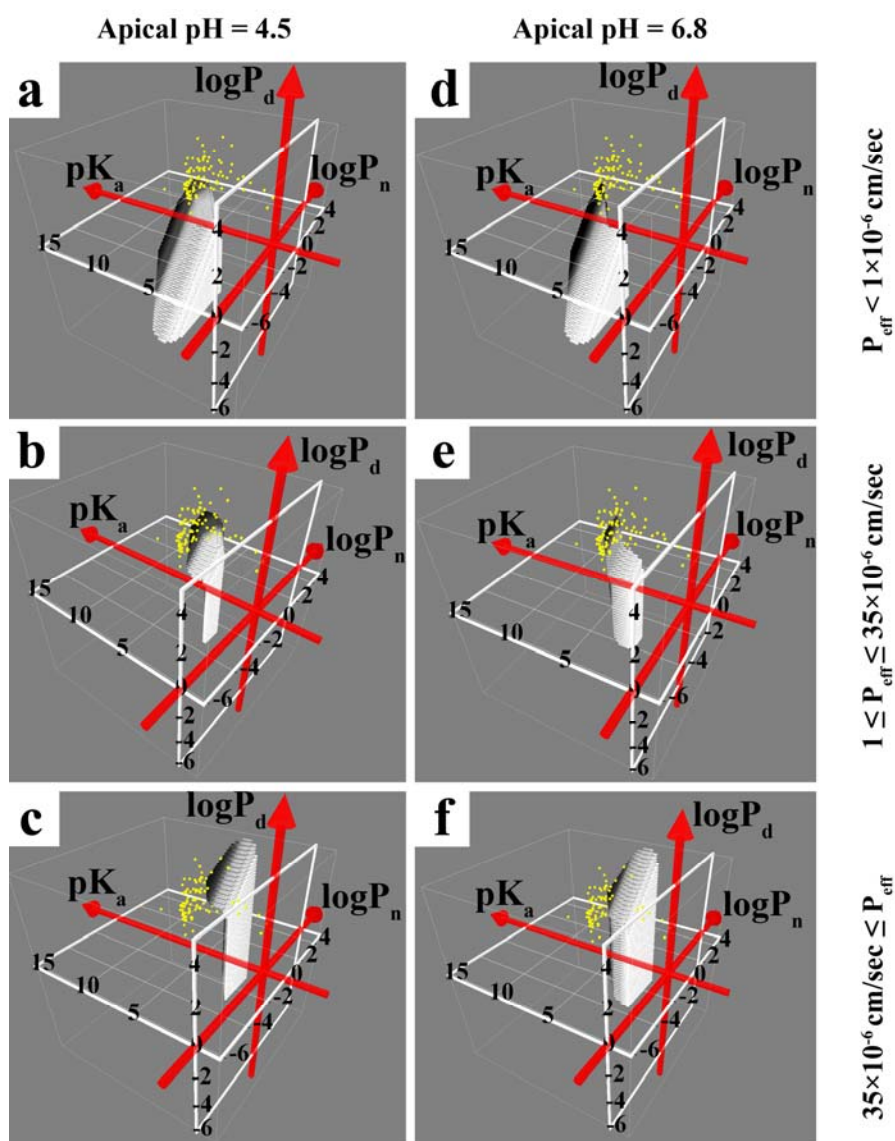


Figure 3.7. Visualizing the effect of extracellular pH on physicochemical property space occupied by selectively-lysosomotropic molecules. Simulations were carried out using an apical pH of 4.5 (a-c) and 6.8 (d-f) in the R-Model. Yellow dots indicate individual molecules in the test set. Each row shows the physicochemical property space occupied by molecules in different permeability classes, as follows: (a) and (d) $P_{\text{eff}} < 1 \times 10^{-6} \text{ cm/s}$; (b) and (e) $1 \times 10^{-6} \text{ cm/s} < P_{\text{eff}} < 35 \times 10^{-6} \text{ cm/s}$; (c) and (f) $P_{\text{eff}} > 35 \times 10^{-6} \text{ cm/s}$.

References

1. A.M. Kaufmann and J.P. Krise. Lysosomal sequestration of amine-containing drugs: analysis and therapeutic implications. *J Pharm Sci.* 96:729-746 (2007).
2. M. Duvvuri, Y.P. Gong, D. Chatterji, and J.P. Krise. Weak base permeability characteristics influence the intracellular sequestration site in the multidrug-resistant human leukemic cell line HL-60. *J Biol Chem.* 279:32367-32372 (2004).
3. C. de Duve, T. de Barsey, B. Poole, A. Trouet, P. Tulkens, and F. Van Hoof. Commentary. Lysosomotropic agents. *Biochem Pharmacol.* 23:2495-2531 (1974).
4. M.J. Reasor and S. Kacew. Drug-induced phospholipidosis: are there functional consequences? *Exp Biol Med (Maywood).* 226:825-830 (2001).
5. H. Fujimura, E. Dekura, M. Kurabe, N. Shimazu, M. Koitabashi, and W. Toriumi. Cell-based fluorescence assay for evaluation of new-drugs potential for phospholipidosis in an early stage of drug development. *Exp Toxicol Pathol.* 58:375-382 (2007).
6. G. Cramb. Selective lysosomal uptake and accumulation of the beta-adrenergic antagonist propranolol in cultured and isolated cell systems. *Biochem Pharmacol.* 35:1365-1372 (1986).
7. B. Styrt and M.S. Klempner. Lysosomotropic behavior of adrenergic antagonists in interactions with human neutrophils. *Biochem Pharmacol.* 37:435-441 (1988).
8. J.P. Ploemen, J. Kelder, T. Hafmans, H. van de Sandt, J.A. van Burgsteden, P.J. Salemink, and E. van Esch. Use of physicochemical calculation of pKa and CLogP to predict phospholipidosis-inducing potential: a case study with structurally related piperazines. *Exp Toxicol Pathol.* 55:347-355 (2004).
9. P.O. Seglen and P.B. Gordon. Effects of lysosomotropic monoamines, diamines, amino alcohols, and other amino compounds on protein degradation and protein synthesis in isolated rat hepatocytes. *Mol Pharmacol.* 18:468-475 (1980).
10. S. Ohkuma and B. Poole. Cytoplasmic vacuolation of mouse peritoneal macrophages and the uptake into lysosomes of weakly basic substances. *J Cell Biol.* 90:656-664 (1981).
11. U.E. Honegger, G. Quack, and U.N. Wiesmann. Evidence for lysosomotropism of memantine in cultured human cells: cellular kinetics and effects of memantine on phospholipid content and composition, membrane fluidity and beta-adrenergic transmission. *Pharmacol Toxicol.* 73:202-208 (1993).
12. U.E. Honegger, A.A. Roscher, and U.N. Wiesmann. Evidence for lysosomotropic action of desipramine in cultured human fibroblasts. *J Pharmacol Exp Ther.* 225:436-441 (1983).
13. G. Morissette, E. Moreau, C.G. R, and F. Marceau. Massive cell vacuolization induced by organic amines such as procainamide. *J Pharmacol Exp Ther.* 310:395-406 (2004).
14. G. Morissette, E. Moreau, C.G. R, and F. Marceau. N-substituted 4-aminobenzamides (procainamide analogs): an assessment of multiple cellular effects concerning ion trapping. *Mol Pharmacol.* 68:1576-1589 (2005).

15. S.J. Hurwitz, M. Terashima, N. Mizunuma, and C.A. Slapak. Vesicular anthracycline accumulation in doxorubicin-selected U-937 cells: participation of lysosomes. *Blood*. 89:3745-3754 (1997).
16. J. Ishizaki, K. Yokogawa, F. Ichimura, and S. Ohkuma. Uptake of imipramine in rat liver lysosomes in vitro and its inhibition by basic drugs. *J Pharmacol Exp Ther*. 294:1088-1098 (2000).
17. B. Lemieux, M.D. Percival, and J.P. Falguyret. Quantitation of the lysosomotropic character of cationic amphiphilic drugs using the fluorescent basic amine Red DND-99. *Anal Biochem*. 327:247-251 (2004).
18. W.C. Yang, F.F. Strasser, and C.M. Pomerat. Mechanism of Drug-Induced Vacuolization in Tissue Culture. *Exp Cell Res*. 38:495-506 (1965).
19. A. Bulychev, A. Trouet, and P. Tulkens. Uptake and intracellular distribution of neutral red in cultured fibroblasts. *Exp Cell Res*. 115:343-355 (1978).
20. M. Duvvuri and J.P. Krise. A novel assay reveals that weakly basic model compounds concentrate in lysosomes to an extent greater than pH-partitioning theory would predict. *Mol Pharm*. 2:440-448 (2005).
21. Z.I. Cabantchik, J. Silfen, R.A. Firestone, M. Krugliak, E. Nissani, and H. Ginsburg. Effects of lysosomotropic detergents on the human malarial parasite *Plasmodium falciparum* in in vitro culture. *Biochem Pharmacol*. 38:1271-1277 (1989).
22. R.W. Horobin, S. Trapp, and V. Weissig. Mitochondriotropics: a review of their mode of action, and their applications for drug and DNA delivery to mammalian mitochondria. *J Control Release*. 121:125-136 (2007).
23. R.J. Gonzalez-Rothi, D.S. Zander, and P.R. Ros. Fluoxetine hydrochloride (Prozac)-induced pulmonary disease. *Chest*. 107:1763-1765 (1995).
24. X. Zhang, K. Shedden, and G.R. Rosania. A cell-based molecular transport simulator for pharmacokinetic prediction and cheminformatic exploration. *Mol Pharm*. 3:704-716 (2006).
25. S. Trapp and R.W. Horobin. A predictive model for the selective accumulation of chemicals in tumor cells. *Eur Biophys J Biophys Lett*. 34:959-966 (2005).
26. L.M. Loew, R.A. Tuft, W. Carrington, and F.S. Fay. Imaging in five dimensions: time-dependent membrane potentials in individual mitochondria. *Biophys J*. 65:2396-2407 (1993).
27. S.L. Rybak and R.F. Murphy. Primary cell cultures from murine kidney and heart differ in endosomal pH. *J Cell Physiol*. 176:216-222 (1998).
28. C.C. Cain and R.F. Murphy. A chloroquine-resistant Swiss 3T3 cell line with a defect in late endocytic acidification. *J Cell Biol*. 106:269-277 (1988).
29. R.A. Preston, R.F. Murphy, and E.W. Jones. Assay of vacuolar pH in yeast and identification of acidification-defective mutants. *Proc Natl Acad Sci U S A*. 86:7027-7031 (1989).
30. R.W. Van Dyke. Proton pump-generated electrochemical gradients in rat liver multivesicular bodies. Quantitation and effects of chloride. *J Biol Chem*. 263:2603-2611 (1988).
31. S.M. Felber and M.D. Brand. Factors determining the plasma-membrane potential of lymphocytes. *Biochem J*. 204:577-585 (1982).

32. S. Simon, D. Roy, and M. Schindler. Intracellular pH and the control of multidrug resistance. *Proc Natl Acad Sci U S A*. 91:1128-1132 (1994).
33. X. Zhang and G.R. Rosania. A virtual cell-based simulator for pharmaceutical project management, risk assessment and decision making., *Proceedings of the 4th International Conference on Computer Science and its Applications*, San Diego, CA, 2006, pp. 58-65.
34. K. Balon, B.U. Riebesehl, and B.W. Muller. Drug liposome partitioning as a tool for the prediction of human passive intestinal absorption. *Pharm Res*. 16:882-888 (1999).
35. W.N. Charman, C.J. Porter, S. Mithani, and J.B. Dressman. Physiochemical and physiological mechanisms for the effects of food on drug absorption: the role of lipids and pH. *J Pharm Sci*. 86:269-282 (1997).
36. G.R. Rosania, J.W. Lee, L. Ding, H.S. Yoon, and Y.T. Chang. Combinatorial approach to organelle-targeted fluorescent library based on the styryl scaffold. *J Am Chem Soc*. 125:1130-1131 (2003).
37. V.Y. Chen, S.M. Khersonsky, K. Shedden, Y.T. Chang, and G.R. Rosania. System dynamics of subcellular transport. *Mol Pharm*. 1:414-425 (2004).
38. M.M. Posada, K. Shedden, Y.T. Chang, Q. Li, and G.R. Rosania. Prospecting for live cell bioimaging probes with cheminformatic assisted image arrays (CAIA), *Proceedings of the 4th IEEE International Symposium on Biomedical Imaging*, 2007.
39. K. Shedden, J. Brumer, Y.T. Chang, and G.R. Rosania. Chemoinformatic analysis of a supertargeted combinatorial library of styryl molecules. *J Chem Inf Comput Sci*. 43:2068-2080 (2003).
40. V.Y. Chen, M.M. Posada, L.L. Blazer, T. Zhao, and G.R. Rosania. The role of the VPS4A-exosome pathway in the intrinsic egress route of a DNA-binding anticancer drug. *Pharm Res*. 23:1687-1695 (2006).
41. V.Y. Chen, M.M. Posada, L. Zhao, and G.R. Rosania. Rapid Doxorubicin Efflux from the Nucleus of Drug-Resistant Cancer Cells Following Extracellular Drug Clearance. *Pharm Res* (2007).
42. M. Duvvuri, W. Feng, A. Mathis, and J.P. Krise. A cell fractionation approach for the quantitative analysis of subcellular drug disposition. *Pharm Res*. 21:26-32 (2004).
43. Y. Gong, Z. Zhao, D.J. McConn, B. Beaudet, M. Tallman, J.D. Speake, D.M. Ignar, and J.P. Krise. Lysosomes contribute to anomalous pharmacokinetic behavior of melanocortin-4 receptor agonists. *Pharm Res*. 24:1138-1144 (2007).
44. P.V. Balimane and S. Chong. Cell culture-based models for intestinal permeability: a critique. *Drug Discov Today*. 10:335-343 (2005).
45. J.D. Irvine, L. Takahashi, K. Lockhart, J. Cheong, J.W. Tolan, H.E. Selick, and J.R. Grove. MDCK (Madin-Darby canine kidney) cells: A tool for membrane permeability screening. *J Pharm Sci*. 88:28-33 (1999).
46. C.M. McCloud, T.L. Beard, S. Kacew, and M.J. Reasor. In vivo and in vitro reversibility of chlorphentermine-induced phospholipidosis in rat alveolar macrophages. *Exp Mol Pathol*. 62:12-21 (1995).

47. M. Matsumoto, K. Funami, M. Tanabe, H. Oshiumi, M. Shingai, Y. Seto, A. Yamamoto, and T. Seya. Subcellular localization of Toll-like receptor 3 in human dendritic cells. *J Immunol.* 171:3154-3162 (2003).
48. T. Kawai and S. Akira. TLR signaling. *Semin Immunol.* 19:24-32 (2007).
49. S. Fletcher, K. Steffy, and D. Averett. Masked oral prodrugs of toll-like receptor 7 agonists: a new approach for the treatment of infectious disease. *Curr Opin Investig Drugs.* 7:702-708 (2006).
50. P. Cristofaro and S.M. Opal. Role of Toll-like receptors in infection and immunity: clinical implications. *Drugs.* 66:15-29 (2006).
51. J.P. Falgout, S. Desmarais, R. Oballa, W.C. Black, W. Cromlish, K. Khougaz, S. Lamontagne, F. Masse, D. Riendeau, S. Toulmond, and M.D. Percival. Lysosomotropism of basic cathepsin K inhibitors contributes to increased cellular potencies against off-target cathepsins and reduced functional selectivity. *J Med Chem.* 48:7535-7543 (2005).
52. P.R. van Ginkel, D. Sareen, L. Subramanian, Q. Walker, S.R. Darjatmoko, M.J. Lindstrom, A. Kulkarni, D.M. Albert, and A.S. Polans. Resveratrol inhibits tumor growth of human neuroblastoma and mediates apoptosis by directly targeting mitochondria. *Clin Cancer Res.* 13:5162-5169 (2007).
53. E. Jacotot, A. Deniaud, A. Borgne-Sanchez, Z. Touat, J.P. Briand, M. Le Bras, and C. Brenner. Therapeutic peptides: Targeting the mitochondrion to modulate apoptosis. *Biochim Biophys Acta.* 1757:1312-1323 (2006).
54. V.R. Fantin, M.J. Berardi, L. Scorrano, S.J. Korsmeyer, and P. Leder. A novel mitochondriotoxic small molecule that selectively inhibits tumor cell growth. *Cancer Cell.* 2:29-42 (2002).
55. G.G. D'Souza, S.V. Boddapati, and V. Weissig. Gene therapy of the other genome: the challenges of treating mitochondrial DNA defects. *Pharm Res.* 24:228-238 (2007).
56. V. Weissig and V.P. Torchilin. Mitochondriotropic cationic vesicles: a strategy towards mitochondrial gene therapy. *Curr Pharm Biotechnol.* 1:325-346 (2000).
57. G.G. D'Souza, R. Rammohan, S.M. Cheng, V.P. Torchilin, and V. Weissig. DQAsome-mediated delivery of plasmid DNA toward mitochondria in living cells. *J Control Release.* 92:189-197 (2003).
58. J.P. Overington, B. Al-Lazikani, and A.L. Hopkins. How many drug targets are there? *Nat Rev Drug Discov.* 5:993-996 (2006).
59. G.R. Rosania. Supertargeted chemistry: identifying relationships between molecular structures and their sub-cellular distribution. *Curr Top Med Chem.* 3:659-685 (2003).
60. M. Duvvuri, S. Konkar, K.H. Hong, B.S. Blagg, and J.P. Krise. A new approach for enhancing differential selectivity of drugs to cancer cells. *ACS Chem Biol.* 1:309-315 (2006).
61. W. Li, X.M. Yuan, S. Ivanova, K.J. Tracey, J.W. Eaton, and U.T. Brunk. 3-Aminopropanal, formed during cerebral ischaemia, is a potent lysosomotropic neurotoxin. *Biochem J.* 371:429-436 (2003).
62. P. Schneider. Drug-induced lysosomal disorders in laboratory animals: new substances acting on lysosomes. *Arch Toxicol.* 66:23-33 (1992).

63. B.P. Schmid, R.E. Hauser, and P. Donatsch. Effects of cyproheptadine on the rat yolk sac membrane and embryonic development in vitro. *Xenobiotica*. 15:695-699 (1985).
64. W.A. Daniel, J. Wojcikowski, and A. Palucha. Intracellular distribution of psychotropic drugs in the grey and white matter of the brain: the role of lysosomal trapping. *Br J Pharmacol*. 134:807-814 (2001).
65. J. Ishizaki, K. Yokogawa, M. Hirano, E. Nakashima, Y. Sai, S. Ohkuma, T. Ohshima, and F. Ichimura. Contribution of lysosomes to the subcellular distribution of basic drugs in the rat liver. *Pharm Res*. 13:902-906 (1996).
66. D. Drenckhahn, L. Kleine, and R. Lullmann-Rauch. Lysosomal alterations in cultured macrophages exposed to anorexigenic and psychotropic drugs. *Lab Invest*. 35:116-123 (1976).
67. M. Hetman, W. Danysz, and L. Kaczmarek. Increased expression of cathepsin D in retrosplenic cortex of MK-801-treated rats. *EXP NEUROL*. 147:229-237 (1997).
68. D. Pessayre, M. Bichara, C. Degott, F. Potet, J.P. Benhamou, and G. Feldmann. Perhexiline maleate-induced cirrhosis. *Gastroenterology*. 76:170-177 (1979).

CHAPTER IV

CELLS ON PORES: A SIMULATION-DRIVEN ANALYSIS OF TRANSCELLULAR SMALL MOLECULE TRANSPORT

Abstract

A biophysical framework for modeling cellular pharmacokinetics (1CellPK) is being developed for enabling prediction of the intracellular accumulation and transcellular transport properties of small molecules using their physicochemical properties as input. To demonstrate how 1CellPK can be used to generate quantitative hypotheses and guide experimental analysis of the transcellular transport kinetics of small molecules, epithelial cells were grown on impermeable polyester membranes with cylindrical pores. The effect of the number of pores and their diameter on transcellular transport of chloroquine (CQ) was measured in apical-to-basolateral or basolateral-to-apical directions, at pH 7.4 and 6.5 in the donor compartment. Experimental and simulation results with CQ support a cell monolayer-limited, passive diffusion transport mechanism. Consistent with 1CellPK simulations, CQ mass and the net rate of mass transport varied <2-fold although total pore area per cell varied >10-fold. Thus, by normalizing the net rate of mass by the pore area available for transport, cell permeability on 3 μ m pore diameter membranes appeared to be more than an order of magnitude less than on 0.4 μ m pore diameter membranes. Transcellular transport predictions remained accurate for the first four hours of drug exposure, but CQ mass accumulation predictions were accurate only for short CQ exposure times (5 minutes or

less). The kinetics and total mass of intracellular CQ indicates that CQ-induced lysosomal volume expansion does not fully account for the total intracellular CQ mass accumulation , especially in the basolateral-to-apical direction, although it can partly account for the gradual increase in CQ mass observed in apical-to-basolateral direction.

Keywords: Systems biology; Epithelial cells; Membrane transport; Mathematical models; Pharmacokinetics; Cell permeability

Introduction

The cell permeability of a small molecule (P_{cell}) is its rate of mass transport across an individual cell, as a function of the transcellular concentration gradient, normalized by the area over which transport occurs. P_{cell} is an important factor affecting the distribution of lipophilic nutrients (e.g. fat soluble vitamins), metabolites and signaling molecules (e.g. prostaglandins) inside and outside cells. P_{cell} can also influence the effects of lipophilic growth factors and morphogens (e.g. retinoids) affecting cell growth, differentiation, and motility. At the systemic level, P_{cell} can also affect the synthesis, uptake, distribution, metabolism and activity of lipophilic hormones (e.g. estrogen, testosterone), as well as that of xenobiotics and drugs.(1) Several different molecular mechanisms may mediate transcellular mass transport including passive diffusion across membranes and protein channels, ATP-dependent transmembrane carriers and transporter proteins, paracellular transport, and vesicle-mediated transcytosis.(2) Independently, the permeability of the matrix to which the cells are attached and the patterns - size and microscopic distribution of aqueous pores on this matrix - could affect the routes and rates of mass transport across cells.(2)

Here, we used a biophysical model (3, 4) to analyze the transcellular transport route of a small molecule. Certainly, cell-substratum interactions can affect cell morphology, differentiation, gene expression and apoptosis,(5-7) and can impose steric constraints to the passive diffusion of small lipophilic molecules. Hence, we tested how cell monolayer architecture, as well as apical-to-basolateral (AP→BL) and basolateral-to-apical (BL→AP) transport routes, may be influenced by the porosity properties of the underlying polyester membrane film to which cells are attached. For experiments, a

metabolically stable small molecule drug with high lipophilicity and high solubility (CQ) was used as a transport probe, while varying extracellular pH in drug donor or acceptor compartments. Our results demonstrate how a biophysical model like 1CellPK can be used to guide quantitative experimental analysis of transcellular transport properties of small molecules, potentially providing a framework for computational *ab initio* prediction of drug ADME properties.

Materials and Methods

Imaging of Cells on Pores.

Madin-Darby canine kidney (MDCK) cells were purchased from ATCC (CCL-34™) and maintained in DMEM (Gibco 11995) plus 10% FBS (Gibco 10082), 1X non-essential amino acids (Gibco 11140) and 1% penicillin/streptomycin (Gibco 15140), at 37°C with 5% CO₂. Transwell® inserts (12-well, pore size is 3µm or 0.4µm) were purchased from Corning Incorporated (Cat No. 3460 and 3462). For confocal microscopy, a Zeiss LSM 510 microscope (Carl Zeiss Inc.) was used for both membrane and cells imaging with a 60X water immersion objective. Inserts (with or without cells) were put directly in the wells of two-well Lab-Tek® II chamber #1.5 coverglasses (Nalge Nunc International Corp., Naperville, IL) for imaging. Cells were pre-stained with 5 µg/mL Hoechst 33342 (Molecular Probes H3570) for 30 minutes. LysoTracker® Green DND-26 (LTG, Molecular Probes L7526) and MitoTracker® Red (MTR, Molecular Probes M7512) were diluted with transport buffer (HBSS, 10mM HEPES, 25mM D-glucose, pH 7.4) to 2.5 µM and 1 µM respectively. The insert with cells was put onto the Lab-Tek® II chamber's cover glass. 1.5 mL of diluted dyes solution was added into the

chamber, and 0.5 mL of dyes free transport buffer was added into the apical compartment of the insert. After 10 minutes, the cells on the insert were imaged with the confocal microscope using enterprise laser (364 nm), argon laser (488 nm), helium neon 1 laser (543 nm) and the corresponding emission filters (BP 385-470, BP 505-530, and LP 560).

Polyester Membrane Permeability Analysis.

Polyester membranes without pores were purchased from AR Brown-US (One Oxford Centre 301 Grant Street, Ste: 4300, Pittsburgh, PA) and glued on the 12-well Transwell[®] inserts using ELMER's instant glue. Trypan blue was used to test the leakage of the edges. Transport experiments of CQ and LY (Lucifer yellow, Sigma L0144) were performed at 8 different initial concentrations ranging from 0 to 7500 μM .

Permeability Measurements of CQ on Membranes with MDCK Cells.

Cells were seeded on Transwell[®] inserts (12-well, polyester membranes with 3 μm or 0.4 μm pores) with density at least 2×10^5 cells/cm² for 1 or more days to form a monolayer. Transepithelial electrical resistance (TEER) values were measured both before and after transport experiments by Millipore Millicell[®] ERS. Cell monolayers were considered intact if both TEER values (background subtracted) were higher than 100 $\Omega \cdot \text{cm}^2$. CQ diphosphate (Sigma C6628) was dissolved in transport buffer, HBSS (Sigma H1387) without phenol red and sodium bicarbonate, supplemented with 25 mM D-glucose (Sigma G7021) and buffered with either 10 mM HEPES (pH 7.4) or 10 mM MES (pH 6.5). Inserts with cell monolayers were washed with drug free transport buffer (pH 7.4) twice, and then incubated for 20 minutes with 0.5 mL/1.5 mL transport buffer in apical/basolateral compartment (pH 7.4/7.4) respectively. After measuring TEER values,

0.5 mL/1.5 mL of CQ solutions (concentration ranges from 0-10 mM, pH 7.4 or 6.5) was added into the apical/basolateral compartment and 1.5 mL/0.5 mL of drug free buffer (pH 7.4) was added into basolateral/apical compartment. 0.75 mL/0.4 mL of the donor solutions was taken out and replaced with the same volume of drug free transport buffer (pH 7.4) every 30 minutes. Transport experiments were performed at 37 °C with shaking. Transport experiments were ended 4 hours after starting and both apical and basolateral solutions were collected for analyses. Every insert was washed twice with fresh buffer and TEER values were measured again. CQ concentration was determined with a standard curve, by absorbance measurement at 343 nm wavelength using a BioTek Synergy 2 plate reader (BioTek Instruments, Inc.).

Intracellular CQ Mass Measurements.

Cells on membrane inserts were quickly washed with buffer and then lysed 1% Triton X-100 in transport buffer (pH7.4, 1.5 mL) for 1.5 hours following 5 minutes to 4 hours CQ transport experiments in transwell inserts. CQ uptake was measured with 1mM concentration in the donor compartment The lysis solutions were centrifuged at 12,000 rpm for 8 minutes. CQ concentration was measured with the aid of a standard curve, by absorbance at 343 nm wavelength using BioTek Synergy 2 plate reader. To normalize the intracellular mass by the density of cells on membranes, cell counts were performed by staining the cells on inserts with Hoechst dye. Cells were then imaged by Nikon TE2000S epifluorescence microscope using a 20X objective at DAPI channel. At least five 12-bit images were taken for every insert. Cell counts were automated with an imaging algorithm programmed in Metamorph[®] software (Molecular Devices Corporation, Sunnyvale, CA).

CQ Binding Measurements.

Inserts were incubated with 1 mM CQ (pH 6.5 and pH 7.4) for 4 hours. Then inserts were washed with buffer for twice and incubated with 1.5 mL 1% Triton X-100 for 1.5 hours. The solution was centrifuged at 12,000 rpm for 8 minutes and CQ absorbance in the supernatant was measured at 343 nm and the concentration established with a standard curve. In order to measure the binding of CQ to MDCK cells, cells were permeabilized with 60 µg/mL digitonin in HBSS-HEPES buffer (pH 7.4) or 1% Triton X-100 for 5 minutes on ice. Cells then were stained with trypan blue and checked under microscope to ensure that more than 95% cells were permeabilized with digitonin or Triton X-100 based on the appearance of stained nuclei. Cells were diluted with buffer and the same volume of CQ solutions (pH 7.4) were added into cell solutions. The mixture solutions of cells and CQ were incubated at 4°C for 4 hours. The cells were centrifuged at 12,000 rpm for 8 minutes and the supernatant's CQ absorbance was measured at 343 nm. CQ concentration in the supernatant was then calculated with a standard curve. The difference of the initial CQ mass and the final CQ mass in the supernatant was used as a measure of CQ binding to cells.

Assessment of CQ Metabolism in MDCK Cells.

A 1200 Series HPLC system (Agilent Technologies, Santa Clara, CA) coupled with a QTRAP 3200 mass spectrometer (Applied Biosystems, Foster City, CA) was employed for chemical analysis. Separation was performed on a Zorbax RX-C18 column (5 µm, 150 mm × 2.1 mm) (Agilent Technologies, Santa Clara, CA). The isocratic elution profile was 35% (v/v) of aqueous solution containing 5 mM ammonium acetate and 0.1% formic acid and 65% (v/v) of MeOH, maintained for 2.5 minutes. The flow rate was 1

mL/min and injection volume was 10 μ L. An electrospray ionization source was used under positive ionization mode. Multiple reaction monitoring (MRM) scan was employed and ion transition is m/z 320.2 \rightarrow 247.2. Data acquisition and processing were performed using Analyst[®] software (Applied Biosystems, Foster City, CA). To construct the linear calibration curves, the mixed working standard solutions at each concentration (0, 51, 102, 204, 408, 816, 1020 ng/mL) were injected in triplicate. A 30 minutes gradient elution (the percentage of MeOH increased from 10% to 90% in 16 minutes and then maintained at 90% for additional 4 minutes and dropped to 10% at 21 minutes and maintained at 10% for another 9 minutes) and a full scan (m/z 150-500) were used to detect any possible metabolites of CQ. The MS parameters for full scan were similar with those of MRM scan except that CE is decreased to 20 units. The product ions of protonated CQ at m/z 179.1 and 247.1 were selected as the daughter ions for two precursor scans to detect the possible metabolites which also generate a product ion at m/z 179.1 or 247.1 or both of them. The scan range is m/z 150-800 and CE is 51 units. All the other LC and MS parameters of precursor scans were the same as those of full scan. Furthermore, based on a literature search,(8-10) 34 previously reported biotransformation processes were considered for CQ, such as mono- (+16 Da), di- (+32 Da), trihydroxylation (or oxidation) (+48 Da), dehydrogenation (-2 Da) and oxidative dechlorination (-18 Da). The 4 most abundant product ions (m/z 247.1, 179.1, 142.2 and 86.1) of protonated CQ were selected to generate 272 MRM scan channels by using Metabolite ID software (Applied Biosystems, Foster City, CA). With this method, no significant metabolism was detected through any one of the 34 possible CQ biotransformation processes.

Modeling CQ Transport.

In 1CellPK (3, 4) we modeled five compartments: apical, cytosolic, mitochondria, lysosomes, and basolateral compartment. Simulations consider compartment volumes, pH, and membrane potential, and areas as constant. Equations 4.1-4.4 are the concentration changing over time in each compartment express by net fluxes (J).

$$\frac{dC_c}{dt} = \frac{A_a}{V_c} J_{a,c} - \frac{A_m}{V_c} J_{c,m} - \frac{A_l}{V_l} J_{c,l} - \frac{A_b}{V_c} J_{c,b}, \quad (4.1)$$

$$\frac{dC_m}{dt} = \frac{A_m}{V_m} J_{c,m}, \quad (4.2)$$

$$\frac{dC_l}{dt} = \frac{A_l}{V_l} J_{c,l}, \quad (4.3)$$

$$\frac{dC_b}{dt} = \frac{A_b}{V_b} J_{c,b}, \quad (4.4)$$

In the above equations, C indicates the *total concentration*, J indicates the *flux*, A and V indicate the *membrane surface area* and *volume* respectively. The subscripts a , c , m , l , and b indicate *apical compartment*, *cytosol*, *mitochondria*, *lysosomes*, and *basolateral compartment* respectively. The directions of fluxes are indicated by the orders of the subscripts, e.g. $J_{c,m}$ represents the flux from cytosol to mitochondria. Equation (4.1) to (4.4) expressed apical to basolateral transport. Basolateral to apical transport can be easily derived. A molecule with two ionizable groups can be an ampholyte, a diacid or a dibase. In the case of CQ, it is a bivalent base and the pK_a values of the two ionizable groups are 7.47 and 9.96 calculated by ChemAxon[®]. Three main species exist in solutions with pH ranging from 0 to 14, the neutral form, ionized forms with one positive charge or two positive charges (Table 4.1). Thus the total flux across each membrane is contributed by those three species freely dissolved in solutions.

Considering membrane permeation as the main rate limiting step governing the intracellular distribution and transcellular transport of CQ, mass transport across the membranes delimiting each compartment can be calculated with Fick's equation and Nernst-Planck equation:

$$J_{o,i} = P_n(f_{n,o}C_o - f_{n,i}C_i) + P_{d1} \frac{N_{d1}}{e^{N_{d1}} - 1} (f_{d1,o}C_o - f_{d1,i}C_i e^{N_{d1}}) + P_{d2} \frac{N_{d2}}{e^{N_{d2}} - 1} (f_{d2,o}C_o - f_{d2,i}C_i e^{N_{d2}}) \quad , \quad (4.5)$$

where, subscripts *o* and *i* indicate *outer-* and *inner-* respectively. *o* could be *a*, *b* and *c*; *i* could be *a*, *c*, *m*, *l*, and *b*. Subscripts *n*, *d1*, and *d2* indicate *neutral form*, *ionized form with one charge*, and *ionized form with two charges*, respectively. *P* represents the *permeability across the bilayer membranes* of each species and can be calculated from lipophilicity (logP) of that species (11, 12); *f* is the calculated activity coefficient of each species that can be calculated as described previously (11, 12); $N = zEF/(RT)$, where $z = +1$ for N_{d1} (ionized base with one charge), and $z = +2$ for N_{d2} (ionized base with two charges); *E*, *F*, *R*, and *T* are *membrane potential*, *Faraday constant*, *universal gas constant*, and *absolute temperature*, respectively. Calculated logP values are 3.93, 0.43, and -0.91 for the neutral form, ionized form with one charge, and ionized form with two charges, respectively (Table 4.1), as calculated by ChemAxon[®]. After plugging in all parameters on the right hand of equation (4.1) to (4.4), the ordinary differential equations can be numerically solved. Once the concentration in the receiver compartment is calculated, the permeability of one cell (P_{cell}) can be calculated with equation 4.6:

$$P_{cell} = \frac{dC_r}{dt} \cdot \frac{V_r}{A_{pore} \cdot C_d} \quad , \quad (4.6)$$

Where, C_r and V_r are the *concentration in the receiver compartment* and *volume of the receiver compartment* respectively; A_{pore} is the *pore area underneath one cell*; and C_d is the *initial concentration* in the donor compartment. The effective permeability can be calculated by equation 4.7:

$$P_{app} = \frac{dC_r}{dt} \cdot \frac{V_r \cdot cellNo}{A_{insert} \cdot C_d}, \quad (4.7)$$

Where, $cellNo$ is the *total cell number per insert*, and A_{insert} is the *total area per insert*.

Monte Carlo Simulations.

Monte Carlo simulations were performed with MATLAB[®]. In 1CellPK the input parameters can be categorized into biological parameters and physiochemical parameters of the compounds. Physicochemical properties of CQ that used as input parameters are lipophilicity of neutral form and ionized forms with one or two charge ($\log P_n$, $\log P_{d1}$ and $\log P_{d2}$), and pK_a values of two ionizable groups (pK_{a1} and pK_{a2}). Biological parameters were apical membrane area (A_a), basolateral membrane area (A_b), mitochondrial membrane area (A_m), lysosomal membrane area (A_l), cytosolic volume (V_c), mitochondrial volume (V_m), lysosomal volume (V_l), volume of the receiver compartment (V_b for AP \rightarrow BL transport and V_a for BL \rightarrow AP transport), pH value in the donor compartment (pH_a for AP \rightarrow BL transport and pH_b for BL \rightarrow AP transport), pH value in the receive compartment (pH_b for AP \rightarrow BL transport and pH_a for BL \rightarrow AP transport), pH value in mitochondria and lysosomes (pH_m and pH_l), apical membrane potential (E_a), basolateral membrane (E_b), mitochondrial membrane potential (E_m), lysosomal membrane potential (E_l), lipid fraction in cytosol (L_c), mitochondria (L_m), and lysosomes (L_l), cell density, and pore density. Independent Monte Carlo simulations were performed

for pH 6.5 and pH 7.4, on 0.4 μ m- and 3 μ m- membranes, and in AP \rightarrow BL and BL \rightarrow AP transport directions. For each condition, 10,000 simulations were performed. In each simulation parameters were randomly sampled from uniform distributions (Table 4.2). Lipophilicity (logP) values for both neutral and ionized forms of CQ varied \pm 0.5 log units based on weighted method prediction provided by ChemAxon[®]. Boundaries of lysosomal volume were determined based on experimental measurements. Details of the calculations are described in legend of Table 4.2.

Measurement of Lysosomal Volume Changes.

MDCK cells were seeded on 96-well optical bottom glass-based plates (Nunc[™] Cat. 164588) at the density of 1×10^5 cells/cm² and let grown for 1 or 2 days in 150 μ L fully supplemented DMEM. CQ diphosphate was dissolved in DPBS buffer (Gibco 14190) to a final concentration of 50 mM and diluted in cell culture medium to 50 μ M. Cells were incubated with 150 μ L DMEM-CQ for 3.5 hours. LTG was added to CQ-treated and untreated cell culture to a final concentration of 0.5 μ M for another 30 minutes incubation. For fluorescence microscopy, a Nikon TE2000S microscope with a 100X oil immersion objective was used to image the lysosomes using the FITC filter set. Image analysis was carried out with MetaMorph[®] software. In calibration experiments, we determined this system could accurately resolve and measure objects >200 nm diameter, using fluorescent bead standards (Molecular Probes T14792) ranging from 100 to 4000 nm diameters. We also determined the objective was capable of capturing fluorescent signals within 2 μ m vertical spaces. For analysis, images were background subtracted, and each individual lysosome vesicle of each individual cell was manually outlined with the Circular Region Tool. Next, assuming spherical shape, the diameter of each

individual lysosome was estimated from the area of the regions. Because the height of cell monolayer was estimated to be 5-10 μm (Figure 4.1) and the depth of the focal plane is in the order of 2 μm , the total number of lysosomes associated with one cell was calculated by multiplying the region count by a factor of 2.5. The average diameter and total number of lysosomes in treated and untreated cells was calculated as the average value of those acquired from at least 5 images under the corresponding condition.

Lysosomal pH Measurements.

MDCK cells were seeded on 96-well optical bottom polymer-based plates (Nunc™ Cat. 165305) at the density of 1×10^5 cells/cm² and let grown for 1 to 2 days in 150 μL fully supplemented DMEM. FITC-dextran (FD, Sigma FD150S) was dissolved in DPBS buffer to a final concentration of 10mg/mL and diluted in cell culture medium to 0.2 mg/mL. Cells were incubated with 150 μL DMEM-FD for 24 hours to allow cell uptake of FD via endocytosis. To measure lysosomal pH during 50 μM CQ treatment, cells were washed twice with 100 μL DPBS buffer before incubation in 150 μL FD-free medium with or without CQ. At the end of 1 to 4 hours incubation, cells were washed with 100 μL DPBS buffer twice, immersed in 150 μL buffer, and scanned for fluorescent signal with BioTek Synergy 2 plate reader using Ex.485/20 and Em.528/20 filter set as well as Ex.450/50 and Em.528/20 filter set. For pH standard curves, FD pretreated cells were washed with 100 μL DPBS buffer twice, immersed in 150 μL DPBS-based solutions (pH 3 to 10) with 10 $\mu\text{g}/\text{mL}$ Nigericin (Sigma N7143), let equilibrate for 10 minutes and scanned for fluorescent signal with the same settings. Background fluorescence from MDCK cells without FD treatment was also recorded after wash. The fluorescence ratio (FR) was calculated based on equation 8:

$$FR = \frac{F485_i - F485_{bg}}{F450_i - F450_{bg}} \quad (4.8)$$

where $F485_i$ and $F450_i$ stand for integrated fluorescent intensity from the i^{th} well of cells under Ex.485 nm and Ex.450 nm, respectively, and subscript bg indicates background fluorescence signal without FD treatment. FR values were plotted against known pH values to create a standard curve, or compared with the standard curve to calculate the lysosomal pH.

Results

Microscopic Analysis of Cells on Polyester Membranes.

Optically-transparent track-etched polyester membranes of similar membrane thickness ($\sim 10 \mu\text{m}$) were used for experiments. The fractional pore area of the $3\mu\text{m}$ -membranes was about 28 times higher than the $0.4\mu\text{m}$ -membranes based on the manufacturer's specification, and >10 times higher based on our measurements (Figure 4.1). TEER values of $0.4\mu\text{m}$ -membrane was similar to that of $3\mu\text{m}$ -membranes (mean \pm SD: 126 ± 8 vs. $118 \pm 9 \Omega \cdot \text{cm}^2$, $n = 8$; p value = 0.0784). MDCK cells grown on polyester $0.4\mu\text{m}$ - or $3\mu\text{m}$ -membranes formed regular monolayers (Figure 4.1). No difference in monolayer architecture was visually apparent on $0.4\mu\text{m}$ - and $3\mu\text{m}$ -membranes. TEER value of cells grown on $0.4\mu\text{m}$ - membrane was higher than on $3\mu\text{m}$ -membrane (mean \pm SD: 221 ± 16 vs. $117 \pm 16 \Omega \cdot \text{cm}^2$, $n = 48$, background subtracted; p value $< 10^{-4}$). This behavior can be explained by the difference in pore area available for transport or by differences in tightness of intercellular junctions. Seeded at the same density ($2 \times 10^5 \text{ cells/cm}^2$) and grown for two days, the cell number on $0.4\mu\text{m}$ -membrane

was slightly higher than the cell number on 3 μ m-membrane (mean \pm SD: $4.9 \times 10^5 \pm 6.4 \times 10^4$ vs. $3.9 \times 10^5 \pm 4.5 \times 10^4$, n = 8), which almost corresponded to the difference in surface area available for cell attachment (Figure 4.1). We did not observe any MDCK cells migrating through the pores.

CQ Transcellular Transport Is Nonsaturable and Directly Proportional to the Transcellular Concentration Gradient.

CQ and Lucifer Yellow (LY) transport across polyester membranes without pores is negligible: in the absence of pores, the amount of CQ or LY in the receiver compartment was undetectable after a 6 hour transport experiment (data not shown). Therefore, transport of small molecules across cell monolayers on nucleopore polyester membranes is driven primarily by the flux of molecules through the pores (not through the polyester film). On 0.4 μ m- and 3 μ m-membrane, CQ mass transport rate linearly correlated with the initial concentration in the donor compartment at pH 7.4 or 6.5, both over low concentration range (Figure 4.2) and even at higher concentrations (data not shown). The intercepts of the regression lines were all zero, after statistical testing for the intercept values. LY, a hydrophilic, cell membrane-impermeant small molecule, was used as a control probe to assess paracellular transport. Average apparent permeability of LY (AP \rightarrow BL) was 0.70 ± 0.33 nm/sec (mean \pm SD, n = 27) and 1.7 ± 2.1 nm/sec (mean \pm SD, n = 23) measured on MDCK cells grown on 0.4 μ m- and 3 μ m-membranes, respectively (p value = 0.0273) with an apical pH value of 7.4. This is consistent with LY transport occurring mostly through a paracellular route. The P_{app} of CQ was approximately two orders of magnitude greater than the P_{app} of LY. We conclude that CQ traverses MDCK

cells mainly through a transcellular pathway, with the rate of transport being directly proportional to the concentration gradient in either AP → BL or BL → AP directions.

Effects of pH and Pore Geometry on CQ Transport Routes and Cellular Uptake in AP → BL or BL → AP Directions.

Comparing cells on 3 μ m- or 0.4 μ m-diameter pore membranes was used to study how differences in the porosity of the substratum can affect the transport route small molecules through epithelial cells (Figure 4.2). Comparing the regression coefficients, if the other conditions are the same (such as the pH and the transport direction), the mass transport rate of CQ on 3 μ m diameter pore membranes was only slightly greater (< 2-fold) than on 0.4 μ m-membranes. However, the total pore area of the 3 μ m diameter pore membranes is >10-fold greater than that of a 0.4 μ m-membrane. If P_{cell} was an intrinsic, invariant property of the cells, one would have expected the mass transport rate to be directly proportional to the total pore area available for transport. Thus, P_{cell} is greatly affected by the porosity of the substratum.

CQ is a weak base, with two amine groups that can be protonated within physiological pH values. The fraction of CQ with two charges is higher at pH 6.5 relative to pH 7.4 (Table 4.1). Conversely, the proportion of neutral CQ species is higher at pH 7.4 than at pH 6.5. Consistent with transmembrane transport being a function of the charge and lipophilicity of CQ, the pH of the donor compartment exerted a major effect on CQ transcellular transport rate (Figure 4.2) with the rate of transport at pH 7.4 being seven times greater than that at pH 6.5, as expected based on transmembrane diffusion being the rate limiting step of CQ transport across cells.

For CQ, the BL \rightarrow AP transport rate is only slightly higher than AP \rightarrow BL transport rate for the same pH values and same membranes. Linear relationship of transport rate with initial concentration in the donor compartment was observed as well. Thus, unidirectional active transport mechanisms cannot be invoked to explain CQ transport across MDCK cells. Overall, the experiments are consistent with passive diffusion and transmembrane gradients being primarily responsible for driving the bulk of CQ transport across MDCK cells.

During transport experiments, intracellular mass accumulation of CQ was linearly correlated with the initial concentration when the concentration in the donor compartment was lower than 1 mM and reached a plateau when the concentration in the donor compartment was higher (Figure 4.3) after 4 hours exposure to the drug. This plateau was related to cytotoxicity of CQ at high concentrations, apparent as nuclear shrinkage, chromatin condensation and cell monolayer disintegration (Figure 4.4). At pH 6.5, the CQ accumulation plateau is reached when the apical concentration is higher than 8 mM for AP \rightarrow BL transport (Figure 4.3A); however the plateau is reached when the basolateral concentration is higher than 2 mM (Figure 4.3B). When the pH is 7.4, the plateau is reached when the concentration in the donor compartment is higher than 1 mM for both AP \rightarrow BL and BL \rightarrow AP transport (Figure 4.5C and 4.5D). This pH sensitivity of the intracellular accumulation is consistent with higher CQ lipophilicity at higher apical pH values, leading to greater influx from the donor compartment into the cytosol, and presumably, higher cytosolic concentration. Comparing AP \rightarrow BL transport with BL \rightarrow AP transport for the same conditions, the intracellular accumulation is similar for pH 6.5 and pH 7.4 (Figure 4.5). Intracellular accumulation of CQ on 3 μ m-membranes and

0.4 μ m- membrane is similar for the same conditions (Figure 4.5), except for BL \rightarrow AP transport when pH = 7.4 (Figure 4.5D) where it is slightly different (which could be due to an experimental measurement outlier, evident in the larger error bars).

Simulation-Driven Quantitative Analysis of CQ Transport and Uptake.

Monte Carlo simulations were used to assess the effect of measurement variability, experimental errors and other uncertainties in the input variables of the 1CellPK model, on the calculated mass transport rate (dM/dt ; Figure 4.5A) , P_{cell} (Figure 4.5B), P_{app} , (Figure 4.5C) and intracellular mass accumulation (Figure 4.5D). Because of the observed toxicity occurring upon 4h exposure to CQ (Figure 4.3 and 4.4) mass accumulation of CQ was measured after 5 minutes incubation with 1mM CQ in the donor compartment. Results showed that CQ uptake after 5 minutes incubation (Figure 4.5D, red lines) is much lower than that after 4 hours transport experiment (Figure 4.3) under the same conditions.

For simulations, the apparent permeability (P_{app}) was calculated from measured dM/dt by normalizing over the initial concentration in the donor compartment and the total insert area. Unlike P_{cell} measurements which normalize mass transport rate over the aqueous pore area of the polyester membrane, P_{app} measurements normalize the mass transport rate over both pore and non-pore regions of the polyester membrane. Comparing permeability normalized by the pore area (P_{cell} ; Figure 4.5B, red lines) with the permeability normalized by total insert area (P_{app} ; Figure 4.5C, red lines), P_{cell} of CQ on 0.4 μ m-membrane is at least an order of magnitude higher than that on 3 μ m-membrane. However, P_{app} of CQ on 3 μ m-membrane is only slightly higher than on 0.4 μ m-membrane (<2-fold). Per cell, the total pore area on 3 μ m-membrane is more than

an order of magnitude greater than on 0.4 μ m-membrane. Arguably, P_{cell} most accurately reflects a difference in the actual flux of CQ molecules across the basolateral membrane of cells on 0.4 μ m- vs. 3 μ m-membrane, at the single cell level. Most importantly, for dM/dt , P_{cell} , and P_{app} , most of measured values fall between 10% and 90% quantiles of simulated distributions, and very close to the median (Figure 4.5A-C and Table 4.3). Simulations also capture the CQ uptake after 5 minutes incubation for AP \rightarrow BL transport (Figure 4.5D, rows 1 – 4 and Table 4.3), although measured CQ uptake in the BL \rightarrow AP direction was greater than predicted by the model (Figure 4.5D, rows 5 – 8 and Table 4.3).

Probing the Mechanisms of Mass Accumulation upon Prolonged CQ Exposure.

Although the initial input parameters for the simulations yielded dM/dt , P_{cell} , P_{app} values and CQ uptake after 5 minutes incubation consistent with experimental measurements, they consistently underestimated the intracellular mass of CQ after 4 hours transport experiment (Figure 4.7A). Based on the simulation, intracellular CQ mass should reach steady state levels by 5 min incubation, but this was not observed experimentally (Figure 4.7A). We also found that binding of CQ to detergent-extracted (triton-treated) or permeabilized (digitonin-treated) cells was much lower than its measured cellular uptake at 37°C (Figure 4.6). Measurements on triton-extracted cells indicated that the high, measured intracellular CQ mass was not due to DNA binding or to absorption to insoluble proteins or cytoskeletal elements. CQ binding to digitonin-permeabilized cells is similar to that of triton-extracted cells, so CQ binding to soluble proteins, to intracellular membranes or to lipid droplets cannot account for the missing intracellular

mass. Biochemical analysis with LC/MS reveals no metabolites of CQ, with all the intracellular CQ present in intact form (data not shown).

CQ is a weakly basic molecule that accumulates in lysosomes through an ion trapping mechanism dependent on the acidic microenvironment (pH 4.5 to 5.5) of lysosomes. CQ incubation gradually expanded the lysosomal compartment in MDCK cells (Figure 4.7B). The average number of lysosomes per cell was slightly lower in CQ-treated cells as compared with untreated cells: 200 ± 35 ($n = 6$) vs. 253 ± 45 ($n = 5$) (mean \pm SD, p -value = 0.059). However, the diameter of lysosomes is significantly increased in treated cells in comparison with untreated cells: $1.74 \pm 0.19 \mu\text{m}$ ($n = 6$) vs. $0.50 \pm 0.03 \mu\text{m}$ in untreated cells ($n = 5$) (mean \pm SD, p -value = $7.8\text{E-}12$). The total lysosomal volume is $16.5 \mu\text{m}^3$ in untreated cells and $551.4 \mu\text{m}^3$ after 4 hours treatment with $50 \mu\text{M}$ CQ. Overall, there was a 33.5-fold increase in the total lysosomal volume. The measured lysosomal pH of untreated cells was 5.03 ± 0.18 (mean \pm SD, $n = 4$) and the lysosomal pH of CQ-treated cells slowly increased from 5.2 ± 0.2 at 1 hour incubation to 6.0 ± 0.3 at 4 hour incubation (mean \pm SD, $n = 6$).

Given that CQ exposure alters the lysosomal volume and pH over a 4 hour period, simulations were repeated with an average lysosomal pH value of 5.5 and an expanded lysosomal volume (Figure 4.7C). The experimental measured intracellular mass accumulation of CQ was extrapolated down to $50 \mu\text{M}$ CQ using the regression equations in Figure 4.3 for different conditions. After taking lysosomal swelling and pH increase into account, the predicted intracellular CQ mass is closer to experimental measurement for AP \rightarrow BL transport with pH 7.4 in apical compartment. However, in BL \rightarrow AP transport, the measured intracellular accumulation of CQ still exceeded the simulated

distributions by more than an order of magnitude, at least as much as was observed during the shorter, 5 minutes exposure (Figure 4.5D).

Discussion

In this study, a mathematical model (11-13) was employed to analyze the transport route of CQ across an MDCK monolayer, while studying how extracellular pH, substratum porosity, and transcellular concentration gradients affected the drug's transport behavior. In the computational simulations, pore size and density effects on P_{cell} can be largely accounted for as a steric constraint on the basolateral membrane surface area (A_b) and the effective cell cross sectional area (A_{aa}) over which flux effectively occurs. Biological variability, experimental errors, and other uncertainties (such as the effective basolateral surface area over which transport takes place, and the absolute concentration and permeability of different ionic species of CQ at any given pH) may lead to variations in experimental measurements and predictions. Monte Carlo simulations were used to account for parameter variations and uncertainties in input variables, yielding probabilistic distributions of 1CellPK results that were reasonably accurate with respect to experimental measurements.

In the 1CellPK model, CQ is postulated to undergo very fast (instantaneous) mixing within the each subcellular compartment, with the transport of CQ across cellular membranes being the rate-limiting step determining the net rate of mass transport across the cell monolayer. Both simulations and experiments are consistent with CQ traversing MDCK cell monolayers via a passive, transcellular membrane-limited diffusion route. However, discrepancies between CQ uptake measured after 4 hour incubations and model predictions point to a physiological mechanism responsible for the gradual intracellular

mass accumulation of CQ that is not captured by the model. Experimentally, CQ accumulated intracellularly to a level higher than expected by lipid partitioning, macromolecular binding, ion trapping or membrane potential dependent sequestration in cytosol, lysosomes or mitochondria –all of which were included in the 1CellPK model or were controlled for in the experimental measurements. Other amine-containing molecules also accumulate to very high concentrations inside cells(14). CQ induced a gradual but significant increase in lysosomal volume in MDCK cells.

One of the limitations of 1CellPK is that the compartment volumes, pH, membrane potentials are fixed and constant from the start of the simulations. Thus gradual biological effects of a drug on cell physiological parameters are not readily taken into account. Nevertheless, by using an expanded lysosomal volume (and an increased lysosomal pH) as input, simulations revealed that this lysosomal volume change can account for a significant increase in the total intracellular CQ mass especially in the AP \rightarrow BL with pH 7.4 (Figure 4.7C). In BL \rightarrow AP direction, the volume expansion cannot fully account for the additional mass, so an unknown factor affecting higher-than-expected BL \rightarrow AP mass sequestration remains to be identified. Another plausible reason that leads to under-prediction could be missing of cations and acidic phospholipids interactions, which could be dominant for moderate to strong basic drugs (15) because the ionic species are the major forms at physiological pH. In order to test how the electrostatic interactions would affect predictions, the lipid partitioning coefficient for ionic species, $\log K_d = 2.3$, was used in Monte Carlo simulations in stead of $\log P_{d1} = 0.43$ and $\log P_{d2} = -0.91$ in equation 2.17. $\log K_d$ was estimated using digitonin experiments data as the following: (1). Get the slopes of pmol/cell vs. CQ concentration in

the supernatant. Pool them together and the mean = 1.0×10^{-5} (pmol/cell : μM); (2). Assume cell volume = $10^3 \mu\text{m}^3$ and lipid fraction = 5% in each compartment. (3). $K_d = C_{\text{cell pellet}}:CQ \text{ in supernatant} = 1.0 \times 10^{-5} / (1000 \times 5\%) \times 10^9 = 190$, thus $\log K_d = 2.3$. Comparison of simulation and experimental measurement of intracellular accumulation of CQ after 4 hours accumulation is shown in Figure 4.8. After considering the electrostatic interactions, predictions for AP \rightarrow BL intracellular uptake are close to measurements (red lines) after 4 hours simulation. After considering the electrostatic interactions, lysosomal swelling effects, and intralysosomal pH increment, predictions are close to measurement for all conditions. Thus our hypothesis is that under-prediction could be explained by missing of interactions between cations and acidic phospholipids. And the experiments will be designed to measure the partitioning of cations into acidic phospholipids.

As related to drug discovery and development, permeability measurements, including *in vitro*, *in situ*, and *in vivo* methods are low throughput and costly.(16-18) Permeability assays on cell monolayers are usually done *in vitro*, growing cells on semi-permeable support membranes, and monitoring the rate of mass transport across the membranes, through time.(19-21) Cell permeability measurements often show huge variability between laboratories.(22, 23) and many factors have been proposed to contribute to these experimental variations. Indeed, mathematical models are being increasingly used to facilitate empirical interpretation of cell-based transport mechanisms (24, 25). The ability to make predictions by using a molecule's physicochemical properties (e.g. $\log P$ and pK_a) as input may allow 1CellPK to be applied at the earliest

phases of drug development, to facilitate the rational design of drug candidates with the most desirable, cellular pharmacokinetic characteristics (3, 4, 13).

To conclude, although the interplay between the physicochemical properties of small molecules and their cellular transport and disposition mechanisms are complex, they can be analyzed quantitatively with the aid of mathematical models.^{(13),23,24} As our analysis demonstrates, 1CellPK is a good starting point for formulating mechanism-based, quantitative hypotheses to guide additional experimental design to further refine our understanding of transcellular transport and subcellular distribution in the presence of a transcellular concentration gradient. The 1CellPK model can capture the effects of cell biological variables (pH values in donor and receiver compartment, pore size and density of the support filter, transmembrane concentration gradients, organellar volumes and pH) on small molecule transport mechanisms. To test 1CellPK, cells on pores can be used to manipulate intracellular transport routes of small molecules while minimally perturbing cellular biochemistry. In future experiments, more precise patterning of pore number and geometry should allow more detailed exploration of the phenotypic effects of spatial gradients of small molecules inside individual epithelial cells in a monolayer. In addition, with the Michaelis-Menten equation, transporters or enzymatic mechanisms can be incorporated into the model, to capture their phenotypic effects on transcellular transport routes.

Table 4.1. Calculated distribution and logP values for each microspecies of CQ at pH 6.5 and pH 7.4, used as input for 1CellPK. The numbers 7.47 and 9.96 correspond to the pK_a values of the protonation sites of the molecule, calculated by ChemAxon[®].

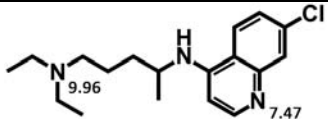
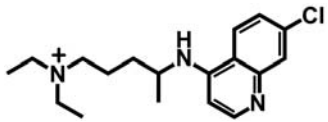
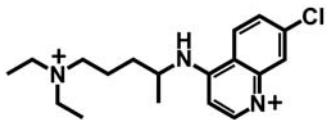
Structure	calculated logP	fraction at pH6.5 (%)	fraction at pH7.4 (%)
	3.93	0.00	0.04
	0.43	5.49	31.55
	-0.91	94.49	68.33

Table 4.2. Parameter ranges for Monte Carlo simulations.

$\log P_n$	[3.43, 4.43]
pK_{a1}	[9.46, 10.46]
pK_{a2}	[6.97, 7.97]
$\log P_{d1}$	[-0.07, 0.93]
$\log P_{d2}$	[-1.41, -0.41]
cell number / insert	$[2 \times 10^5, 4 \times 10^5]$
pore density	$[3.2 \times 10^6, 4.8 \times 10^6]$ for membranes with $0.4 \mu\text{m}$ pores
(pore number / cm^2)	$[1.6 \times 10^6, 2.4 \times 10^6]$ for membranes with $3 \mu\text{m}$ pores
$A_a (\mu\text{m}^2)$	[100, 1000]
$A_{\text{insert}} (\text{cm}^2)$	1.12
$A_{\text{pore}} (\mu\text{m}^2)$	$\text{average pore area/cell} = \frac{\text{cell number/insert}}{\text{pore density} \times A_{\text{insert}}} \times \text{area of single pore}$
$A_b (\mu\text{m}^2)$	$[A_{\text{pore}}, 100]$
$V_c (\mu\text{m}^3)$	[500, 3000]
^b $V_l (\mu\text{m}^3)$	$[9.24, 23.8] / [196.5, 906.3]$
$V_m (\mu\text{m}^3)$	[10.48, 262]
^a $A_l (\mu\text{m}^2)$	314
^a $A_m (\mu\text{m}^2)$	314
^a $V_b (\mu\text{m}^3)$	1.5mL for AP->BL transport, volume of donor compartment 0.5mL for BL->AP transport, volume of donor compartment
$E_a (\text{mV})$	[-14.3, -4.3]
$E_l (\text{mV})$	[5, 15]
$E_b (\text{mV})$	[6.9, 16.9]
^a $E_m (\text{mV})$	-160mV
pH_c	[7.0, 7.4]
^c pH_l	$[4.8, 5.2] / [4.63, 6.37]$
pH_m	[7.8, 8.2]
pH_a	[7.0, 7.4] for $\text{pH}=7.4$ in the donor compartment [6.4, 6.6] for $\text{pH}=6.5$ in the donor compartment
L_c	[0.05, 0.15]
L_m	[0.05, 0.15]
L_l	[0.05, 0.15]
^a $\text{pH}_{a/b}$	7.4; pH value in the receiver compartment

^a indicates parameters that do not influence permeability or intracellular accumulation calculations shown by performing parametric studies

^b Uniform distribution upper and lower boundaries for lysosomal volume were calculated based on experimental measurement and calculated as described below. The measured lysosomal volume was calculated by equation (s)E1 using measured number and diameter of lysosomes.

$$V_l = n \times \left(\frac{1}{6} \pi (d)^3\right), \text{ (s)E1}$$

where n is the number of lysosomes / cell, and d is the diameter of a lysosome. The average number of lysosomes per cell was 200 ± 35 ($n = 6$) and 253 ± 45 ($n = 5$) for treated (50 μ M CQ for 4hours) and untreated cells, respectively. The diameter of lysosomes was $1.74 \pm 0.19 \mu\text{m}$ ($n = 6$) and $0.50 \pm 0.03 \mu\text{m}$ ($n = 5$) for treated (50 μ M CQ for 4hours) and untreated cells, respectively. Thus the measured lysosomal volume was 551.4 ± 204.9 and $16.5 \pm 4.19 \mu\text{m}^3$ (mean \pm SD) for treated and untreated cells, respectively. The standard deviation of lysosomal volume was estimated by equation (s)E2 (partial derivative method for error propagation estimation) (25) assuming there is no correlation between n and d .

$$SD_{V_l} = \sqrt{\left(\frac{\partial V_l}{\partial n}\right)^2 SD_n^2 + \left(\frac{\partial V_l}{\partial d}\right)^2 SD_d^2}, \text{ (s)E2}$$

The equations (s)E3 and (s)E4 were applied to calculate the upper (b) and lower (a) boundaries of the uniform distribution of V_l .

$$\text{mean} = \frac{1}{2}(a + b), \text{ (s)E3}$$

$$\text{variance} = \frac{1}{12}(b - a)^2, \text{ (s)E4}$$

By plugging in the above measurement, uniform distribution [9.24, 23.8] and [196.5, 906.3] μm^3 were used for V_l for untreated and treated cells, respectively.

^c Uniform distribution upper and lower boundaries of lysosomal pH for Monte Carlo Simulations with CQ-expanded lysosomal volume (Figure 4.7) were calculated as the following. The measured mean value and maximum standard deviation are 5.5 and 0.5, respectively. Thus the variance is 0.25. The upper (b) and lower (a) boundaries of the distributions were calculated from equations (s)E3 and (s)E4, which are derived for uniform distribution probability function. Thus uniform distribution [4.63, 6.37] was set for pH in lysosomes of cells under 50 μ M CQ treatment.

Table 4.3. Simulation and quantitative experimental data of CQ transport across MDCK cells on polyester membranes of varying porosity, at donor compartment pH 6.5 and 7.4. The prefix ‘sim.’ indicates simulation data corresponding to 10%, 50%, and 90% quantiles of simulated dM/dt (10^{-6} pmol/sec/cell), P_{cell} (10^{-6} cm/sec), P_{app} (10^{-6} cm/sec) and intracellular mass accumulation (10^{-3} pmol/cell) after 5 minutes incubation, using the parameters in Table 4.2 (non-lysosomal swelling cells). The prefix ‘exp.’ indicates the experimental data.

	pH = 6.5, 0.4 μ m			pH = 6.5, 3 μ m			pH = 7.4, 0.4 μ m			pH = 7.4, 3 μ m		
	10%	50%	90%	10%	50%	90%	10%	50%	90%	10%	50%	90%
A. overall effects of parameters (AP→BL)												
sim.dM/dt	1.78	7.75	23.7	5.00	12.0	31.3	11.7	54.7	229	29.2	91.8	321
exp.dM/dt	2.20 ± 0.718			5.19 ± 1.01			22.8 ± 0.741			46.6 ± 6.28		
sim.P _{cell}	91.0	407	1264	9.26	22.6	59.7	602	2904	12401	54.1	172	612
exp. P _{cell}	218 ± 34.4			14.0 ± 3.33			1560 ± 161			85.9 ± 15.6		
sim.P _{app}	0.455	2.04	6.24	1.31	3.17	8.35	3.04	14.5	62.3	7.64	23.9	84.4
exp.P _{app}	1.35 ± 0.442			1.98 ± 0.471			7.85 ± 0.810			12.1 ± 2.21		
sim.mass	0.490	1.04	2.16	0.451	0.971	2.03	3.14	7.61	18.0	2.99	7.23	17.8
exp.mass	3.73 ± 0.14			1.88 ± 0.54			8.72 ± 0.94			8.90 ± 0.26		
B. overall effects of parameters (BL→AP)												
sim.dM/dt	1.70	7.42	22.9	4.88	12.0	30.9	10.7	52.9	214	27.2	84.6	309
exp.dM/dt	5.25 ± 1.24			7.12 ± 0.473			29.4 ± 1.54			63.8 ± 15.9		
sim.P _{cell}	85.4	390	1228	9.10	22.3	58.9	548	2767	11616	50.8	159	585
exp. P _{cell}	382 ± 81.7			15.8 ± 2.45			2000 ± 353			114 ± 19.0		
sim.P _{app}	0.439	1.96	6.19	1.28	3.13	8.18	2.77	13.8	57.4	7.11	22.4	82.3
exp.P _{app}	1.92 ± 0.411			2.24 ± 0.346			10.0 ± 1.77			16.2 ± 2.69		
sim.mass	0.020	0.091	0.309	0.060	0.151	0.425	0.137	0.679	2.56	0.378	1.11	3.56
exp.mass	3.52 ± 0.93			4.94 ± 1.06			8.28 ± 0.75			11.8 ± 1.9		

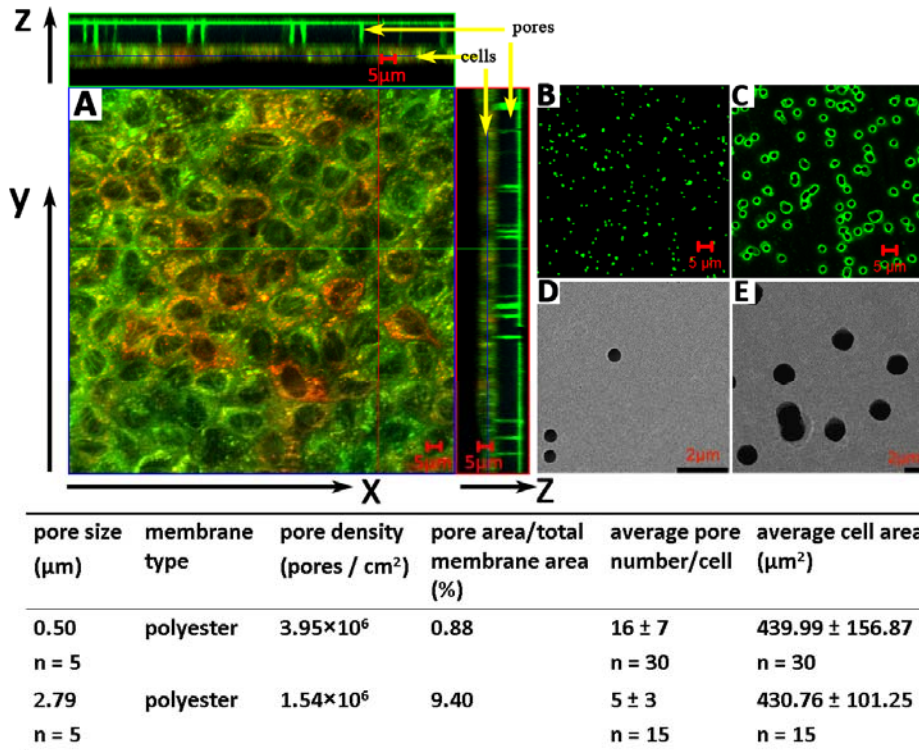


Figure 4.1. Microscopic images of polyester membranes and MDCK cells grown on a 0.4μm-membrane. (A) shows orthogonal planes of 3D reconstructions of MDCK monolayers grown on a polyester membrane with 0.4 μm pores. Cells were stained with LTG, MTR and Hoechst and imaged as detailed in the methods. (B) and (C) show confocal microscope images of membranes with 0.4μm- and 3μm- pores, respectively. (D) and (E) are scan electron microscope (SEM) images of membranes with 0.4μm - and 3μm- pores, respectively. The table details microscopic measurements of pore geometry, density and cell monolayer characteristics, as analyzed in this study.

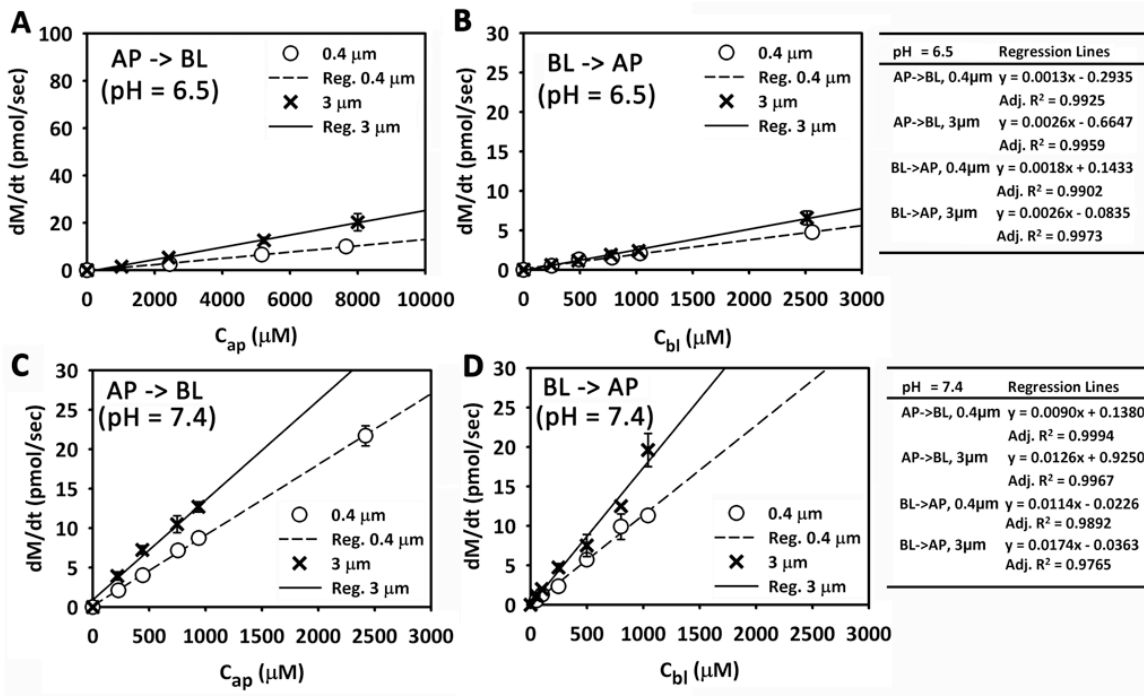


Figure 4.2. The relationship between mass transport rate and the initial concentration of CQ in the donor compartment. (A) represents AP → BL transport (pH_a = 6.5), and (B) represents BL → AP transport (pH_b = 6.5). (C) represents AP → BL transport (pH_a = 7.4), and (D) represents BL → AP transport (pH_b = 7.4). The linear regression equations are included in the tables.

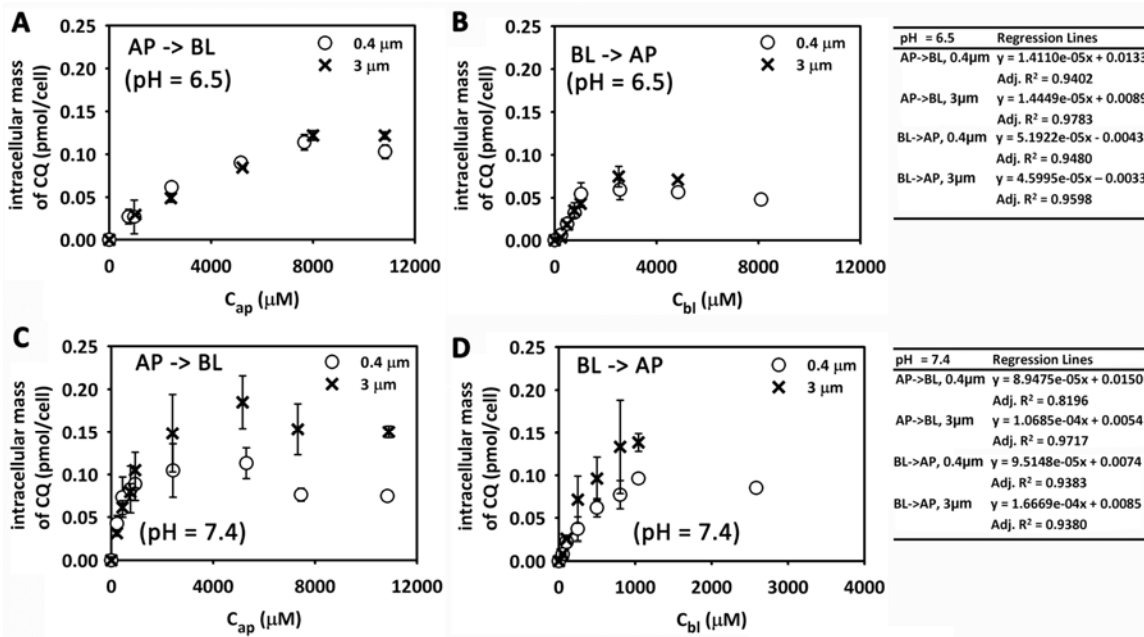


Figure 4.3. The relationship between intracellular CQ mass and the initial concentration of CQ in the donor compartment. (A) represents AP → BL transport ($pH_a = 6.5$), and (B) represents BL → AP transport ($pH_b = 6.5$). (C) represents AP → BL transport ($pH_a = 7.4$), and (D) represents BL → AP transport ($pH_b = 7.4$). The linear regression equations shown in the table (right) were obtained by performing regressions on the data obtained from the four lowest concentrations tested.

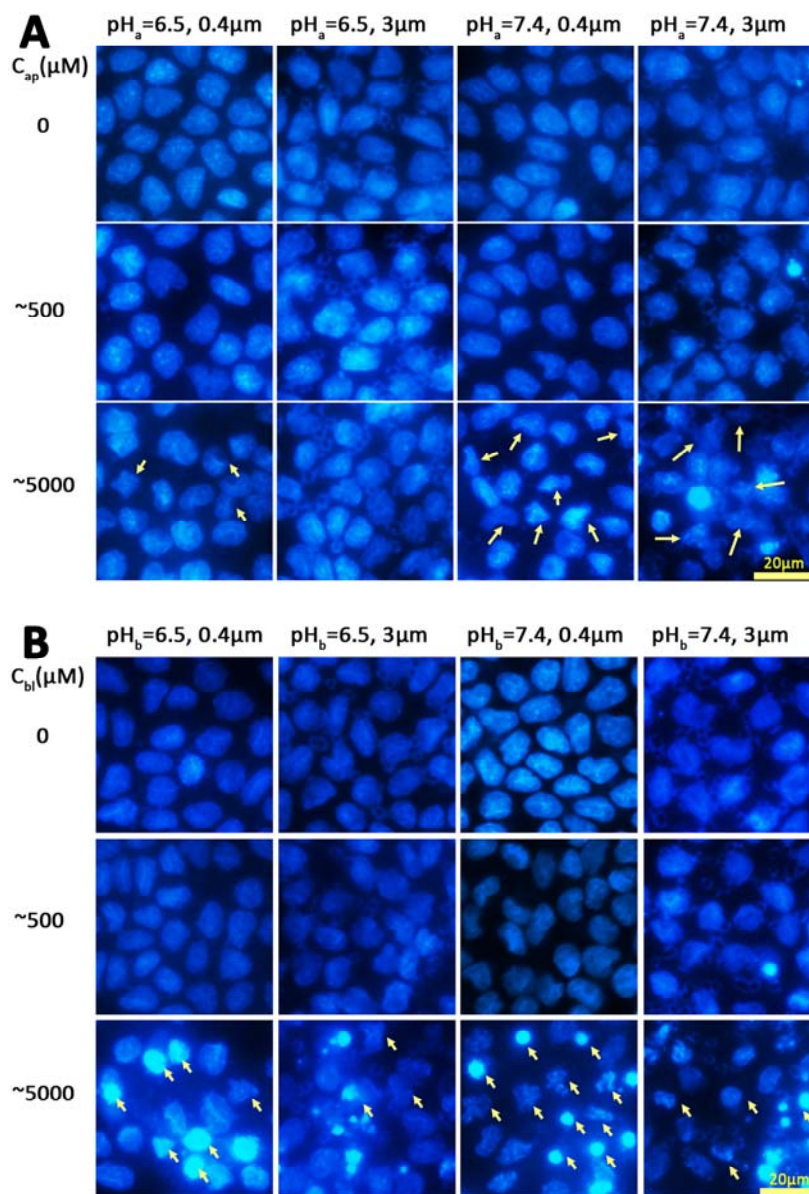


Figure 4.4. Cell images stained with DAPI after transport experiments. (A) Images were taken for AP→BL transport. (B) Images were taken for BL→AP transport. Images in the same row were taken for the transport experiments with the same concentration in the donor compartment. Images in the same column were taken for the transport experiments with the same type of membrane and pH value in the donor compartment.

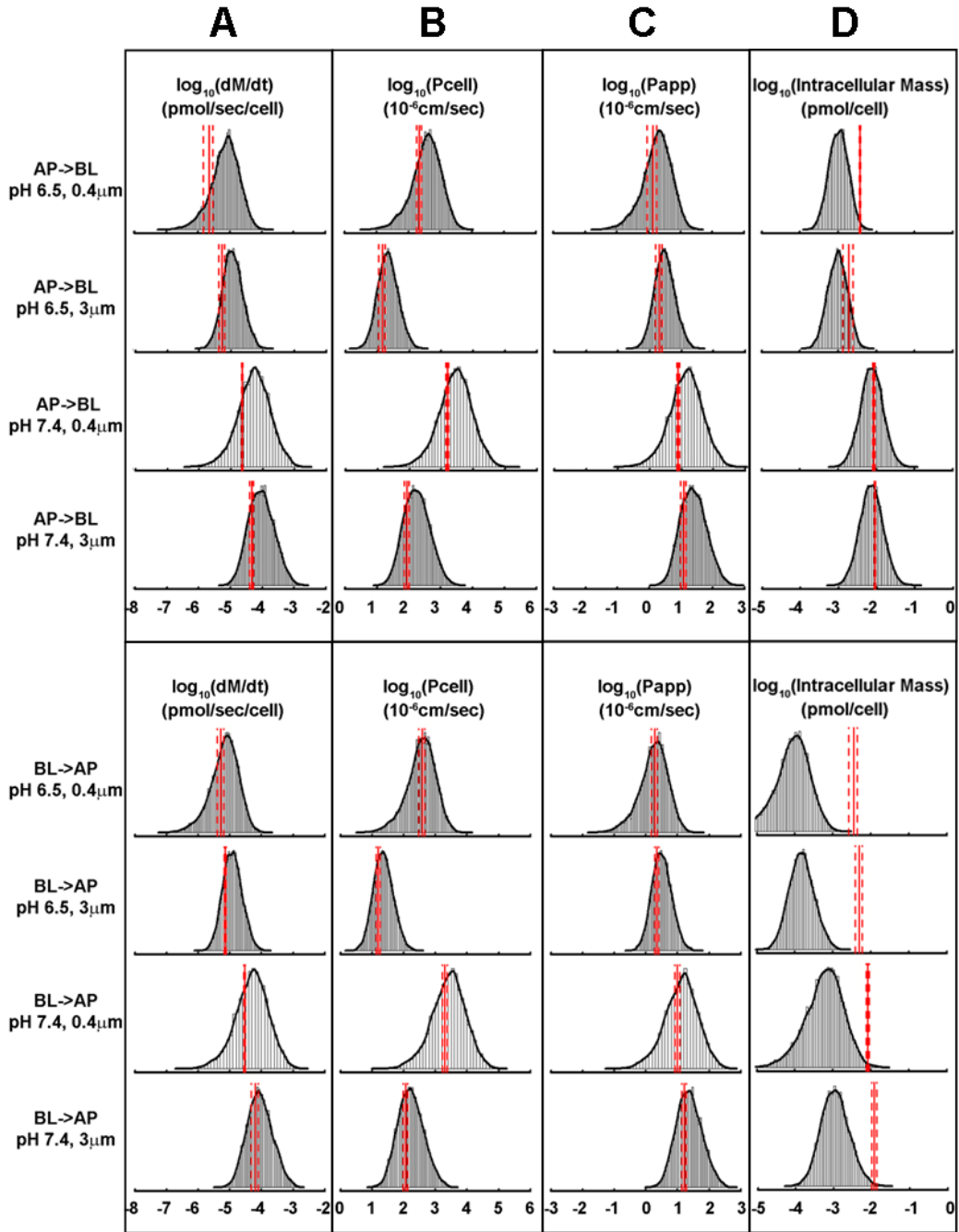


Figure 4.5. Histogram plots of Monte Carlo simulations showing calculated dM/dt (A), P_{cell} (B), P_{app} (C), and intracellular CQ mass accumulation at 5 minutes incubation (D), for the various experimental conditions analyzed in this study. The solid red lines indicate experimentally-measured mean values and the dashed red lines indicate measured standard deviation.

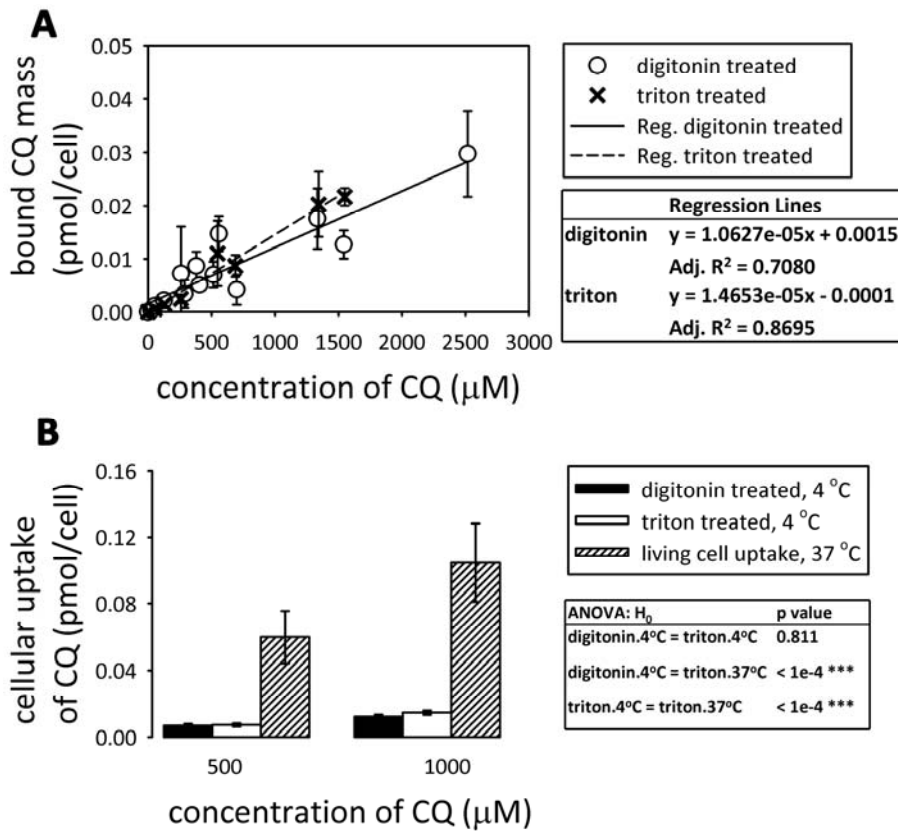


Figure 4.6. CQ binding experiments. (A) The change of bound CQ mass is proportional to CQ concentration in digitonin-treated and triton-treated cells; (B) comparison of CQ binding at 4°C (digitonin-treated and triton-treated cells) and 37°C (triton-treated cells). The values and standard deviations were calculated from the regression lines using CQ concentration equal to 500 or 1000 μM : for uptake at 4°C, regression lines in the table of Figure 4.7A were used; for uptake at 37°C, the regression line for AP→BL transport on 0.4 μm - membrane in Figure 4.5C was used.

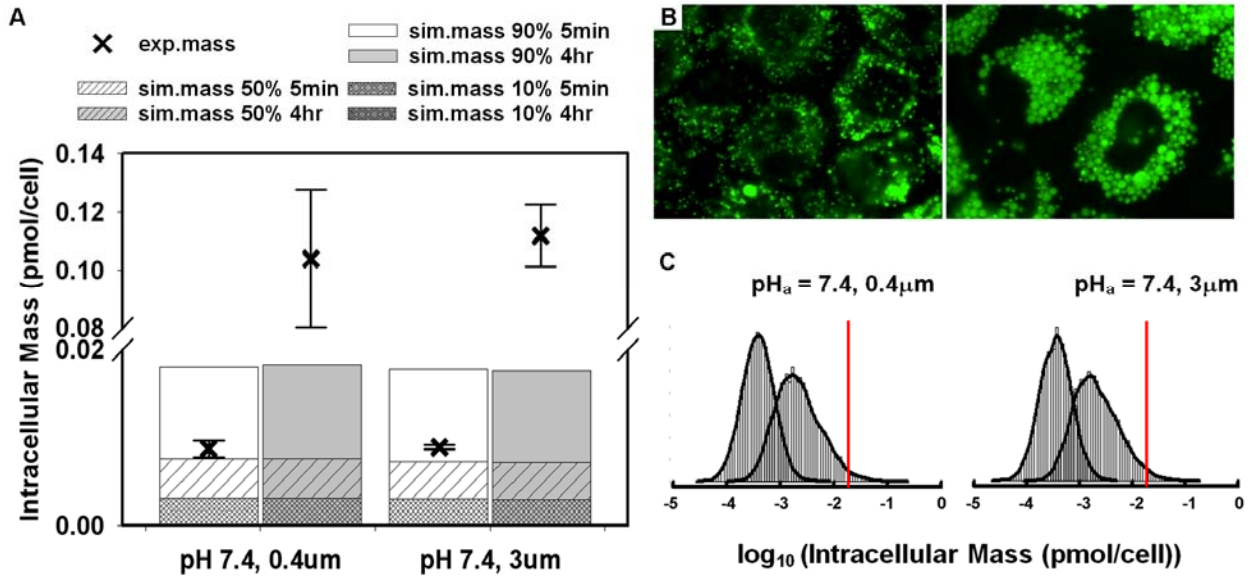


Figure 4.7. Effects of lysosomal swelling on CQ intracellular mass accumulation. (A) Comparison of simulated intracellular mass and experimental data at the end of a 5 minute and 4 hour of AP \rightarrow BL transport experiment. 1CellPK model is capable of predicting CQ accumulation in MDCK cells at early time point but not after prolonged treatment, indicating the presence of biological changes in response to CQ treatment. The simulations in the panel were performed with non-swollen lysosomes. (B) LysoTracker Green (LTG) staining of MDCK cells treated with CQ free medium (left) and 50 μ M CQ diluted in medium (right) for 4 hours. (C) Histograms of Monte Carlo simulation of lysosomal expansion and pH effect on intracellular CQ mass accumulation. All model parameters were kept the same as in Figure 4.5 except that the measured lysosomal volume and pH values were used as input (as median values of a uniform distribution, see legend of Table 4.2 for boundary calculation). The red lines show intracellular mass accumulation of CQ with initial concentration of 50 μ M extrapolated from regression lines of experimental measurements (Figure 4.3C). The left-most histograms in each figure are the same as in Figure 4.5D (the third and fourth rows).

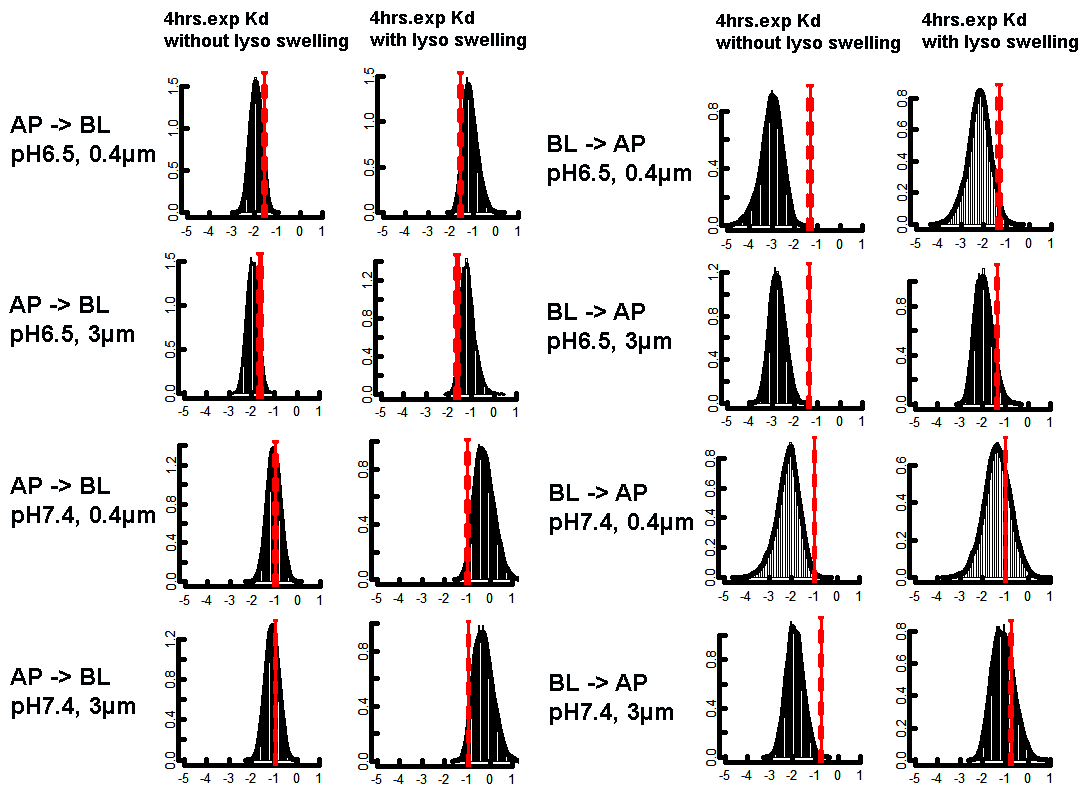


Figure 4.8. Histograms of $\log_{10}(\text{intracellular mass, pmol/cell})$. X-axis indicates $\log_{10}(\text{intracellular mass, pmol/cell})$ and y-axis indicates density. Red solid lines indicate mean values of measured intracellular accumulation of CQ (pmol/cell) after 4 hours incubation. The first and third column indicates simulations without lysosomal swelling or intra-lysosomal pH incensement. The second and fourth column indicated simulation with lysosomal swelling and intra-lysosomal pH incensement.

References

1. A. Malkia, L. Murtomaki, A. Urtti, and K. Kontturi. Drug permeation in biomembranes: in vitro and in silico prediction and influence of physicochemical properties. *Eur J Pharm Sci.* 23:13-47 (2004).
2. H. Yu and P.J. Sinko. Influence of the microporous substratum and hydrodynamics on resistances to drug transport in cell culture systems: calculation of intrinsic transport parameters. *J Pharm Sci.* 86:1448-1457 (1997).
3. X. Zhang, K. Shedden, and G.R. Rosania. A cell-based molecular transport simulator for pharmacokinetic prediction and cheminformatic exploration. *Mol Pharm.* 3:704-716 (2006).
4. X. Zhang, N. Zheng, and G.R. Rosania. Simulation-based cheminformatic analysis of organelle-targeted molecules: lysosomotropic monobasic amines. *J Comput Aided Mol Des.* 22:629-645 (2008).
5. C.S. Chen, M. Mrksich, S. Huang, G.M. Whitesides, and D.E. Ingber. Geometric control of cell life and death. *Science.* 276:1425-1428 (1997).
6. L.E. Dike, C.S. Chen, M. Mrksich, J. Tien, G.M. Whitesides, and D.E. Ingber. Geometric control of switching between growth, apoptosis, and differentiation during angiogenesis using micropatterned substrates. *In Vitro Cell Dev Biol Anim.* 35:441-448 (1999).
7. C.S. Chen, J.L. Alonso, E. Ostuni, G.M. Whitesides, and D.E. Ingber. Cell shape provides global control of focal adhesion assembly. *Biochem Biophys Res Commun.* 307:355-361 (2003).
8. D. Projean, B. Baune, R. Farinotti, J.P. Flinois, P. Beaune, A.M. Taburet, and J. Ducharme. In vitro metabolism of chloroquine: identification of CYP2C8, CYP3A4, and CYP2D6 as the main isoforms catalyzing N-desethylchloroquine formation. *Drug Metab Dispos.* 31:748-754 (2003).
9. R. Kostianen, T. Kotiaho, T. Kuuranne, and S. Auriola. Liquid chromatography / atmospheric pressure ionization-mass spectrometry in drug metabolism studies. *J Mass Spectrom.* 38:357-372 (2003).
10. M.R. Anari, R.I. Sanchez, R. Bakhtiar, R.B. Franklin, and T.A. Baillie. Integration of knowledge-based metabolic predictions with liquid chromatography data-dependent tandem mass spectrometry for drug metabolism studies: application to studies on the biotransformation of indinavir. *Anal Chem.* 76:823-832 (2004).
11. S. Trapp, G.R. Rosania, R.W. Horobin, and J. Kornhuber. Quantitative modeling of selective lysosomal targeting for drug design. *Eur Biophys J.* 37:1317-1328 (2008).
12. S. Trapp and R.W. Horobin. A predictive model for the selective accumulation of chemicals in tumor cells. *European Biophysics Journal With Biophysics Letters.* 34:959-966 (2005).
13. S. Balaz. Modeling kinetics of subcellular disposition of chemicals. *Chem Rev.* 109:1793-1899 (2009).
14. H. Chanteux, I. Paternotte, M.P. Mingeot-Leclercq, R. Brasseur, E. Sonveaux, and P.M. Tulkens. Cell handling, membrane-binding properties, and membrane-

- penetration modeling approaches of pivampicillin and phthalimidomethylampicillin, two basic esters of ampicillin, in comparison with chloroquine and azithromycin. *Pharm Res.* 20:624-631 (2003).
15. T. Rodgers, D. Leahy, and M. Rowland. Physiologically based pharmacokinetic modeling 1: predicting the tissue distribution of moderate-to-strong bases. *J Pharm Sci.* 94:1259-1276 (2005).
 16. P.V. Balimane and S. Chong. Cell culture-based models for intestinal permeability: a critique. *Drug Discov Today.* 10:335-343 (2005).
 17. S. Winiwarter, N.M. Bonham, F. Ax, A. Hallberg, H. Lennernas, and A. Karlen. Correlation of human jejunal permeability (in vivo) of drugs with experimentally and theoretically derived parameters. A multivariate data analysis approach. *Journal Of Medicinal Chemistry.* 41:4939-4949 (1998).
 18. H. Bohets, P. Annaert, G. Mannens, L. Van Beijsterveldt, K. Anciaux, P. Verboven, W. Meuldermans, and K. Lavrijsen. Strategies for absorption screening in drug discovery and development. *Curr Top Med Chem.* 1:367-383 (2001).
 19. P. Artursson and J. Karlsson. Correlation between oral drug absorption in humans and apparent drug permeability coefficients in human intestinal epithelial (Caco-2) cells. *Biochem Biophys Res Commun.* 175:880-885 (1991).
 20. E. Walter, S. Janich, B.J. Roessler, J.M. Hilfinger, and G.L. Amidon. HT29-MTX/Caco-2 cocultures as an in vitro model for the intestinal epithelium: In vitro in vivo correlation with permeability data from rats and humans. *Journal Of Pharmaceutical Sciences.* 85:1070-1076 (1996).
 21. J.D. Irvine, L. Takahashi, K. Lockhart, J. Cheong, J.W. Tolan, H.E. Selick, and J.R. Grove. MDCK (Madin-Darby canine kidney) cells: A tool for membrane permeability screening. *J Pharm Sci.* 88:28-33 (1999).
 22. P. Artursson, K. Palm, and K. Luthman. Caco-2 monolayers in experimental and theoretical predictions of drug transport. *Advanced Drug Delivery Reviews.* 46:27-43 (2001).
 23. A. Braun, S. Hammerle, K. Suda, B. Rothen-Rutishauser, M. Gunthert, S.D. Kramer, and H. Wunderli-Allenspach. Cell cultures as tools in biopharmacy. *Eur J Pharm Sci.* 11 Suppl 2:S51-60 (2000).
 24. I. Gonzalez-Alvarez, C. Fernandez-Teruel, T.M. Garrigues, V.G. Casabo, A. Ruiz-Garcia, and M. Bermejo. Kinetic modelling of passive transport and active efflux of a fluoroquinolone across Caco-2 cells using a compartmental approach in NONMEM. *Xenobiotica.* 35:1067-1088 (2005).
 25. T.T. Tran, A. Mittal, T. Aldinger, J.W. Polli, A. Ayrton, H. Ellens, and J. Bentz. The elementary mass action rate constants of P-gp transport for a confluent monolayer of MDCKII-hMDR1 cells. *Biophys J.* 88:715-738 (2005).
 26. H. Ku. Notes on the Use of Propagation of Error Formulas, *J Research of National Bureau of Standards-C. Engineering and Instrumentation*, Vol. 70C, No.4, pp. 263-273. (1966).

CHAPTER V

SINGLE-CELL PHYSIOLOGICALLY-BASED PHARMACOKINETIC (1CELLPBPK) MODELING OF DRUG DISTRIBUTION IN THE LUNG

Abstract

Purpose: Use a computational, multiscale predictive model to explore the effects of drug sequestration within lysosomes and mitochondria on the uptake, accumulation, and efflux of small molecule drugs in rat lungs.

Methods: A single cell-based virtual lung model (the Cyberlung) was developed. This Cyberlung (including airways and alveoli) was plugged into a whole body physiologically-based pharmacokinetic model. Using this 1CellPBPK model, we explored the theoretical distribution of beta-blockers (atenolol, metoprolol, and propranolol). For the Cyberlung, input parameters were physicochemical properties (pK_a and $\log P$) of the drugs, and physiological parameters for each type of cells in the lung, such as intracellular pH values, cellular membrane areas, cellular membrane potential, cellular/subcellular organelle volumes, lipid fractions, number of cells, etc. For the rest of the PBPK model, input parameters are blood flow rate to each organ, volume of each organ, tissue : blood partition coefficients (K_p) for each drug in each organ, and clearance rate. Tissue distribution data were obtained from different published research articles to validate models. Differential equations were solved numerically using Matlab[®].

Results: For all three drugs, the model predicts lung distribution kinetics close to experimental measurements (atenolol and propranolol) or experimentally measured K_p for the lung (metoprolol). If subcellular organelles (lysosomes and mitochondria) are included the drug accumulation in the lung will be increased, but not significantly, due to the small volume of lung. The volume and lipid fraction of mitochondria or lysosomes in the lung has a minimal effect on the systemic drug concentration in blood.

Conclusions: Weak basic molecules show significant sequestration in acidic subcellular organelles at cellular level. However, at tissue level, subcellular sequestration contributes to increment of drug distribution in the lung but not significantly, because the relative volume fraction of subcellular compartment is small. Successful integration of a single-cell based Cyberlung model with a whole-body PBPK model constitutes an important step towards ab initio single-cell based predictive modeling of drug pharmacokinetics at the whole body level.

Keywords: Cellular pharmacokinetics; Physiologically-based pharmacokinetic (PBPK) modeling; Drug transport; Permeability; Subcellular localization; Lung distribution

Introduction

Quantitative predictions from pre-clinical data to human situation are always challenging, however are critical to drive the decision making as drug candidates move to later stage of drug development (1-3). Whole body physiologically-based pharmacokinetic (WBPBPK) models are mathematical models that integrate anatomical and physiological parameters (such as organ regional blood flow rate and organ volumes), and compound specific properties (such as physicochemical properties, tissue-to-blood partition coefficient, blood-to-plasma partition coefficient, unbound fraction in plasma, intrinsic clearance, and even formulation effects) to predict absorption, distribution, metabolism and excretion (ADME) of compounds in animals and humans (1-7). Beside WBPBPK models, specific PBPPK models also have been reported to predict absorption (8-11), clearance (12), volume of distribution (13), tissue distribution (14-18), and drug-drug interaction in humans (19-23).

In WBPBPK modeling, tissue-to-plasma partition coefficients (K_p) are one of the most costly and labor intensive parameters to be experimentally measured. To facilitate the application of PBPK modeling various *in silico* models have been developed to predict K_p values (13, 16, 17, 24-27). Poulin and coworkers (24-27) developed tissue-composition based equations to predict compound distribution in various tissues. Their models assumed that compounds are homogeneously distributed within each tissue, or predominantly distributed in the interstitial space of the tissue. Passive diffusion was assumed to govern the distribution of molecules. In their prediction, the most pronounced discrepancy observed between predicted and measured K_p values was for the lung for lipophilic basic molecules ($pK_a > 7$). Rodgers and coworkers (16, 17) modified

Poulin *et al.* equations. They categorized molecules into moderate-to-strong bases and acids, very weak bases, neutrals, and zwitterions. For the moderate-to-strong bases, electrostatic interactions between the ionized form and intracellular acidic phospholipids were assumed to be predominant (16). Passive distribution between compartments and non-saturating binding were also assumed (16). Although by incorporating electrostatic interactions, K_p predictions in the lung were improved, under-prediction was still prevailed, suggesting other mechanisms contributing to the distribution in the lung (16).

Previously, single cell-based pharmacokinetic model (1CellPK) has been developed to predict intracellular / subcellular accumulation and transcellular permeability of small molecules in polarized and non-polarized cells (28-31). The 1CellPK model was validated for compounds with published measured permeability (28), and ninety-nine monobasic amines (29). It was tested quantitatively for prediction of intracellular mass accumulation and transcellular permeability of a lipophilic basic compound, chloroquine (CQ), and showed good agreement with measured transcellular permeability up to 4 hours and intracellular mass accumulation after 5 minutes incubation. Based on single cell prediction, we observed that for monobasic amines, their intracellular distribution was not homogenous. For most of them, high lysosomal or mitochondrial accumulation was observed (29).

Extensive distribution in the lung has been observed for many lipophilic bases (32-37). Lysosomal trapping was proposed as a mechanism contributing to high accumulation in the lung (35-39). Here we constructed WBPBPK models incorporating a Cyberlung, which was developed based on 1CellPK, to quantitatively explore the impact of organellar accumulation on the distribution in the lung of several beta-blockers

(atenolol, metoprolol, and propranolol) with similar structures, similar pK_a values, different logP values, and different plasma binding affinity. We test the hypothesis that organellar accumulation of drugs could have a significant effect on lung tissue pharmacokinetics depending on the drugs' physicochemical properties.

Methods

Development of the 1CellPBPK model

The structure of the cell-based PBPK model (1CellPBPK) is illustrated in Figure 5.1. Briefly, the Cyberlung consists of eight cellular compartments: 1: surface lining liquid (aEp); 2: macrophage (imEp); 3: epithelial cells (cEp); 4: interstitium (int); 5: immune cells (imInt); 6: smooth muscle (sm); 7: endothelial cells (cEd); and 8: plasma (plung). Both tracheobronchial airways and alveolar region were included in the model. Amongst the eight compartments, epithelial cells and endothelial cells are modeled with the R-model and other compartments are modeled with the T-model (J. Yu, manuscript in preparation). Lysosomes and mitochondria are integrated in the cEp (*cEpMito* and *cEpLyso*) and cEd (*cEdMito* and *cEdLyso*) for alveolar region and in the cEp (*cEpMito* and *cEpLyso*), cEd (*cEdMito* and *cEdLyso*), and sm (*smMito* and *smLyso*) for the tracheobronchial airways. Mass change with time (dM/dt) can be expressed by mass balance equations (5.1-5.14).

$$V_{v,lu} \frac{dC_{v,lu}}{dt} = Q_{lu} C_{vb} - A_{aEd} J_{plung,cEd} - Q_{lu} C_{v,lu} , \quad (5.1)$$

$$\frac{dM_{cEd}}{dt} = A_{aEd} J_{cEd,plung} - A_{cEdMito} J_{cEd,cEdMito} - A_{cEdLyso} J_{cEd,cEdLyso} - A_{bEd} J_{int,cEd} , \quad (5.2)$$

$$\frac{dM_{cEdLyso}}{dt} = A_{cEdLyso} J_{cEd,cEdLyso} , \quad (5.3)$$

$$\frac{dM_{cEdMito}}{dt} = A_{cEdMito} J_{cEd,cEdMito} , \quad (5.4)$$

$$\frac{dM_{int}}{dt} = A_{bEd} J_{int,cEd} - A_{sm} J_{int,sm} - A_{imInt} J_{int,imInt} - A_{bEp} J_{bEp,int} , \quad (5.5)$$

$$\frac{dM_{sm}}{dt} = A_{sm} J_{int,sm} - A_{smMito} J_{sm,smMito} - A_{smLyso} J_{sm,smLyso} , \quad (5.6)$$

$$\frac{dM_{smMito}}{dt} = A_{smMito} J_{sm,smMito} , \quad (5.7)$$

$$\frac{dM_{smLyso}}{dt} = A_{smLyso} J_{sm,smLyso} , \quad (5.8)$$

$$\frac{dM_{imInt}}{dt} = A_{imInt} J_{int,imInt} , \quad (5.9)$$

$$\frac{dM_{cEp}}{dt} = A_{bEp} J_{bEp,int} - A_{cEpMito} J_{cEp,cEpMito} - A_{cEpLyso} J_{cEp,cEpLyso} - A_{aEp} J_{aEp,cEp} , \quad (5.10)$$

$$\frac{dM_{cEpMito}}{dt} = A_{cEpMito} J_{cEp,cEpMito} , \quad (5.11)$$

$$\frac{dM_{cEpLyso}}{dt} = A_{cEpLyso} J_{cEp,cEpLyso} , \quad (5.12)$$

$$\frac{dM_{imEp}}{dt} = A_{imEp} J_{aEp,imEp} , \quad (5.13)$$

$$\frac{dM_{aEp}}{dt} = A_{aEp} J_{aEp,cEp} - A_{imEp} J_{aEp,imEp} - K_{e,mucus} M_{aEp} , \quad (5.14)$$

The subscripts indicate each compartment as described above. A and J indicate membrane surface area and flux, respectively. The two subscripts of J indicate the

transport direction. For example, in equation 5.1, $J_{plung,cEd}$ is the flux from lung plasma to endothelial cytosol. $K_{e,mucus}$ is the mucus clearance. The Cyberlung is connected with other tissues by the plasma compartment (Figure 5.1, equation 5.1). $V_{v,lu}$ is the blood volume in the lung, $C_{v,lu}$ is the venous blood concentration in the lung, and Q_{lu} is the blood flow of the lung.

All other organs were assumed to be well-stirred compartments (perfusion-limited model). For a non-elimination organ/tissue, the mass change within that organ/tissue can be expressed by equation 5.15.

$$V_t \frac{dC_t}{dt} = Q_t C_{ab} - Q_t C_{v,t}, \quad (5.15)$$

where, subscript t stands for a non-elimination organ, such as heart (ca), bone (bo), muscle (mu), fat (fa), skin (sk), thymus (th), brain (br), spleen (sp), gut (gu), and rest of body (rob). V stands for volume of the tissue; C_t stands for total tissue concentration; Q_t stands for blood flow rate of that organ; C_{ab} stands for arterial blood concentration; and $C_{v,t}$ is venous tissue concentration. Venous tissue concentration can be converted to total tissue concentration by equation (5.16).

$$C_{v,t} = \frac{C_t}{K_{p,t} / B : P}, \quad (5.16)$$

where, $K_{p,t}$ is tissue : plasma partition coefficient, and B:P is blood : plasma partition coefficient. If a drug is delivered orally, the mass balance equation for the gut is described by equation (5.17).

$$V_{gu} \frac{dC_{gu}}{dt} = R_{abs} + Q_{gu} C_{ab} - Q_{gu} C_{v,gu}, \quad (5.17)$$

where, R_{abs} is the absorption rate. For liver (hv) mass balance is expressed by equation 5.18 (7).

$$V_{hv} \frac{dC_{hv}}{dt} = Q_{ha} C_{ab} + Q_{sp} C_{v,sp} + Q_{gu} C_{v,gu} - Q_{hv} C_{v,hv} - in\ vivo\ CL_{int,u} C_{v,hv,u}, \quad (5.18)$$

where, *in vivo* $CL_{int,u}$ is scaled, unbound *in vivo* intrinsic clearance, $C_{v,hv,u}$ is unbound venous liver concentration, Q_{ha} is hepatic arterial blood flow, and Q_{hv} is the total liver blood flow. For kidney (re) mass balance is expressed by equation 5.19.

$$V_{re} \frac{dC_{re}}{dt} = Q_{re} C_{ab} - Q_{re} C_{v,re} - CL_{re,u} C_{v,re,u}, \quad (5.19)$$

where, $CL_{re,u}$ is unbound renal clearance. For arterial blood and venous blood, mass balance can be expressed by equation (5.20) and (5.21), respectively.

$$V_{ab} \frac{dC_{ab}}{dt} = Q_{lu} C_{v,lu} - Q_{lu} C_{ab}, \quad (5.20)$$

$$V_{vb} \frac{dC_{vb}}{dt} = \sum_i Q_i C_{v,i} - Q_{lu} C_{vb} + K_{iv}, \quad (5.21)$$

where, K_{iv} is the intravenous injection or infusion rate, C_{vb} is venous blood concentration, and $Q_i C_{v,i}$ is production of blood flow rate (Q_i) and venous tissue concentration ($C_{v,i}$).

Input parameters for the Cyberlung are described in another paper (J. Yu, manuscript submitted, appendix E). The thickness of surface lining liquid in alveoli = 5 μ m is used in all simulations; otherwise, it will be specified. Other physiological parameters were collected from published research papers and summarized in Table 5.1 and 5.2. Differential equation systems were solved numerically using Matlab[®] ode15s function.

Modeling pharmacokinetics of atenolol using the 1CellPBPK model

For atenolol, a semi-empirical PBPK model was constructed due to the limited experimental data for tissue : plasma partition coefficients ($K_{p,t}$). A seventeen-compartment model was constructed including arterial blood, venous blood, brain, liver, Cyberlung (as described by equation 5.1-5.14), and rest of body. Observed pharmacokinetic data in each tissue were extracted from Street J.A. et al. (34) by a computer program ‘Grab graph data’ (<http://www.frantz.fi/software/g3data.php>). Tissue kinetic data were analyzed using noncompartmental analysis with WinNonlin (Pharsight Corporation, Mountain View, CA). Tissue : blood partition coefficient ($K_{p,b}$) was calculated by the ratio of $AUC_{0-\text{inf}, \text{tissue}} / AUC_{0-\text{inf}, \text{blood}}$ and summarized in Table 5.2. The tissue concentration was measured by total radioactivity (34). However since the most component in the major circulation is parent compound (40), total radioactivity can be considered as a surrogate of parent compound concentration. To determine the $K_{p,b}$ for the rest of body, several values were tested (0.1, 0.5, 1, 5, and 10), and the $K_{p,b,\text{rest of body}}$ value that gave the best prediction was chosen. Atenolol is mainly eliminated by the kidney and negligibly bound to plasma proteins (41). *In vivo* plasma clearance was obtained from published literature (41) and converted to blood clearance by assuming the clearance rate is the same using equation 5.22.

$$CL_b = \frac{CL_p}{B:P}, \quad (5.22)$$

where, CL_b and CL_p are blood and plasma clearance, respectively. Clearance was allocated to venous blood compartment. Thus the mass change in venous blood is expressed by equation 5.23.

$$V_{vb} \frac{dC_{vb}}{dt} = Q_{br} C_{v,br} + Q_{hv} C_{v,hv} + Q_{rob} C_{v,rob} - Q_{lu} C_{vb} - CL_b C_{vb} + K_{iv}, \quad (5.23)$$

In the simulation, a 300mg rat was given 1mg/kg i.v. bolus injection to mimic the experiment (34). Thus K_{iv} was set to 0 and the initial concentration given to venous blood was dose / venous blood volume. Initial concentration given to other compartments was 0. Two scenarios were simulated: with lyso/mito and without lyso/mito. With lyso/mito was defined as: V_{mito} or $V_{lyso} = 0.1 V_{cyto}$ and lipid fraction in mitochondria and lysosome = 0.05. Experimental data were obtained from literature to compare with simulation (34).

Modeling pharmacokinetics of metoprolol using the 1CellPBPK model

Metoprolol is a beta-blocker with intermediate lipophilicity and plasma binding. The difference is not significant between R- and S- metoprolol for blood : plasma ratio, unbound fraction in plasma, and tissue : plasma partition coefficient of most tissues (42) as summarized in Table 5.2. Observed values for S-metoprolol were used in simulations. A 39-compartment model was developed including arterial blood, venous blood, heart, brain, liver, gut, spleen, kidney, muscle, skin, adipose, bone, rest of body, and the Cyberlung (14 compartments in the tracheobronchial airways and 12 compartments in the alveolar region). Clearance of metoprolol was obtained from literature (43), and was modeled using equation 5.24.

$$V_{hv} \frac{dC_{hv}}{dt} = Q_{ha} C_{ab} + Q_{sp} C_{v,sp} + Q_{gu} C_{v,gu} - Q_{hv} C_{v,hv} - \frac{V_{max} V_{hv}}{K_m + C_{vp,hv,u}} C_{vp,hv,u}, \quad (5.24)$$

where V_{max} has the unit of ng/min/g liver, and K_m has the unit of ng/mL, $C_{vp,hv,u}$ is the unbound plasma concentration in the liver. For the tissue, it is assumed that 1g = 1mL.

V_{hv} is the weight / volume of the liver. Intravenous injection was modeled with the infusion rate = 2.3 μ g/min.

Modeling pharmacokinetics of propranolol using the 1CellPBPK model

Propranolol is a beta-blocker with high lipophilicity and high plasma binding. Unbound fraction in the plasma may differ ten fold for R-propranolol and S-propranolol (0.017 and 0.13, respectively), and blood : plasma ratio differs within two fold (0.77 and 1.29, respectively) (16). Input parameters were obtained from literature and summarized in Table 5.2 (27). The liver was modeled using equation 5.25 (27).

$$V_{hv} \frac{dC_{hv}}{dt} = Q_{ha} C_{ab} + Q_{sp} C_{v,sp} + Q_{gu} C_{v,gu} - (Q_{ha} C_{ab} + (Q_{gu} C_{v,gu} + Q_{sp} C_{v,sp}) E_h), \quad (5.25)$$

where E_h is the hepatic extraction ratio and was calculated by equation 5.26 and the intrinsic clearance CL_{int} was also obtained from Poulin et al. (27).

$$E_h = CL_{int} / (CL_{int} + Q_{hv}), \quad (5.26)$$

Simulated kinetics in tissues were compared with experimental data (44). For simulation in this study, dose = 1.5mg/kg was used. For i.v. injection, initial concentration in venous blood was calculated by equation 5.27.

$$C_{0,vb} = Dose / V_{vb}, \quad (5.27)$$

Effects of the thickness of surface lining liquid in alveoli on drug accumulation in the lung

Since the volume of surface lining liquid contribute a large proportion to the total lung volume, we investigated the effect of the thickness of surface lining liquid in alveoli on drug accumulation in the lung, two values, 1 μ m and 5 μ m, were used in simulation.

Results

Subcellular sequestration affects accumulation of atenolol, metoprolol, and propranolol in the lung but not significantly, and has little effect on distribution kinetics in other tissues and plasma

To validate the 1CellPBPK model, experimental pharmacokinetic data were obtained from literature (34, 42, 44) and plotted to compare with simulated results. For atenolol, only lung, brain, and liver were included, which are organs with relatively small volumes (Table 5.1). Other organs were lumped together as the rest of body. Several $K_{p,b}$ for the rest of body were tested (0.1, 0.5, 1, 5, and 10), and $K_{p,b,\text{rest of body}} = 1$ gave the best prediction for all tissues and plasma among five tested values, and thus was chosen. Pharmacokinetics in all tissues was closely predicted for atenolol (Figure 5.2 and 5.3). Figure 5.2 shows the lung accumulation (plotted in mass, right axis) and plasma concentration - time profile (plotted in concentration, left axis). After adding subcellular compartments (lysosomes / mitochondria), the total lung mass was increased, but not significantly. The pharmacokinetics in the lung follows the pharmacokinetics in the plasma because lung is a highly perfused organ and the elimination phase is mainly clearance driven. Tissue distribution in other organs is not affected by subcellular sequestration in the lung because the volumes of subcellular organelles are small. On the other hand, the rest of body has significant effects on the pharmacokinetics in other tissues and plasma, due to its large volume.

For metoprolol, since pharmacokinetics in tissues are not available, predicted lung: unbound plasma partition coefficient ($K_{p,u}$) was compared with observed $K_{p,u}$ and values predicted by other two *in silico* method (16, 26). Cyberlung predicted $K_{p,u}$ is closer to observed value than other two *in silico* methods (Table 5.3). Since current

Cyberlung model does not include non-specific binding, such as binding to proteins, and the binding fraction of metoprolol in the lung is not available, the calculated values in Table 5.3 represent unbound lung : unbound plasma partition coefficient. If binding fraction is considered for the lung, predicted lung accumulation by the Cyberlung will be increased based on current prediction. Comparing with and without subcellular organelles, $K_{p,u}$ values predicted by the Cyberlung are not significantly different.

For propranolol, 1CellPBPK predictions closely agree with observed pharmacokinetics in tissues and plasma (Figure 5.4 and 5.5) (44). Propranolol highly binds to plasma (87%) (27) and lung tissue (90%) (45). Current Cyberlung does not include protein binding component, thus predicted values are compared with lung accumulation after binding correction (Figure 5.4). Free lung mass predicted by Cyberlung is slightly higher than observed lung accumulation. Subcellular sequestration increases lung accumulation but not significantly, and has no effects on distribution in other tissues and organs.

Drug accumulation in the lung decreases with the decreasing thickness of surface lining liquid in alveoli

Total lung volume calculated for the Cyberlung (Table 5.1) is slightly higher than measured total lung volume (2.8 mL vs. 1.25 mL). Surface lining liquid contribute a large proportion to lung volume. The measure thickness of surface lining liquid may vary from 1 μm to 10 μm . To investigate the effect of thickness of surface lining liquid on drug accumulation in the lung, simulations were running with two values, 1 μm and 5 μm . Figure 5.6 shows the results for atenolol and propranolol. After the thickness of surface liquid lining is decreased to 1 μm , the mass accumulation in the lung is decreased as well

due to the decreasing of total lung volume. The difference between with and without subcellular organelles is more significant, which is because the volume of surface lining liquid is a large proportion of lung volume, but it does not contain subcellular organelles. The drug concentration in the lung also decreases with the decreasing volume of surface lining liquid (Table 5.3).

Conclusion and Discussion

The ultimate goal of cell based pharmacokinetic modeling and simulation is to predict human situation. This chapter includes some preliminary study of integrating cell based pharmacokinetic model to whole body PBPK model. The first organ developed based on cellular pharmacokinetic model was the lung (J. Yu, manuscript submitted). Lung is a functionally important, but with relatively simple anatomy organ.

In PBPK modeling, tissue : plasma partition coefficients (K_p) are one of the most costly input parameters, which are time consuming and labor intensive. Tissue composition-based *in silico* methods have been developed to predict K_p (13, 16, 17, 24-27). K_p values in the lung are often under-predicted for lipophilic moderate-to-strong bases (16). We modeled three beta-blockers with different lipophilicity, different protein binding, but similar pK_a values using 1CellPBPK. For all three compounds, atenolol, metoprolol, and propranolol, predicted lung accumulation is close to observed kinetics (Figure 5.2, 5.4, and Table 5.3). After adjusting the thickness of surface lining liquid within a physiologically reasonable range, the prediction accuracy can be improved (Figure 5.5). Adding 10% subcellular compartment (i.e. $V_{mito} = V_{lyso} = 0.1 V_{cyto}$), lung accumulation of three compounds is increased, but not significantly, depending on the relative volume fraction of subcellular organelles. With whole body PBPK model, we can

evaluate the effects that have been observed at cellular level to systemic level. Similar to subcellular sequestration, 1CellPBPK could also be used as a cost effective tool to evaluate the effects transporters and metabolic enzymes at systemic level.

Exploring current 1CellPBPK model, it can be used: (1). to optimize physicochemical properties ($\log P$ and pK_a) to find compounds having lung distribution that does not follow plasma pharmacokinetics; (2). to simulate the pharmacokinetics for pulmonary delivery drugs; (3) to analyze the drug distribution in the airways, alveoli, and different cell types in the lung.

With the increasing number of parameters in the PBPK models, uncertainties and variabilities associated with the parameters will become important and need to be paid attention to.

Table 5.1. Physiological parameters for tissue volumes and blood flow rates in a 250 g rat. Values are obtained from Poulin et al. (27). Both tissue volumes and blood flow rates are expressed as fractions or functions of body weight.

Tissues		Volumes (V)			Blood Flow Rates (Q)	
		fraction of total body volume	volume (mL)		fraction of cardiac output	blood flow rate (L/min)
Arterial blood		0.0272	6.8		---	---
Venous blood		0.0544	13.6		---	---
Adipose		0.076	19.0		0.07	5.82
Bone		0.04148	10.37		0.122	10.14
Brain		0.0057	1.425		0.02	1.66
Gut		0.027	6.75		0.131	10.88
Heart		0.0033	0.825		0.049	4.07
Kidney		0.0073	1.825		0.141	11.72
Liver		0.0366	9.15		0.175 b	14.54
			total	surface lining liquid		
Lung	airways	0.005 a	0.292	0.162	0.01	0.831
	alveoli		2.544	1.935	1	83.09 c
Muscle		0.404	101.0		0.278	23.10
Skin		0.19	47.5		0.058	4.82
Spleen		0.002	0.5		0.02	1.66
Rest of body		0.12002	30.005		0.077	6.3979

^a. The lung volume used in this study was calculated by summing up the total cell volume and surface lining liquid volume of the Cyberlung (including airways and alveoli). The reported lung volume is 0.005 of body weight by Poulin et al. (27), thus for a 250g rat, the lung volume is about 1.25 mL by assuming that tissue density is 1 g/mL. The lung volume of rat reported by different studies may vary from 0.0045 – 0.0071 of body weight for different strains and genders of rats (46).

^b. The blood flow rate for the liver corresponds to the summation of portal vein and hepatic artery. The portal vein represents 15.1%, where 13.1% for gut and other and 2% for spleen.

^c. Total cardiac output was calculated with an allometric equation ($0.235 \cdot \text{body weight}^{0.75}$) in L/min (27).

Table 5.2. Summary of in vivo, in vitro and physicochemical properties for atenolol, metoprolol, and propranolol

	atenolol	metoprolol (R- / S-)	propranolol
MW	266.3	267.4	259.4
logP _n	0.16 ^a	1.88 ^a	2.98 ^a
logP _d	-3.54 ^a	-1.82 ^a	-0.72 ^a
pK _a	9.6 ^a	9.70 ^a	9.49 ^a
unbound fraction in plasma (f _{up})	0.96 ^b	0.80 / 0.81 ^e	0.13 (27) ^g
blood : plasma ratio (B:P)	1.11 ^b	1.52 / 1.51 ^e	0.80 (27) ^g
tissue : plasma partition coefficient (K _p)	Adipose	---	1.05 / 0.97 ^e
	Bone	---	5.17 / 5.35 ^e
	Brain	0.11 ^c	6.47 / 6.97 ^e
	Gut	---	13.12 / 11.34 ^e
	Heart	---	6.90 / 6.24 ^e
	Kidney	---	26.72 / 26.73 ^e
	Liver	3.21 ^c	40.08 / 44.55 ^e
	Lung	---	---
	Muscle	---	5.64 / 5.59 ^e
	Skin	---	3.18 / 2.92 ^e
Spleen	---	22.69 / 22.45 ^f	
Rest of body	1.00 ^c	0.66 ^c	1.25 ^c
CL	38.9 ml/min/kg (41) ^d	V _{max} = 10215 ng/min/g liver K _m = 959.97 ng/mL (43) ^d	1000 μl/min/10 ⁶ cells (27) ^d

^a Physicochemical properties of atenolol were obtained from Zhang et al. (28)

^b *In vitro* data measured in humans were used as surrogate for rats.

^c Tissue : blood partition coefficients were calculated as described in method “Modeling pharmacokinetics of atenolol using the 1CellPBPK model”. For atenolol K_p of rest of body was optimized, for metoprolol and propranolol, K_p values of rest of body were arbitrary numbers and not optimized.

^d Observed clearance was adapted from literature.

^e Measured tissue : plasma partition coefficients were obtained from Rodgers T. et al. (42)

^f Tissue : plasma partition coefficients for the spleen were calculated in GastroPlusTM using the equations published by Rodgers T., Leahy D., and Rowland M. (16, 17)

^g Measured values were obtained from Poulin P. et al. (27)

^h Calculated tissue : plasma partition coefficients were obtained from Poulin P. et al. (27)

ⁱ Measured tissue : plasma partition coefficient obtained from Poulin P. et al. (27)

Table 5.3. Comparison of tissue : unbound plasma partition coefficient ($K_{p,u}$) values in the lung of S-metoprolol

Observed (42)	32 ± 4.9
In silico (Rodgers T. et al.) (16)	22.9
<i>In silico</i> (Poulin P. et al.) (26)	3.72
Cyberlung without lyso/mito ^a	23.56
Cyberlung with lyso/mito ^a	25.52
Cyberlung without lyso/mito ^b	15.67
Cyberlung with lyso/mito ^b	20.32

- a. The thickness of surface lining liquid in alveoli = 5 μ m.
b. The thickness of surface lining liquid in alveoli = 1 μ m.

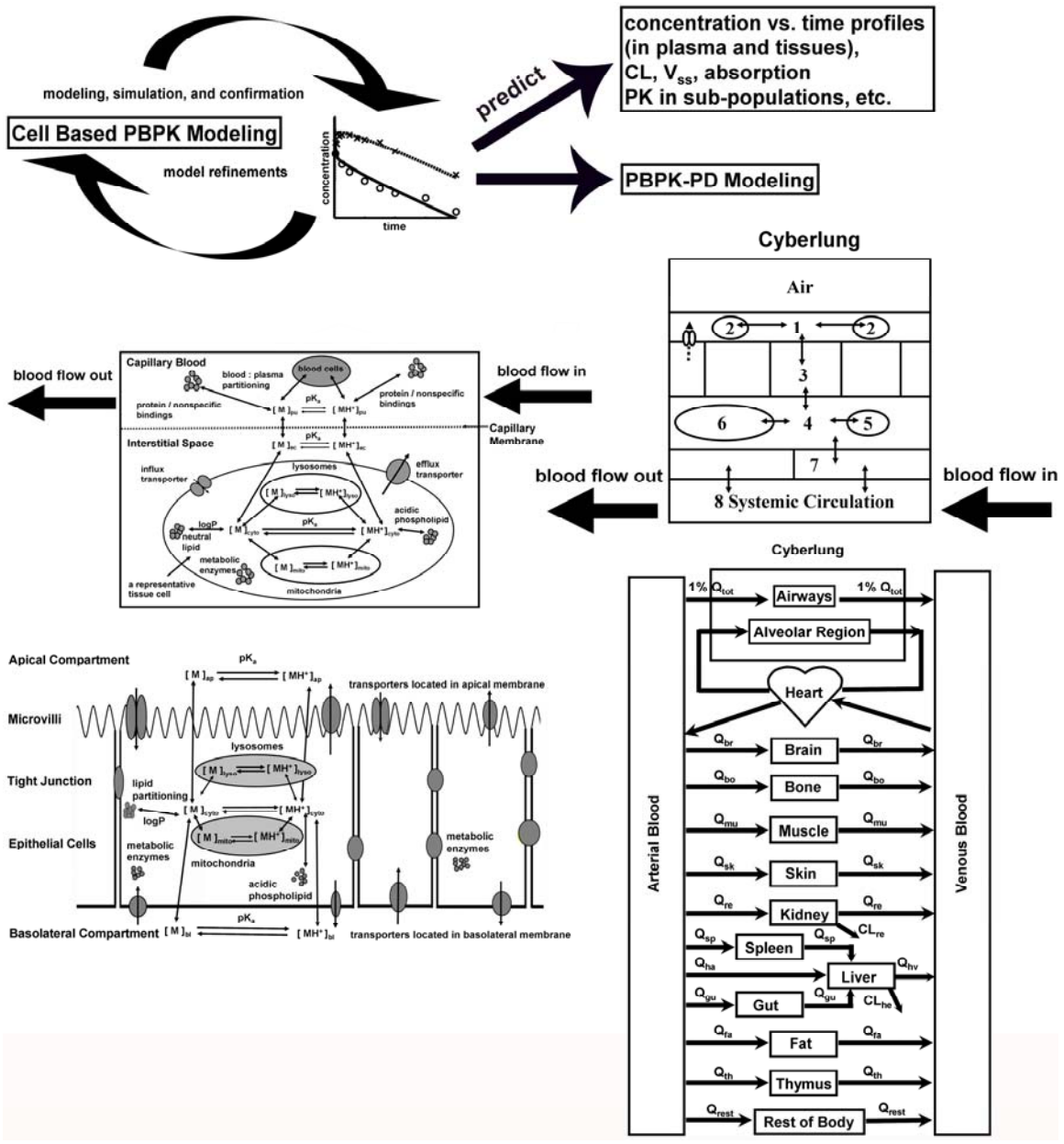


Figure 5.1. Integration of 1CellPK to 1CellPBPK model

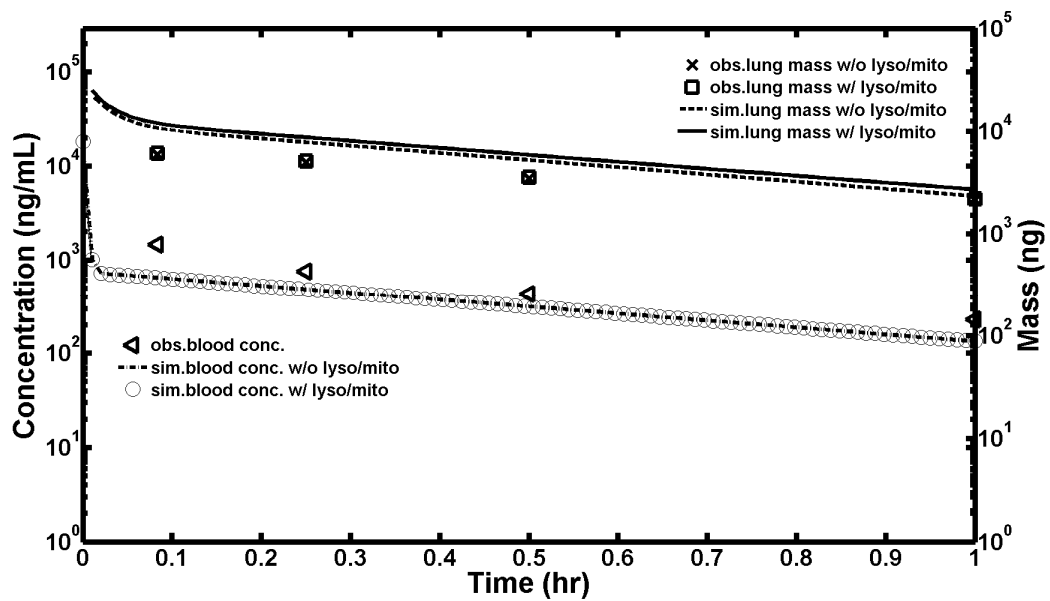


Figure 5.2. Comparison of predicted pharmacokinetics of atenolol in the lung and plasma with observed pharmacokinetics.

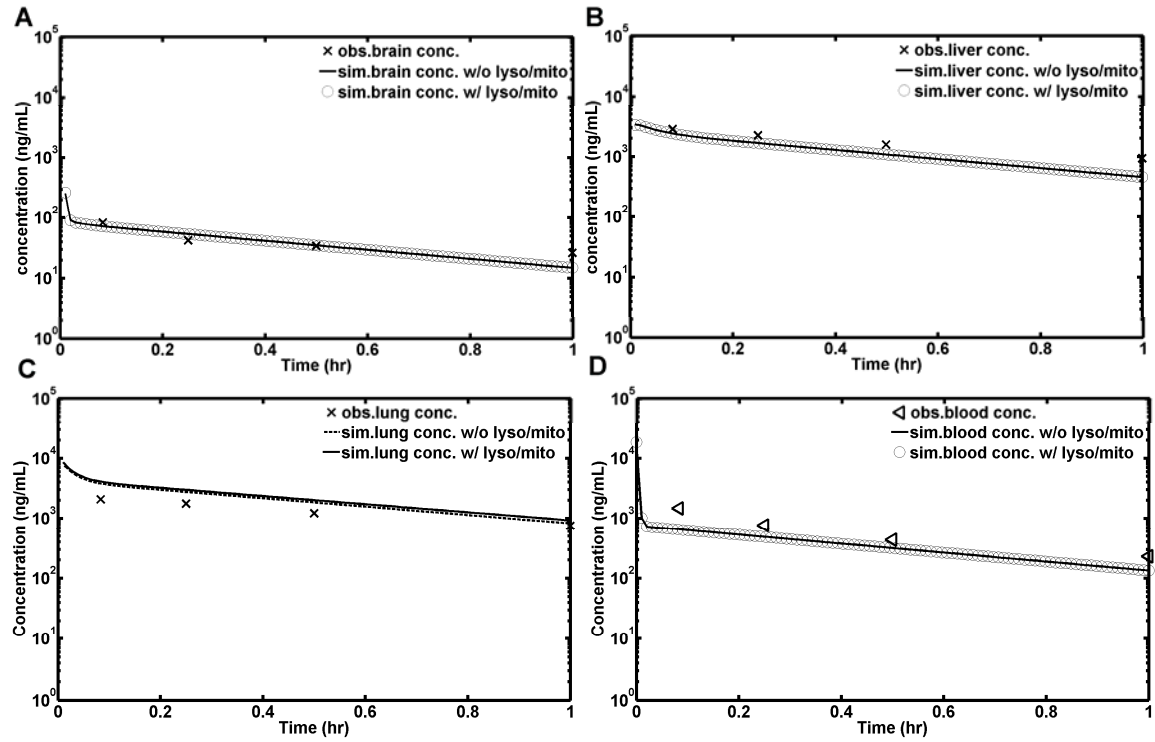


Figure 5.3. Comparison of predicted pharmacokinetics of atenolol in the various tissues with observed pharmacokinetics. (A) brain, (B) liver, (C) lung, and (D) blood.

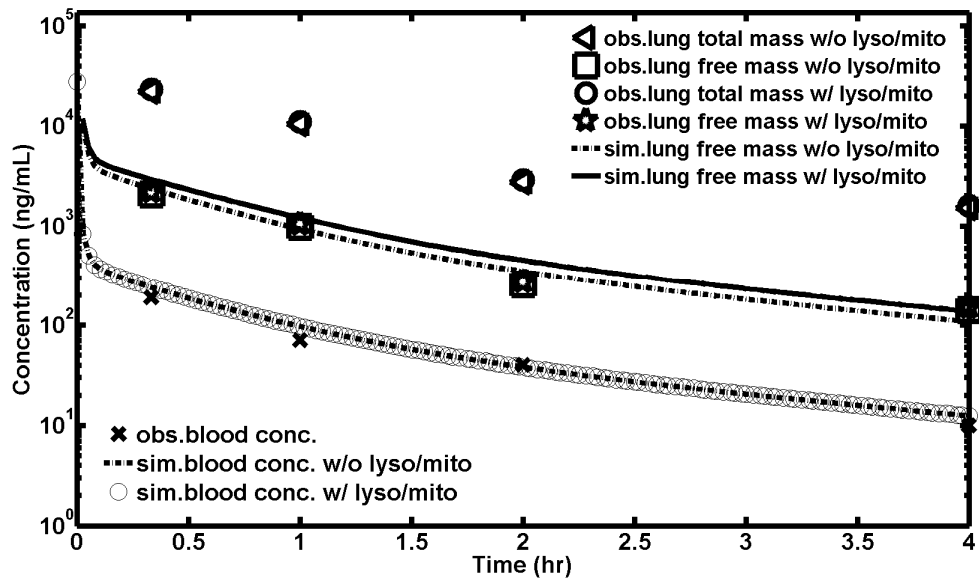


Figure 5.4. Comparison of predicted pharmacokinetics of propranolol in the lung and plasma with observed pharmacokinetics.

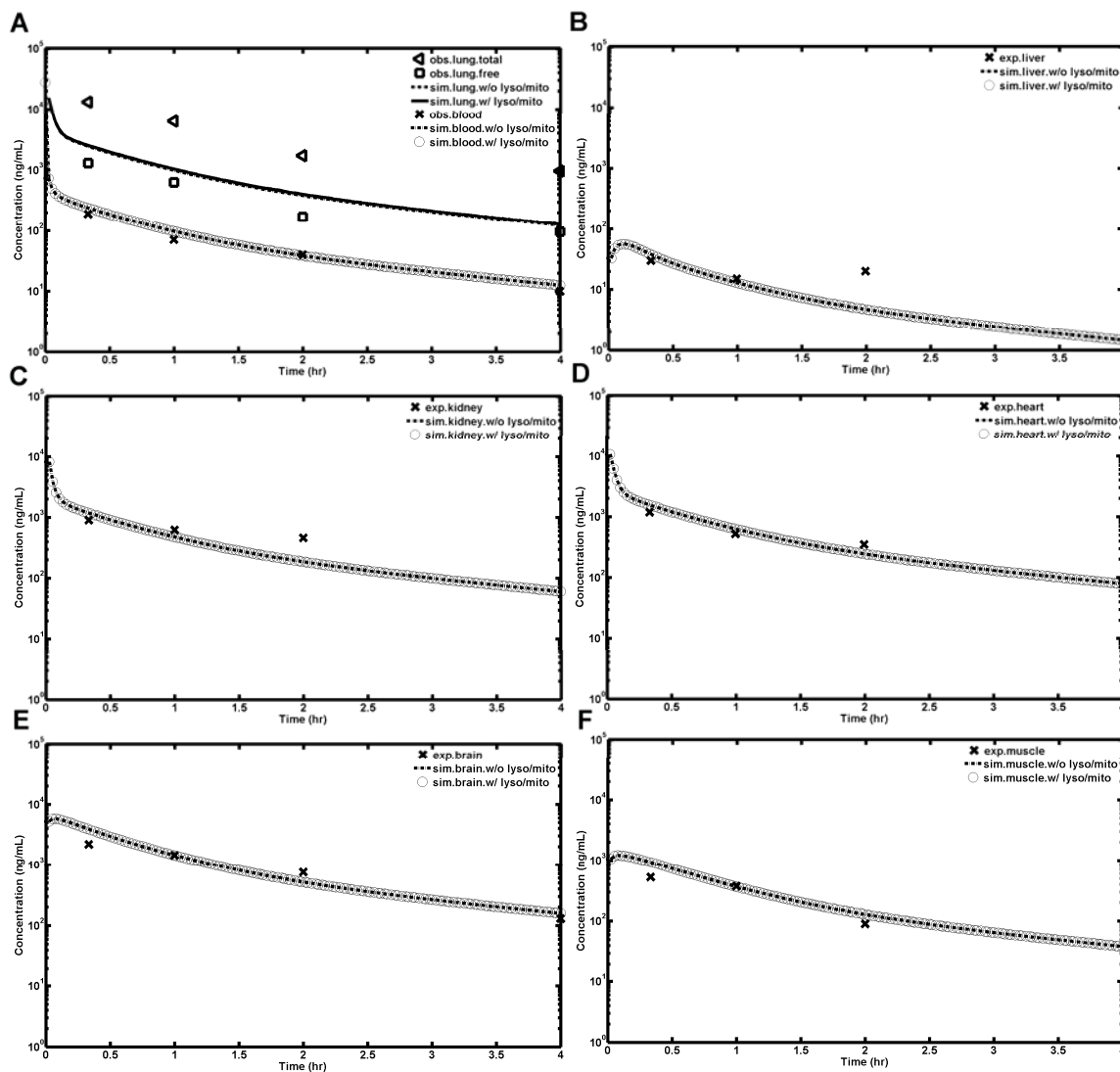


Figure 5.5. Comparison of predicted pharmacokinetics of propranolol in the various tissues with observed pharmacokinetics. (A) lung and blood, (B) liver, (C) kidney, (D) heart, (E) brain, and (F) muscle.

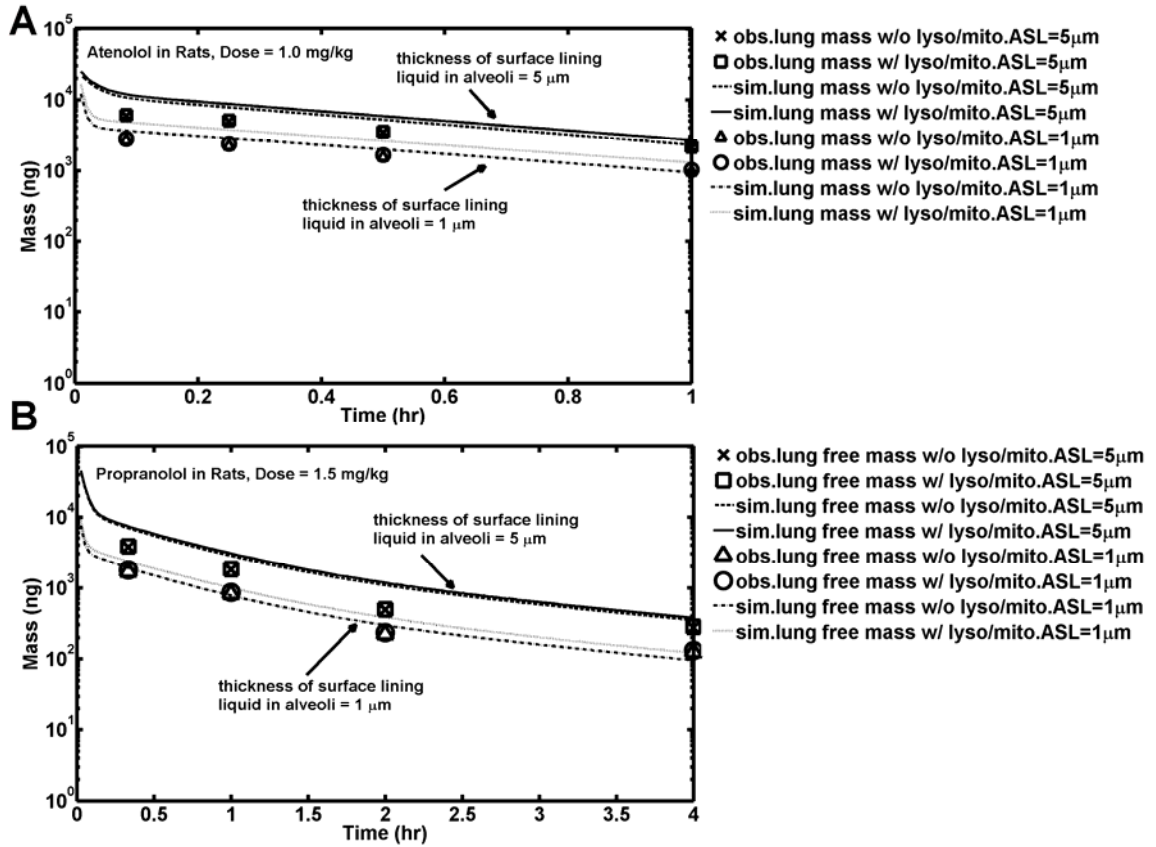


Figure 5.6. Effects of the thickness of surface lining liquid in alveoli on drug accumulation in the lung. (A) atenolol, (B) propranolol.

References

1. F.P. Theil, T.W. Guentert, S. Haddad, and P. Poulin. Utility of physiologically based pharmacokinetic models to drug development and rational drug discovery candidate selection. *Toxicol Lett.* 138:29-49 (2003).
2. T. Lave, N. Parrott, H.P. Grimm, A. Fleury, and M. Reddy. Challenges and opportunities with modelling and simulation in drug discovery and drug development. *Xenobiotica.* 37:1295-1310 (2007).
3. H.M. Jones, I.B. Gardner, and K.J. Watson. Modelling and PBPK Simulation in Drug Discovery. *Aaps Journal.* 11:155-166 (2009).
4. I. Nestorov. Whole-body physiologically based pharmacokinetic models. *Expert Opin Drug Metab Toxicol.* 3:235-249 (2007).
5. S.S. De Buck, V.K. Sinha, L.A. Fenu, M.J. Nijssen, C.E. Mackie, and R.A. Gilissen. Prediction of human pharmacokinetics using physiologically based modeling: a retrospective analysis of 26 clinically tested drugs. *Drug Metab Dispos.* 35:1766-1780 (2007).
6. P.J. Lowe, Y. Hijazi, O. Luttringer, H. Yin, R. Sarangapani, and D. Howard. On the anticipation of the human dose in first-in-man trials from preclinical and prior clinical information in early drug development. *Xenobiotica.* 37:1331-1354 (2007).
7. H.M. Jones, N. Parrott, K. Jorga, and T. Lave. A novel strategy for physiologically based predictions of human pharmacokinetics. *Clin Pharmacokinet.* 45:511-542 (2006).
8. L.X. Yu and G.L. Amidon. A compartmental absorption and transit model for estimating oral drug absorption. *Int J Pharm.* 186:119-125 (1999).
9. S. Willmann, W. Schmitt, J. Keldenich, and J.B. Dressman. A physiologic model for simulating gastrointestinal flow and drug absorption in rats. *Pharm Res.* 20:1766-1771 (2003).
10. S. Willmann, W. Schmitt, J. Keldenich, J. Lippert, and J.B. Dressman. A physiological model for the estimation of the fraction dose absorbed in humans. *J Med Chem.* 47:4022-4031 (2004).
11. N. Parrott and T. Lave. Applications of physiologically based absorption models in drug discovery and development. *Mol Pharm.* 5:760-775 (2008).
12. T. Watanabe, H. Kusuhara, K. Maeda, Y. Shitara, and Y. Sugiyama. Physiologically based pharmacokinetic modeling to predict transporter-mediated clearance and distribution of pravastatin in humans. *J Pharmacol Exp Ther.* 328:652-662 (2009).
13. T. Rodgers and M. Rowland. Mechanistic approaches to volume of distribution predictions: understanding the processes. *Pharm Res.* 24:918-933 (2007).
14. L.T. Baxter, H. Zhu, D.G. Mackensen, W.F. Butler, and R.K. Jain. Biodistribution of monoclonal antibodies: scale-up from mouse to human using a physiologically based pharmacokinetic model. *Cancer Res.* 55:4611-4622 (1995).
15. M. von Kleist and W. Huisinga. Physiologically based pharmacokinetic modelling: a sub-compartmentalized model of tissue distribution. *J Pharmacokinet Pharmacodyn.* 34:789-806 (2007).

16. T. Rodgers, D. Leahy, and M. Rowland. Physiologically based pharmacokinetic modeling 1: predicting the tissue distribution of moderate-to-strong bases. *J Pharm Sci.* 94:1259-1276 (2005).
17. T. Rodgers and M. Rowland. Physiologically based pharmacokinetic modelling 2: predicting the tissue distribution of acids, very weak bases, neutrals and zwitterions. *J Pharm Sci.* 95:1238-1257 (2006).
18. O. Luttringer, F.P. Theil, P. Poulin, A.H. Schmitt-Hoffmann, T.W. Guentert, and T. Lave. Physiologically based pharmacokinetic (PBPK) modeling of disposition of epiroprim in humans. *J Pharm Sci.* 92:1990-2007 (2003).
19. A. Poirier, C. Funk, T. Lave, and J. Noe. New strategies to address drug-drug interactions involving OATPs. *Curr Opin Drug Discov Devel.* 10:74-83 (2007).
20. M. Chenel, F. Bouzom, L. Aarons, and K. Ogungbenro. Drug-drug interaction predictions with PBPK models and optimal multiresponse sampling time designs: application to midazolam and a phase I compound. Part 1: comparison of uniresponse and multiresponse designs using PopDes. *J Pharmacokinet Pharmacodyn.* 35:635-659 (2008).
21. M. Chenel, F. Bouzom, F. Cazade, K. Ogungbenro, L. Aarons, and F. Mentre. Drug-drug interaction predictions with PBPK models and optimal multiresponse sampling time designs: application to midazolam and a phase I compound. Part 2: clinical trial results. *J Pharmacokinet Pharmacodyn.* 35:661-681 (2008).
22. M. Kato, Y. Shitara, H. Sato, K. Yoshisue, M. Hirano, T. Ikeda, and Y. Sugiyama. The quantitative prediction of CYP-mediated drug interaction by physiologically based pharmacokinetic modeling. *Pharm Res.* 25:1891-1901 (2008).
23. M. Vossen, M. Sevestre, C. Niederalt, I.J. Jang, S. Willmann, and A.N. Edginton. Dynamically simulating the interaction of midazolam and the CYP3A4 inhibitor itraconazole using individual coupled whole-body physiologically-based pharmacokinetic (WB-PBPK) models. *Theor Biol Med Model.* 4:13 (2007).
24. P. Poulin and F.P. Theil. A priori prediction of tissue:plasma partition coefficients of drugs to facilitate the use of physiologically-based pharmacokinetic models in drug discovery. *J Pharm Sci.* 89:16-35 (2000).
25. P. Poulin, K. Schoenlein, and F.P. Theil. Prediction of adipose tissue: plasma partition coefficients for structurally unrelated drugs. *J Pharm Sci.* 90:436-447 (2001).
26. P. Poulin and F.P. Theil. Prediction of pharmacokinetics prior to in vivo studies. I. Mechanism-based prediction of volume of distribution. *J Pharm Sci.* 91:129-156 (2002).
27. P. Poulin and F.P. Theil. Prediction of pharmacokinetics prior to in vivo studies. II. Generic physiologically based pharmacokinetic models of drug disposition. *J Pharm Sci.* 91:1358-1370 (2002).
28. X. Zhang, K. Shedden, and G.R. Rosania. A cell-based molecular transport simulator for pharmacokinetic prediction and cheminformatic exploration. *Mol Pharm.* 3:704-716 (2006).
29. X. Zhang, N. Zheng, and G.R. Rosania. Simulation-based cheminformatic analysis of organelle-targeted molecules: lysosomotropic monobasic amines. *J Comput Aided Mol Des.* 22:629-645 (2008).

30. S. Trapp and R.W. Horobin. A predictive model for the selective accumulation of chemicals in tumor cells. *Eur Biophys J Biophys Lett.* 34:959-966 (2005).
31. S. Trapp, G.R. Rosania, R.W. Horobin, and J. Kornhuber. Quantitative modeling of selective lysosomal targeting for drug design. *Eur Biophys J.* 37:1317-1328 (2008).
32. N. Yata, T. Toyoda, T. Murakami, A. Nishiura, and Y. Higashi. Phosphatidylserine as a determinant for the tissue distribution of weakly basic drugs in rats. *Pharm Res.* 7:1019-1025 (1990).
33. A. Hayes and R.G. Cooper. Studies on the absorption, distribution and excretion of propranolol in rat, dog and monkey. *J Pharmacol Exp Ther.* 176:302-311 (1971).
34. J.A. Street, B.A. Hemsworth, A.G. Roach, and M.D. Day. Tissue levels of several radiolabelled beta-adrenoceptor antagonists after intravenous administration in rats. *Arch Int Pharmacodyn Ther.* 237:180-190 (1979).
35. J. Ishizaki, K. Yokogawa, E. Nakashima, S. Ohkuma, and F. Ichimura. Uptake of basic drugs into rat lung granule fraction in vitro. *Biol Pharm Bull.* 21:858-861 (1998).
36. A.G. Wilson, R.D. Pickett, T.E. Eling, and M.W. Anderson. Studies on the persistence of basic amines in the rabbit lung. *Drug Metab Dispos.* 7:420-424 (1979).
37. J.K. Seydel and O. Wassermann. NMR-studies on the molecular basis of drug-induced phospholipidosis. Interaction between chlorphentermine and phosphatidylcholine. *Naunyn Schmiedebergs Arch Pharmacol.* 279:207-210 (1973).
38. K. Yokogawa, J. Ishizaki, S. Ohkuma, and K. Miyamoto. Influence of lipophilicity and lysosomal accumulation on tissue distribution kinetics of basic drugs: a physiologically based pharmacokinetic model. *Methods Find Exp Clin Pharmacol.* 24:81-93 (2002).
39. A.C. MacIntyre and D.J. Cutler. The potential role of lysosomes in tissue distribution of weak bases. *Biopharm Drug Dispos.* 9:513-526 (1988).
40. S.A. Tabacova and C.A. Kimmel. Atenolol: pharmacokinetic/dynamic aspects of comparative developmental toxicity. *Reprod Toxicol.* 16:1-7 (2002).
41. F.M. Belpaire, F. de Smet, L.J. Vynckier, A.M. Vermeulen, M.T. Rosseel, M.G. Bogaert, and L. Chauvelot-Moachon. Effect of aging on the pharmacokinetics of atenolol, metoprolol and propranolol in the rat. *J Pharmacol Exp Ther.* 254:116-122 (1990).
42. T. Rodgers, D. Leahy, and M. Rowland. Tissue distribution of basic drugs: accounting for enantiomeric, compound and regional differences amongst beta-blocking drugs in rat. *J Pharm Sci.* 94:1237-1248 (2005).
43. B.O. Wang and H.A. Semple. Inhibition of metoprolol metabolism by amino acids in perfused rat livers. Insights into the food effect? *Drug Metab Dispos.* 25:287-295 (1997).
44. D.W. Schneck, J.F. Pritchard, and A.H. Hayes, Jr. Studies on the uptake and binding of propranolol by rat tissues. *J Pharmacol Exp Ther.* 203:621-629 (1977).
45. C.T. Dollery and A.F. Junod. Concentration of (+/-)-propranolol in isolated, perfused lungs of rat. *Br J Pharmacol.* 57:67-71 (1976).

46. R.P. Brown, M.D. Delp, S.L. Lindstedt, L.R. Rhomberg, and R.P. Beliles. Physiological parameter values for physiologically based pharmacokinetic models. *Toxicol Ind Health*. 13:407-484 (1997).

CHAPTER VI

FINAL DISCUSSION

A mechanism base cellular pharmacokinetic model (1CellPK) has been developed to simulate the transcellular permeability and subcellular distribution (1). This project is the first step toward building a ‘bottom-up’ model to simulate drug transport in humans. Cells are the smallest living unit in organism. Understanding and modeling of drug transport at cellular and subcellular level are essential for developing physiologically-based pharmacokinetic (PBPK) models. In the current model, the simplest but the most important transport mechanism, passive diffusion, was considered. For the transport ionized molecules across biomembrane, the combination of Fick’s law of diffusion and Nernst–Planck equation was used. Input parameters of the model are cellular physiological parameters and physicochemical properties of small molecules, including pH values in each compartment, membrane potential of each biomembrane, volume and surface area of each compartment, lipid fraction in each compartment, and lipophilicity and acid dissociation constant of small molecules. The model performs well in predicting highly permeable molecules and lysosomotropic phenomenon. Nevertheless, the model is still a relatively simple model and many important factors have not been included. In the following we will be discussing several aspects that the current 1CellPK model can be improved and the future outlook of 1CellPK.

Integration of molecular size

Current 1CellPK model assumes the diffusion coefficient of small molecules is constant, which limits the application 1CellPK model to molecules with certain range of molecular radius. Diffusion coefficient in liquid essentially is a function of molecular radius s described by Stoke-Einstein equation (equation 6.1) (2).

$$D = \frac{kT}{n\pi a\eta} \quad 4 \leq n \leq 6, \quad (6.1)$$

where k is the Boltzmann's constant, a is the radius of the solute and η is the solution viscosity, and n is related to the radii of solute. When the solutes are large with radii greater than 5-10 Å, $n = 6$. From Stokes-Einstein equation, one sees that the diffusion coefficient is proportional to the reciprocal of the radius, which is approximately proportional to the cube root of the molecular weight. Studies showed that paracellular pathway is molecular size and charge selective (3-5). Paracellular passive permeability might play a major role in small molecules passive transport with molecular weight less than 200 Dalton (6). Thus integrating the molecular size into current 1CellPK may improve both the transcellular and paracellular transport prediction.

Integration of molecular interactions

During the transport process across the cells or into the cells, there are many steps may involve molecular interactions. For example, when the molecules transport across the biomembrane, they may interact with the lipid and be trapped in the lipid bilayer. After entering the cellular membrane, molecules may interact with macro molecules located inside cells, such as DNA and proteins. Current 1CellPK model takes into account lipid partitioning with neutral lipid in each compartment (cytosol, mitochondria,

and lysosomes). However for moderate - to - strong bases ($pK_a \geq 7$), they exist mainly as ionic species in physiological pH (~ 7). Thus electrostatic interaction between ionic species and acidic phospholipids might be an important factor determining intracellular accumulation of small molecules (7), which is not included in the current 1CellPK model.

Besides passive interactions with macromolecules and acidic phospholipids, interactions with transporters and metabolic enzymes are also important mechanisms to be included for specific classes of molecules. With the discovery of structures of transporter proteins, 1CellPK model can also include the structures of transmembrane transporters for modeling of transporter mediated transport.

Mechanistic models for hypothesis testing and experimental design

In chapter 4, chloroquine was used as a compound to test 1CellPK prediction of permeability and intracellular accumulation. While 1CellPK can capture the transcellular permeability and intracellular accumulation after short time incubation, the intracellular accumulation was under-predicted after 4 hours incubation. That suggests that the current 1CellPK does not include some mechanisms that are involved in chloroquine uptake up to 4 hours. We observed lysosomal swelling and intralysosomal pH increment during the uptake. In order to capture the lysosomal volume and intralysosomal pH increment, we ran Monte Carlo simulation with measured lysosomal volume and pH after incubation. Lysosomal swelling can explain part of the under-prediction but the model still under-predicts the uptake of chloroquine after long time incubation. We further observed two-phase uptake kinetics of chloroquine within 4 hours incubation while the model predicts the steady state reached within 1 minute. To bridge the discrepancy between model prediction and observation, the model is proposed to include

the following mechanisms for chloroquine or other similar drugs uptake. (1) To include the volume change as a function time. Monte Carlo simulation suggests the volume change has significant effects on chloroquine uptake. However, it was a rough estimation. A more accurate method is to integrate volume change as a function of time or concentration in 1CellPK model. (2) Another mechanism that may cause under-prediction is intracellular inclusion formation due to the high intracellular concentration (8). (3) Chloroquine is well known to induce autophagy, organellar sequestration in autophagosomes and cytoplasmic vacuolization, followed by chromatin condensation, caspase activation, DNA loss and shrinkage (9-12). That complicated process may also increase chloroquine uptake assuming the autophagosome is an acidic compartment.

It is always desired that prediction closely agrees with observed data. However, if discrepancies between predictions and observations are observed, it encourages researchers to explore the mechanisms that are not included in the current model.

Extension of 1CellPK towards multiorgan PBPK modeling

In this thesis, the 1CellPK was developed into a multiscale virtual lung model (the Cyberlung). And the lung model was further integrated into whole body PBPK model to study the effects of subcellular distribution on systemic distribution. That will be one of the directions for future development. Potentially, multiscale organs developed from the cell-based pharmacokinetic model can be used to predict absorption, tissue distribution, and clearance. 1CellPK has been used to predict transcellular permeability, which is one of the critical factors determining oral absorption (13-17). By combining the GI anatomy, drug dissolution profiles, transit time, precipitation, metabolism enzymes in the GI track, transporters, and other procedures involved in absorption, 1CellPK can be extended to

predict drug absorption (18-21). The Cyberlung has shown the ability of predicting the distribution of several beta-blockers in the lung. With the same strategy, 1CellPK model can be extended to other organs or tissues for tissue distribution predictions (22). The cellular pharmacokinetic model may also be extended for clearance prediction by integrating transporters and metabolic enzymes (23-25). The ultimate goal is to elaborate cell based pharmacokinetic model to multiorgan PBPK models for absorption, distribution, and elimination predictions, and furthermore link to pharmacodynamic modeling.

While extrapolating 1CellPK to the virtual lung, we have not considered microcirculation, which is responsible for the distribution of blood within tissues. The flow rate could be different from the macro blood flow rate to or from the tissue or organ to account for heterogeneity in tissue distribution (26). The flow rate could be determined by the diameter and the length of the vessels of the microcirculation and could be predicted by Hagen-Poiseuille equation. Some models have been reported to model the solute change between blood and tissue including microcirculation and cell metabolism of nutrients (26, 27). For the lung computational models of the human pulmonary microcirculation was developed to simulate regional variations in blood flow (28, 29). They could be adapted and integrated with 1CellPK to take into account of the heterogeneous distribution of compounds.

Disseminating 1CellPK

Current 1CellPK model, the Cyberlung, and 1CellPBPK model are all developed in Matlab[®] platform, which is not user-friendly software and requires programming skills. In order to share the 1CellPK model with other pharmaceutical scientists,

implementing the model in user-friendly software is necessary. Virtual Cell is a user-friendly computational tool for systems biologists to model, analyze, and interpret complicated cellular events, such as calcium dynamics in a neuronal cell, and nucleocytoplasmic transport (26, 27). By porting 1CellPK into Virtual Cell, mathematical models of small molecule transport could be easily shared amongst the systems biology community, and used to study the synthesis, metabolism and transport of lipophilic hormones and xenobiotics, as well as studying of the effect of exogenous membrane-permeant small molecule probes on biochemical signaling networks. Within Virtual Cell, 1CellPK can be integrated with biochemical signaling networks or reaction-diffusion models for *in silico* analysis.

References

1. X. Zhang, K. Shedden, and G.R. Rosania. A cell-based molecular transport simulator for pharmacokinetic prediction and cheminformatic exploration. *Mol Pharm.* 3:704-716 (2006).
2. R. Baker. *Membrane Technology and Applications*, 2004.
3. V. Pade and S. Stavchansky. Estimation of the relative contribution of the transcellular and paracellular pathway to the transport of passively absorbed drugs in the Caco-2 cell culture model. *Pharm Res.* 14:1210-1215 (1997).
4. P. Stenberg, K. Luthman, and P. Artursson. Virtual screening of intestinal drug permeability. *J Control Release.* 65:231-243 (2000).
5. G.M. Pauletti, F.W. Okumu, and R.T. Borchardt. Effect of size and charge on the passive diffusion of peptides across Caco-2 cell monolayers via the paracellular pathway. *Pharm Res.* 14:164-168 (1997).
6. H. Lennernas. Does fluid flow across the intestinal mucosa affect quantitative oral drug absorption? Is it time for a reevaluation? *Pharm Res.* 12:1573-1582 (1995).
7. T. Rodgers, D. Leahy, and M. Rowland. Physiologically based pharmacokinetic modeling 1: predicting the tissue distribution of moderate-to-strong bases. *J Pharm Sci.* 94:1259-1276 (2005).
8. F. Rashid, R.W. Horobin, and M.A. Williams. Predicting the behaviour and selectivity of fluorescent probes for lysosomes and related structures by means of structure-activity models. *Histochem J.* 23:450-459 (1991).
9. P. Boya, R.A. Gonzalez-Polo, N. Casares, J.L. Perfettini, P. Dessen, N. Larochette, D. Metivier, D. Meley, S. Souquere, T. Yoshimori, G. Pierron, P. Codogno, and G. Kroemer. Inhibition of macroautophagy triggers apoptosis. *Mol Cell Biol.* 25:1025-1040 (2005).
10. P. Boya, K. Andreau, D. Poncet, N. Zamzami, J.L. Perfettini, D. Metivier, D.M. Ojcius, M. Jaattela, and G. Kroemer. Lysosomal membrane permeabilization induces cell death in a mitochondrion-dependent fashion. *J Exp Med.* 197:1323-1334 (2003).
11. P. Boya, R.A. Gonzalez-Polo, D. Poncet, K. Andreau, H.L. Vieira, T. Roumier, J.L. Perfettini, and G. Kroemer. Mitochondrial membrane permeabilization is a critical step of lysosome-initiated apoptosis induced by hydroxychloroquine. *Oncogene.* 22:3927-3936 (2003).
12. J.J. Shacka, B.J. Klocke, M. Shibata, Y. Uchiyama, G. Datta, R.E. Schmidt, and K.A. Roth. Bafilomycin A1 inhibits chloroquine-induced death of cerebellar granule neurons. *Mol Pharmacol.* 69:1125-1136 (2006).
13. B. Press and D. Di Grandi. Permeability for intestinal absorption: Caco-2 assay and related issues. *Curr Drug Metab.* 9:893-900 (2008).
14. V.E. Thiel-Demby, J.E. Humphreys, L.A. St John Williams, H.M. Ellens, N. Shah, A.D. Ayrton, and J.W. Polli. Biopharmaceutics Classification System: Validation and Learnings of an in Vitro Permeability Assay. *Mol Pharm* (2008).
15. D.A. Volpe. Variability in Caco-2 and MDCK cell-based intestinal permeability assays. *J Pharm Sci.* 97:712-725 (2008).

16. C.Y. Han, Y. Li, and G. Liu. Drug-likeness: Predication and practice. *Prog Chem.* 20:1335-1344 (2008).
17. G.L. Amidon, H. Lennernas, V.P. Shah, and J.R. Crison. A theoretical basis for a biopharmaceutic drug classification: the correlation of in vitro drug product dissolution and in vivo bioavailability. *Pharm Res.* 12:413-420 (1995).
18. K.S. Pang. Modeling of intestinal drug absorption: roles of transporters and metabolic enzymes (for the Gillette Review Series). *Drug Metab Dispos.* 31:1507-1519 (2003).
19. D. Tam, H. Sun, and K.S. Pang. Influence of P-glycoprotein, transfer clearances, and drug binding on intestinal metabolism in Caco-2 cell monolayers or membrane preparations: a theoretical analysis. *Drug Metab Dispos.* 31:1214-1226 (2003).
20. D. Tam, R.G. Tirona, and K.S. Pang. Segmental intestinal transporters and metabolic enzymes on intestinal drug absorption. *Drug Metab Dispos.* 31:373-383 (2003).
21. D. Cong, M. Doherty, and K.S. Pang. A new physiologically based, segregated-flow model to explain route-dependent intestinal metabolism. *Drug Metab Dispos.* 28:224-235 (2000).
22. L. Yan, S. Sheihk-Bahaei, S. Park, G.E.P. Ropella, and C.A. Hunt. Predictions of hepatic disposition properties using a mechanistically realistic, physiologically based model. *Drug Metab Dispos.* 36:759-768 (2008).
23. T. Watanabe, H. Kusuhara, K. Maeda, Y. Shitara, and Y. Sugiyama. Physiologically based pharmacokinetic modeling to predict transporter-mediated clearance and distribution of pravastatin in humans. *J Pharmacol Exp Ther.* 328:652-662 (2009).
24. K.S. Pang, M. Weiss, and P. Macheras. Advanced pharmacokinetic models based on organ clearance, circulatory, and fractal concepts. *AAPS J.* 9:E268-283 (2007).
25. L. Liu and K.S. Pang. An integrated approach to model hepatic drug clearance. *Eur J Pharm Sci.* 29:215-230 (2006).
26. J.B. Bassingthwaighe, G.M. Raymond, J.D. Ploger, L.M. Schwartz, and T.R. Bukowski. GENTEX, a general multiscale model for in vivo tissue exchanges and intraorgan metabolism. *Philos Transact A Math Phys Eng Sci.* 364:1423-1442 (2006).
27. D.A. Beard, F. Wu, M.E. Cabrera, and R.K. Dash. Modeling of Cellular Metabolism and Microcirculatory Transport. *Microcirculation.* 15:777-793 (2008).
28. K.S. Burrowes, M.H. Tawhai, and P.J. Hunter. Modeling RBC and neutrophil distribution through an anatomically based pulmonary capillary network. *Ann Biomed Eng.* 32:585-595 (2004).
29. Y. Huang, C.M. Doerschuk, and R.D. Kamm. Computational modeling of RBC and neutrophil transit through the pulmonary capillaries. *J Appl Physiol.* 90:545-564 (2001).

APPENDICES

APPENDIX A

1CellPK Matlab Code

```
% The following section is to calculate the intracellular
% concentration and permeability of each drug given pKa, logPn(o/c) and
% electrical charges.

% Clear the memory
clear

% Constant
T = 273.15+37; % Body temperature (37centigrade)
R = 8.314; % Universal gas constant
F = 96484.56; % Faraday constant
La = 0; % Lipid fraction in apical compartment
Lc = 0.05; % Lipid fraction in cytosol
Lm = 0; % Lipid fraction in mitochondria
Lb = 0; % Lipid fraction in basolateral compartment
Wa = 1-La; % Water fraction in apical compartment
Wc = 1-Lc; % Water fraction in cytosol
Wm = 1-Lm; % Water fraction in mitochondria
Wb = 1-Lb; % Water fraction in basolateral compartment
gamma_na = 1; % Activity coefficient of neutral molecules in apical compartment
gamma_da = 1; % Activity coefficient of ionic molecules in apical compartment
gamma_nc = 1.23026877; % Activity coefficient of neutral molecules in cytosol
gamma_dc = 0.73799822; % Activity coefficient of ionic molecules in cytosol
gamma_nm = 1; % Activity coefficient of neutral molecules in mitochondria
gamma_dm = 1; % Activity coefficient of ionic molecules in mitochondria
gamma_nb = 1; % Activity coefficient of neutral molecules in basolateral compartment
gamma_db = 1; % Activity coefficient of ionic molecules in basolateral compartment
Ca = 1 ; % Apical initial drug concentration (mM)

% Areas and volumes (units in m^2 and m^3)
Aa = 50*10^(-10) ; % The apical membrane surface area
Aaa = 20*10^(-10) ; % The monolayer area
Am = 100*3.14*10^(-12); % The mitochondrial membrane surface area
Ab = 10^(-10); % The basolateral membrane surface area
Vc = 10*10^(-15); % The cytosolic volume
Vm = 100*5.24*10^(-19); % The mitochondrial volume
```

```

Vb = 4.7*10^(-3);           % The volume of basolateral compartment

% Membrane potential (units in 'Voltage')
Ea = -0.0093 ;             % The membrane potential of apical membrane
Em = -0.16;               % The membrane potential of mitochondrial membrane
Eb = 0.0119 ;             % The membrane potential of basolateral membrane

% pH values
pHa = 6.8;                % pH in apical compartment
pHc = 7.0;                % pH in cytosol
pHm = 8.0;                % pH in mitochondria
pHb = 7.4;                % pH in basolateral compartment

% Read the drug properties
% If the drug is neutral at physiological pH
% the z is given 10^(-6) in stead of 0 since if z=0 the differential
% equations can't be solved
[DrugName,pKaall,logPnall,ZNall] = textread('drug.dat', '%s %f
%f%f','commentstyle','matlab');

% Calculate the ionized logP(o/w);
logPdall = logPnall-3.7 ;

% The calculated results are saved in this file 'Peff_all.dat'
len = length(pKaall) ;
fid1 = fopen('Peff_all.dat','w');
str1 = ' Name ----- pKa ----- logP_n,lip ---logP_d,lip---Cc(mM)-----Cm(mM)-----
--Cb(mM)-----Peff(cm/sec) ' ;
fprintf(fid1,'%s\n',str1) ;

for n = 1:len
    if ( abs(ZNall(n)-1) <= 10^(-6) )
        logP_nlipT(n) = 0.33*logPnall(n)+2.2 ;
        logP_dlipT(n) = 0.37*logPdall(n)+2 ;
    end
    if ( abs(ZNall(n)+1) <= 10^(-6) )
        logP_nlipT(n) = 0.37*logPnall(n)+2.2 ;
        logP_dlipT(n) = 0.33*logPdall(n)+2.6 ;
    end
    if ( abs(ZNall(n)-0) <= 10^(-5) )
        logP_nlipT(n) = 0.33*logPnall(n)+2.2 ;
        logP_dlipT(n) = 0.33*logPdall(n)+2.2 ;
    end
end
end

% Get the first two decimals

```

```

logP_nlip = round(logP_nlipT*100)/100 ;
logP_dlip = round(logP_dlipT*100)/100 ;

% Solve the differential equation system for each drug:
% Given a system of linear ODE's expressed in matrix form:
% Y' = AY+G with initial conditions Y(0) = RR,

for n = 1:len
    pKa = pKaall(n);
    logP_n = logP_nlip(n) ;
    logP_d = logP_dlip(n) ;
    z = ZNall(n) ;

    % Parameters Calculation
    i = -sign(z) ;
    Na = ((z)*(Ea)*F)/(R*T);
    Nm = ((z)*(Em)*F)/(R*T);
    Nb = ((z)*(-Eb)*F)/(R*T);

    Pn = 10^(logP_n-6.7);
    Pd = 10^(logP_d-6.7);
    Kn_a = La*1.22*10^(logP_n);
    Kd_a = La*1.22*10^(logP_d);
    Kn_c = Lc*1.22*10^(logP_n);
    Kd_c = Lc*1.22*10^(logP_d);
    Kn_m = Lm*1.22*10^(logP_n);
    Kd_m = Lm*1.22*10^(logP_d);
    Kn_b = Lb*1.22*10^(logP_n);
    Kd_b = Lb*1.22*10^(logP_d);

    % Construct the matrix A and G
    fn_a = 1/(Wa/gamma_na+Kn_a/gamma_na+Wa*10^(i*(pHa-pKa))/gamma_da...
        +Kd_a*10^(i*(pHa-pKa))/gamma_da);
    fd_a = fn_a*10^(i*(pHa-pKa));
    fn_c = 1/(Wc/gamma_nc+Kn_c/gamma_nc+Wc*10^(i*(pHc-pKa))/gamma_dc...
        +Kd_c*10^(i*(pHc-pKa))/gamma_dc);
    fd_c = fn_c*10^(i*(pHc-pKa));
    fn_m = 1/(Wm/gamma_nm+Kn_m/gamma_nm+Wm*10^(i*(pHm-
pKa))/gamma_dm...
        +Kd_m*10^(i*(pHm-pKa))/gamma_dm);
    fd_m = fn_m*10^(i*(pHm-pKa));
    fn_b = 1/(Wb/gamma_nb+Kn_b/gamma_nb+Wb*10^(i*(pHb-pKa))/gamma_db...
        +Kd_b*10^(i*(pHb-pKa))/gamma_db);
    fd_b = fn_b*10^(i*(pHb-pKa));

```

```

k11 = -(Aa/Vc)*Pn*fn_c-(Aa/Vc)*Pd*Na*fd_c*exp(Na)/(exp(Na)-1)...
      -(Am/Vc)*Pn*fn_c-(Am/Vc)*Pd*Nm*fd_c/(exp(Nm)-1)...
      -(Ab/Vc)*Pn*fn_c-(Ab/Vc)*Pd*Nb*fd_c/(exp(Nb)-1) ;
k12 = (Am/Vc)*Pn*fn_m+(Am/Vc)*Pd*Nm*fd_m*exp(Nm)/(exp(Nm)-1) ;
k13 = (Ab/Vc)*Pn*fn_b+(Ab/Vc)*Pd*Nb*fd_b*exp(Nb)/(exp(Nb)-1) ;
S1 = (Aa/Vc)*Ca*(Pn*fn_a+Pd*Na*fd_a/(exp(Na)-1)) ;

k21 = (Am/Vm)*Pn*fn_c+(Am/Vm)*Pd*Nm*fd_c/(exp(Nm)-1) ;
k22 = -(Am/Vm)*Pn*fn_m-(Am/Vm)*Pd*Nm*fd_m*exp(Nm)/(exp(Nm)-1) ;
k23 = 0;
S2 = 0;

k31 = (Ab/Vb)*Pn*fn_c+(Ab/Vb)*Pd*Nb*fd_c/(exp(Nb)-1) ;
k32 = 0;
k33 = -(Ab/Vb)*Pn*fn_b-(Ab/Vb)*Pd*Nb*fd_b*exp(Nb)/(exp(Nb)-1) ;
S3 = 0;

A = [k11, k12, k13; k21, k22, k23; k31, k32, k33];
G = [S1, S2, S3]';
RR = [0,0,0]';
t = 1000; % Calculate the intracellular concentration and permeability and t=1000s,
which is at steady state

[V,E] = eig(A);
E = diag(E);
H = inv(V)*G;
B = V \ RR;
C = B + H./E;
Z = -(H./E) + exp(t * E).*C ;
Y = real(V * Z);
Y = Y';
Peff = Y(3)*Vb/(t*Aaa*Ca);
NA = [pKa, logP_n, logP_d, Y, Peff*10^(8)];
str = DrugName{n};
fprintf(fid1,'%s\t %12.2f %12.2f %12.2f %12.2f %12.2f %+12.4e %12.2f\n',str, NA')
;
end
fclose(fid1);

```

APPENDIX B

Examples of Matlab Code of Monte Carlo Simulations

```
% This script is to perform Monte Carlo simulations for 1CellPK
% This script uses Case#1 as an example:
% Case# 1: AP->BL transport, pHa = 6.5, 0.4um-membrane, 5min
% Case# 2: AP->BL transport, pHa = 6.5, 3um-membrane, 5min
% Case# 3: AP->BL transport, pHa = 7.4, 0.4um-membrane, 5min
% Case# 4: AP->BL transport, pHa = 7.4, 3um-membrane, 5min

% Case# 5: BL->AP transport, pHb = 6.5, 0.4um-membrane, 5min
% Case# 6: BL->AP transport, pHb = 6.5, 3um-membrane, 5min
% Case# 7: BL->AP transport, pHb = 7.4, 0.4um-membrane, 5min
% Case# 8: BL->AP transport, pHb = 7.4, 3um-membrane, 5min

% Case#1: AP->BL transport, pHa = 6.5, 0.4um-membrane,5min
clear ;          % Clear the memory
z1 = 1 ;        % ionization group 1 of CQ
z2 = 2 ;        % ionization group 2 of CQ
i1 = sign(z1) ;
i2 = sign(z2) ;

T = 310.15 ;    % temperature
R = 8.314 ;     % universal gas constant
F = 96484.56 ; % faraday constant
C_a = 1 ;      % initial drug concentration (mM)

sim = 10000;    % number of simulations
paraNo = 25;
outputNo = 7;  % number of output parameters
Para = zeros(sim,paraNo);
Results = zeros(sim,outputNo);

dMdt_exp = 2.2E-6; % +/- 7.18E-7, pmol/sec/cell, measured after 4hrs
Ppore_exp = 2.18E+02; % +/- 34.4, 10^-6 cm/sec, measured after 4hrs
Peff_exp = 1.35; % +/- 0.442, 10^-6 cm/sec, measured after 4hrs
IntraMass_exp = 0.00373; % +/- 0.00014 pmol/cell , measured after 5min

for i = 1:sim
```

```

% Drug information -- ChemAxon calculation including logPn, pKa1, and pKa2
logPn = 3.93-0.5+rand(); % unif [3.43, 4.43] ;
pKa1 = 9.96-0.5+rand(); % unif [9.46, 10.46] ;
pKa2 = 7.47-0.5+rand(); % unif [6.97, 7.97] ;
logPd1 = 0.43-0.5+rand(); % unif [-0.07, 0.93] ;
logPd2 = -0.91-0.5+rand(); % unif [-1.41, 0.41] ;
Pn = 10^(logPn-6.7);
Pd1 = 10^(logPd1-6.7);
Pd2 = 10^(logPd2-6.7);

CellNo = 2*10^5*(1+rand()); % cell number/insert: unif [2*10^5, 4*10^5]
PoreDens = 4*10^6*0.4*(2+rand()); % pore number/cm^2: unif [3.2*10^6, 4.8*10^6]
A_insert = 1.12*10^(-4) ; % insert area: 1.12 cm^2
PoreNo_insert = PoreDens*A_insert*10^(4); % pore number/insert
PoreNo_cell = PoreNo_insert/CellNo ; % average pore number/cell
A_pore_insert = 3.14*((0.4/2)*10^(-6))^2*PoreNo_insert ; % pore area / insert (m^2)
A_pore_cell = 3.14*((0.4/2)*10^(-6))^2*PoreNo_cell ; % average pore area / cell
(m^2)

A_a = 10^(-10)*(1+9*rand()); % apical membrane surface area: unif [10^(-
10),10*(10)^(-10)] (m^2)
A_aa = A_pore_cell; % pore area/cell (m^2)
A_b = A_aa+(10^(-10)-A_aa)*rand(); % basolateral membrane surface area: unif
[A_aa, 10^(-10)] (m^2)
A_l = 100*3.14*10^(-12); % lysosomal membrane surface area (m^2)
A_m = 100*3.14*10^(-12); % mitochondrial membrane surface area (m^2)
V_c = 0.5*10^(-15)*(1+5*rand()); % cytosolic volume: unif [0.5*10^(-15),
3*10^(-15)] (m^3)
V_l = 10^(-18)*(9.24+(23.8-9.24)*rand()); % lysosomal volume: unif [9.24*10^(-
18), 23.8*10^(-18)] (m^3)
V_m = 100*5.24*10^(-19)/5*(1+24*rand()); % mitochondrial volume: unif
[10.48*10^(-18), 262*10^(-18)](m^3)
V_b = 1.5*10^(-6); % basolateral volume: 1.5 mL

% Membrane potential (unit in 'Voltage')
E_a = -0.0093-0.005+0.01*rand(); % apical membrane potential: unif [-0.0143, -
0.0043]
E_l = 0.01-0.005+0.01*rand(); % lysosomal membrane potential: unif [0.005, 0.015]
E_m = -0.16 ; % mitochondrial membrane potential
E_b = 0.0119-0.005+0.01*rand(); % basolateral membrane potential: unif [0.0069,
0.0169]

% pH values
pH_a = 6.4+0.2*rand(); % pH in apical compartment: unif [6.4, 6.6]
pH_c = 7.0+0.4*rand(); % pH in cytosol: unif [7.0, 7.4]

```

```

pH_1 = 4.8+0.4*rand();    % pH in lysosomes: unif [4.8, 5.2]
pH_m = 7.8+0.4*rand();    % pH in mitochondria: unif[7.8, 8.2]
pH_b = 7.4;                % pH in basolateral compartment

% Apical Compartment
fn_a = 1 / (1 + 10^(i1*(pKa1-pH_a)) + 10^(i1*(pKa1-pH_a)+i2*(pKa2-pH_a))) ;
fd2_a = fn_a * 10^(i1*(pKa1-pH_a)+i2*(pKa2-pH_a)) ;
fd1_a = fn_a * 10^(i1*(pKa1-pH_a)) ;
Nd2_a = z2*E_a*F/(R*T) ;
Nd1_a = z1*E_a*F/(R*T) ;

% Cytoplasm
L_c = 0.05+0.1*rand();    % lipid fraction in cytosol: unif [0.05, 0.15]
W_c = 1-L_c ;            % water fraction in cytosol
Is_c = 0.3 ;             % ion strength in cytosol (mol)
gamman_c = 10^(0.3*Is_c) ; % activity coefficient of neutral molecules in cytosol
gammad1_c = 10^(-0.5*z1*z1*(sqrt(Is_c)/(1+sqrt(Is_c))-0.3*Is_c)); % activity
coefficient of monovalent base in cytosol
gammad2_c = 10^(-0.5*z2*z2*(sqrt(Is_c)/(1+sqrt(Is_c))-0.3*Is_c)); % activity
coefficient of bivalent base in cytosol
Kn_c = L_c*1.22*10^(logPn) ;
Kd1_c = L_c*1.22*10^(logPd1) ;
Kd2_c = L_c*1.22*10^(logPd2) ;
an_c = 1 / (1 + 10^(i1*(pKa1-pH_c)) + 10^(i1*(pKa1-pH_c)+i2*(pKa2-pH_c))) ;
ad2_c = an_c * 10^(i1*(pKa1-pH_c)+i2*(pKa2-pH_c)) ;
ad1_c = an_c * 10^(i1*(pKa1-pH_c)) ;
Dd2_c = ad2_c / an_c ;
Dd1_c = ad1_c / an_c ;
fn_c = 1 / (W_c/gamman_c + Kn_c/gamman_c + Dd2_c*W_c/gammad2_c +
Dd2_c*Kd2_c/gammad2_c + Dd1_c*W_c/gammad1_c + Dd1_c*Kd1_c/gammad1_c) ;
fd2_c = fn_c * Dd2_c ;
fd1_c = fn_c * Dd1_c ;

% Mitochondria
L_m = 0.05+0.1*rand();    % lipid fraction in mitochondria: unif [0.05, 0.15]
W_m = 1-L_m ;            % water fraction in mitochondria
Is_m = 0.3 ;             % ion strength in mitochondria (mol)
Nd2_m = z2*E_m*F/(R*T) ;
Nd1_m = z1*E_m*F/(R*T) ;
gamman_m = 10^(0.3*Is_m) ; % activity coefficient of neutral molecules in
mitochondria
gammad1_m = 10^(-0.5*z1*z1*(sqrt(Is_m)/(1+sqrt(Is_m))-0.3*Is_m)); % activity
coefficient of monovalent base in mitochondria
gammad2_m = 10^(-0.5*z2*z2*(sqrt(Is_m)/(1+sqrt(Is_m))-0.3*Is_m)); % activity
coefficient of bivalent base in mitochondria
Kn_m = L_m*1.22*10^(logPn) ;

```



```

Kd1_m = L_m*1.22*10^(logPd1) ;
Kd2_m = L_m*1.22*10^(logPd2) ;
an_m = 1 / (1 + 10^(i1*(pKa1-pH_m)) + 10^(i1*(pKa1-pH_m)+i2*(pKa2-pH_m))) ;
ad2_m = an_m * 10^(i1*(pKa1-pH_m)+i2*(pKa2-pH_m)) ;
ad1_m = an_m * 10^(i1*(pKa1-pH_m)) ;
Dd2_m = ad2_m / an_m ;
Dd1_m = ad1_m / an_m ;
fn_m = 1 / (W_m/gamman_m + Kn_m/gamman_m + Dd2_m*W_m/gammad2_m +
Dd2_m*Kd2_m/gammad2_m ...
+ Dd1_m*W_m/gammad1_m + Dd1_m*Kd1_m/gammad1_m) ;
fd2_m = fn_m * Dd2_m ;
fd1_m = fn_m * Dd1_m ;

% Lysosomes
L_1 = 0.05+0.1*rand(); % lipid fraction in mitochondria: unif [0.05, 0.15]
W_1 = 1-L_1 ; % water fraction in lysosomes
Is_1 = 0.3 ; % ion strength in lysosomes (mol)
Nd2_1 = z2*E_1*F/(R*T) ;
Nd1_1 = z1*E_1*F/(R*T) ;
gamman_1 = 10^(0.3*Is_1) ; % activity coefficient of neutral molecules in lysosomes
gammad1_1 = 10^(-0.5*z1*z1*(sqrt(Is_1)/(1+sqrt(Is_1))-0.3*Is_1)) ; % activity
coefficient of monovalent base in lysosomes
gammad2_1 = 10^(-0.5*z2*z2*(sqrt(Is_1)/(1+sqrt(Is_1))-0.3*Is_1)) ; % activity
coefficient of bivalent base in lysosomes
Kn_1 = L_1*1.22*10^(logPn) ;
Kd1_1 = L_1*1.22*10^(logPd1) ;
Kd2_1 = L_1*1.22*10^(logPd2) ;
an_1 = 1 / (1 + 10^(i1*(pKa1-pH_1)) + 10^(i1*(pKa1-pH_1)+i2*(pKa2-pH_1))) ;
ad2_1 = an_1 * 10^(i1*(pKa1-pH_1)+i2*(pKa2-pH_1)) ;
ad1_1 = an_1 * 10^(i1*(pKa1-pH_1)) ;
Dd2_1 = ad2_1 / an_1 ;
Dd1_1 = ad1_1 / an_1 ;
fn_1 = 1 / (W_1/gamman_1 + Kn_1/gamman_1 + Dd2_1*W_1/gammad2_1 +
Dd2_1*Kd2_1/gammad2_1 ...
+ Dd1_1*W_1/gammad1_1 + Dd1_1*Kd1_1/gammad1_1) ;
fd2_1 = fn_1 * Dd2_1 ;
fd1_1 = fn_1 * Dd1_1 ;

% Basolateral Compartment
fn_b = 1 / (1 + 10^(i1*(pKa1-pH_b)) + 10^(i1*(pKa1-pH_b)+i2*(pKa2-pH_b))) ;
fd2_b = fn_b * 10^(i1*(pKa1-pH_b)+i2*(pKa2-pH_b)) ;
fd1_b = fn_b * 10^(i1*(pKa1-pH_b)) ;
Nd2_b = z2*(-E_b)*F/(R*T) ;
Nd1_b = z1*(-E_b)*F/(R*T) ;

% Solve the differential equation system:

```

```

% Given a system of linear ODE's expressed in matrix form:
% Y' = AY+G with initial conditions Y(0) = RR,
k11 = -(A_a/V_c)*Pn*fn_c-
(A_a/V_c)*Pd1*Nd1_a*fd1_c*exp(Nd1_a)/(exp(Nd1_a)-1)...
-(A_a/V_c)*Pd2*Nd2_a*fd2_c*exp(Nd2_a)/(exp(Nd2_a)-1)...
-(A_m/V_c)*Pn*fn_c-(A_m/V_c)*Pd1*Nd1_m*fd1_c/(exp(Nd1_m)-1)...
-(A_m/V_c)*Pd2*Nd2_m*fd2_c/(exp(Nd2_m)-1)...
-(A_l/V_c)*Pn*fn_c-(A_l/V_c)*Pd1*Nd1_l*fd1_c/(exp(Nd1_l)-1)...
-(A_l/V_c)*Pd2*Nd2_l*fd2_c/(exp(Nd2_l)-1)...
-(A_b/V_c)*Pn*fn_c-(A_b/V_c)*Pd1*Nd1_b*fd1_c/(exp(Nd1_b)-1)...
-(A_b/V_c)*Pd2*Nd2_b*fd2_c/(exp(Nd2_b)-1) ;
k12 =
(A_m/V_c)*Pn*fn_m+(A_m/V_c)*Pd1*Nd1_m*fd1_m*exp(Nd1_m)/(exp(Nd1_m)-1)...
+(A_m/V_c)*Pd2*Nd2_m*fd2_m*exp(Nd2_m)/(exp(Nd2_m)-1);
k13 = (A_l/V_c)*Pn*fn_l+(A_l/V_c)*Pd1*Nd1_l*fd1_l*exp(Nd1_l)/(exp(Nd1_l)-
1)...
+(A_l/V_c)*Pd2*Nd2_l*fd2_l*exp(Nd2_l)/(exp(Nd2_l)-1);
k14 =
(A_b/V_c)*Pn*fn_b+(A_b/V_c)*Pd1*Nd1_b*fd1_b*exp(Nd1_b)/(exp(Nd1_b)-1)...
+(A_b/V_c)*Pd2*Nd2_b*fd2_b*exp(Nd2_b)/(exp(Nd2_b)-1);
S1 = (A_a/V_c)*C_a*(Pn*fn_a+Pd1*Nd1_a*fd1_a/(exp(Nd1_a)-1)...
+Pd2*Nd2_a*fd2_a/(exp(Nd2_a)-1)) ;

k21 = (A_m/V_m)*Pn*fn_c+(A_m/V_m)*Pd1*Nd1_m*fd1_c/(exp(Nd1_m)-1)...
+(A_m/V_m)*Pd2*Nd2_m*fd2_c/(exp(Nd2_m)-1) ;
k22 = -(A_m/V_m)*Pn*fn_m-
(A_m/V_m)*Pd1*Nd1_m*fd1_m*exp(Nd1_m)/(exp(Nd1_m)-1)...
-(A_m/V_m)*Pd2*Nd2_m*fd2_m*exp(Nd2_m)/(exp(Nd2_m)-1) ;
k23 = 0;
k24 = 0 ;
S2 = 0;

k31 = (A_l/V_l)*Pn*fn_c+(A_l/V_l)*Pd1*Nd1_l*fd1_c/(exp(Nd1_l)-1)...
+(A_l/V_l)*Pd2*Nd2_l*fd2_c/(exp(Nd2_l)-1) ;
k32 = 0;
k33 = -(A_l/V_l)*Pn*fn_l-(A_l/V_l)*Pd1*Nd1_l*fd1_l*exp(Nd1_l)/(exp(Nd1_l)-
1)...
-(A_l/V_l)*Pd2*Nd2_l*fd2_l*exp(Nd2_l)/(exp(Nd2_l)-1) ;

k34 = 0 ;
S3 = 0;

k41 = (A_b/V_b)*Pn*fn_c+(A_b/V_b)*Pd1*Nd1_b*fd1_c/(exp(Nd1_b)-1)...
+(A_b/V_b)*Pd2*Nd2_b*fd2_c/(exp(Nd2_b)-1) ;
k42 = 0;
k43 = 0;

```

```

k44 = -(A_b/V_b)*Pn*fn_b-
(A_b/V_b)*Pd1*Nd1_b*fd1_b*exp(Nd1_b)/(exp(Nd1_b)-1)...
-(A_b/V_b)*Pd2*Nd2_b*fd2_b*exp(Nd2_b)/(exp(Nd2_b)-1);
S4 = 0;

A = [k11, k12, k13, k14; k21, k22, k23, k24; k31, k32, k33, k34; k41, k42, k43,
k44];
G = [S1, S2, S3, S4]';
RR = [0,0,0,0]';
t = 300 ; % time in sec (5min)

[V,E] = eig(A);
E = diag(E);
H = inv(V)*G;
B = V \ RR;
C = B + H./E;
Z = -(H./E) + exp(t * E).*C ;
Y = real(V * Z);
Y = Y' ;

Ppore = Y(4)*V_b/(t*A_aa*C_a)*10^(2)*10^6 ; % Pcell, 10^(-6)cm/sec
Peff = Y(4)*V_b*CellNo/(t*A_insert*C_a)*10^(2)*10^6; % Peff, 10^(-6)cm/sec,
normalized by insert area, which is 1.12 cm^2
Mass_cell = (Y(1)*V_c + Y(2)*V_m + Y(3)*V_l)*10^12 ; % cellular mass,
pmol/cell
dMdt = Y(4)*V_b/t*10^12; % transport rate: pmol/sec/cell

Para(i,:) = [A_a*10^12,PoreNo_cell,
A_l*10^12,A_m*10^12,A_b*10^12,V_c*10^18,V_l*10^18,V_m*10^18,V_b*10^6,E_a
*1000,E_l*1000,E_m*1000,E_b*1000,...
pH_a,pH_c,pH_l,pH_m,pH_b,CellNo,PoreDens, pKa1,pKa2,logPn,logPd1,
logPd2];
Results(i,:)=[Y(1),Y(2),Y(3),Ppore, Peff, dMdt, Mass_cell];

end

comb = [Results(:,1:7),Para];
fid5 = fopen('AtoB_pH65_04um_5min.dat','w');
fprintf(fid5,'%12.4e %12.4e %12.4e %12.4e %12.4e %12.4e %12.4e %12.2e %12.0f
%12.4e %12.4e %12.4e %12.4e %12.4e %12.4e %12.4e %12.4f %12.4f %12.4f %12.4f
%12.2f %12.2f %12.2f %12.2f %12.2f %12.0f %12.0f %12.2f %12.2f %12.2f %12.2f
%12.2f\n', comb) ;
fclose(fid5);

figure(1) ; clf ; hold on ;

```

```

grid on;
hist (log10(comb(:,4)),1000);
line([log10(Ppore_exp), log10(Ppore_exp)], [0,50], 'Color', 'r', 'LineWidth', 3);
xlabel('log_{10} (P_{cell}, 10^{-6}
cm/sec)', 'FontSize', 30, 'FontWeight', 'Bold', 'FontName', 'Times');
xlim([0, 6]);
ax1 = gca;
set(get(ax1, 'Ylabel'), 'String', 'Frequency', 'FontSize', 30, 'FontWeight', 'Bold', 'FontName', 'Times');
set(ax1, 'LineWidth', 2.0, 'FontSize', 30, 'FontWeight', 'Bold', 'FontName', 'Times');
title ('histogram of cell
permeability', 'FontSize', 30, 'FontWeight', 'Bold', 'FontName', 'Times');

```

```

figure(2) ; clf ; hold on ;
grid on;
hist (log10(comb(:,5)),1000);
xlim([-3, 3]);
line([log10(Peff_exp), log10(Peff_exp)], [0,50], 'Color', 'r', 'LineWidth', 3);
xlabel('log_{10} (P_{app}, 10^{-6}
cm/sec)', 'FontSize', 30, 'FontWeight', 'Bold', 'FontName', 'Times');
ax1 = gca;
set(get(ax1, 'Ylabel'), 'String', 'Frequency', 'FontSize', 30, 'FontWeight', 'Bold', 'FontName', 'Times');
set(ax1, 'LineWidth', 2.0, 'FontSize', 30, 'FontWeight', 'Bold', 'FontName', 'Times');
title ('histogram of apparent
permeability', 'FontSize', 30, 'FontWeight', 'Bold', 'FontName', 'Times');

```

```

figure(3) ; clf ; hold on ;
grid on;
hist (log10(comb(:,6)),1000);
xlim([-8,-2]);
line([log10(dMdt_exp), log10(dMdt_exp)], [0,50], 'Color', 'r', 'LineWidth', 3);
xlabel('log_{10} (dM/dt,
pmol/sec/cell)', 'FontSize', 30, 'FontWeight', 'Bold', 'FontName', 'Times');
ax1 = gca;
set(get(ax1, 'Ylabel'), 'String', 'Frequency', 'FontSize', 30, 'FontWeight', 'Bold', 'FontName', 'Times');
set(ax1, 'LineWidth', 2.0, 'FontSize', 30, 'FontWeight', 'Bold', 'FontName', 'Times');
title ('histogram of transport rate', 'FontSize', 30, 'FontWeight', 'Bold', 'FontName', 'Times');

```

```

figure(4) ; clf ; hold on ;
grid on;
hist (log10(comb(:,7)),1000);
xlim([-5,-0]);
line([log10(IntraMass_exp), log10(IntraMass_exp)], [0,50], 'Color', 'r', 'LineWidth', 3);

```

```
xlabel('log_{10} (intracellular mass, pmol/cell)'  
, 'FontSize', 30, 'FontWeight', 'Bold', 'FontName', 'Times');  
ax1 = gca;  
set(get(ax1, 'Ylabel'), 'String', 'Frequency', 'FontSize', 30, 'FontWeight', 'Bold', 'FontName', 'Times');  
set(ax1, 'LineWidth', 2.0, 'FontSize', 30, 'FontWeight', 'Bold', 'FontName', 'Times');  
title ('histogram of intracellular  
mass', 'FontSize', 30, 'FontWeight', 'Bold', 'FontName', 'Times');
```

APPENDIX C

Scripts

Symbols:

a ---- activity

A ---- membrane area

A_{aa} ---- effective cross-sectional area

$B:P$ ---- blood : plasma partition coefficient

C ---- concentration

CL ---- clearance

E ---- membrane potential

F ---- the Faraday constant

J ---- net flux cross the membrane

K ---- sorption coefficients

K_{ow} ---- lipophilicity of small molecules

$K_{p,t}$ ---- tissue : plasma partition coefficient

K_{iv} ---- the intravenous injection or infusion rate

L ---- lipid fraction

$\log P$ ---- octanol water partition coefficient

$\log P_{lip}$ ---- liposomal partition coefficient

m ---- mass

pK_a ---- the negative logarithm(\log_{10}) of the dissociation constant

P ---- permeability of molecules through the membrane

P_{app} ---- apparent permeability

P_{cell} ---- cell permeability

P_{eff} ---- effective permeability

Q ---- blood flow rate

R ---- the universal gas constant

R_{abs} ---- absorption rate

T ---- temperature

V ---- volume

W ---- Volumetric water fraction

z ---- electric charge

γ ---- activity coefficient

Subscripts

a ---- apical

b ---- basolateral

c ---- cytosol

d ---- ionic form
m ---- mitochondria
n ---- neutral form
aEp ---- surface lining liquid
imEp ---- macrophage
cEp ---- epithelial cells
cEpMito ---- mitochondria in epithelial cells
cEpLyso ---- lysosomes in epithelial cells
int ---- interstitium
imInt ---- immune cells
sm ---- smooth muscle cells
smMito ---- mitochondria in smooth muscle cells
smLyso ---- lysosomes in smooth muscle cells
cEd ---- endothelial cells
cEdMito ---- mitochondria in endothelial cells
cEdLyso ---- lysosomes in endothelial cells
plung ---- plasma in the lung
ca ---- heart
bo ---- bone
mu ---- muscle
fa ---- fat
sk ---- skin
th ---- thymus
br ---- brain
sp ---- spleen
gu ---- gut
rob ----rest of body
lv ---- liver
ha ---- hepatic arterial blood
vb ---- venous blood
ab ---- arterial blood

APPENDIX D

Tables and Figures Regenerated at 410K for Chapter II

Table Appd.D.1. Structures, physicochemical properties, average Caco2 permeabilities, and predictive permeabilities of seven β -adrenergic blockers in Figure Appd.D.2. The $\log P_{n, lip}$ values are the calculated liposomal $\log P_n$ which were used in permeability calculation.

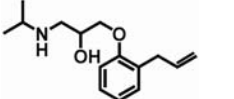
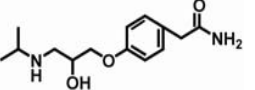
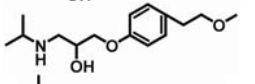
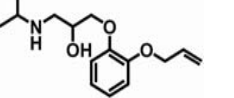
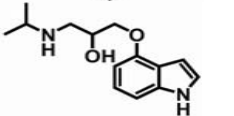
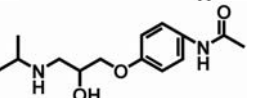
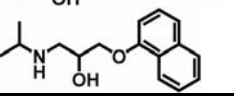
Name	Structures	pK_a	$\log P_n$	$\log P_{n, lip}$	Caco-2 P_{eff} (10^{-6} cm/s)	P_{eff}	C_{cyto} (mM)	C_{mito} (mM)
						(10^{-6} cm/s)	Calculated	
alprenolol		9.60	3.10	3.22	95.70	91.18	7.89	7.82
atenolol		9.60	0.16	2.25	1.07	7.44	2.07	5.99
metoprolol		9.70	1.88	2.82	40.15	32.28	3.82	8.69
oxprenolol		9.50	2.10	2.89	97.25	39.16	4.25	5.76
pindolol		9.70	1.75	2.78	54.53	28.78	3.57	8.50
practolol		9.50	0.79	2.46	2.91	12.71	2.41	5.03
propranolol		9.49	2.98	3.18	34.80	81.73	7.19	6.03

Table Appd.D.2. Comparison of predicted permeability with average Caco2 permeability and PAMA permeability of drugs within the predictive circle in Figure Appd.D.3. Permeability values are in unit of 10^{-6} cm/sec. Metoprolol was chosen a reference compound. (H stands for ‘high permeability’, L stands for ‘low permeability’)

Drugs	Predicted Permeability		PAMPA		PAMPA (at pH7.4)		PAMPA (at pH7.4)		Human intestinal permeability		FDA Waiver Guidance	Tentative BCS Classification
alprenolol	91.18	H	11.5	H			15.1	H				
antipyrine	209.00	H	2.87	L	0.82	L	13.2	H	560	H	H	
chlorpromazine	653.08	H					4.0	H				1
clonidine	43.82	H	10.41	H			14.0	H				
desipramine	410.18	H	16.98	H			14.6	H	450	H		
diazepam	196.71	H										
diltiazem	122.32	H	19.21	H	14	H	18.5	H				2
ibuprophen	321.84	H	21.15	H			6.8	H				2
imipramine	391.33	H	19.36	H			8.4	H				
indomethacin	406.52	H					2.4	L				
ketoprofen	167.04	H	2.84	L	0.043	L	16.7	H	870	H	H	
lidocaine	126.50	H										
metoprolol	32.28	ref	7.93	ref	1.2	ref	3.5	ref	134	ref	H	
naproxen	175.61	H	5.01	L	0.23	L	10.6	H	850	H	H	
oxprenolol	39.16	H	14.64	H								
phenytoin	86.02	H	38.53	H			5.1	H				
pindolol	28.78	L	4.91	L			4.9	H				
piroxicam	1541.60	H	10.87	H			8.2	H	665	H		
propranolol	79.41	H	26.33	H	12	H	23.5	H	291	H	H	1
trimethoprim	194.22	H	3.14	L	2.2	H	5.0	H				4
valproic acid	144.11	H										3

verapamil	191.16	H	23.02	H	14	H	7.4	H	680	H	H	1
warfarin	129.23	H					12.3	H				

Table Appd.D.3: Correlation of predicted permeability vs. human intestinal permeability. (Permeability values are in unit of 10^{-6} cm/sec.)

Name	Human Permeability	$\log(P_{\text{eff, human}})$	Predicted Permeability	$\log(P_{\text{eff, predicted}})$
antipyrine	560.00	-3.25	209.00	-3.68
atenolol	20.00	-4.70	7.44	-5.13
desipramine	450.00	-3.35	410.18	-3.39
ketoprofen	870.00	-3.06	167.04	-3.78
metoprolol	134.00	-3.87	32.28	-4.49
naproxen	850.00	-3.07	175.61	-3.76
piroxicam	665.00	-3.18	1542.75	-2.81
propranolol	291.00	-3.54	81.73	-4.09
terbutaline	30.00 <i>c</i>	-4.52	22.96	-4.64
verapamil	680.00	-3.17	191.16	-3.72

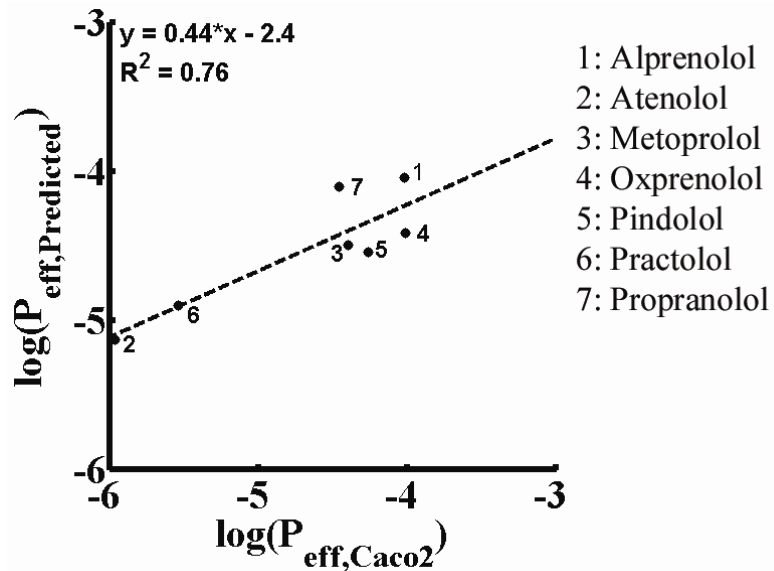


Figure Appd.D.1. Correlation of Caco2 permeability and predicted permeability of seven β -adrenergic blockers. The X-axis indicates the logarithm values of average measured Caco2 permeability (cm/sec) and the Y-axis indicate the logarithm values of predicted permeability (cm/sec). The dotted line is the linear regression line. The linear regression equation is $y = 0.44x - 2.4$ ($R^2 = 0.76$), the significance F of regression given by EXCEL is 0.011 (confidence level is 95%). Numbers 1 through 7 indicate alprenolol, atenolol, metoprolol, oxprenolol, pindolol, practolol, and propranolol respectively. The structures, physicochemical properties, average Caco2 permeability and predictive permeability were summarized in Table Appd.D.1.

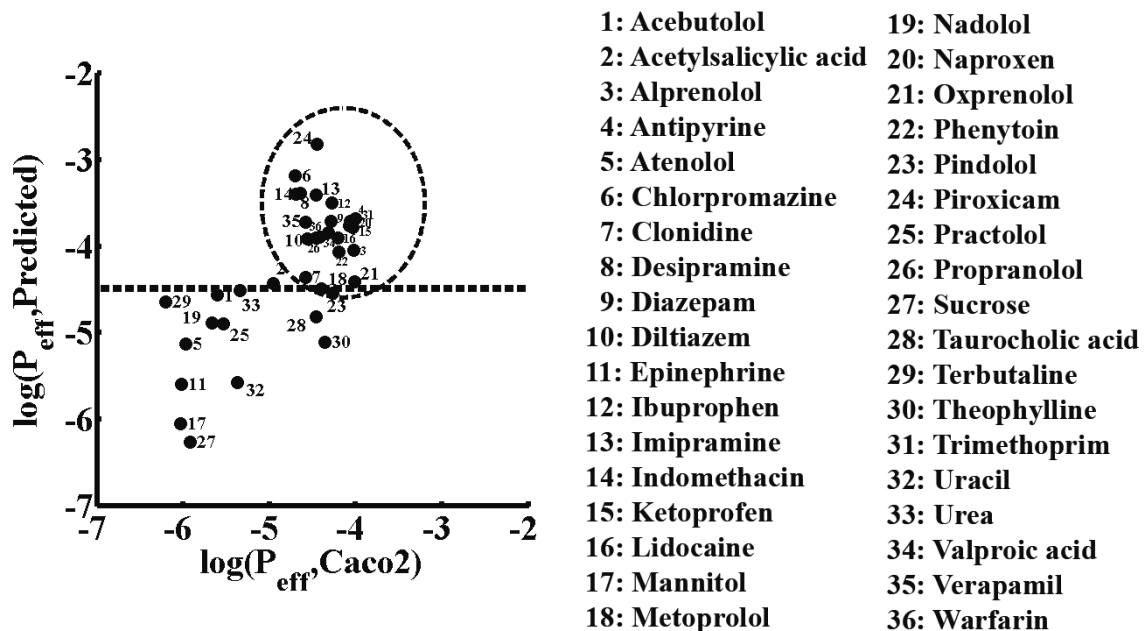


Figure Appd.D.2. Correlation of Caco2 permeability and predicted permeability of thirty-six drugs. The X-axis indicates the logarithm values of average measured Caco2 permeability (cm/sec) and the Y-axis indicate the logarithm values of predicted permeability (cm/sec). Metoprolol (No.18) was used as a reference drug. Details of calculated permeability and average Caco2 permeability were included in the Supplementary Materials.

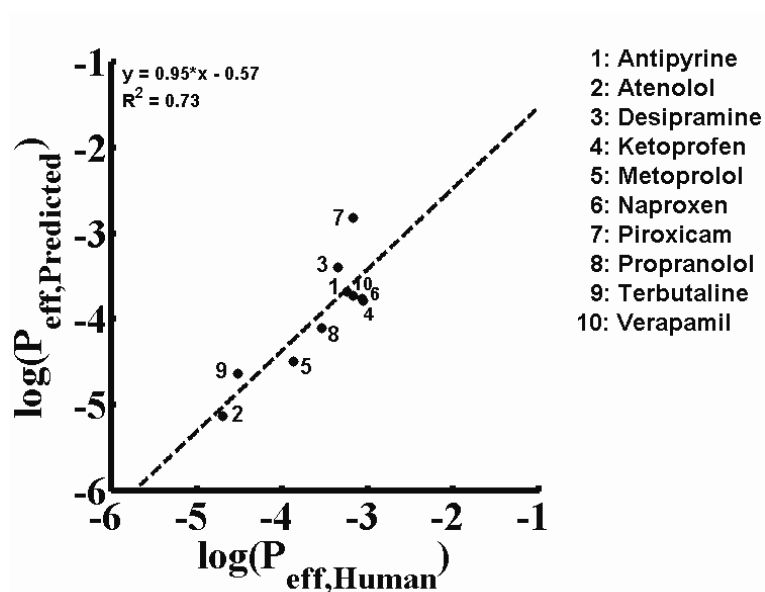


Figure Appd.D.3. Correlation of human intestinal permeability and predicted permeability. The X-axis indicates the logarithm values of measured human intestinal permeability (cm/sec) and the Y-axis indicate the logarithm values of predicted permeability (cm/sec). A simple linear relation was obtained and expressed by the equation: $y = 0.95x - 0.57 (R^2 = 0.73)$, the significance F of regression given by EXCEL is 0.0016 (confidence level is 95%). Calculated permeability and human intestinal permeability numbers were listed in Table Appd.D.3.

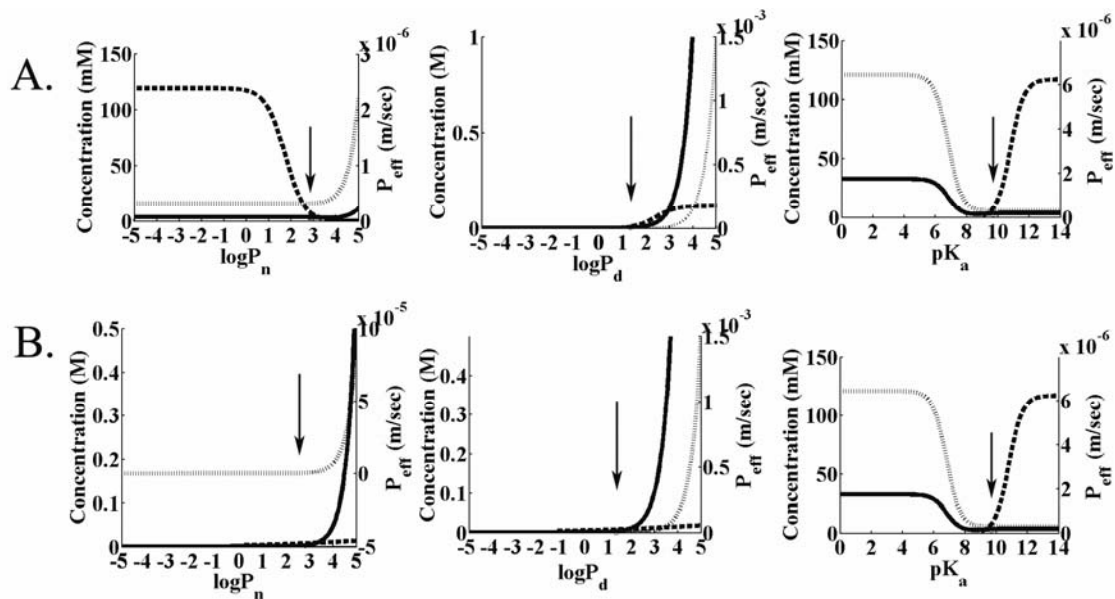


Figure Appd.D.4. Effects of physicochemical properties on intracellular concentration (solid line = cytosolic; dark dotted line = mitochondrial) and permeability (light stippled line) at steady state, of a molecule with metoprolol-like properties (arrows). A. $\log P_n$ and $\log P_d$ are not associated. B. $\log P_n$ and $\log P_d$ are associated by a simple linear relationship expressed as equations 2.27-2.29. The arrows indicate the liposomal $\log P_{n, lip}$ and $\log P_{d, lip}$, which were used in permeability calculation.

APPENDIX E

Parameters for the Tracheobronchial Airways and Alveolar Region in the Rat

Compartments	Tracheobronchial Airways ^a			Alveolar Region ^a		
	Average thickness (μm)	Surface area (cm ²)	Volume (cm ³)	Average thickness (μm)	Surface area (cm ²)	Volume (cm ³)
Surface lining liquid	15 ^b	108	0.162	5	3870	1.935
Macrophage	-	-	-	-	42	0.0282
Epithelium	24-9 ^c	108	0.072 ^d	0.384	3870	0.148
Interstitialium	1 ^d	108	0.0108 ^d	0.693	3870	0.268
Immune cells	-	1.08 ^b	0.000108 ^d	-	4.2 ^d	0.00282 ^d
Smooth muscle	19.3-4.3 ^e	216 ^d	0.047 ^d	-	-	-
Endothelium	0.4 ^f	5.4 ^d	0.000216 ^d	0.358	4520	0.162

a. All parameters were extracted from (1) unless otherwise specified

b. (2) c. (3) d. Calculated or estimated e. (4) f. (5)

References:

1. R.A. Parent. *Treatise on Pulmonary Toxicology: Comparative biology of the normal lung*, CRC Press Boca Raton, 1992.
2. J.G. Widdicombe. Airway liquid: a barrier to drug diffusion? *Eur Respir J.* 10:2194-2197 (1997).
3. M.D. Cohen, J.T. Zelikoff, and R.B. Schlesinger (eds.). *Pulmonary Immunotoxicology*, Springer, 2000.
4. M. Salmon, D.A. Walsh, T.J. Huang, P.J. Barnes, T.B. Leonard, D.W. Hay, and K.F. Chung. Involvement of cysteinyl leukotrienes in airway smooth muscle cell DNA synthesis after repeated allergen exposure in sensitized Brown Norway rats. *Br J Pharmacol.* 127:1151-1158 (1999).
5. G.J. Crane, N. Kotecha, S.E. Luff, and T.O. Neil. Electrical coupling between smooth muscle and endothelium in arterioles of the guinea-pig small intestine. *Phys Med Biol.* 46:2421-2434 (2001).